# Small Scale Mechanics Applied to Nuclear Materials


**James Herring**

St Anne's College,
University of Oxford

A thesis submitted for the degree of Doctor of Philosophy

Trinity Term 2015

# Abstract

Ion implantation is increasingly used as a cost effective and safe alternative to neutron irradiation in the study of materials for future nuclear applications. However, the micron-sized layers of radiation damage necessitate the use of small scale testing techniques to obtain mechanical properties data from these materials. This thesis explores such techniques, highlighting the relative merits and limitations of nanoindentation, and the deflection of FIB-machined specimens, in a variety of applications.

As a simple starting point, the effect of crystal orientation on nanoindentation hardness and modulus is explored in a pure Fe polycrystal, with selected indents examined further post-test by HR-EBSD and AFM. Hardness in grains with <111> and <110> surface normal directions is found to be ~20 % higher (~1.1 GPa) than those with <100> surface normals (~0.95 GPa), whilst no discernible trend is seen for modulus.

A novel L-shaped micro-cantilever technique is developed and used to extract single crystal elastic constants within a single grain of Fe. A computational routine minimising the difference between experimental data and the response of an FE model is used to extract such constants, with a good agreement between experiment and literature found after two runs.

Slip transfer across grain boundaries is studied in unirradiated and ion-irradiated samples using nanoindentation. Grain boundaries in the irradiated specimen show less resistance to slip transfer, and the presence of dislocation bursts associated with the operation of dislocation sources in adjacent grains is reduced compared to the unirradiated sample.

Finally, the effects of size and orientation on plastic properties are examined in FIB-machined micro-cantilevers. Two different functions are used to fit flow stresses evaluated at different maximum strains to beam width, and compared. Cantilevers orientated for multiple slip are observed to have lower flow stresses than those aligned for single slip with a Schmid factor of 0.5.

The work in this thesis highlights the importance of both types of small scale mechanical test in providing information of relevance to candidate materials for nuclear applications. Nanoindentation is able to quickly probe mechanical characteristics, but at the expense of a well-defined stress state under the indenter tip, whereas FIB-machined specimens can provide a simpler stress state to test, for higher costs of time and instrument usage.

# Preface

This thesis describes research carried out in the Department of Materials at the University of Oxford between October 2010 and June 2015, under the supervision of Professor Angus Wilkinson, as part of the Materials for Fusion & Fission Power group (EPSRC grant EP/H018921/1). No part of this thesis has been previously submitted for a degree at this or any other university. Where the work of other authors has been drawn upon, this has been referenced and acknowledged in the text. A full list of cited references is given at the end of the thesis.

Some of the work in Chapter 4 on L-shaped cantilevers has been presented as a poster at the ECI Nanomechanical Testing in Materials Research and Development conference in Olhão, Portugal, October 2013.

# Acknowledgements

First and foremost I would like to thank Professor Angus Wilkinson, my supervisor, for his patient guidance and support throughout my time at Oxford, especially during the write up period.

Thanks to Professor Steve Roberts for giving me the opportunity and providing within the MFFP group an exciting and stimulating environment in which to work.

Dr. Ben Britton deserves thanks for helping to show me the ropes at the start and putting up with many of my stupid questions in the process.

Thanks to Chris Hardie for providing the irradiated samples used in Chapter 6, and to Jicheng Gong and Ed Tarleton for support on several aspects of the thesis.

Many thanks to office buddies past and present, in particular Chris Burrows, Sean Yardley, Katie Plummer, Chris Hardie, Kris Bhojwani, Christian Beck, Mike Gorley and Ele Grieveson, Yi Guo and Junnan Jiang.

I wouldn't be the person I am today without the continuous love and support of my parents and sister over the past 28 years.

Finally I'd like to thank my girlfriend Karen for her love and support, for always cheering me up when I needed it, and for making my final year in Oxford the best by far.

# Contents

# Glossary

| | |
|---|---|
| AFM | Atomic Force Microscopy/Microscope |
| bcc | Body Centred Cubic |
| CCFE | Culham Centre for Fusion Energy |
| CRSS | Critical Resolved Shear Stress |
| CSM | Continuous Stiffness Measurement |
| DCM | Dynamic Contact Module |
| DD | Dislocation Dynamics |
| dpa | Displacements Per Atom |
| EBSD | Electron Backscatter Diffraction |
| EBSP | Electron Backscatter Pattern |
| EFDA | European Fusion Development Agreement |
| FE | Finite Element |
| FEG | Field Emission Gun |
| fcc | Face Centred Cubic |
| FIB | Focussed Ion Beam |
| GND | Geometrically Necessary Dislocation |
| hcp | Hexagonal close packed |
| HR-EBSD | High Resolution Electron Backscatter Diffraction |
| IPF | Inverse Pole Figure |
| ISE | Indentation Size Effect |
| JET | Joint European Torus |
| LMIS | Liquid Metal Ion Source |
| MCO | Metal Crystals and Oxides |
| MFFP | Materials for Fusion & Fission Power group |
| OIM | Orientation Imaging Microscopy |
| ppm | Parts Per Million |
| RAFM | Reduced Activation Ferritic/Martensitic |
| SE | Secondary Electron |
| SEM | Scanning Electron Microscopy/Microscope |
| SGP | Strain Gradient Plasticity |
| SRIM | Stopping Range of Ions in Matter |
| TEM | Transmission Electron Microscopy/Microscope |

# 1 Introduction

The combined effects of population growth and continued economic development mean that the world demand for energy is expanding at an ever increasing rate. 80 % of the world's energy is currently supplied by fossil fuels, which due to their high level of $CO_2$ emissions threaten to cause potentially catastrophic climate change, in addition to high levels of pollution. Against this backdrop, it is imperative that clean sources of energy are developed.

Nuclear fusion has the potential to provide electricity with minimal greenhouse gas emissions, and enough fuel to last many millions of years. Inside a fusion reactor, two isotopes of hydrogen (dueterium and tritium) combine to produce a helium nucleus and a high energy neutron, which is rapidly emitted and strikes the walls of the reactor, heating them as it is slowed down. This heat is used to drive turbines and extract electricity from the process.

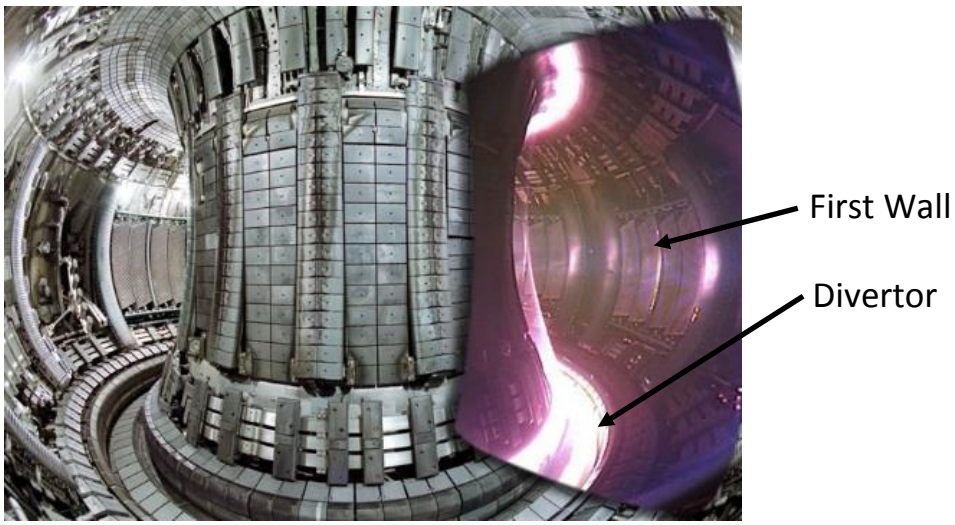


Figure 1-1: Inside view of the Joint European Tokamak (JET), based at Culham Centre for Fusion Energy (CCFE) (from [1]).

Due to the strong electrostatic repulsion between the positively charged deuterium and tritium ions, very high temperatures must be sustained in the reactor vessel to overcome this

potential barrier. The requirements for the components of future fusion power plants are therefore some of the most extreme in materials science. Structural materials face a combination of elevated temperatures (775 to 3475K for the plasma facing components [2], see Figure 1-1), high levels of neutron irradiation (20 to 30 displacements per atom (dpa) a year) and high mechanical stresses in service.

Furthermore, in order to minimise the long term environmental impact of fusion, many of the conventional alloying elements for steels cannot be used, as under irradiation they would transmute into long-lived radionuclides, leaving a semi-permanent waste legacy (see Figure 1-2). Currently materials meeting all of these criteria do not exist, and will need to be developed and comprehensively tested before fusion energy can become a viable alternative to current forms of electricity generation.

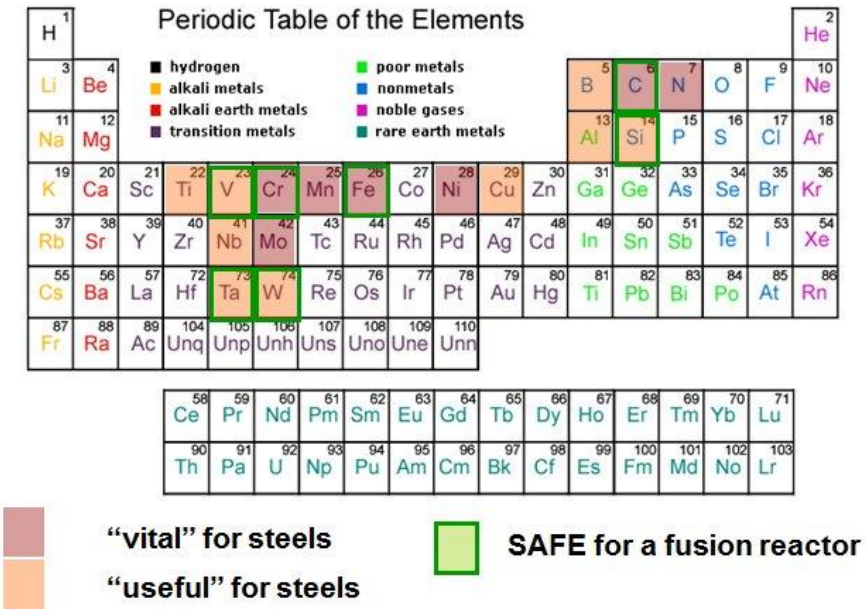


Figure 1-2: Periodic table showing materials which do not transmute into long-lived radioactive waste (green), in addition to elements commonly used in steels (from [3]).

Currently, materials test reactors are used to test the response of materials to neutron irradiation. In these reactors sample specimens are placed close to the fission core, and

exposed for a period of several months or years. However, due to nuclear transmutation effects, these samples become radioactive, and can only be tested in specialised ‘hot cells’. Furthermore, the rate of damage production in fusion power plants is calculated to be many times that of fission plants. To counteract such problems, ion implantation has recently been used as a proxy for neutron irradiation, enabling a high rate of damage production, and avoiding problems to do with handling ‘active’ samples.

In such experiments, ions of the same species as the material being implanted are fired at target specimens, with parameters such as temperature, ion energy, dose and dose rate being specified by the experimenter. Dual (or triple) implantation is also possible, so the effect that transmutation products (e.g. He or H) have on the irradiated microstructure can be emulated and studied. Furthermore, implantations can be performed in-situ, so that the formation and motion of crystalline defects can be directly observed with TEM imaging.

Despite these advantages, heavy ions only generate irradiation damage to depths of a few microns, which means that conventional mechanical tests on bulk samples cannot be used. To this end, techniques have been developed which use focussed ion beam (FIB) machining to make test specimens located entirely within the ion damaged layer. However, it is known that there are very strong effects of specimen size on measured quantities, making it difficult to relate the results obtained on the micro-scale to the mechanical properties of bulk materials.

The aim of this research project is to use and develop the small scale mechanical testing methods of both nanoindentation, and the deflection of FIB-machined specimens, to investigate the plastic and elastic properties of materials. The material systems of interest

are Fe and Fe-Cr alloys, which form the basis of candidate structural materials for fusion power plants.

The effect of crystal orientation on the measured hardness and modulus of iron during nanoindentation shall be determined, in order to establish the advantages and limitations of using such a method to investigate anisotropy in micron-sized layers. A method capable of determining the full set of single crystal elastic constants for cubic crystals shall be established, feeding into fusion relevant modelling for which elastic anisotropy is of key importance. The role of grain boundaries in providing a barrier to plastic flow in fusion relevant materials will be investigated by nanoindenting close to boundaries in ion-irradiated polycrystals, and comparing the hardening behaviour to that seen near boundaries in unirradiated polycrystals. Finally, the relationship between specimen size and plastic behaviour in FIB machined micro-cantilevers will be investigated, with the aim to establish which theory of size dependence is best supported by the data. In addition, the effect of crystal orientation on the plastic behaviour of micro-cantilevers will be studied, highlighting the importance of anisotropy when using micro-mechanical tests to investigate and develop materials for nuclear fusion power generation.

Following this brief introduction, the structure for the remainder of the thesis is as follows:

- In Chapter 2, a review of relevant literature will give an overview into the fields of nanoindentation and small scale mechanical testing, with a particular focus on FIB-machined micro specimens;
- In Chapter 3, the major experimental methods used for this DPhil will be outlined, including a description of the main instruments and their operation;

- In Chapter 4, a study into the effect of crystal orientation on nanoindentation hardness and modulus will be detailed;
- Chapter 5 will describe a novel technique using an L-shaped micro-cantilever to extract single crystal elastic constants;
- In Chapter 6, a nanoindentation study into slip transfer at grain boundaries using both unirradiated and ion-irradiated Fe-C will be described;
- In Chapter 7, a micro-cantilever experiment examining the effects of size and orientation will be presented;
- Finally, a summary of the experimental results detailed in this thesis will be given in Chapter 8.

# 2 Literature Review

This literature review will focus on the various methods by which mechanical properties have been measured, using limited testing volumes. Following this introduction, I will give an overview of micromechanical testing techniques developed thus far, from the use of nanoindentation to obtain the local mechanical properties of thin films and ion implanted layers, to the more recent advent of using FIB-machined specimens to conduct well-defined tests at the micro-scale.

## 2.1 Nanoindentation

Hardness testing is one of the most important mechanical property characterisation techniques in materials science, due to its ease of use, speed, and wide applicability to a variety of material systems, in addition to being essentially non-destructive [4,5]. Hardness ($H$) can also be loosely correlated with other parameters such as flow stress ($\sigma$), as described by Tabor's hardness rule [6,7]:

$$H \approx 3\sigma \tag{2-1}$$

Static indentation hardness tests, such as the Vickers test, involve measuring the residual impression left by pressing into a material's surface an indenter of well-defined shape, under a reference force. The hardness is typically given by the force divided by the contact area that the indenter makes with the material, which can be calculated based on a knowledge of the indenter tip geometry, and the projected area of the indentation. However, for small loads, measuring the indent area becomes an increasing source of uncertainty, as the resolution limits of optical microscopy are reached (and systematic SEM/TEM imaging would be too time consuming to use).

Pethica et al. [5] were the first to develop a system capable of making continuous measurements of load and displacement during indentation, which they used to measure the hardness of steel implanted with nitrogen ions, at depths of ~20 – 300 nm [8]. Their nanoindenter used a coil and magnet assembly to apply the load, with a resolution of 2 μN, whilst the diamond indenter tip was attached to a capacitive displacement transducer, sensitive to movements of 0.2 nm. In this early work, the size of the impression made by the indent was determined by making replicas of the indents, and using TEM imaging to measure the size of the indent area from these replicas.

By making continuous measurements of load and displacement during indentation, and with unloading steps, nanoindentation allows hardness to be measured as a function of depth, and without the need to independently measure the contact area (see below). Furthermore, the unloading portion of the curve can be used to determine elastic properties, and time dependent plastic properties (such as creep) can be measured by incorporating a hold sequence into the experiment [9]. Following is a brief review of the methods used to obtain mechanical data (primarily hardness and modulus) from nanoindentation experiments.

### 2.1.1 Determination of mechanical properties

A typical load-displacement ($P$-$h$) curve obtained by nanoindentation is shown in Figure 2-1. The most widely used method for analysing this data to obtain mechanical properties is by Oliver and Pharr [9]. The following is a review of their approach.

The key parameters from Figure 2-1 for the determination of mechanical properties are the maximum load, $P_{max}$, the depth at maximum load, $h_{max}$, the depth of the contact impression upon unloading, $h_f$, and the initial unloading contact stiffness, $S = {dP}/{dh}$.

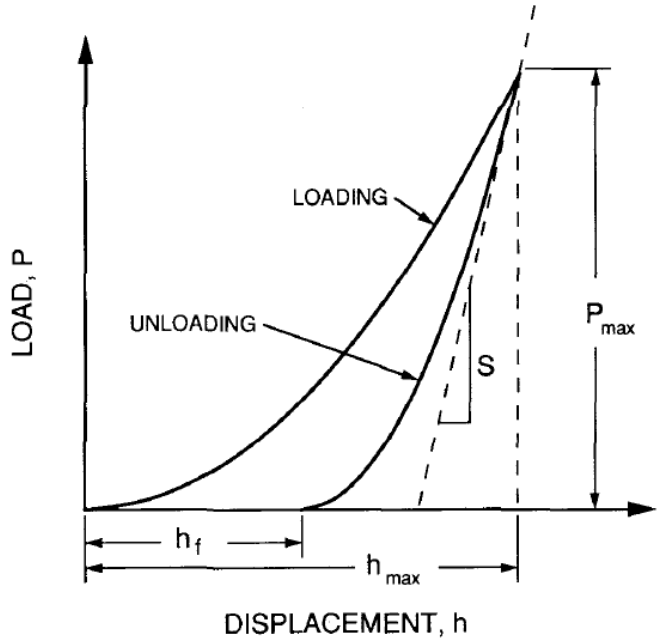


Figure 2-1: Typical $P$-$h$ curve obtained by nanoindentation (from [9]).

#### *2.1.1.1 Elastic Properties*

At any point on the curve of Figure 2-1 after initial yielding (see section 2.1.2), the displacement is made up of both an elastic and a plastic component. Upon unloading, the elastic component relaxes, and a permanent hardness impression is left. Much work on the analysis of $P$-$h$ curves of this type has concerned the exact form of the empirical expression governing the unload portion, with Doerner and Nix [10] suggesting that a linear function could be fitted to the upper third of the unloading curve. Such a linear function also describes a rigid flat punch indenting a surface, and therefore implies that the contact area between the indenter tip and surface remains constant during an unload (even for non-flat punch indenter tips). However, Oliver and Pharr [11] have argued, with reference to experimental data, that the unload behaviour is more accurately described by a power law, of the form:

$$P = B(h - h_f)^m \tag{2-2}$$

where constants $B$ and $m$ are fitted using a least squares method. Empirically determined values of $m$ have been found to vary between 1.2 and 1.6 ($m = 1$ for the flat punch approximation).

The initial unloading contact stiffness, $S$, is then found by differentiating equation (2-2) (see Figure 2-1), and substituting in $P_{max}$ and $h_{max}$. The elastic modulus is obtained via:

$$S = \frac{dP}{dh} = \beta \frac{2}{\sqrt{\pi}} E_r \sqrt{A} \tag{2-3}$$

where $\beta$ is a dimensionless parameter which varies according to the indenter tip, $A$ is the projected area of the elastic contact, and $E_r$, the reduced modulus is defined as:

$$\frac{1}{E_r} = \frac{1 - \upsilon^2}{E} + \frac{1 - {\upsilon_i}^2}{E_i} \tag{2-4}$$

where $E$ and $\upsilon$ are the Young's modulus and Poisson's ratio, respectively, of the specimen, and $E_i$ and $\upsilon_i$ are those of the indenter. Thus, if the contact area at maximum indentation can be established, the elastic modulus of the indented specimen can be obtained. Doerner and Nix estimated the contact area by extrapolating the linear portion of the unload curve to zero load, to obtain the plastic depth. However, as previously noted, this approach is only valid for flat punch indenters. Another approach which was previously mentioned uses TEM imaging of indent replicas, however this would be time consuming to perform for every set of indentation experiments [9].

Oliver and Pharr's approach assumes that the contact area can be related to the indentation depth, via an area function. For a perfect Berkovich indenter tip (see Figure 3-2), the area function is:

$$A(h_c) = 24.5h_c^2 \tag{2-5}$$

where the contact depth $h_c$ at $P_{max}$ is given by:

$$h_c = h_{max} - \epsilon\frac{P_{max}}{S} \tag{2-6}$$

where $\epsilon$ is a geometric constant depending on the type of indenter. Equation (2-5) can be used as a first approximation of the contact area. For more accurate results, the total measured compliance is first modelled as:

$$C = C_s + C_f \tag{2-7}$$

where $C_s$ is the sample compliance and $C_f$ is the load frame compliance. The sample compliance is simply the inverse of equation (2-3), giving:

$$C = C_f + \frac{1}{\beta}\frac{\sqrt{\pi}}{2E_r}\frac{1}{\sqrt{A}} \tag{2-8}$$

Assuming that elastic modulus is independent of indentation depth, a plot of $C$ vs $A^{-0.5}$ will be linear, with the y-axis intercept giving the load frame compliance. Large indents, for which the 2nd term on the right is small, will give the most accurate values of $C_f$. Typically, indents

are made in a metal of low hardness such as aluminium, to obtain large indents, from which initial estimates of $E_r$ and $C_f$ can be made. Following this, equation (2-8) is rewritten as:

$$A = \frac{\pi}{4\beta^2}\frac{1}{E_r^2}\frac{1}{(C - C_f)^2} \tag{2-9}$$

and data from indents of a variety of depths are used to fit $A$ vs $h_c$, to the relationship:

$$A(h_c) = 24.5h_c^2 + C_1h_c^1 + C_2h_c^{1/2} + C_3h_c^{1/4} + \cdots + C_8h_c^{1/128} \tag{2-10}$$

where $C_1$ to $C_8$ are constants. Following the leading term on the right hand side, additional terms represent imperfections of the tip due to blunting. As $E_r$ and $C_f$ both depend on contact area, the new area function is re-inserted into equation (2-8), and the process is iterated, until the calculated values converge.

Since its publication 23 years ago [9], the Oliver-Pharr method for the analysis of $P$-$h$ curves has become widely used, and is now featured in the analysis software of many commercial nanoindentation systems. One of its major attractions is that no imaging of indents is required, so that the number of measurements can be greatly increased. A key drawback is that no account is taken of material "piling-up" around the indenter tip. This effect, often observed in elastic-plastic materials [11], causes the contact area to increase, and can therefore lead to significant overestimates of hardness and modulus.

The Oliver-Pharr method also assumes elastic isotropy, whereas most real materials are elastically anisotropic [12]. Theoretical models have been developed to predict the indentation moduli of anisotropic materials, based on known elastic constants [13].

However, it is much more difficult to extract elastic constants from measured indentation moduli, as this result is of many elastic constants averaged over a complicated stress field (see chapters 4 and 5).

#### *2.1.1.2 Hardness*

With the contact area established, the analysis in the previous section can be easily extended to give a measure of hardness, using the standard definition:

$$H = \frac{P_{max}}{A} \tag{2-11}$$

#### *2.1.1.3 Applications*

Since this initial work provided the theoretical and experimental underpinnings of the field, nanoindentation has been used extensively, with its widest use being in the measurement of the mechanical properties of thin films and coatings. Often, higher strengths are reported in thin films as compared with bulk materials. This is often thought to be due to the presence of the substrate, which has a confining effect on dislocation motion in the film, and hence can cause dislocation pile-ups [14]. However, this research project is motivated by the need to extract mechanical properties from ion-irradiated layers, and as such the use of the nanoindenter to probe thin films will not be reviewed here (see the review by Kraft and Volkert for more information on this topic [15]).

In recent years, there has been renewed interest in using nanoindentation to measure the properties of ion-irradiated layers, motivated by the need to develop radiation resistant materials for nuclear applications. For example, Hosemann et al. [16] have conducted nanoindentation on ion-irradiated steels, finding that radiation induced hardening is a

sensitive function of microstructure, with larger grained ferritic material (~100 – 300 µm) showing greater hardening than finer grained material (~5 – 10 µm). Heintze et al. have also conducted such tests on ion-irradiated steels [17] and iron-chromium alloys [18], demonstrating that nanoindentation is an appropriate tool for investigating hardening as a function of irradiation temperature, dose, and chromium content.

Nanoindentation into different grains of a polycrystalline sample allows the effect of crystal orientation on hardness to be measured (see chapter 4). Miura et al. [19] used this type of testing to investigate the crystallographic dependence of hardness in ion-irradiated stainless steels. Although no clear trend was found (see Figure 2-2), this could be due a lack of grains sampled, combined with the inevitable scatter in indentation hardness results.

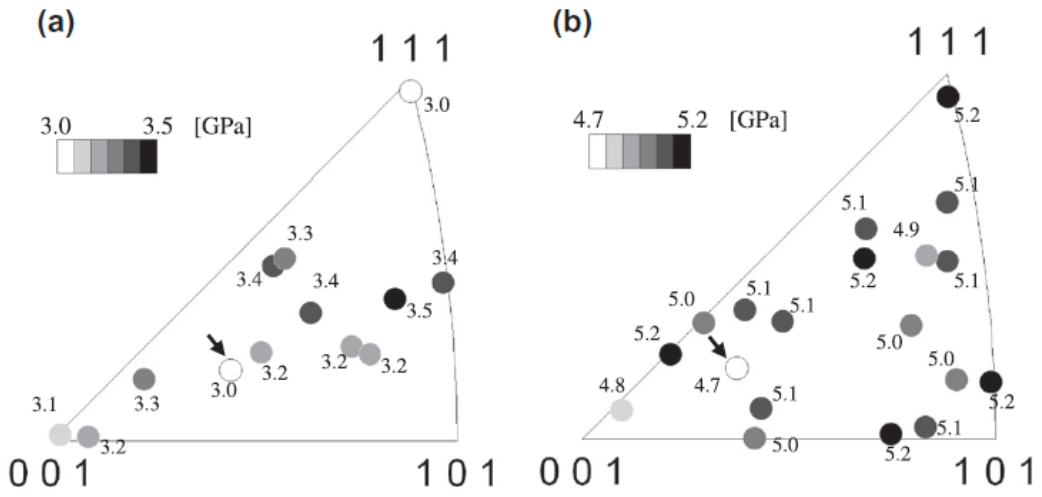


Figure 2-2: Dependence of hardness on crystallographic orientation in a) unirradiated stainless steel; b) stainless steel ion-irradiated at 10 dpa (from [19]).

### 2.1.2 Elastic-plastic transition

A common feature seen in many indentation experiments at low loads, is the so-called 'pop-in' effect, whereby a significant displacement burst occurs in the $P$-$h$ curve (Figure 2-3). This is thought to result from the homogeneous nucleation of dislocations, in a previously defect

free crystal, as the maximum shear stress corresponding to the pop-in load approaches the theoretical strength of the crystal [14,20].

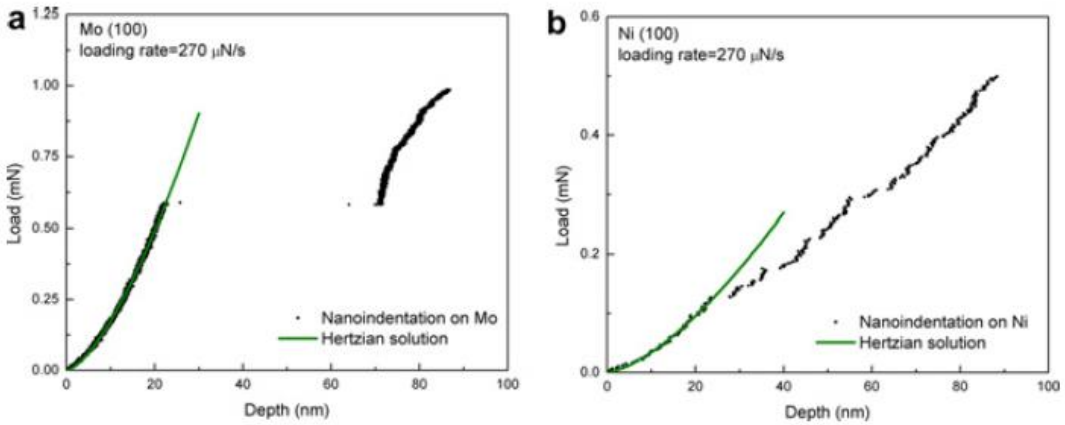


Figure 2-3: a) Load-displacement 'pop-in' in single crystal Mo (bcc) and b) much smaller bursts in single crystal Ni (fcc) (from [21]).

Prior to the pop-in, the $P$-$h$ curve follows the equation of an elastic Hertzian contact [22], given by:

$$P = \frac{4}{3} E_r \sqrt{R h^3} \tag{2-12}$$

where $R$ is the indenter tip radius; all other parameters have been previously defined. In this section of the curve, the displacement is completely reversible, and therefore no impression would be left if the tip was withdrawn. Such displacement bursts therefore mark the division between elastic and elasto-plastic indentation.

Pop-in behaviour has been investigated as a function of parameters such as crystal orientation [20], surface polishing [23] (Figure 2-4a), and FIB damage [24] (Figure 2-4b), among others. For the latter two conditions, pop-ins are suppressed with poorer polishing,

and increasing amounts of FIB damage, as dislocations introduced by these two factors mean that nucleation of new dislocations is not needed to generate plastic flow.

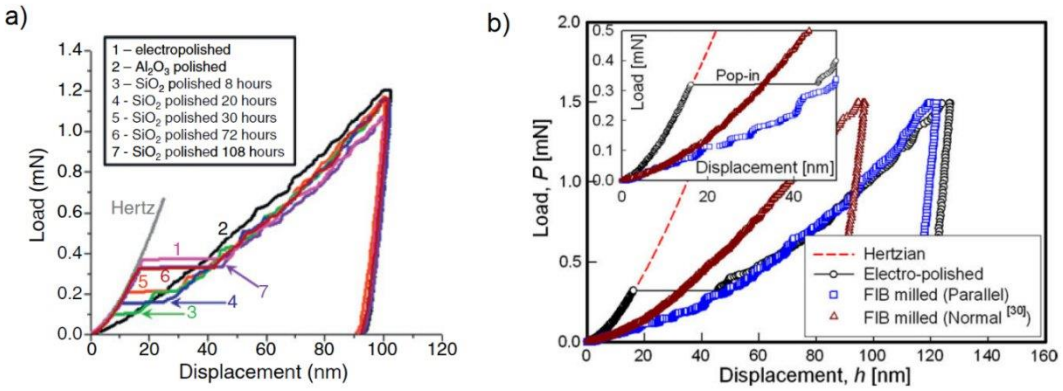


Figure 2-4: a) Pop-in behaviour in Mo, as a function of polishing time, with increasing loads reached for longer polishes (see curves 3 → 7) (from [23]); b) Pop-in suppression, along with radiation hardening seen for two FIB conditioned Mo surfaces (from [24]).

In general, pop-ins clearly demonstrate the stochastic deformation behaviour often observed at the small scale. Such behaviour will also be seen later in the deformation of FIB-machined micro and nano-specimens.

### 2.1.3 Indentation Size Effect

A phenomenon commonly encountered in nanoindentation experiments is an increase in hardness at shallower indent depths, known as the "indentation size effect" (ISE). McElhaney et al. [25] reported such an effect in both strain hardened polycrystalline copper and single crystal annealed copper (Figure 2-5). Although the presence of oxide layers has sometimes been invoked to account for this behaviour, it has been observed across a wide range of materials, including those for which oxide layers are not usually present [5].

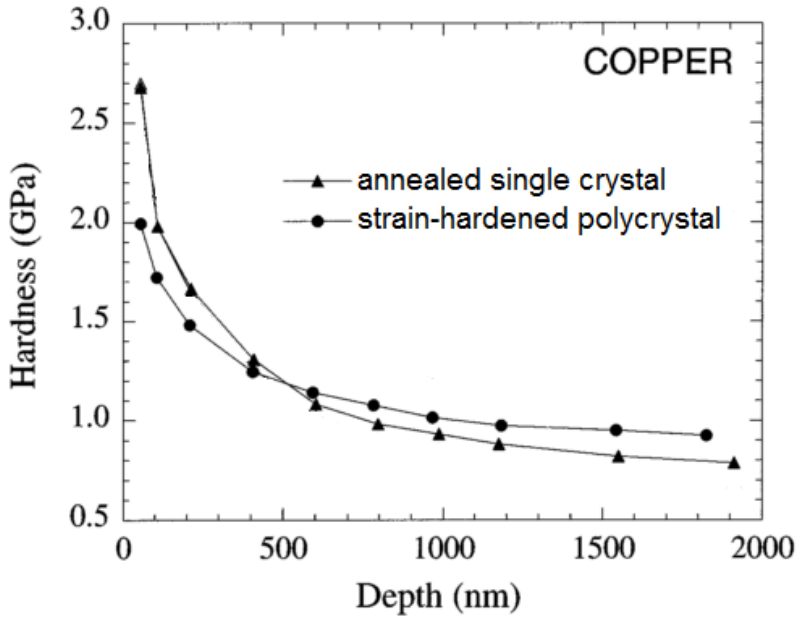


Figure 2-5: Hardness as a function of indent depth in Cu, as measured by McElhaney et al. [25].

Nix and Gao [7] have developed a mechanistic model to explain the ISE, based upon the fact that plastic strain gradients in materials must be supported by the presence of so called "geometrically necessary dislocations" (GNDs), i.e. those which are necessary to support curvature in the crystal lattice (Figure 2-6).

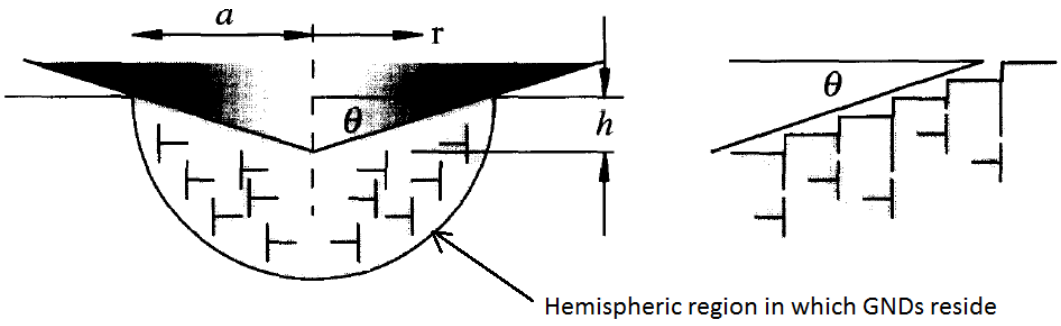


Figure 2-6: Schematic representation of the Nix-Gao model, showing GNDs residing inside a hemispherical region, under a conical indenter (from [7]).

Indents of shallower depth will produce larger strain gradients than those of larger depth, and will therefore require a higher density of GNDs. This results in greater hardening at lower

depths, causing the observed ISE. The starting point of the Nix-Gao model is the Taylor relation, which relates flow stress to the square root of dislocation density:

$$\sigma = \sqrt{3}\alpha G b\sqrt{\rho_T} \tag{2-13}$$

where $\alpha$ is the Taylor factor (which varies between 0.1 and 0.5 [26]), $G$ is the shear modulus, $b$ is the Burgers vector, and $\rho_T$ is the total dislocation density, composed of both the GND density ($\rho_G$) and the density of the statistically stored dislocations (SSDs) ($\rho_S$). Based on the assumption that the GNDs are all located within a hemispherical region with a radius equal to the radius of the contact area (Figure 2-6), and using geometric considerations, the density of GNDs can be considered as:

$$\rho_G = (3\tan^2\theta)/(2bh) \tag{2-14}$$

Inserting this into equation (2-13), via $\rho_T = \rho_G + \rho_S$, and using Tabor's relationship (equation (2-1)), one can obtain a depth-dependent relationship for hardness:

$$H = H_0\sqrt{1 + \frac{h^*}{h}} \tag{2-15}$$

where $H_0 = 3\sqrt{3}\alpha G b\sqrt{\rho_S}$ is the macroscopic hardness and $h^* = (3\tan^2\theta)/(2b\rho_S)$ is the scale length below which hardness appreciably increases [27]. The validity of the Nix-Gao model can be tested by noting that:

$$H^2 = H_0^2\left(1 + \frac{h^*}{h}\right) \tag{2-16}$$

and therefore plotting $H^2$ against $1/h$ should result in a straight line with an intercept at $H_0^2$ and a slope related to $h^*$. This is demonstrated in Figure 2-7 for McElhaney's single crystal copper data (shown in Figure 2-5). The linearity of the curve provides good support for Nix-Gao model, except at small indents (i.e. large $1/h$), where the data diverges from the straight line fit. It is possible that this is due to the larger relative errors in the determination of contact area at smaller depths; however, a similar divergence from the predicted Nix-Gao behaviour has also been observed in Ir and MgO for the smallest depths [27].

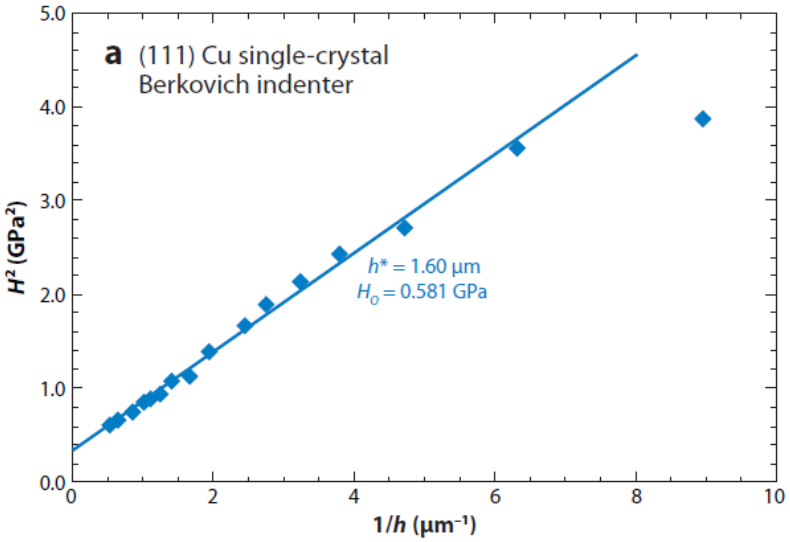


Figure 2-7: Plot of $H^2$ vs $1/h$ for the annealed single crystal data shown in Figure 2-5, from McElhaney et al. [25]

A possible reason for the breakdown of the Nix-Gao model for small indents has to do with the assumption that the radius of the hemispherical region containing the GNDs is equal to the radius of the contact area. This suggests that GND density will continue to scale with $1/h$ at small indent depths, via equation (2-15). However, if the dislocations are of similar signs, then mutually repulsive forces will prevent the size of the plastic zone from contracting without limit, meaning that the model will overestimate hardness for smaller indents (as seen in Figure 2-7).

Another shortcoming of the Nix-Gao model is that it is continuum based model, and so cannot take into account inhomogeneities in deformation, instead relying on a spatial average of GNDs to be used [28].

Experimental evidence in which the plastic zone size is directly measured (see below) is at odds with the Nix-Gao assumption of a hemispherical distribution of GNDs under the indenter tip. In reality, dislocations are heterogeneous during deformation, forming networks of cells and other structures. The Nix-Gao model is also unable to take account of stochastic displacement bursts, e.g. the initial elastic to elasto-plastic pop-in event seen in nanoindentation studies (see section 2.1.2).

### 2.1.4 Limitations of Nanoindentation

Nanoindentation provides an easy and relatively non-destructive way of measuring a range of mechanical parameters, such as indentation modulus and hardness in addition to time dependent properties such as creep. However, the stress state under the indenter tip is complex, and varies strongly with position, meaning that it is not clear exactly what volume is being probed. For determining elastic properties, this means that the measured indentation modulus will be an average over many crystallographic directions, making the extraction of single crystal elastic constants difficult [29]. From post analysis of indentations using EBSD [30--32] and TEM [33,34], it is clear that the plastic zone is heterogeneous (see section 6.1.4), with multiple slip systems being activated, such that obtaining critical resolved shear stress (CRSS) values is also non-trivial.

Due to the size of the elastic and plastic zones, the presence of substrates in thin film measurements can have a significant effect on results. Such effects may need to be taken

into account when measuring the indentation response of ion-irradiated layers, where the interface between irradiated and non-irradiated regions may produce results which diverge from the bulk behaviour [35].

Due to these limitations, techniques have been developed which use nanoindentation systems to compress, bend, or pull test pieces with well-defined geometries and stress states.

## 2.2 Focussed Ion Beam Fabricated Specimens

The recent application of focussed ion beam systems to the fabrication of micro-test specimens has led to an explosion in the field of small scale mechanical testing. Using such an approach, test pieces of micron and even sub-micron size and with differing geometries can be produced, enabling testing in compression [14,36], bending [37--39], and tension [40].

These micro-specimens can be deflected using a high sensitivity instrumented indentation device such as a nanoindenter, enabling the testing of mechanical properties on length scales similar to those on which fundamental deformation mechanisms operate. Following on from the historical development of this field, the testing of micro-pillars will reviewed first, before a discussion of micro-cantilevers.

### 2.2.1 Pillars

Since Uchic et al. first published their work in 2004 on the compression of FIB-machined Ni and Ni alloy micro-pillars [36,41], the field has grown enormously, with many groups now using this technique to study fundamental deformation mechanisms occurring at the micro and nano-scale, in a wide range of materials. It would be impossible to provide a comprehensive overview of such research in this review; however, a few key results and

some now standard methodologies are presented below (see reviews by Uchic et al. [42,43], Kraft et al. [44], and Greer et al. [45], for a more thorough summary).

In Uchic et al.'s study, micro-pillars were FIB milled in a Ni single crystal in a single slip orientation, with pillar diameters ranging from 0.5 to 40 μm, and aspect ratios (i.e. the ratio of pillar height to pillar diameter) of 2:1 to 4:1. Once an appropriate site had been selected on the sample surface using FIB imaging, a "series of concentric annular milling patterns" [41] were used to produce a pillar like structure with tapered sides, centred in a cavity (Figure 2-8a). For this stage, relatively high milling currents of 20 to 5 nA were used. The sample was then tilted so that the angle between the plane of the sample surface and the ion beam was as small as possible (28° for their system), and a lathe-like technique was used, whereby the sample was rotated about the pillar axis in small steps, and beam currents of 7 to 0.05 nA were used to remove the taper. This process was aided by image-recognition software, enabling the pillar to be re-centered after each rotation (guided by a fiducial mark milled on top of the pillar, see Figure 2-8b) and the whole process to be automated.

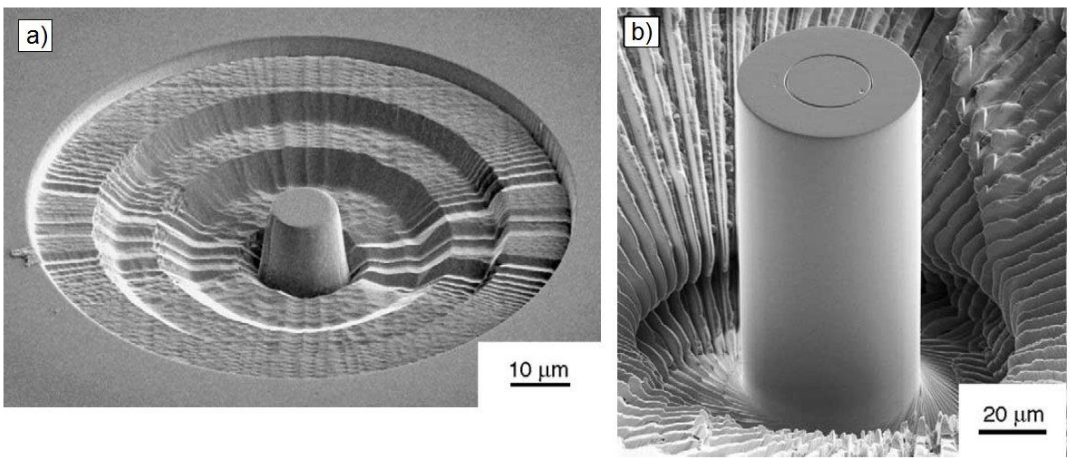


Figure 2-8: (a) The annular milling stage of micro-pillar production in Uchic et al.'s method; (b) a completed micro-pillar (from [41]).

Although relatively time intensive, this technique of annular milling followed by lathe milling produced micro-pillars with straight parallel sides and cylindrical cross sections of a constant diameter. A nanoindenter equipped with a diamond flat punch tip was used to uniaxially compress the pillars, at a constant rate of between 1 and 5nm/s. The load displacement curves obtained from these tests (Figure 2-9A) show that when decreasing the pillar diameter from 20 µm to 5 µm, the yield strength of the Ni pillars increased by 70 MPa (> 100 %), indicating that sample size plays a key role in determining mechanical properties in such tests. Furthermore, the behaviour of the deformation varied significantly with sample size, going from a smooth load-displacement curve in the large pillars to a jerky stochastic regime in the smaller pillars, where yield was followed by large displacement bursts (of up to 19 % strain) similar to the pop-ins described earlier in section 2.1.2. These results were explained with reference to post testing SEM images (see Figure 2-9B and Figure 2-9C), which showed that smaller pillars contained fewer but more active slip bands than larger pillars, suggesting that decreasing pillar diameter resulted in fewer slip systems being activated.

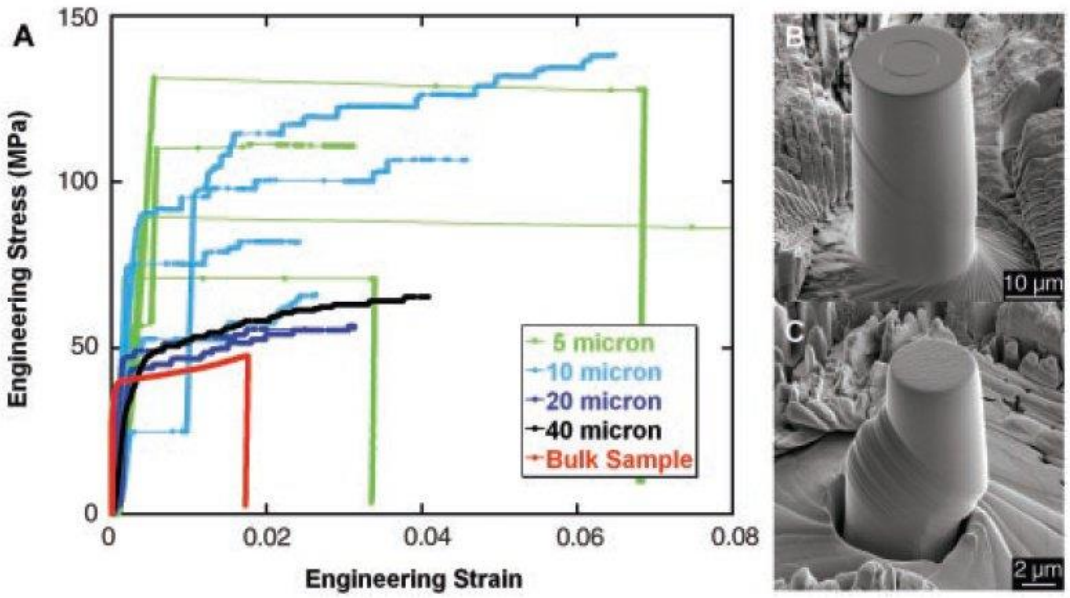


Figure 2-9: A) Stress strain curves for micro-pillars with diameters from 5 – 40 µm, in addition to bulk sample results for comparison. B) SEM image of 20 µm pillar at 4% strain. C) SEM image of 5 µm pillar at ~19% strain (following displacement burst) (from [36]).

Subsequent to Uchic's work, the lathe-like milling technique has been rarely used, most likely because it requires specialist image recognition software, and is also very time consuming compared to other methods. An alternative approach to pillar fabrication, which has subsequently been the most widely used method, was pioneered by Greer et al. [14]. This simply uses annular milling at a variety of different currents and tilt angles, to obtain pillars with tapered sides, at a much wider possible range of diameters than seen in Uchic's study (Figure 2-10). Greer used this technique to mill micro-pillars in gold, orientated parallel to the <001> direction and with diameters in the range 250 – 7450 nm. Upon compression, the stress-strain curves from these showed the same size dependent behaviour seen by Uchic, in addition to the increasingly stochastic, burst driven deformation with decreasing diameter (see Figure 2-11).

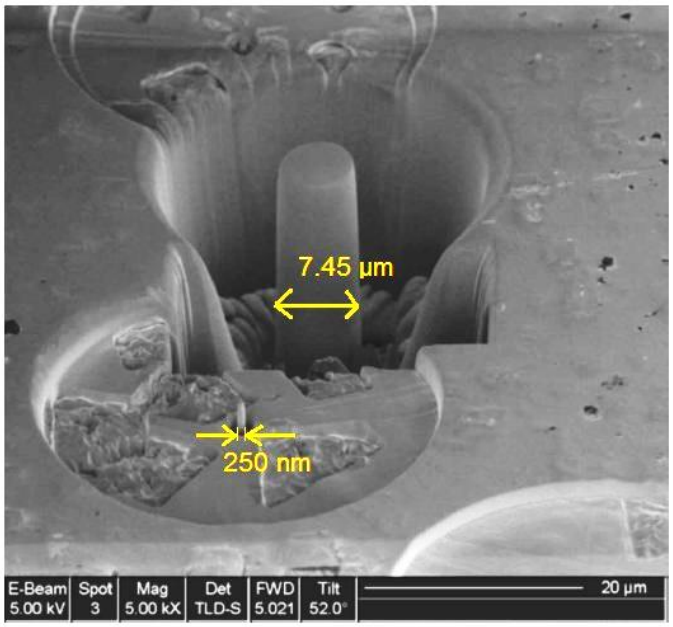


Figure 2-10: FIB-machined gold pillars by Greer, with differing diameters (from [46]).

For the smallest pillar, the flow stress at 10% strain reaches 800 MPa, roughly half the theoretical shear stress (resolved on the {111}/<00-1> slip system), and ~50 times the figure for bulk gold [46]. The mechanism proposed by Greer et al. to take account of this dramatic

increase in strength with decreasing sample size, is 'dislocation starvation'. In normal plastic behaviour, applied shear stress causes dislocations to mobilise, and multiply, via processes such as double cross slip. These dislocations then interact with each other and can become tangled and immobile, causing strain hardening (as seen for the 7.45 µm diameter pillar, Figure 2-11a). However, when the pillar size is sufficiently reduced, and the surface area to volume ratio increases, there is a high chance that a dislocation will annihilate at a free surface before having a chance to multiply. This will therefore cause the pillar to become dislocation starved, and further deformation will require the nucleation of new dislocations. This behaviour is confirmed by the stress-strain curve of a 400 nm pillar (Figure 2-11b), where displacement bursts are followed by periods of linear elastic loading.

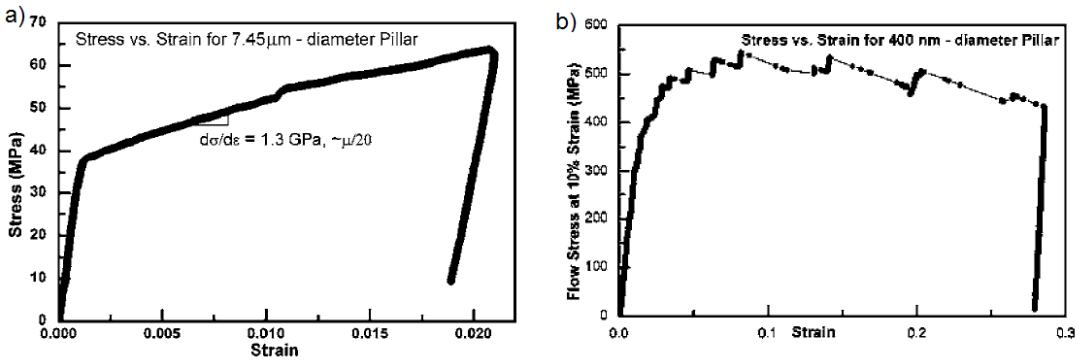


Figure 2-11: Stress-strain curves of compressed gold pillars, with diameters of 7.45 µm (a) and 400 nm (b) (from [46]).

These bursts can be interpreted as the points during deformation when new dislocations are nucleated, and proceed to rapidly exit the pillar's surface. TEM work by Greer confirmed this starvation theory, with only immobile dislocations being seen in deformed pillars [46].

In both of these papers, the discovered increase in strength with decreasing pillar diameter, or "smaller is stronger", was deemed highly significant, since it occurred in the absence of

strain gradients, and hence the increased strength could not be attributed to GNDs causing Taylor hardening (see section 2.1.3).

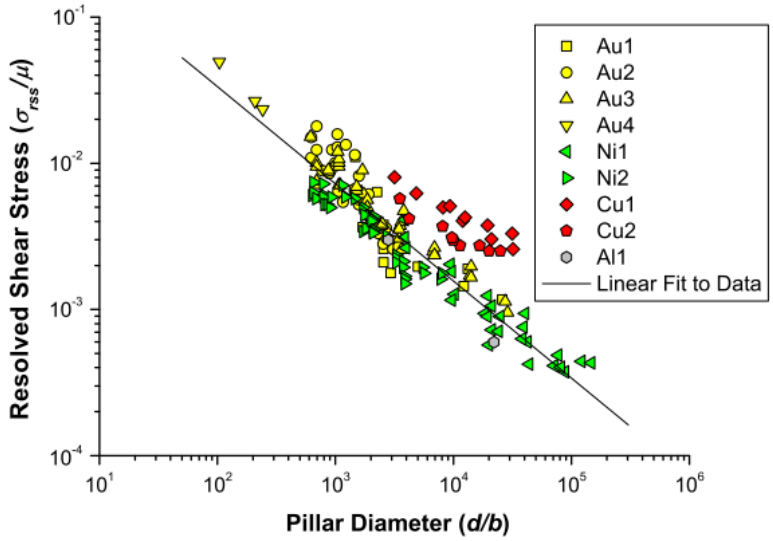


Figure 2-12: Resolved shear stress (normalised by shear modulus) vs pillar diameter (normalised by Burger's vector) for numerous fcc micro-pillars, with a linear fit to the Au, Ni, and Al data (from [47]).

Since this initial work, there have been numerous similar studies looking at the effects of specimen size on yield stress in micro and nano pillars, primarily in fcc materials. Considering several of these studies, Dou and Derby [47] empirically deduced a relationship between shear stress resolved onto a slip system ($\sigma_{rss}$) and pillar diameter ($d$), for fcc materials, as:

$$\frac{\sigma_{rss}}{G} = 0.71\left(\frac{d}{b}\right)^{-0.66} \tag{2-17}$$

where the numerical constants were found through a linear regression analysis of the data (Figure 2-12). They also suggested that bcc materials follow a similar scaling law.

In addition to the dislocation starvation argument presented by Greer, numerous other theories explaining the size effect have been proposed. One of the most popular is source truncation, which can be explained with reference to Figure 2-13. When a Frank-Read source

operates in a confined geometry such as a pillar, part of the dislocation line will bow out and annihilate at the surface, forming two single armed sources (see Figure 2-13a). The length of these sources is controlled by the distance between the pinning point and the free surface, with shorter sources requiring greater shear stress to move them.

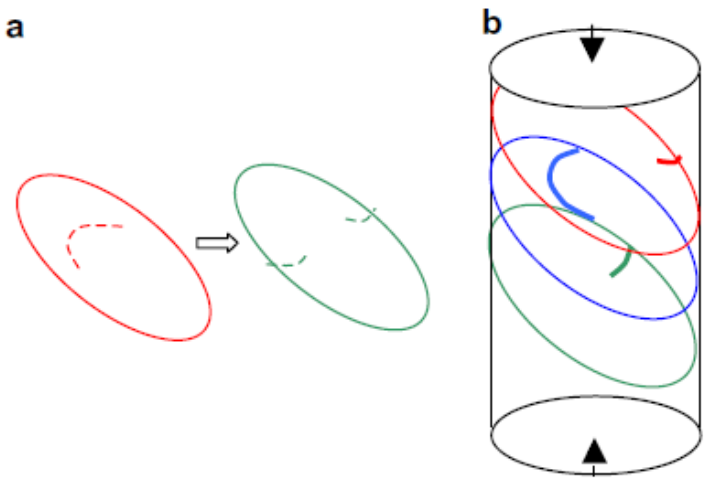


Figure 2-13: a) Schematic diagram showing how a Frank-Read source in a small sized pillar rapidly de-generates into two single armed sources; b) an example distribution of single armed sources of different lengths in a pillar. The longest (and therefore easiest to move) arm is the blue one; hence it will determine the yield strength of the pillar (from [48]).

A pillar with a larger diameter will contain a greater number of sources than a smaller one, and will also be more likely to contain sources of longer length. As longer sources are easier to operate than smaller ones, they will determine the lower bound of the yield strength of pillar, leading to the observed size effect.

#### *2.2.1.1 Advantages*

Compression testing of micro-pillar specimens is now a widely established field, enabling the investigation of fundamental deformation mechanisms, largely in the absence of strain gradients. The simplicity of the FIB based annular fabrication method, as compared with that used for other geometries (see section 2.2.2), means that the technique enables easy

comparison with results obtained by different research groups, over a range of material systems (e.g. bcc [49--52], fcc [14,36,46], hcp [53] and metallic glasses [54,55]), pillar diameters and aspect ratios [14,36], and increasingly, temperatures [56,57], strain rates [58], and irradiation conditions [59,60].

#### *2.2.1.2 Disadvantages*

However, there are several disadvantages in using micro-pillars for the determination of mechanical properties. It is difficult to measure elastic properties accurately, as in addition to the nanoindenter measuring the compliance of the pillar, it also measures the compliance resulting from the pillar acting like a flat punch pushing into the substrate [14]. Furthermore, geometric factors such as the fillet radius of the join to the substrate, the side taper, and aspect ratio can have a significant effect on the measured quantities. Zhang et al. [61] have conducted FE modelling on this subject, finding that taper causes the elastic modulus to be overestimated, and also increases the apparent yield strength, whereas misalignment of the flat punch and the pillar top causes the modulus to be underestimated, and can lead to buckling. Unless testing is conducted in-situ in an SEM or TEM the misalignment remains unobserved but has significant impact on the mechanical response.

In general, although compression tests are nominally uniaxial, the stress distribution inside pillars is not always clear. This is problematic, as areas of increased stress concentration can induce localised failure [61], and in other cases the constraining effect of the flat punch can restrict glide, causing dislocations to pile up and increasing the flow stress needed to re-activate sources, as observed by Kiener et al. [62].

For tests which require a wide range of crystallographic orientations to be probed, micro-pillar compression is unsuitable, as a great many number of surface normals of different planes would be needed [63].

Another problem is that there is currently a lack of consensus on what the exact contributions of different size effect mechanisms leads to the observed size dependence. It is possible to deform micro-pillars in-situ in a TEM [59], and directly observe the dislocation motions during deformation. However, in order to do this, pillars that are electron transparent must be prepared, putting an upper limit on the range of pillar diameters that can be investigated, which is substantially lower than pillar experiments conducted by most research groups. In addition, the geometrical constraints of the test mean that tilting the specimen through a range of angles in order to obtain the diffraction conditions necessary to image dislocations is not always possible.

### 2.2.2 Cantilevers

Thus far, a majority of the work on small-scale testing using FIB-machined specimens has focussed on the deformation of micro-pillars; accordingly, the literature on micro-cantilever testing is far less extensive. Despite this, cantilevers have been used to study a much wider variety of mechanical properties, including elasticity [63--65], fracture [66,67], and fatigue [68], in addition to plasticity at small length scales [26,37--39,69]. In addition, by careful placing of the highly stressed portion of the cantilever beam at particular microstructural features (e.g. grain boundaries), there is the potential to isolate and determine their contribution to the overall mechanical properties of the sample [70].

Before reviewing the use of micro-cantilever tests to study the elastic, plastic, and fracture properties of materials, a standard fabrication route will be briefly described. Armstrong et al. [63] used a relatively simple method for milling cantilevers to study the anisotropy of Young's modulus, in single crystal and polycrystalline copper.

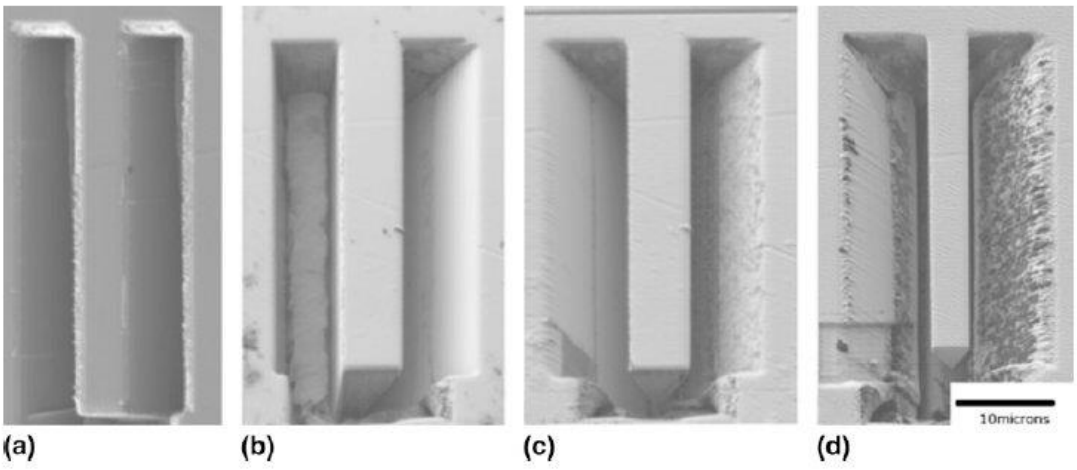


Figure 2-14: Stages of cantilever manufacture: (a) U shaped trench cut; (b) undercut on one side; (c) undercut on other side; (d) final cleaning at low current (from [63]).

As the experiment required that cantilevers be milled along all three major crystallographic axes, a single crystal copper sample was cut so that it had a {110} surface normal. The FIB was used to first mill a U-shaped trench at a current of ~5000 pA, leaving a cantilever-shaped profile comfortably larger than the desired final dimensions (see Figure 2-14a). The sample was then tilted around the long axis of the beam to an angle of 30°, and the cantilever was undercut from one side, at ~3000 pA (Figure 2-14b); this process was repeated after a 180° rotation about the surface normal, so that the beam was only fixed to the bulk material from one end (Figure 2-14c). The final step was to gently clean material that had been re-deposited on the underside of the beam during the previous stages, at ~1000 pA, before milling approximately 1 µm off the end of the beam, ensuring that it had not become attached to bottom of the trench (Figure 2-14d).

This method of milling cantilevers into the surface of materials was first used by DiMaio and Roberts to study the fracture properties of a thin tungsten carbide coating [66] (see section 2.2.2.3), and has since been used in several other materials [39,63,65,69,71,72]. It has the advantage that cantilevers can be positioned with a high degree of freedom compared to other methods restricted to sample edges (see section 2.2.2.2), although it produces cantilevers with inherently triangular (or pentagonal [66]) cross sections. When plastically deforming such triangular cantilevers, due to the vertical position of the neutral axis, strains at the bottom apex are twice as large as those at the top, meaning that plastic flow is always initiated from the bottom half of the cantilever first.

#### *2.2.2.1 Elastic Properties*

Armstrong's elasticity study made use of the above cantilever fabrication method to mill beams in a copper single crystal with a {110} surface at various angles from the [100] direction, and also in a single grain in a copper polycrystal. This latter approach, when combined with EBSD, allows pseudo-single crystal experiments to be performed, which offers a great advantage for the extraction of elastic properties over standard tests in which single crystals must be used (see section 5.1.2), as many orientations can be tested in the same sample. As previously mentioned, pillars are unsuitable for such tests, however cantilevers allow for the stress state to be much better controlled, and are less sensitive to misalignment issues in the indenter contact.

In order to define the cantilever loading point, the sample was mounted on a piezoelectric nano-positioning stage attached to a nanoindentation system. This enabled topographical surface maps to be produced, using low loads, in a similar way to how an AFM operates in

contact mode (see section 3.1.3). Cantilevers were deflected near the free end by 200 nm at a target maximum strain rate of $6 \times 10^{-4}$ $s^{-1}$.

To determine Young's modulus ($E$) from the load-displacement data, several methods were used, all reliant on a simple beam theory analysis (see section 5.3.1). In such cantilever tests, as the beams are not fully fixed to the bulk, there is some flexure of material at the fixed end, which leads to $E$ being underestimated. It was deduced that this flexure scaled with the square of the distance between the fixed end and the loading point, *L*, and hence the deflection predicted by simple beam theory ($\alpha$ $L^3$) would dominate as *L* increased. By deflecting beams at several different loading lengths, it was found that the $L^3$ term dominated for aspect ratios greater than ~6.

Having established this criterion, an alternative method used cantilevers with aspect ratios greater than 6, deflected at a single point only. Data from both the loading and unloading curves was then used to calculate $\delta/P$, from which *E* could be determined. Stiffnesses calculated from the loading part were found to be at least 6 % lower than those calculated from unloading, due to the indenter tip embedding into the material.

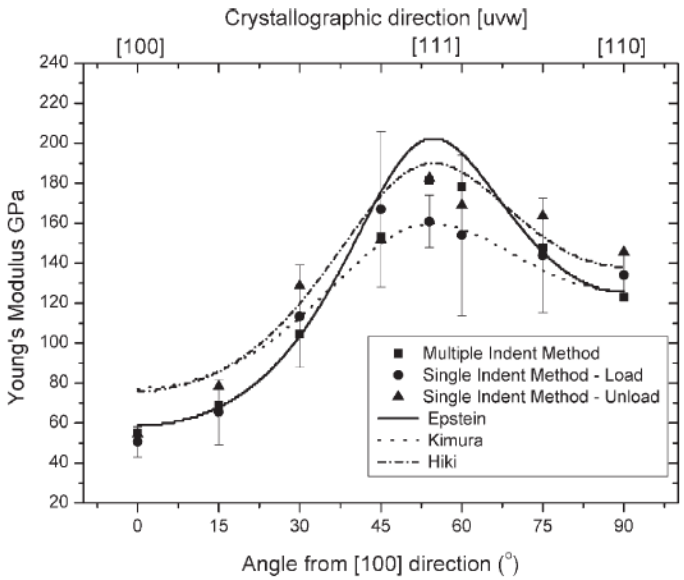


Figure 2-15: Variation of Young's modulus with crystallographic orientation in copper, comparing Armstrong's method to others in the literature (from [63]).

With cantilevers milled across a range of crystallographic orientations, a general trend comparable with that previously reported in the literature was observed (see Figure 2-15). However, the data spread between the different methods that Armstrong uses is considerable, and even the errors of individual methods are quite high (for example, the modulus of a cantilever 45° from the [001] direction is quoted as (152±48) GPa, when using the single point unloading method).

Gong and Wilkinson [65] improved upon this method, by using finite element (FE) analysis to more accurately capture the degree of flexure at the fixed end. Micro-cantilevers were milled in α-Ti at a range of declination angles from the c-axis. Having found a similar discrepancy (of ~6%) between the modulus calculated from unloading data compared to loading data, they deflected the cantilevers a second time within the elastic limit. On the second indentation, the difference between the *P-h* gradients on loading and unloading was only 0.3%, and furthermore the difference between unloading gradients from the first and second indentations was only 0.3%, thus justifying the use of unloading data in further analysis.

The multiple loading point method was again tried, with elastic moduli for a particular cantilever orientated along the c-axis calculated to be 125, 122, and 117 GPa, at loading points getting steadily closer to the fixed end. The drop off represents the increasing contribution of flexure; to account for this, an FE model was developed which the authors claim captures 99% of the flexure. Using this, the same data produced Young's modulus values of 132, 132 and 130 GPa, exhibiting much less scatter, and also demonstrating that even at large aspect ratios (~5.9) flexure can result in a 5% underestimate in modulus. The averaged data for five different cantilever orientations is shown in Figure 2-16, demonstrating a good agreement with other data in the literature.

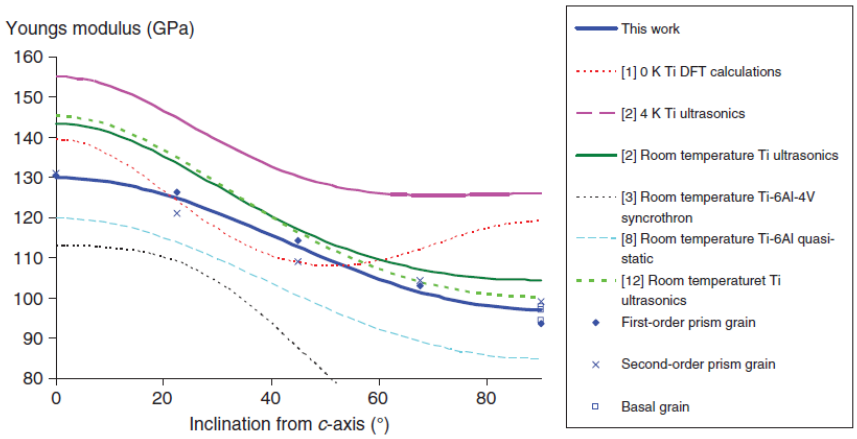


Figure 2-16: Variation of Young's modulus with crystallographic orientation in titanium, comparing Gong's method to others in the literature (from [65]).

A slightly more esoteric example of using micro-cantilevers to determine the elastic properties of materials is work published by Chan et al. [73], on the elastic anisotropy of the dentine-enamel junction of human primary molars. These biomedical components have a complex internal microstructure, the building blocks of which are prism-like fibres, embedded in an organic matrix. Cantilevers milled with their long axes parallel to these structures were found to have Young's moduli comparable to values determined from conventional (or 'straight' nanoindentation). However, cantilevers milled perpendicularly to

the fibre direction had significantly smaller moduli, thus demonstrating the microstructural anisotropy on this scale in the tooth. Although the anisotropy in moduli was clearly demonstrated, the cantilevers had rather low aspect ratios (see Figure 2-17), and therefore the values of Young's modulus they obtained are likely to be significant underestimates, as the effect of flexure at the built-in end was not accounted for.

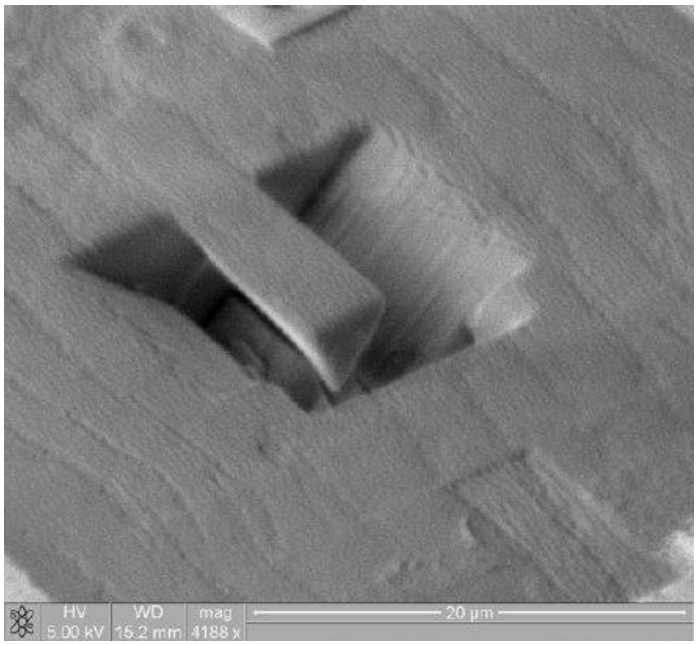


Figure 2-17: A micro-cantilever milled parallel to the prism-like components of the dentine-enamel junction in human primary molars (from [73]).

This limited amount of work shows the potential that micro-cantilevers have in measuring elastic properties on a small scale. In the work by Armstrong et al. [63] and Gong and Wilkinson [65], polycrystalline samples were used, which show that it is possible to perform such tests without having to grow large single crystals. However, neither groups fully determined the single crystal elastic constants of their respective materials. This would require a shear component to the tests in addition to a bending component, enabling the shear modulus to be measured (see chapter 5).

#### 2.2.2.2 Plastic Properties

Motz et al. [37] and Kiener et al. [38], have used FIB-machined micro-cantilevers to study the effects of sample size on flow stress in copper. In contrast to Armstrong's method, the fabrication procedure involved milling a lamella near to the edge of copper single crystal, from which two beams of rectangular or square cross sections could be cut out (see Figure 2-18). Note that this method requires the FIB stage to have a large range of angular motion, as the sample must be tilted by 90° to facilitate undercutting. For many FIB systems, this is not possible. Furthermore, these cantilevers can only be produced at the edge of a sample, and therefore the method is unsuitable if beams in a wide range of orientations must be tested, as this would require cutting single crystals with many different surface normals and edge directions. The simple rectangular cross section does however have the advantage that strains at the top and bottom surfaces are of equal size, whereas for triangular cross sections, plasticity is always initiated at the bottom of the cantilever first [72], due to the larger strains present at the lower apex.

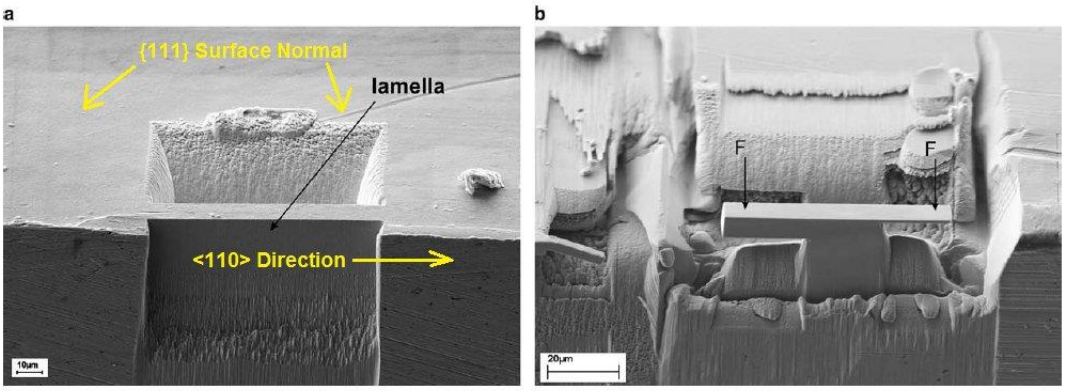


Figure 2-18: Micro-cantilevers prepared at the edge of a single crystal copper sample, by Motz et al. (from [37]).

The final beams produced had thicknesses ranging from 7.5 µm to 1.0 µm, widths from 7.5 µm to 2.5 µm, and lengths from 20 µm to 25 µm, and therefore with aspect ratios smaller than those used by Armstrong and Gong. For the indenting procedure, the same steps were

taken as those by Armstrong et al., namely performing an AFM-like scan in order to precisely define the loading point on the cantilever. The position of this loading point was then verified by imaging the impression made in the SEM post-test.

A sample load-displacement curve from this experiment, shown in Figure 2-19a, shows that the force reaches a plateau ($F_{max}$), after approximately 700 nm. Due to the difficulty of determining the exact point at which yield begins, this force plateau was used to define the flow stress, enabling comparisons to be easily made between the beams. The variation of flow stress with beam thickness is shown in Figure 2-19b, demonstrating a dramatic increase in strength when the critical parameter is reduced below ~5 µm. Calculating a line of best fit to this data reveals that the flow stress scales with beam thickness as $t^{-1.14}$.

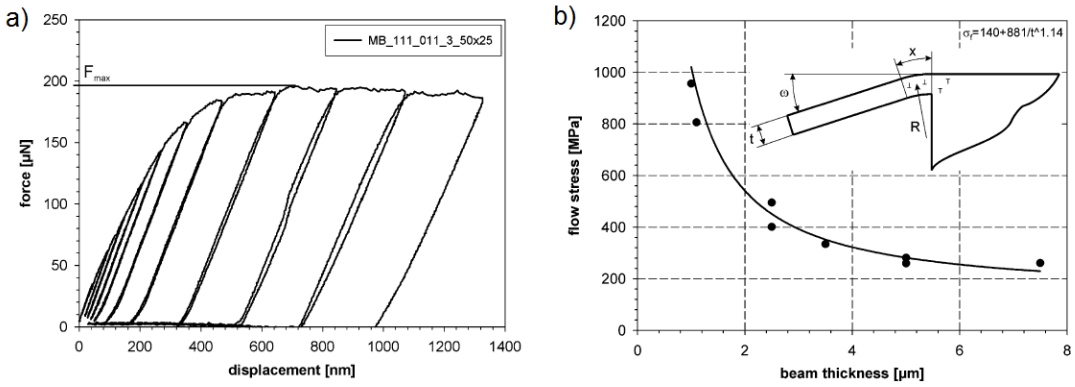


Figure 2-19: a) Sample force vs displacement curve of an copper cantilever indented by Motz et al. b) Flow stress of copper cantilevers as a function of thickness (from [37]).

Several possible mechanisms were discussed by Motz et al. to account for this behaviour. As in any other bending test, a strain gradient is present in the beam upon loading, with the top half of the beam experiencing tension and the bottom half being compressed. As discussed in section 2.1.3, strain gradients can be accommodated in the crystal lattice by GNDs. As the strain gradient increases with decreasing beam thickness, a higher density of GNDs is required, leading to increased Taylor hardening and therefore higher flow stresses for smaller

beams. A simple strain gradient plasticity (SGP) model used by Motz to demonstrate this effect is shown in Figure 2-20, in which the strain gradient is maintained by dislocation arrays, which act like small angle grain boundaries.

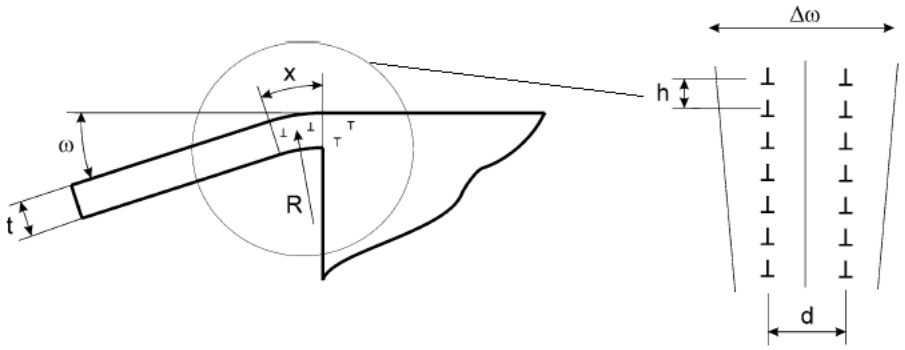


Figure 2-20: Strain gradient plasticity model used by Motz to account for the size effect seen in copper cantilevers (from [37]).

In such a geometry, the average density of GNDs is given by $\rho_{GND} = \omega/xb$, where $\omega$ is the bending angle of the beam, x is the size of the plastically deformed region, and b is the Burger's vector. However, assuming that $x \approx$ the beam thickness, equation (2-13) suggests that flow stress should scale with $t^{-0.5}$, significantly less than that which is observed.

To account for the disparity between the flow stress dependence predicted by the SGP model, and that observed experimentally, two other possibilities are suggested. Firstly, as the sample volume decreases, fewer dislocation sources will be present, restricting dislocation motion to fewer glide planes. To accommodate plasticity, these sources will have to emit more dislocations than would be necessary if many sources were available. Hence, the emitted dislocations are more likely to 'pile up', with their back stresses deactivating sources, thus requiring a greater force to reactivate them.

The second possible reason for a size effect can be explained with reference to Figure 2-21. In this simplified geometry, a cantilever containing dislocation sources operating on a single slip system is subjected to a constant bending moment. In response to an applied shear force, the source emits a dislocation dipole, with the upper dislocation being emitted at the top surface and forming a step, and the bottom dislocation travelling to the neutral axis. At the neutral axis, the shear stress changes sign, as the beam goes from a tensile region to a compressive one. This will naturally lead to dislocations piling up at the neutral axis, and exerting a back stress which hinders further plasticity.

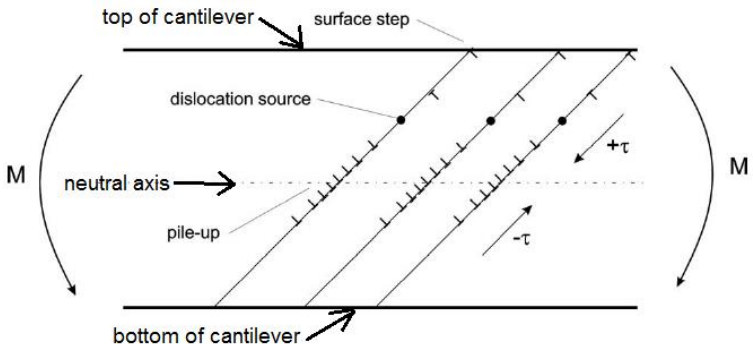


Figure 2-21: Simplified model of a cantilever containing dislocation sources acting on a single slip system, subjected to a constant bending moment (from [37]).

These two effects may combine to account for the observed "smaller is stronger" result as follows: as the beam thickness is decreased, dislocations are confined to fewer glide planes (due to there being fewer sources), and also the average distance from a source to the neutral axis is less thereby leading to pile-ups becoming more frequent, and causing the observed rise in flow stress. Dislocation dynamics modelling by Motz et al. [74] confirms this pile up model, whilst predicting that flow stress should vary with beam thickness as $t^{-1}$, agreeing well with the experimentally observed results.

Gong and Wilkinson [72] have conducted similar experiments on size effects in various Ti alloys, finding that flow stress varies with beam thickness as $t^{-1.1}$. The cantilevers they used were of Armstrong et al.'s triangular cross section design, in which plasticity always initiates from the bottom half. Armstrong's own data on Cu cantilevers also show flow stress varying as ~$t^{-1}$ [75].

#### *2.2.2.3 Fracture*

DiMaio and Roberts used FIB-machined micro-cantilevers to measure the fracture toughness of a tungsten carbide (WC) coating, which was only available at thicknesses of 10 µm or less [66]. In the first such study of its kind, a pentagonal cross section cantilever was milled entirely within the coating, with a notch positioned near the highly stressed fixed end (Figure 2-22).

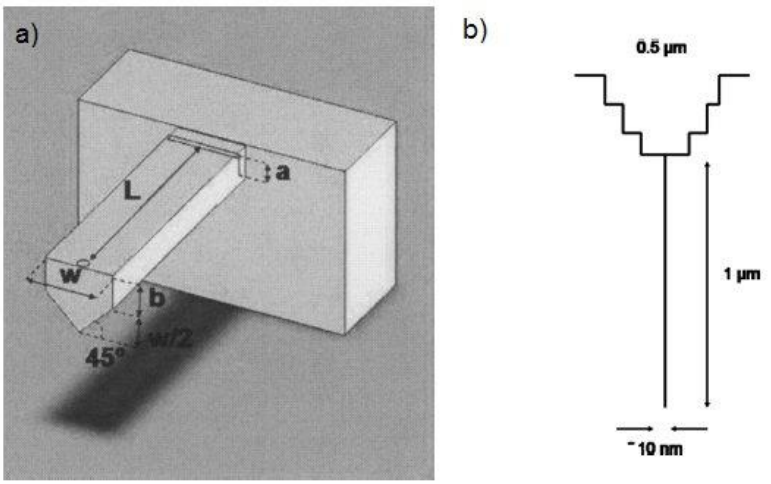


Figure 2-22: Schematic diagrams of a) a 'notched' pentagonal-cross section cantilever; b) the notch profile (from [66]).

The cantilever was scanned using the piezoelectric stage of the nanoindentation system as described previously, to precisely define the loading point, upon which it was loaded at a rate of 20 µN/s until fracture. In order to test if this method was valid for the determination of

fracture toughness, 4 cantilevers were prepared in silicon with (111) fracture planes. Upon testing these, an average fracture toughness of 1.1 $\pm$ 0.016 MPa $\sqrt{m}$ was obtained, broadly agreeing with previously reported values of 0.83 – 0.95 MPa $\sqrt{m}$. The authors note that the value might have been larger than those reported in the literature as an extra load was needed "to nucleate a sharp crack at the bottom of the notch". However, recent evidence has suggested that there may be intrinsic effects of specimen size on toughness, i.e. the "smaller is tougher" hypothesis [76].

Based on this successful validation, the fracture toughness of the WC coating was measured to be 3.2 $\pm$ 0.3 MPa $\sqrt{m}$, giving a result which would have been impossible to produce without such micro-cantilever testing.

Armstrong et al. have also used micro-cantilever testing for the measurement of fracture toughness, in this case of grain boundaries in copper embrittled by bismuth [71]. Using EBSD, it was possible to locate grain boundaries of specific orientations, and then mill cantilevers with a notch at the grain boundary. This allowed a wide range of misorientations to be tested, which would otherwise require many specific bi-crystals to be grown. However, the small specimen size (~5 µm wide) meant that many of the cantilevers yielded rather than fractured, so that only grain boundaries with low fracture toughnesses could be analysed.

#### *2.2.2.4 Summary*

Although the amount of work published on micro-cantilever tests thus far has been relatively limited, the technique has shown promise in being able to test a large range of properties including elasticity, plasticity, and fracture. They have several advantages compared to micro-pillar tests, including the ability to select particular microstructural features, such as

grain boundaries. It is also much easier to mill test pieces in a variety of crystal orientations. This is abundantly clear in Figure 2-23, which shows cantilevers milled by Gong et al. [72] in a single prismatic grain of α-Ti, at a variety of different angles. This allows anisotropy in elastic and plastic properties to be systematically studied, which would be difficult in micro-pillars, as a different surface normal would be required for each orientation.

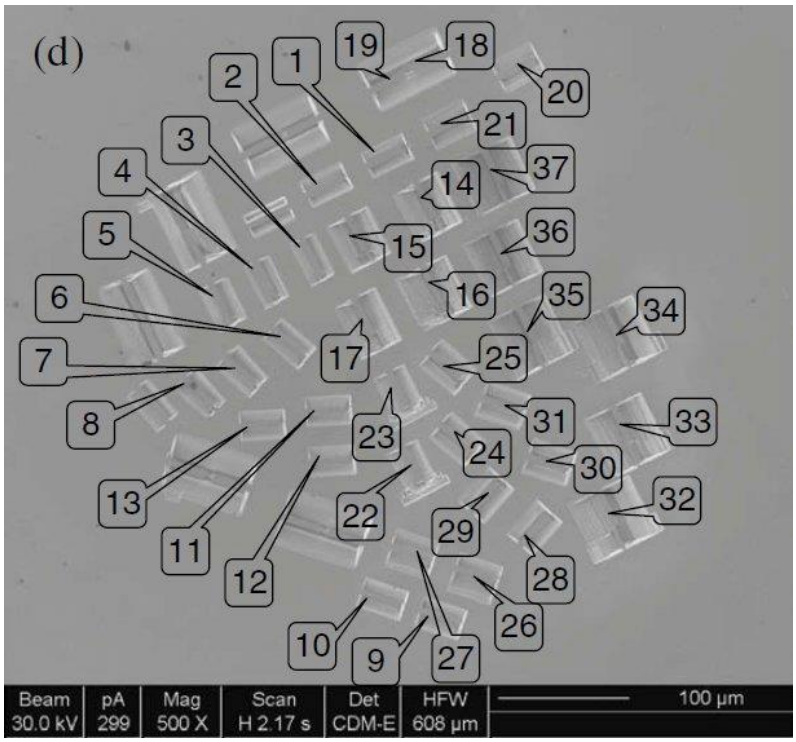


Figure 2-23: Micro-cantilever beams prepared in a single prismatic grain in α-Ti, by Gong (from [72]).

Cantilevers are also advantageous in that it is easier to stop indenting mid-test, and analyse the deformed regions using TEM and EBSD, whereas the indentation of pillars using a flat punch provides a far less controlled environment in which to do this, due to the unstable deformation. Furthermore, cantilevers present the best geometry in which to study the mechanical effects of ion-irradiated layers. Although work has been published on the compression of ion-irradiated Fe and Fe-Cr micro-pillars by Grieveson et al. [60], the sample preparation in this study was difficult, involving irradiated and non-irradiated surfaces being

stuck together and orientated so that pillars could be milled with their axes parallel to the surface. Cantilevers provide more freedom in which to conduct such studies [35,77].

### 2.2.3 FIB Damage

As all of the small scale specimens looked at so far have been manufactured via $Ga^+$ ion sputtering in the FIB, this raises the question of whether any damage is induced by this process that has an effect on the mechanical properties measured. The FIB is well known to produce an amorphous layer next to a milled surface, in addition to introducing crystalline defects and implanting ions [24].

Kiener et al. used the TEM to study the extent of the amorphisation and Auger electron spectroscopy to measure $Ga^+$ concentration as a function of depth, in a FIB damaged Cu film [78]. They found that $Ga^+$ contamination was limited to the amorphous region, the size of which was a sensitive function of the accelerating voltage and ion current (i.e. dose) used, in addition to the angle of incidence of the ion beam. For a current of 2000 pA with an accelerating voltage of 30 kV, an amorphous layer of 50 nm thickness was observed compared with 10 nm for 50 pA and 3 nm for 50 pA at 5 kV. For very high currents of 10000 pA, Ga concentrations of up to 20 at.% were found a few nanometres below the surface, lowering to 2 at.% at depths of ~50 nm (this value was reached at 30 nm for 1000 pA currents).

Bei and Shim et al. have investigated the effect of FIB damage on the mechanical properties of molybdenum alloy micro-pillars [24,79]. A unique fabrication route was used, whereby directional solidification produced Mo-alloy pillars embedded in a NiAl-Mo matrix. The matrix

was subsequently etched away, leaving an array of pillars which had not been subjected to any FIB damage (see Figure 2-24).

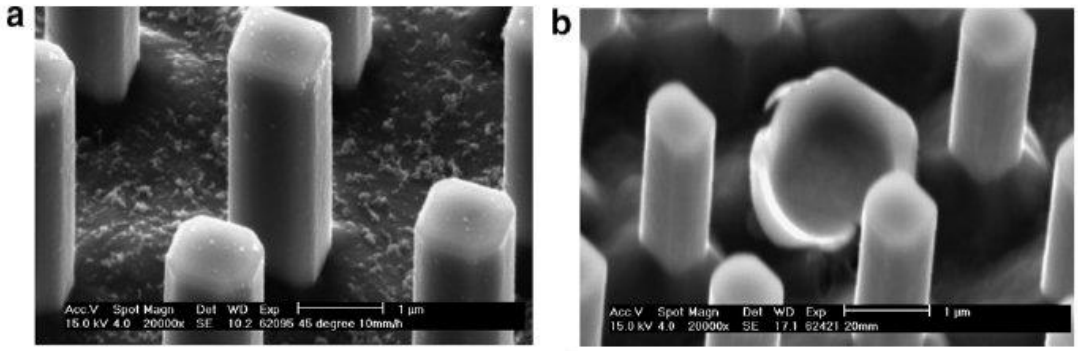


Figure 2-24: a) Mo pillars produced by selective etching of a NiAl-Mo matrix; b) A deformed Mo pillar (from [79]).

The measured yield stress of these pillars, resolved on the slip planes with maximum Schmid factors, was found to be comparable to the expected theoretical strength. Conversely, pillars subjected to the same processing route, but FIB milled at the final stage instead of etched, had yield strengths an order of magnitude below the non-FIB milled pillars (0.85 ± 0.16 GPa as opposed to ~9.2 GPa, see Figure 2-25). The load-displacement behaviour and yield strengths were also found to be similar to as-grown pillars of the same material that had been prestrained before compression [80], suggesting that dislocations introduced in both processes had facilitated plastic flow earlier than in the case of virgin pillars.

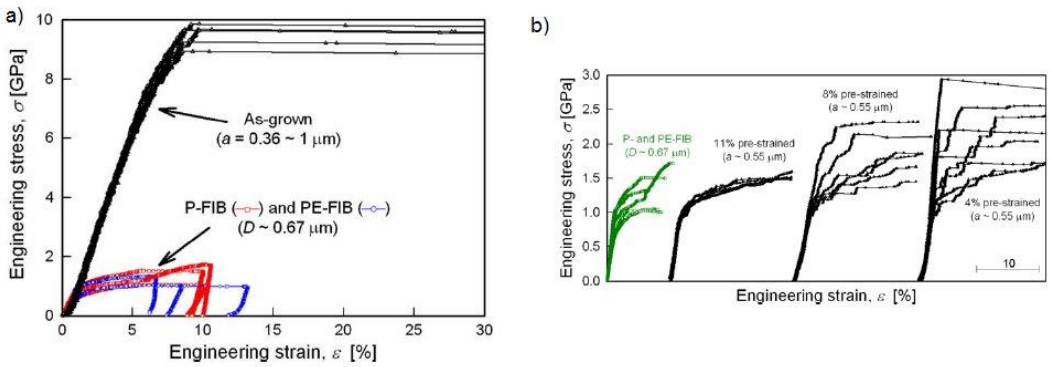


Figure 2-25: a) Comparison of stress strain curves obtained from as-grown Mo pillars (black line) and FIB-machined pillars (red and blue lines); b) FIB-machined pillars (green), compared to virgin pillars with varying amounts of pre-strain (from [24]).

No work has yet been reported on FIB damage in cantilevers, possibly because it is difficult to produce specimens of comparative size and shape using FIB and non-FIB methods (e.g. lithography). However, as the critical dimension of micro-cantilever specimens has general exceeded that of pillars, FIB damage is not thought to contribute so greatly to mechanical properties [81].

### 2.2.4 Conclusion

In summary, this literature review has demonstrated the various ways in which mechanical properties data can be generated from small testing volumes. Nanoindentation has successfully been used over the past 20 years for the testing of thin films and coatings, in addition to the study of fundamental deformation mechanisms at the onset of plasticity. This latter application includes studies devoted to understanding the indentation size effect (ISE), often stated as 'smaller is stronger'. However, despite its success, the stress state underneath the tip of a nanoindenter is complex, making the derivation of e.g. the critical resolved shear stress, or the Young's modulus from the measured data non-trivial.

To surmount this problem, FIB-machined specimens have been used (in conjunction with nanoindentation systems) to provide testing conditions with much better controlled stress states. A survey of the literature shows that even though the huge majority of such tests have been conducted using micro-pillar geometries, cantilevers are able to test a much wider set of mechanical properties.

To date, it is not known with any degree of certainty which of the models of size dependence are in effect in such small scale specimens. Approaches which use a Taylor hardening model to explain the size effect, with arrays of GNDs supporting the beam curvature, predict a size exponent of n = -0.5, however this is at odds with much of the available evidence. Alternatively, the model of back stresses from soft pile-ups at the neutral axis inhibiting dislocation motion and source activation has been shown to lead to a size exponent of n = -1, which closer matches the experimental evidence. However, without further work to explore the dislocation structures formed during testing (e.g. using ex-situ TEM and HR-EBSD), it is difficult to say which underlying mechanisms are responsible for the cantilever size effect.

With greater development, and a more thorough understanding of how the various deformation mechanisms lead to measured properties which are highly dependent on specimen size (for plastic properties), micro-cantilever testing has the potential to provide elastic and plastic data in situations where bulk testing cannot be used.

# 3 Experimental Methods

## 3.1 Nanoindentation

The predominant experimental technique used in this thesis is nanoindentation. This is used both conventionally, to probe the elastic modulus and hardness when indenting directly into materials' surfaces (in chapters 4 and 6), and to deflect micro-cantilever test specimens (in chapters 5 and 7).

As previously mentioned (see section 2.1), the first nanoindentation system was introduced by Pethica et al. in 1983 for studying the hardness of ion-implanted steel [5]. Since then, numerous companies have developed systems capable of carrying out instrumented indentation over a wide range of experimental conditions, e.g. at varying temperatures (-20 to 750°C [82]), and in-situ in the SEM and TEM [83]. Such diversity notwithstanding, the basic operation of the nanoindenter is similar in each case.

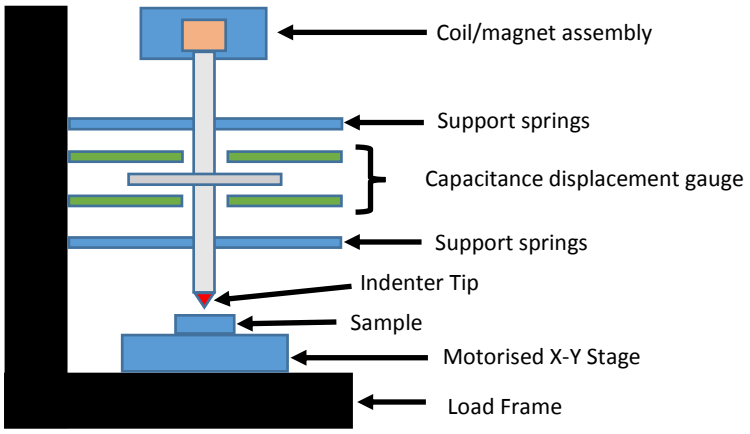


Figure 3-1: Schematic diagram of a typical nanoindenter setup (redrawn from [84]).

Figure 3-1 shows the main features of a typical nanoindenter. The indenter tip is attached to a vertical shaft which is prevented from lateral movement by support springs. The load is applied via a calibrated electromagnetic coil, which drives the indenter tip into the sample,

whilst displacement is measured using a capacitive displacement sensor. Although nanoindenters are inherently load controlled instruments, a proportional-integral-derivative (PID) controller can be used to enable displacement control, via a fast feedback loop.

### 3.1.1 Instrumentation

Two nanoindenter systems were used to collect the results in this thesis. 'Straight' nanoindentation was performed using the MTS NANO Indenter XP (MTS NANO Oak Ridge Tennessee, USA), hereafter referred to as the "Nano XP", whereas micro-cantilevers were displaced using either the Nano XP or the Agilent Nano Indenter G200 (Agilent Technologies Santa Clara California, USA), hereafter referred to as the "G200". The Nano XP is equipped with a low load Dynamic Contact Module (DCM) mode, with which measurements can be made at higher resolutions of load and displacement. This DCM head was used for some of the micro-cantilever experiments.

For the MTS system, the theoretical load and displacement resolutions of the XP head are 50 nN and 0.04 nm, respectively, whereas those of the DCM head are 1 nN and 0.0002 nm (in practise, such numbers are limited by noise). For the Agilent system, the theoretical load and displacement resolutions are 50 nN and <0.01 nm, respectively.

Diamond Berkovich indenter tips were used for all experiments (see Figure 3-2), with a relatively blunt tip used to scan and indent micro-cantilevers, and a sharper tip used for elastic modulus and hardness measurements (tip radius $\approx$ 40 nm).

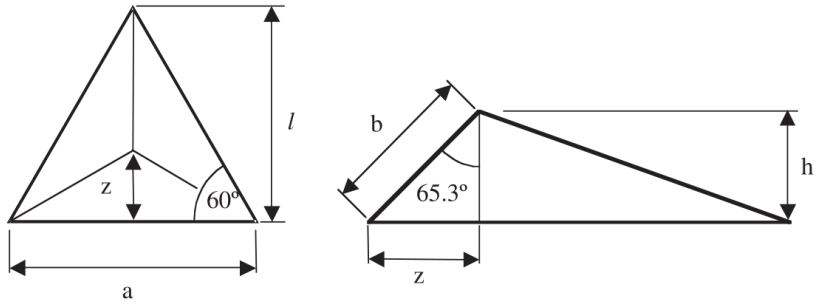


Figure 3-2: Schematic diagram of a Berkovich indenter (from [85]).

### 3.1.2 Continuous Stiffness Measurement (CSM)

Although in a conventional test elastic modulus and hardness are determined from the unload curve (see section 2.1.1), they can also be measured continually during loading, by applying a small sinusoidal oscillation to the load signal (see Figure 3-3). This allows such quantities to be given as a function of depth, which is advantageous for studying thin films, or samples with ion-irradiated layers for example (see Chapter 6).

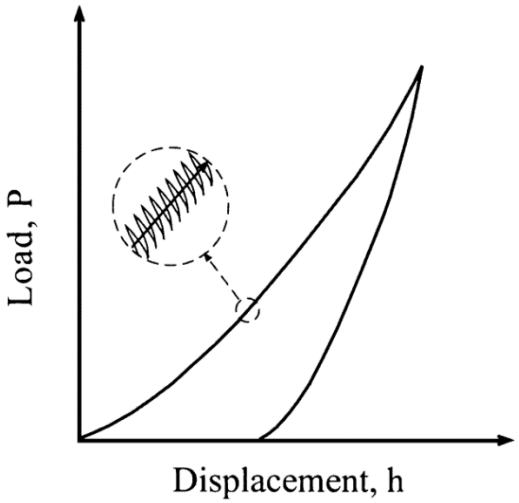


Figure 3-3: Schematic load-displacement curve of a CSM test, showing a sinusoidal oscillation applied to the load signal (from [86]).

A dynamic model representing such a CSM test is shown in Figure 3-4. Springs representing the load frame stiffness ($K_f$), the column support springs stiffness ($K_s$), and the contact stiffness of the sample ($S$) are shown, in addition to a damping component ($D$), and the mass

of the indenter and shaft ($m$). The damping component is caused predominantly by air in the gaps of the capacitive displacement sensor. It has been shown by Oliver and Pharr [9] that given a driving force $P = P_{os}\exp(i\omega t)$, which produces a displacement response $h(\omega) = h_0\exp(i\omega t + \phi)$, the contact stiffness $S$ can be calculated from either the amplitude of the displacement signal:

$$\left|\frac{P_{os}}{h(\omega)}\right| = \sqrt{\left\{(S^{-1} + C_f)^{-1} + K_s - m\omega^2\right\}^2 + \omega^2 D^2} \tag{3-1}$$

or the phase difference between the load and displacement signals:

$$\tan(\phi) = \frac{\omega D}{(S^{-1} + C_f)^{-1} + K_s - m\omega^2} \tag{3-2}$$

where $P_{os}$ is the magnitude of the force oscillation, $h(\omega)$ is the magnitude of the displacement oscillation, $C_f$ is compliance of the load frame, $\omega$ is the frequency of the oscillation, and $\phi$ is phase difference between the force and displacement signals.

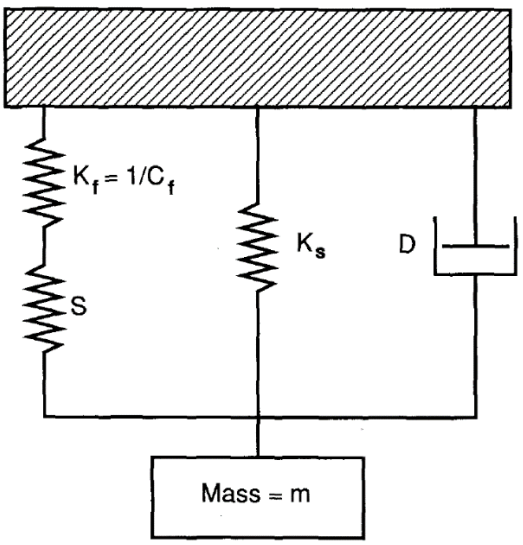


Figure 3-4: Dynamic model of the CSM mode, with springs representing the load frame stiffness ($K_f$), contact stiffness ($S$), and support springs stiffness ($K_s$), in addition to a damping component ($D$), and an indenter and shaft mass ($m$) (from [9]).

Once $S$ has been determined, the modulus and hardness can be calculated as before. Due to the ease and usefulness of this method, all indentation reported in this thesis was carried out with CSM. In all cases, a frequency of 45 Hz and an oscillation amplitude of 2 nm were used.

### 3.1.3 Micro-Cantilever Testing

In order to use the nanoindenter to accurately displace a micro-cantilever, the beam location must first be known, with a greater precision than is possible simply by using the optical microscope. To accomplish this, a small load is applied to the indenter (e.g. 4 µN), whilst the sample surface in the vicinity of the beam is scanned under the tip using a piezoelectric stage, allowing a topographical map to be produced in a similar manner to using an AFM in 'contact' mode. From this map, the indenter tip can then be accurately positioned on the beam surface, and the desired cantilever displacement applied. In the case of smaller beams, even with low loads the indenter tip can destroy the beams being scanned. To circumvent this, fiducial lines were milled at fixed distances from the beams (Figure 3-5). It was then possible to scan such lines, and set the indenter to indent at a specified distance away from them, on the beam's surface.

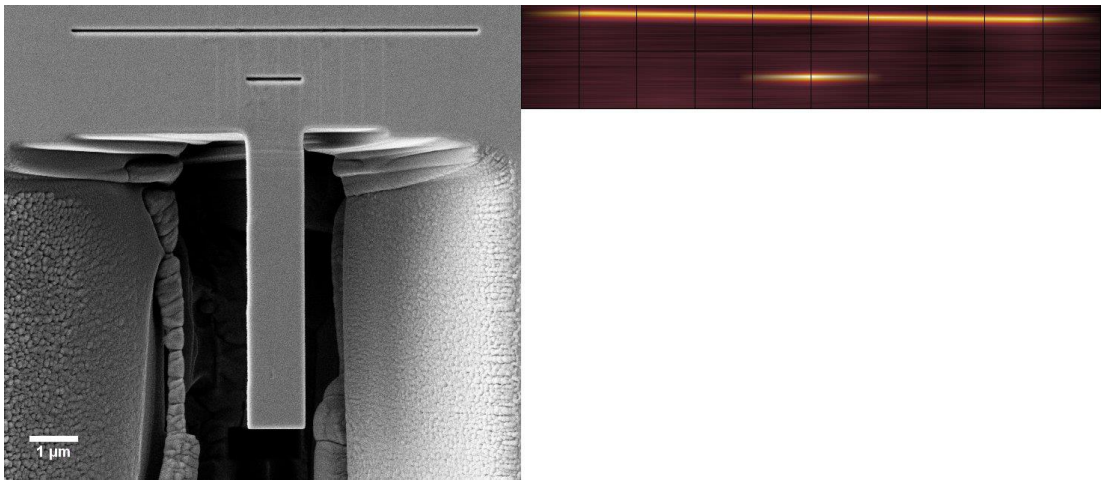


Figure 3-5: SEM of a 1 µm thick micro-cantilever, with two fiducial lines milled at set distances from the beam (left), and a scan of these lines produced using the NanoVision stage of the Nano XP (right).

## 3.2 Scanning Electron Microscopy with Electron Backscatter Diffraction

Scanning electron microscopy (SEM) was used extensively throughout this research project. SEMs were used both for imaging (of indents, micro-cantilevers, and other sample features), and also to extract information about crystal orientation using electron backscatter diffraction (EBSD). Due to the ubiquity of the SEM in materials science, its operation will not be reviewed here, however a brief overview of EBSD will be given below.

EBSD is now a standard technique for obtaining crystal orientation information from the surface of polished metals [87]. A schematic diagram of the EBSD experimental set up is shown in Figure 3-6. During an EBSD run, the incident electron beam is scanned over the sample surface, which is positioned at a steep angle with respect to the beam. Electrons enter the sample, are inelastically scattered and due to the tilt angle, may escape the sample. Some of these escaping electrons satisfy the Bragg condition for a particular lattice plane and produce a characteristic Kikuchi band [88]. Multiple bands are formed by multiple lattice planes (see Figure 3-7) and these bands can be captured by a well-positioned phosphor screen inserted into the microscope chamber.

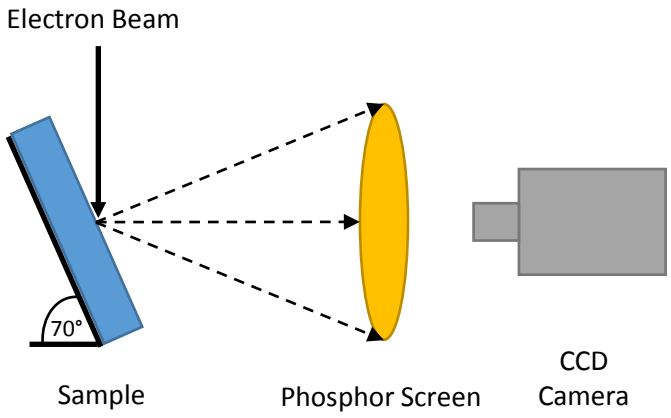


Figure 3-6: Schematic diagram of an EBSD system.

Subsequent analysis of the recorded Kikuchi patterns for each position of the electron beam can yield information about crystal orientation [89], phase [90], elastic strain [91], and excess dislocation content [92].

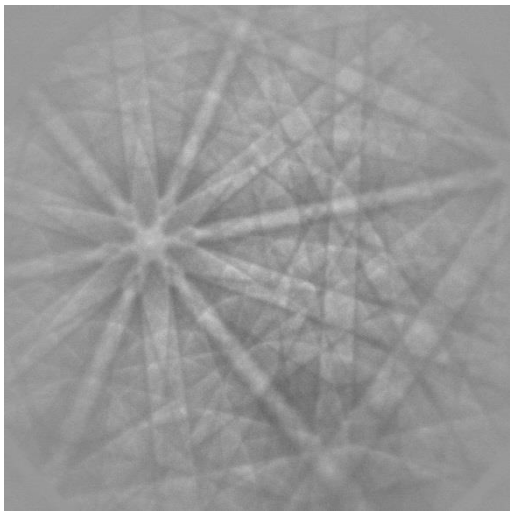

Figure 3-7: Electron backscatter pattern (EBSP) obtained from α-Fe (at 20 kV).

All experimental chapters in this thesis make use of EBSD. The technique is used to make 2D maps of sample surfaces, either to analyse the orientation dependence of parameters measured during indentation experiments (chapters 4 and 6), or for the selection of particular grains from polycrystalline samples in order to perform pseudo single crystal experiments (chapters 5 and 7).

EBSD scans were performed using either the JEOL 6300 or the JEOL 6500F, with an OIM EBSD (EDAX, Mahwah, NJ, USA) system attached to both. The OIM Data Analysis software was used post-test to interpret the scan data. Elastic strains and dislocation density near selected indents were analysed (chapter 4) using MATLAB scripts developed in house by Britton & Wilkinson.

## 3.3 Focused Ion Beam

The focussed ion beam (FIB) is used in this thesis for the manufacture of micro-cantilever test specimens, and additionally for its imaging abilities. In this section, only a brief overview of the FIB and its operation will be given, however for a more complete review see Volkert and Minor [93] and Munroe [94].

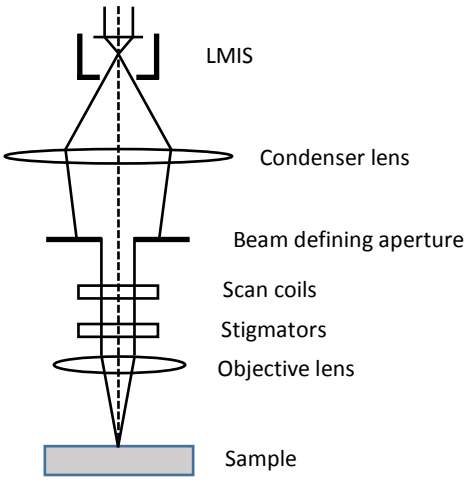


Figure 3-8: Schematic diagram of a FIB system (redrawn from [95]).

The operation of a FIB is similar to that of an SEM in many respects, with the main difference being that a beam of positive ions is rastered across the sample surface under investigation, as opposed to a beam of electrons. A typical FIB system is shown schematically in Figure 3-8. The liquid metal ion source (LMIS) consists of a blunt tungsten needle, onto which liquid gallium flows from a reservoir. A large negative potential between the needle and an extractor electrode causes field emission of the $Ga^+$ ions, which are then collimated using an electrostatic condenser lens. The typical emission current of an LMIS is 2 μA, with a voltage of 30 kV used to accelerate the ions. A strip of apertures of varying sizes is used to reduce the beam current to 1 pA – 20 nA, corresponding to spot sizes of 10 nm – 500 nm (with much reduced sphericity at higher beam currents). Finally, scan coils are used to raster the beam,

a stigmator ensures a spherical beam profile, and an objective lens focuses the beam onto the sample surface.

### 3.3.1 Ion-Solid Interactions

Upon striking the sample surface, the $Ga^+$ ions undergo either inelastic collisions, causing ionisation and the emission of secondary electrons, or elastic collisions, in which secondary ions are ejected from the surface (Figure 3-9). It is this latter process, known as sputtering, which enables the FIB to accurately machine test specimens on a sub-micron scale, using computer software to control the pattern with which the beam is rastered across the surface. The sputter yield is dependent on many factors, including the sample material, the crystallography of the sample, the incident angle of the ion beam, and the accelerating voltage used.

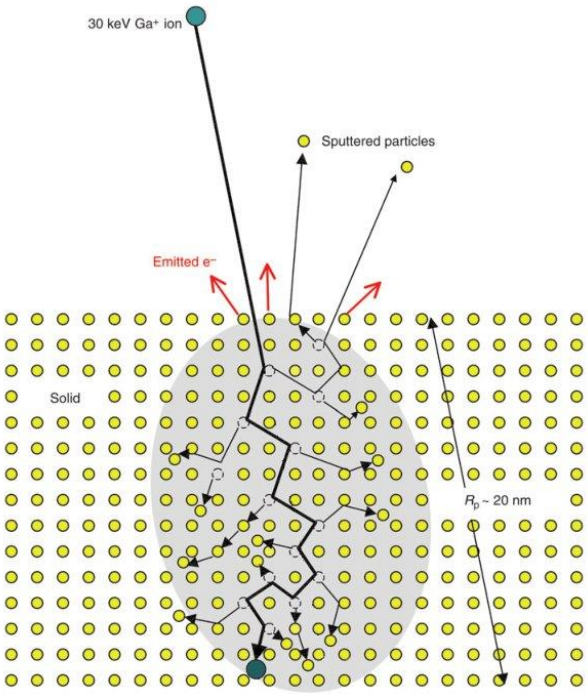


Figure 3-9: Schematic diagram showing the interactions between an incoming $Ga^+$ ion and a crystalline solid (from [93]).

The secondary electrons can be collected by a suitable detector, enabling the scanned surface to be imaged in the same manner as in SEMs. Although FIB imaging is inherently destructive, and offers a lower resolution than the SEM, differing contrast mechanisms mean that there are some advantages over SEM imaging. For example, ion channelling occurs when $Ga^+$ ions penetrate deeper into the sample surface along lower index crystallographic directions. This causes fewer secondary electrons to be emitted, causing the image to be darker at such locations. This contrast mechanism is used in several chapters in this thesis, to locate certain grains and grain boundaries for further experimentation.

### 3.3.2 Instrumentation

Three FIB microscopes were used for all the work in this thesis: the FEI FIB 200 (FEI Hillsboro Oregon, USA), the Zeiss NVision 40 FIB-SEM (Carl Zeiss AG Oberkochen, Germany), and the Zeiss Auriga FIB-SEM. The latter two microscopes are dual beam instruments, which consist of the standard vertical SEM column, in addition to a FIB column 54° from vertical. This allows sample imaging to be conducted at the same time as milling, and for samples to be imaged post milling without causing unnecessary gallium implantation and ion damage.

Due to them offering higher resolution than the SEMs mentioned in section 3.2, the SEM columns of the dual beam instruments were also used to carry out conventional imaging throughout this thesis.

# 4 Investigating the Effect of Crystal Orientation on Mechanical Properties using Nanoindentation

## 4.1 Introduction

In order to demonstrate the possibilities and limitations of using 'straight' nanoindentation to extract mechanical properties, an experiment was performed in which indent arrays were made over many grains of a polycrystalline Fe sample, to probe the anisotropy in indentation modulus and hardness. The advantage of such an experiment is that no FIB-milling of test specimens is required, allowing it to be carried out relatively quickly and easily compared with micro-cantilever experiments. However, such indentation can be difficult to interpret, as the stress state under an indent is very complicated and the modulus values obtained have in practice been averaged over a range of crystallographic orientations [29].

Previously, the variation of indentation modulus and hardness with orientation has been studied in several hcp metals: titanium [32], zirconium [96], zinc [29,97], and magnesium [97]. In several of these studies, high resolution EBSD (HR-EBSD) and atomic force microscopy (AFM) were used to examine selected indents made in a range of differently oriented grains [32,97]. HR-EBSD has also been used to examine the deformation surrounding a single indent in iron [98]. However, to date no work has examined the orientation dependence of hardness and modulus during the nanoindentation of iron.

In this chapter, the complementary techniques of nanoindentation, HR-EBSD and AFM will be used to study an iron sample (following the method of [32]), to highlight the importance of crystal orientation in nanoindentation studies of polycrystals, and also to serve as a useful

comparison with the work in later chapters employing FIB-milled specimens (chapters 5 and 7).

## 4.2 Method

Indent arrays were made in a 99.999% 'specpure' iron sample, supplied by JMC. The sample was one of several ~1 mm thick discs, cut from a ~5 mm diameter rod, and annealed in a vacuum furnace at 830 °C for 12 hours, to produce grains of ~200 µm size (Figure 4-1, left). The discs were then ground using SiC papers up to 2500 grit, and subsequently polished with diamond paste of grades 8 µm, 3 µm, and 1 µm, consecutively. They were then polished to a 20 nm colloidal silica finish, such that clear, crisp patterns could be obtained from EBSD scans (Figure 4-1, right). This step was important, as a relatively low dislocation density was necessary in order that consistent results could be produced with minimal noise.

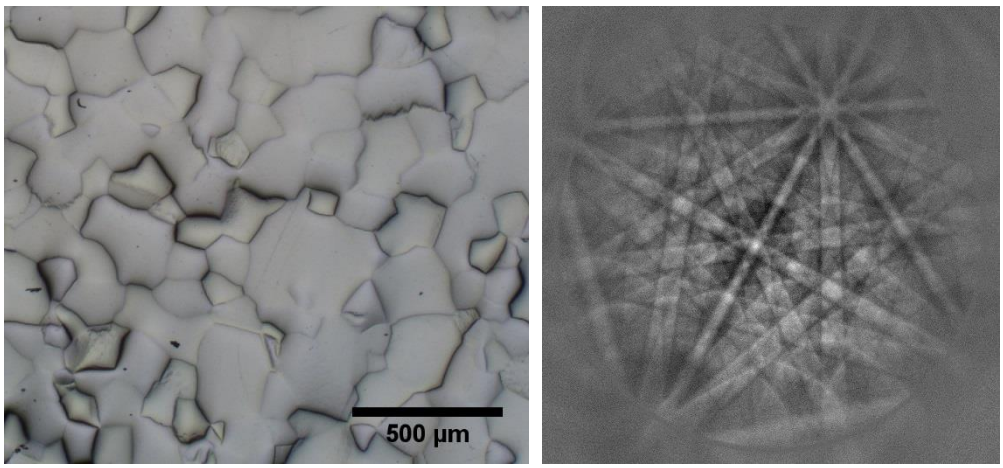


Figure 4-1: Optical micrograph of polished iron sample (right); EBSP obtained from the same sample (right).

A large area EBSD scan of the sample conducted by Ben Britton showed that the sample was weakly textured (with a peak of 1.5 × random, see Figure 4-2), which was expected as the bar had been cold rolled. As a result, it was expected that a sufficient range of orientations

would be obtained from a single axial slice of the rod, without having to make additional angled cuts.

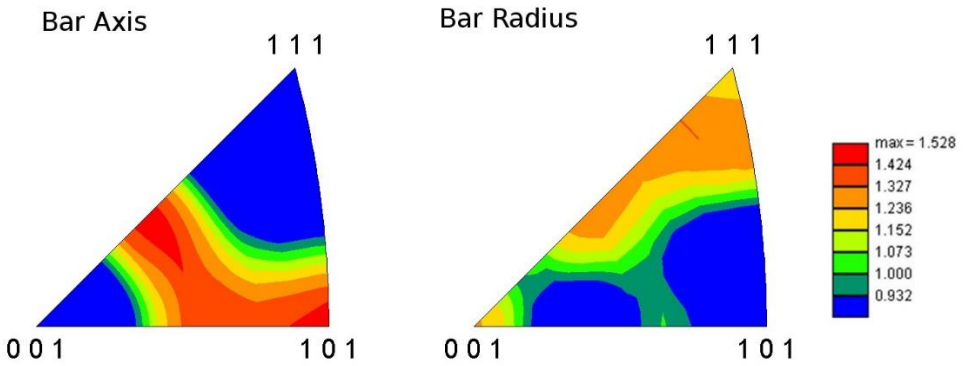


Figure 4-2: Texture plot on an inverse pole figure of the iron sample.

In some previous studies [96,97], the measured indentation modulus was found to be very sensitive to sample mounting, with data taken using the same sample on different occasions showing inconsistent results. To mitigate against this, a sample holder was designed with three grub screws tightening against an adapted JEOL stub with axisymmetrically angled sides (Figure 4-3). In previous studies, in which one grub screw was tightened against a regular stub, the grub screw could potentially apply some torsion to the stub, turning it slightly so that it was no longer flat. In this case, the three grub screws push the sample flat against the bottom of the holder, ensuring that scatter should be minimised between measurements. The sample was mounted to the stub using silver dag.

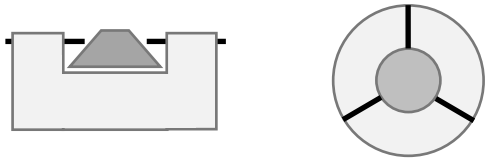

Figure 4-3: Schematic diagram of the nanoindenter sample holder, in a cutaway side view (left), and plan view (right). Grub screws are shown in black on the left (untightened), and the projected position of the screw holes is shown in black on the right. The left diagram also shows an adapted stub in dark grey (axisymmetric).

Two 16 by 16 square indent arrays were defined on the Nano XP, having indent spacings of 50 µm and 100 µm. The indent spacing was double for the second array in order that a greater range of grain orientations could be probed. Each indentation used a target indentation strain rate of 0.05 $s^{-1}$ during the loading period, to a maximum of 1 µm depth, followed by a hold period at peak load for 10 seconds to account for creep. The indenter was unloaded at 1 $mNs^{-1}$ to 10 % of the peak load, held for 50 seconds to measure thermal drift, and finally unloaded completely. The stage was then moved to the next indent position, such that the whole 16 by 16 array was completed in a serpentine pattern. The indentation modulus and hardness were automatically calculated for each indent from the unload curve via the Oliver and Pharr method (see section 2.1.1), using the nanoindenter software.

## 4.3 Results

### 4.3.1 Trends Across Sample

An optical micrograph of the second indent array (100 µm spacing) is shown in Figure 4-4, with the first indent array partially seen in the top left of the image. For further analysis, results for indents made within 20 µm of a grain boundary were rejected, due to the probability that the elastic zone of such indents would extend out into other grains.

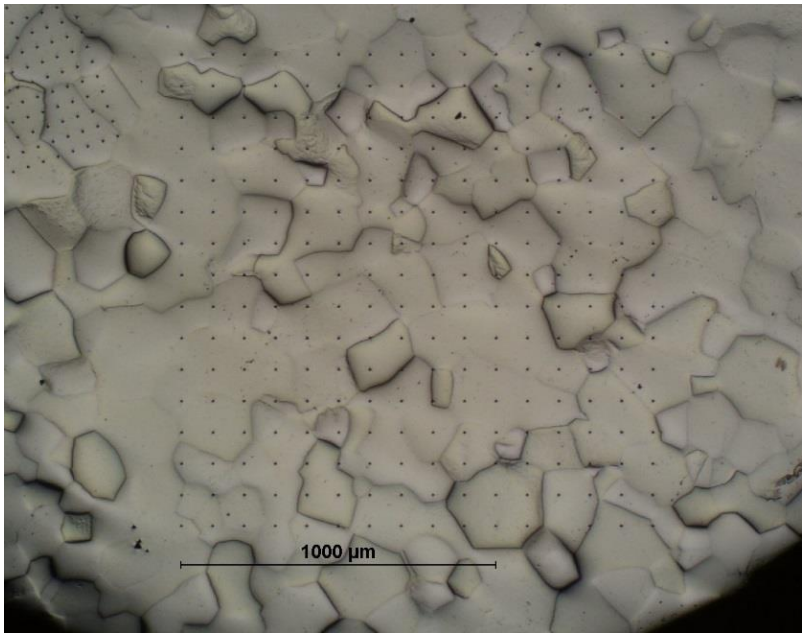


Figure 4-4: Optical micrograph of a 16 by 16, 100 µm spacing indent array, with part of a 16 by 16, 50 µm spacing array in the top left.

In the 50 µm spaced array, after applying this threshold and discarding failed indents, there were 118 indents made in 23 grains, with a median of 3 indents per grain. In the 100 µm spaced array, there were 108 indents made in 70 grains, with a median of 1 per grain.

In order to better organise the results before further analysis, EBSD scans were performed across both arrays using the JEOL 6300, to determine the range of orientations probed. The relatively large array sizes combined with the high tilt angle required for EBSD meant that it was not possible to keep the electron beam focussed during a whole array scan. Therefore several smaller scans were performed on each array, and stitched together afterwards. Inverse pole figure (IPF) maps of the two arrays are shown in Figure 4-5.

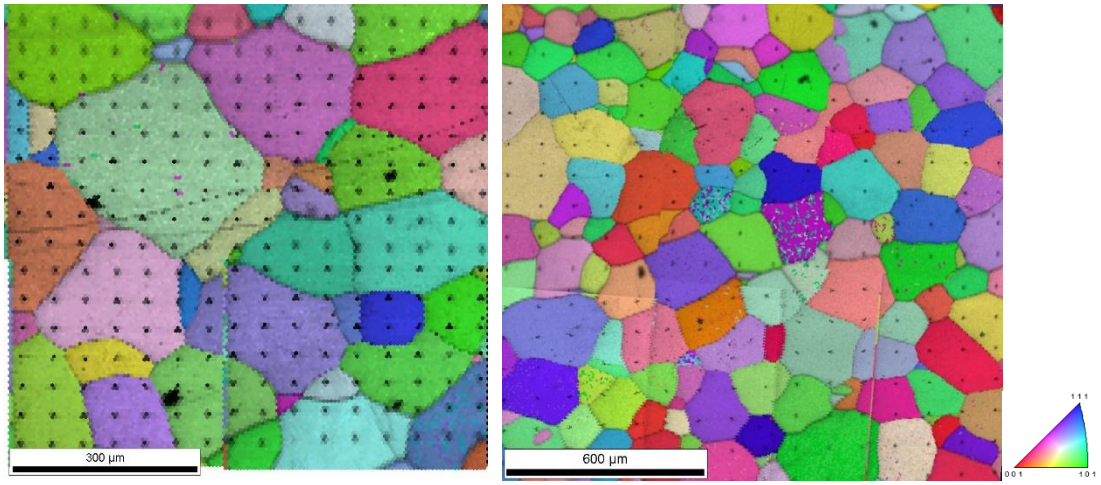


Figure 4-5: Normal direction IPF maps (with image quality overlaid in greyscale), of 16 by 16 indent arrays, with 50 µm spacing (left), and 100 µm spacing (right).

The calculated hardness and indentation modulus were exported from the nanoindenter software, and then grouped according to the grains probed by the two arrays. For each grain, average values of hardness and modulus were calculated, and these averages from both arrays were plotted as a function of orientation on inverse pole figures (see Figure 4-6). These plots show that there is minimal systematic variation in indentation modulus, but a significant variation in hardness, with indents made in grains near the <110> and <111> normal directions approximately 0.2 GPa (20 %) harder than indents made in grains nearer the <100> normal direction.

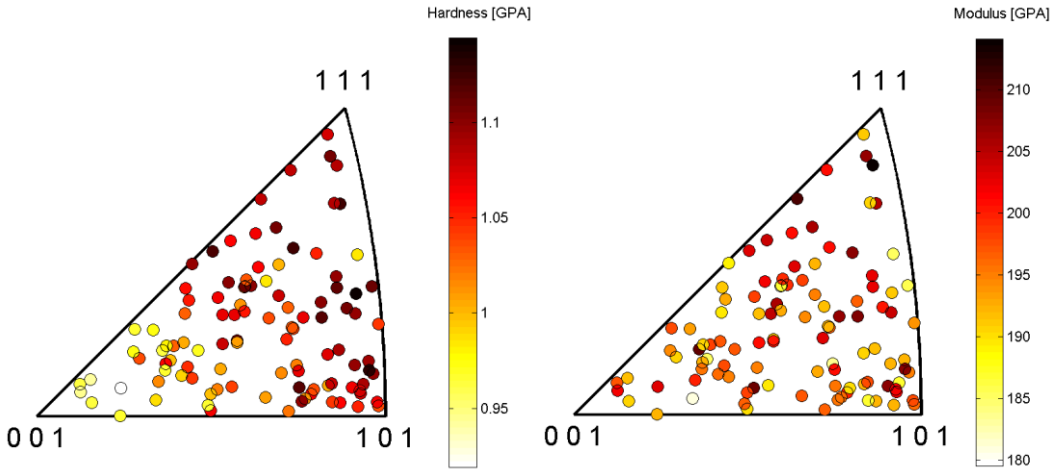


Figure 4-6: Inverse pole figures showing hardness (left) and indentation modulus (right) for indents made in an Fe sample.

### 4.3.2 Selected Indents

In order to gain more insight into the differing mechanical behaviour seen at the three corners of the inverse pole figure, representative load-displacement curves from indents near each corner are shown in Figure 4-7. It is clear that, although the hardness (a function of maximum load) is quite different for each indent, the unloading behaviour is similar, confirming the varying hardness but uniform modulus seen in Figure 4-6.

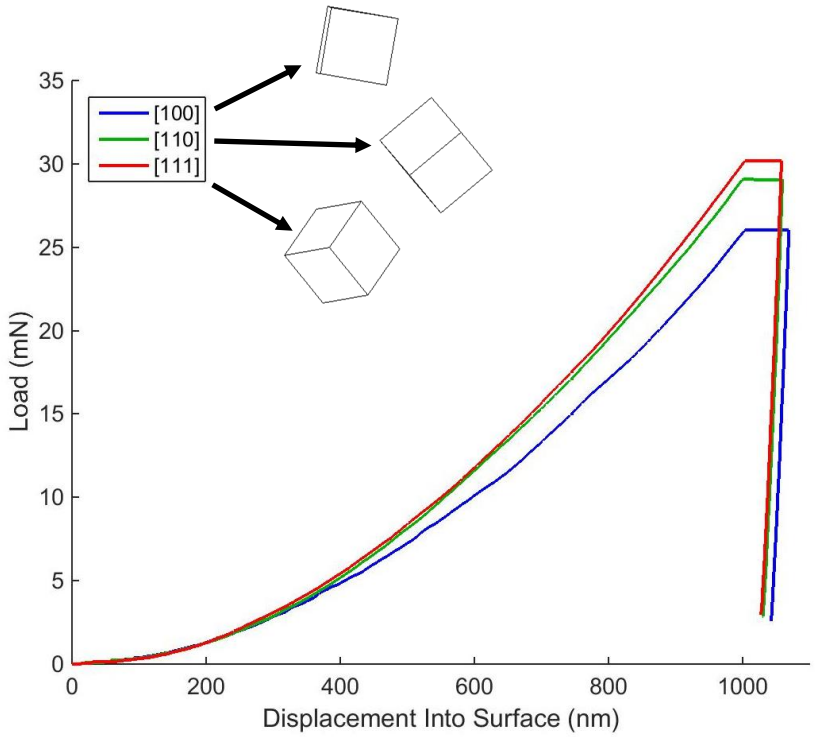


Figure 4-7: Three load-displacement curves showing the mechanical response when indenting in grains with normal directions near the three main crystallographic directions (represented by wireframe models).

#### *4.3.2.1 High Resolution EBSD*

To analyse the elastic strain field and lattice rotations around each of the indents, high angular resolution EBSD was performed by Ben Britton, using a JEOL 6500F FEG SEM operating at 20 kV with a probe current of ~ 1 nA, and a step size of 0.3 µm. Unlike conventional EBSD (see section 3.2), in which diffraction patterns are indexed 'on-line' during a scan and the orientation data saved to disk, in HR-EBSD the diffraction pattern at each point is saved at full resolution, and analysed post-scan. The technique uses a cross-correlation based analysis (described in [91]), in which by comparing patterns in stressed areas to an un-stressed reference pattern, small shifts can be detected (down to a few hundredths of a pixel [99]), which can be related to the elastic strain and lattice rotations. This method is sensitive to elastic strains of $1 \times 10^{-4}$, and lattice rotations of $\pm 0.0001$ rad [32]. The cross-correlation analysis is carried out using CrossCourt 3 (BLG Productions Ltd, Bristol, UK).

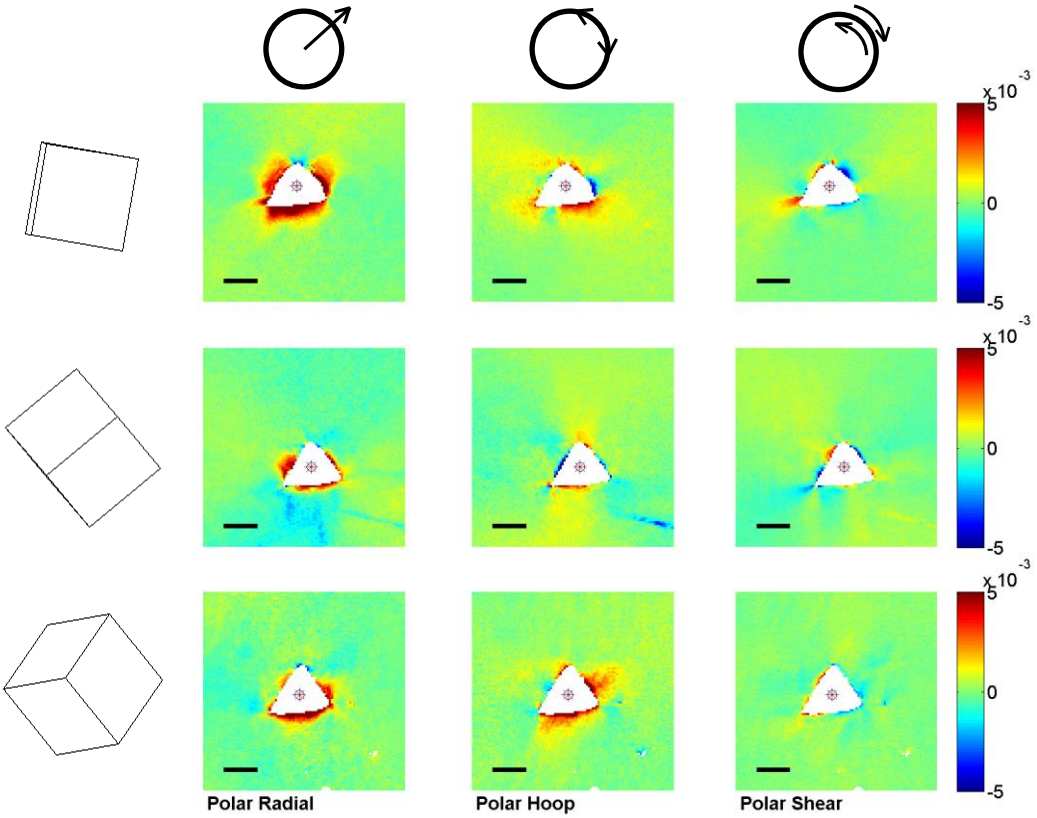


Figure 4-8: Polar elastic strain map of indents (with respect to origin marked in centre of each indent). The colour scale gives the absolute strain; scale bars are 5 µm long.

Figure 4-8 shows maps of the elastic strain fields (resolved into polar coordinates) surrounding indents corresponding to the load-displacement data in Figure 4-7, whereas Figure 4-9 shows maps of the lattice rotations (about fixed Cartesian axes). The lattice rotations, which give an indication of the extent of the plastic zone, are of a greater magnitude than the elastic strains, and hence the maps appear less noisy. The lattice rotations are also more localised around the indents, whereas the elastic strains vary over a wider area. Figure 4-8 and Figure 4-9 demonstrate the large degree of variety seen between the different crystal orientations probed, e.g. the polar radial elastic strain surrounding the <100> oriented indent is largely tensile, whereas surrounding the <110> oriented indent there are also some compressive areas.

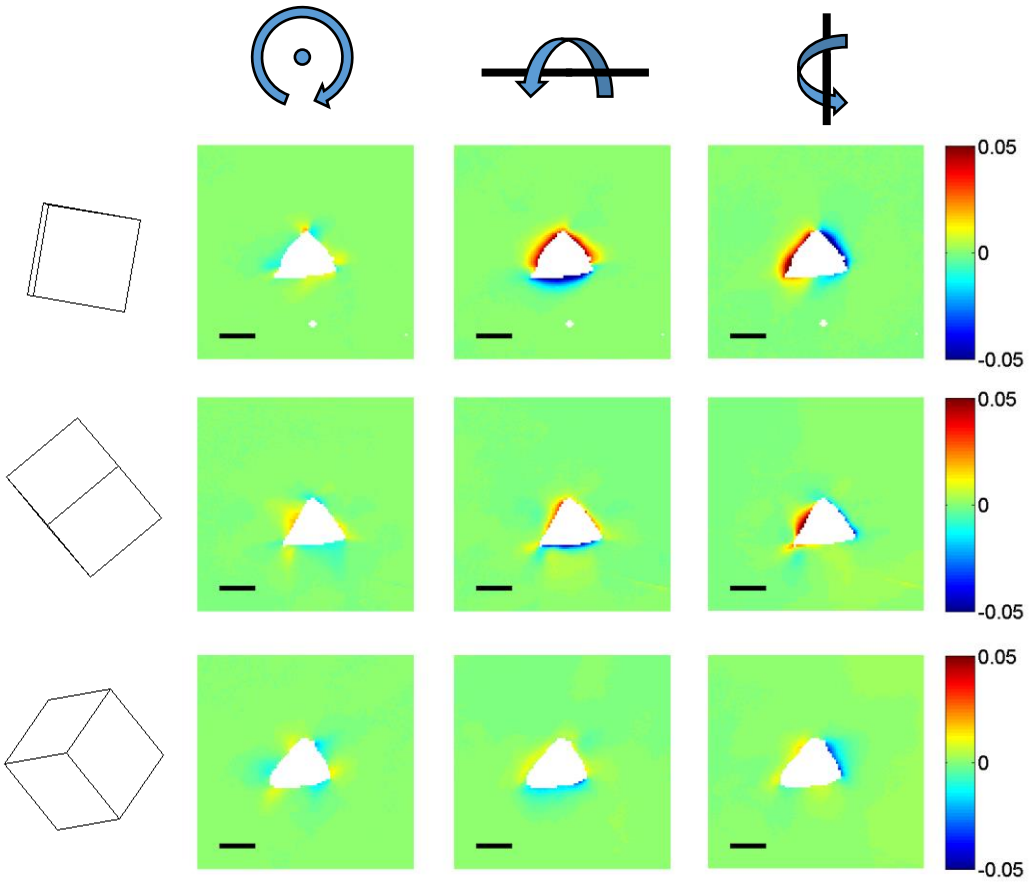


Figure 4-9: Lattice rotation maps of indents. The colour scale gives the rotation in radians; scale bars are 5 µm long.

The extent of the pile-ups surrounding each indent is seen from the second and third columns of Figure 4-9, i.e. the out of plane lattice rotations. A relatively large pile-up surrounds the <100> oriented indent, with increasingly smaller ones seen in the <110> and <111> indents. The in-plane lattice rotations are smaller than the out of plane ones, but also vary substantially for the different orientations, e.g. the positions of the positive and negative 'lobes' seen below the <100> and <111> indents are reversed with respect to each other. The in-plane rotations around the <111> indent, showing a threefold rotational symmetry, are similar to those seen by Britton *et al.* surrounding an indent in titanium into the basal plane [32].

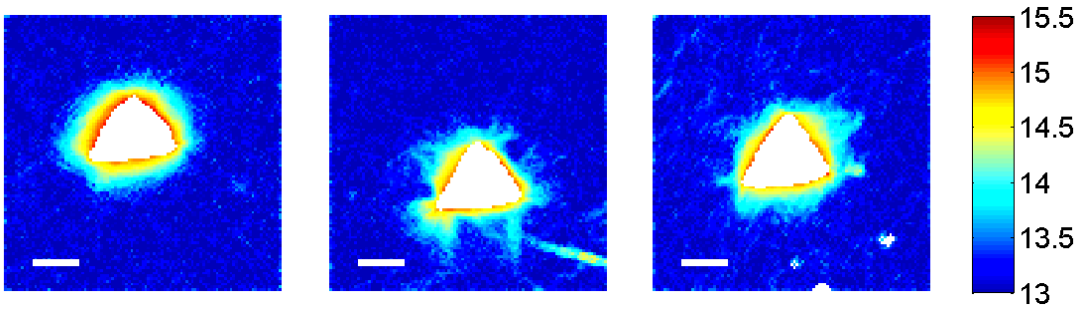


Figure 4-10: Total GND density surrounding indents close to [100] (left), [110] (centre), and [111] (right) normal directions. The colour scale is a log scale representing GND density per $m^2$, and the scale bars are 5 µm long.

From the measured lattice rotations, and a knowledge of the slip systems available in bcc materials, it is possible to calculate a lower bound solution for GND density, using a relationship developed by Nye [100]. Figure 4-10 shows one such 'deconstruction' of the GND densities surrounding the three indents. The distribution of GNDs surrounding the <100> indent extends out further than around the <110> and <111> indents, and also in the latter two, vein like patterns of dislocation activity are apparent (the line towards the bottom right of the <110> map is due to a scratch on the sample).

#### *4.3.2.2 Atomic Force Microscopy (AFM)*

Topographical AFM was performed on the indents seen in Figure 4-7 to Figure 4-10, using a Park Autoprobe CP-II, and analysing the results with Gwyddion 2.4. Figure 4-11 shows the distinctive pile-up lobes seen around each indent, with the positional distribution and magnitude dependent on the crystallography. The <100> indent has the largest amount of material piled-up, with the lobe to the right of the indent approximately 125 nm above the sample surface, whilst the pile-up heights of the other two indents reach lower peaks.

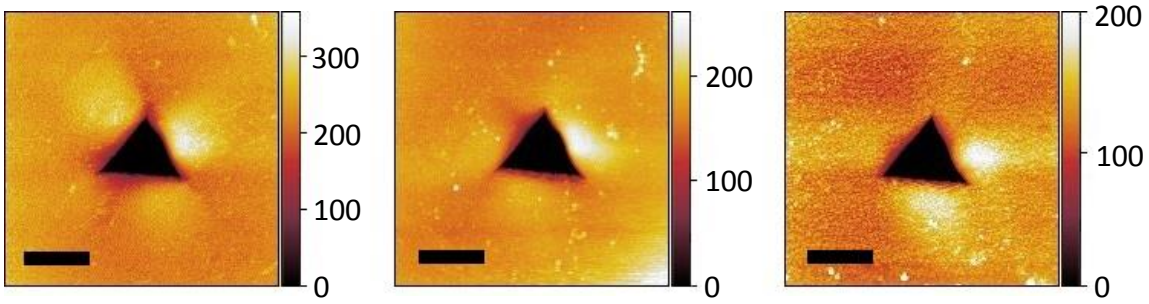

Figure 4-11: Topographical AFM maps of indents seen previously, close to <100> (left), <110> (centre), and <111> (right) normal directions (scale bars are 5 µm long, colour bar in nm).

## 4.4 Conclusion

In this chapter, measurements of indentation modulus and hardness have been conducted over a range of differently orientated grains in an iron polycrystal. In addition to this, selected indents from grains with normal directions close to the three major crystallographic axes have been further studied, using HR-EBSD and AFM.

A systematic variation in hardness is observed, from ~0.95 GPa in the <100> orientation, to 1.05 – 1.1 GPa nearer the <110> and <111> orientations. Due to the complex nature of the stress state beneath an indent, in which multiple slip systems can be in operation, the anisotropy in indentation hardness is less than the anisotropy in the yield strength of single crystals [29]. HR-EBSD and AFM give further information about plastic zones around the indents, showing that the flow patterns are highly heterogeneous in nature.

For the indentation modulus, any trends present in the data are not observable above the scatter in the measurements. This may be partially caused by the varying amounts of pile-up around each indent impression. Indentation modulus is particularly sensitive to the contact area, therefore increases due to pile-up which are unaccounted for are likely to overestimate modulus values. As the crystallographic dependence on the plastic flow patterns around indents is complicated and not well known, it is possible that the varying changes in contact

area in different grains obscure any trend in modulus variation. Hardie used SEM imaging to directly measure the contact area, and correct measured indentation modulus values based on this [101], however this would be time consuming when looking at a large number of indents.

Across the two indent arrays (performed on different dates), the difference in average indentation modulus is 1.7% (Figure 4-12). This compares well with previous studies, in which differences as high as 50% had been observed on the same sample on different testing occasions, demonstrating that the chosen sample holder design was successful in reducing scatter. The average values between each array are unlikely to be exactly the same, due to the different grains sampled in each.

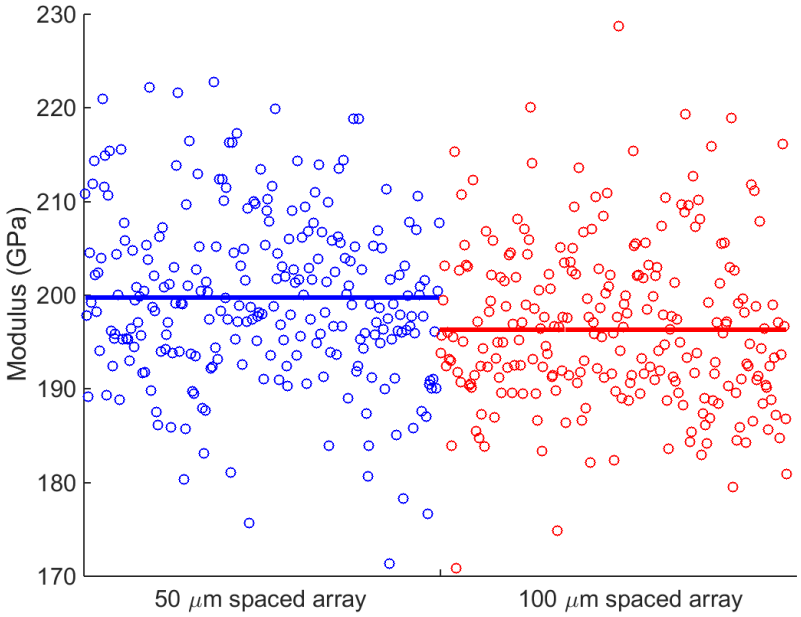


Figure 4-12: Range of indentation moduli for the 50 µm and the 100 µm spaced arrays. The mean value of each array is shown by the two horizontal lines.

The measurements of GND density around indents using HR-EBSD (Figure 4-10), and of pile-up height using AFM (Figure 4-11) give a direct in-plane measure of the extent of the plastic

zone. In Chapter 6, Johnson's cavity model will be used as a proxy for such direct measurements, with the size of the plastic zone (equation (6-4)) being approximated using the applied indenter load, $P$, and the yield stress, $\sigma_{ys}$ (estimated using the Tabor relation, equation (2-1)). Using the parameters obtained for the 3 selected indents in this chapter, Johnson's cavity model gives plastic zone sizes for indents in the <100>, <110>, and <111> normal directions of 6.27 μm, 6.22 μm and 6.26 μm respectively. Conversely, plastic zone size measurements in this chapter (averaged over the three indenter faces) give values for indents in the <100>, <110>, and <111> normal directions of 6.36 μm, 5.11 μm, and 5.82 μm using the data in Figure 4-10, and 5.91 μm, 4.51 μm, and 5.02 μm using the data in Figure 4-11. The similarity in the three values obtained using equation (6-4) is a reflection of the fact that the heterogeneous flow patterns which vary with crystallography are not taken into account in Johnson's model, which assumes a spherical plastic zone (see section 6.1.4). Despite this, the value for the <100> indent agrees well with the plastic zone size obtained using GND data, possibly due to the fact that the distribution of GNDs around the <100> indent (Figure 4-10, left) is more spherical than that for the other two orientations. In general, the plastic zone size values calculated using Johnson's model are closer to the measurements using GND data than those using AFM data.

The measurements of GND density in Figure 4-10 can be compared with the magnitude predicted for a 1 μm indent in iron using the Nix-Gao strain gradient plasticity model (see section 2.1.3). Equation (2-14) gives a GND density of 7.75 x $10^{+14}$ $m^{-2}$, which is consistent with the values seen in Figure 4-10, however the Nix-Gao model predicts a single homogenous GND density rather than the spatially varying GND densities shown.

This experiment demonstrates the limitations in using nanoindentation to extract mechanical properties data. Although nanoindentation is relatively quick and easy to perform, it is much harder to interpret the data compared to tests involving simpler stress states. Additionally, the complex stress state tends to average out behaviour in many different crystallographic directions so that the anisotropy really present in the material properties is missed. Conversely, although using test specimens FIB-milled into single grains is a lot more time consuming and difficult to perform, it is much easier to obtain valid mechanical properties data, particular of elastic properties (see next chapter).

# 5 Determining Single Crystal Elastic Constants Using L-Shaped Micro-Cantilevers

## 5.1 Introduction

Although the assumption of elastic isotropy can be justified in the case of many engineering problems [4], the majority of materials are fundamentally elastically anisotropic [12]. A full understanding of such anisotropy is therefore important for predicting their large scale mechanical behaviour. Furthermore, certain processing routes result in strong crystallographic textures [102], making the variation in elastic moduli (e.g. the Young's modulus and shear modulus) with orientation highly relevant. In other cases, the length scales involved in a particular material's application are sufficiently small that elastic behaviour might be significantly different compared with the bulk isotropic response.

Experimental knowledge of the full anisotropic stiffness tensor (see section 5.1.1) is important for ab-initio modelling work, either as an input [103], or to test the accuracy of interatomic potentials used in solid state physics calculations [104,105]. In addition, dislocation dynamics (DD) modelling requires fully anisotropic elasticity to accurately replicate certain experimental results [106]. Of particular relevance to candidate Ferritic-Martensitic steels for fusion reactors, is the drop in strength seen in iron as the alpha-gamma phase transition temperature is approached (see Figure 5-1). This effect, which is related to the significant increase in elastic anisotropy in iron at high temperatures [107], cannot be replicated using isotropic elasticity (used for the majority of DD modelling due to its analytical and numerical simplicity [106,108]). Models including anisotropic elasticity are also able to replicate the hexagonal or square shaped prismatic dislocation loops seen in electron

microscopy studies of irradiated α-Fe (which are circular under isotropic assumptions) [109,110].

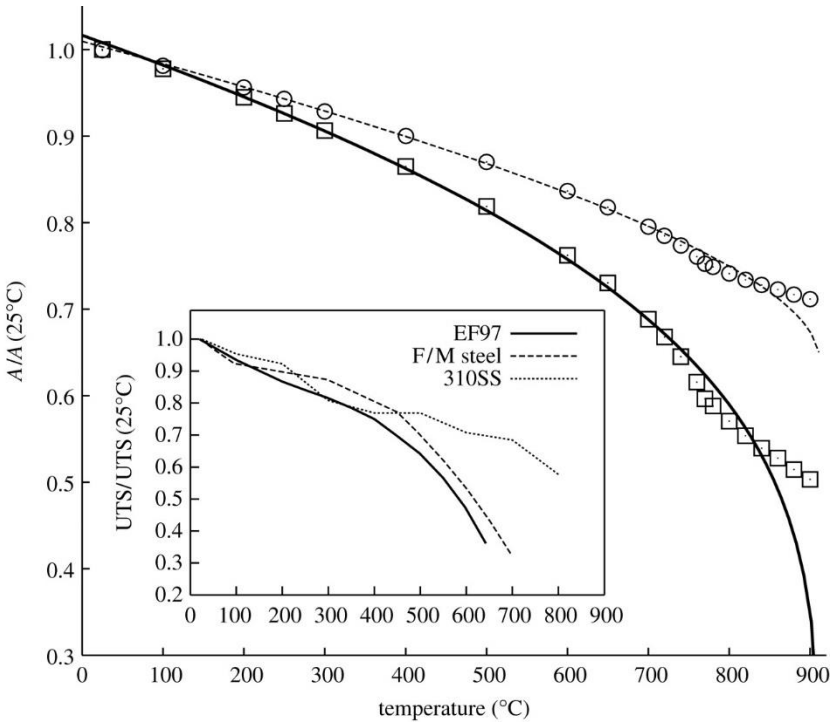


Figure 5-1: Dislocation interaction force constant 'A' (a measure of pile-up 'strength') as a function of temperature, from DD modelling using isotropic (circles) and anisotropic (squares) elasticity. The experimental ultimate tensile strength of three steels versus temperature is shown inset (from [106]).

Well established methods exist to extract elastic constants from bulk specimens (see section 5.1.2), however many of these require the materials of interest to be readily available in single crystal form and in a variety of orientations for measuring anisotropic behaviour. For many alloys this is not possible, due to them not being stable at the macro-scale [65]. Using such bulk methods is also inappropriate for probing the elastic properties of small volumes of material, such as in ion-irradiated specimens.

Elastic constants can be extracted from polycrystalline materials by taking x-ray diffraction measurements during in-situ loading in a synchrotron [111]. However, this requires

significant assumptions to be made in converting the applied stress to the stress carried by the differently orientated grain families [65].

Nanoindentation can be used to probe elastic properties on a highly localised scale, giving the potential to extract properties from within single grains of polycrystals. However, the stress state around the indenter tip varies greatly with position, giving a measured modulus which encompasses many different crystal orientations. Using numerical modelling, it is possible to calculate indentation moduli given a knowledge of the elastic constants and indenter geometry [29]. However, in addition to being analytically complex, such a process is more sensitive to some stiffness components than others, and may not result in a unique solution if attempts are made to solve the inverse problem of determining elastic constants from the indentation modulus.

Taking advantage of a more simplified stress state, micro-cantilever testing has been employed to measure the variation of Young's modulus $(E)$ with orientation, in copper [63] and titanium [65] (see section 2.2.2.1). However, due to the coupling of elastic constants (see section 5.1.1), it is impossible using such tests to fully extract all single crystal elastic constants comprising the full anisotropic stiffness tensor. In this chapter, a novel test making use of an 'L' shaped micro-cantilever will be employed, in order that the full set of elastic constants can be extracted experimentally from a single grain within a polycrystal.

### 5.1.1 Elasticity Theory

In a uniaxial mechanical test, the relationship between stress, $\sigma$, and strain, $\varepsilon$, below the elastic limit (i.e. the point beyond which there is permanent deformation upon the removal of load), is described by Hooke's law as follows:

$$\sigma = E\varepsilon \tag{5-1}$$

where the constant of proportionality, $E$, is Young's Modulus. For a bar loaded in tension, a uniaxial extension in the x-direction will also produce lateral contractions in y and z, given by:

$$\varepsilon_y = \varepsilon_z = -\nu\varepsilon_x \tag{5-2}$$

where $\nu$ is Poisson's ratio. For most metals, $\nu$ varies from 0.28 – 0.42 [112]. Although metals approximate the behaviour described by equations (5-1) and (5-2) within the elastic limit, plasticity often takes place before significant non-linearity in the stress-strain curve occurs [12].

A similar relationship to equation (5-1) exists for cases of pure shear, between shear stress, $\tau$, and shear strain, $\gamma$:

$$\tau = G\gamma \tag{5-3}$$

where $G$ is the shear modulus. Usually states of stress and strain on a body occur in three dimensions, in which case equation (5-1) can be generalised as:

$$\sigma_{ij} = C_{ijkl}\varepsilon_{kl} \quad (i,j,k,l = 1,2,3) \tag{5-4}$$

or equivalently,

$$\varepsilon_{ij} = S_{ijkl}\sigma_{kl} \quad (i,j,k,l = 1,2,3) \tag{5-5}$$

where $\sigma_{ij}$ and $\varepsilon_{ij}$ are the stress and strain tensors, respectively, $C_{ijkl}$ is the stiffness tensor, and $S_{ijkl}$ is the compliance tensor [113]. In equations (5-4) and (5-5), the standard Einstein notation is used, in which a repeated letter in a single term denotes summation over that term for all possible values of the letter. As both $\sigma_{ij}$ and $\varepsilon_{ij}$ are second-rank tensors with 9 terms each, $C_{ijkl}$ and $S_{ijkl}$ must be forth-rank tensors with 81 coefficients each. However, as $\sigma_{ij}$ and $\varepsilon_{ij}$ are both symmetric (i.e. $\sigma_{ij} = \sigma_{ji}$), it follows that $S_{ijkl} = S_{ijlk}$ and $S_{ijkl} = S_{jikl}$ (and similarly for the $C_{ijkl}$). This reduces the number of independent components of $C_{ijkl}$ to 36 (and similarly for $S_{ijkl}$).

This symmetry allows for Voigt's contracted notation to be used [12], in which the following substitutions are made:

$$\begin{bmatrix} \sigma_{11} & \sigma_{12} & \sigma_{31} \\ \sigma_{12} & \sigma_{22} & \sigma_{23} \\ \sigma_{31} & \sigma_{23} & \sigma_{33} \end{bmatrix} \rightarrow \begin{bmatrix} \sigma_1 & \sigma_6 & \sigma_5 \\ \sigma_6 & \sigma_2 & \sigma_4 \\ \sigma_5 & \sigma_4 & \sigma_3 \end{bmatrix} \tag{5-6}$$

and

$$\begin{bmatrix} \varepsilon_{11} & \varepsilon_{12} & \varepsilon_{31} \\ \varepsilon_{12} & \varepsilon_{22} & \varepsilon_{23} \\ \varepsilon_{31} & \varepsilon_{23} & \varepsilon_{33} \end{bmatrix} \rightarrow \begin{bmatrix} \varepsilon_1 & \frac{\varepsilon_6}{2} & \frac{\varepsilon_5}{2} \\ \frac{\varepsilon_6}{2} & \varepsilon_2 & \frac{\varepsilon_4}{2} \\ \frac{\varepsilon_5}{2} & \frac{\varepsilon_4}{2} & \varepsilon_3 \end{bmatrix} \tag{5-7}$$

Equations (5-4) and (5-5) can then be written as:

$$\sigma_i = C_{ij}\varepsilon_j \quad (i,j = 1,2,\dots,6) \tag{5-8}$$

and

$$\varepsilon_i = S_{ij}\sigma_j \quad (i,j = 1,2,\dots,6) \tag{5-9}$$

The factors of ½ in (5-7) prevent such factors from being required in equation (5-9) The components of $C_{ij}$ and $S_{ij}$ in array form are:

$$\begin{pmatrix} c_{11} & c_{12} & c_{13} & c_{14} & c_{15} & c_{16} \\ c_{21} & c_{22} & c_{23} & c_{24} & c_{25} & c_{26} \\ c_{31} & c_{32} & c_{33} & c_{34} & c_{35} & c_{36} \\ c_{41} & c_{42} & c_{43} & c_{44} & c_{45} & c_{46} \\ c_{51} & c_{52} & c_{53} & c_{54} & c_{55} & c_{56} \\ c_{61} & c_{62} & c_{63} & c_{64} & c_{65} & c_{66} \end{pmatrix} \tag{5-10}$$

and

$$\begin{pmatrix} s_{11} & s_{12} & s_{13} & s_{14} & s_{15} & s_{16} \\ s_{21} & s_{22} & s_{23} & s_{24} & s_{25} & s_{26} \\ s_{31} & s_{32} & s_{33} & s_{34} & s_{35} & s_{36} \\ s_{41} & s_{42} & s_{43} & s_{44} & s_{45} & s_{46} \\ s_{51} & s_{52} & s_{53} & s_{54} & s_{55} & s_{56} \\ s_{61} & s_{62} & s_{63} & s_{64} & s_{65} & s_{66} \end{pmatrix} \tag{5-11}$$

Using arguments based on the energy of a strained crystal [114], it can be shown that $C_{ij} = C_{ji}$, and $S_{ij} = S_{ji}$. This further reduces the number of independent coefficients of $C_{ij}$ and $S_{ij}$ to 21. Further simplifications can be made by considering that elasticity is a centrosymmetric property [113], meaning that upon undergoing a rotational transformation about a centre of symmetry the components of $C_{ij}$ and $S_{ij}$ are unchanged. For cubic crystals, this results in just 3 independent elastic constants: $c_{11}$, $c_{12}$ and $c_{44}$ in (5-10) and $s_{11}$, $s_{12}$ and $s_{44}$ in (5-11), with all other components equal to zero:

$$\begin{pmatrix} c_{11} & c_{12} & c_{12} & & & \\ c_{12} & c_{11} & c_{12} & & & \\ c_{12} & c_{12} & c_{11} & & & \\ & & & c_{44} & & \\ & & & & c_{44} & \\ & & & & & c_{44} \end{pmatrix} \tag{5-12}$$

and

$$\begin{pmatrix} s_{11} & s_{12} & s_{12} & & & \\ s_{12} & s_{11} & s_{12} & & & \\ s_{12} & s_{12} & s_{11} & & & \\ & & & s_{44} & & \\ & & & & s_{44} & \\ & & & & & s_{44} \end{pmatrix} \tag{5-13}$$

Thus the elastic response of a cubic crystal can be completely described if these numbers are known. The relationship between the $C_{ij}$ and the $S_{ij}$ is given by:

$$C_{ij}S_{ij} = \mathbf{I} \tag{5-14}$$

where $\mathbf{I}$ is the identity matrix. The components of the stiffness tensor in terms of the compliance tensor components are:

$$\begin{aligned} c_{11} &= \frac{s_{11} + s_{12}}{(s_{11} - s_{12})(s_{11} + 2s_{12})} \\ c_{12} &= \frac{-s_{12}}{(s_{11} - s_{12})(s_{11} + 2s_{12})} \\ c_{44} &= \frac{1}{s_{44}} \end{aligned} \tag{5-15}$$

and similarly for the components of the compliance tensor in terms of the stiffness tensor components, but with the positions of the $C_{ij}$'s and $S_{ij}$'s exchanged.

Further restrictions on the $C_{ij}$ and $S_{ij}$ values are found by ensuring that the strain energy of a crystal must be positive (see Nye for details [113]). For a cubic crystal, these are:

$$c_{44} > 0, \;\; c_{44} > |c_{12}|, \;\; c_{11} + 2c_{12} > 0 \tag{5-16}$$

Using these elastic constants, the Young's modulus can be given in any arbitrary direction, described by the direction cosines $u$, $v$, and $w$, by:

$$\frac{1}{E} = s_{11} - 2(s_{11} - s_{12} - \frac{s_{44}}{2})(u^2v^2 + v^2w^2 + w^2u^2) \tag{5-17}$$

And similarly the shear modulus by [115]:

$$\frac{1}{G} = s_{44} + 4(s_{11} - s_{12} - \frac{s_{44}}{2})(u^2v^2 + v^2w^2 + w^2u^2) \tag{5-18}$$

Figure 5-2 shows Young's modulus as a function of orientation for several bcc metals at room temperature and pressure, using data from [116]. It can be seen that of these iron exhibits the greatest degree of anisotropy.

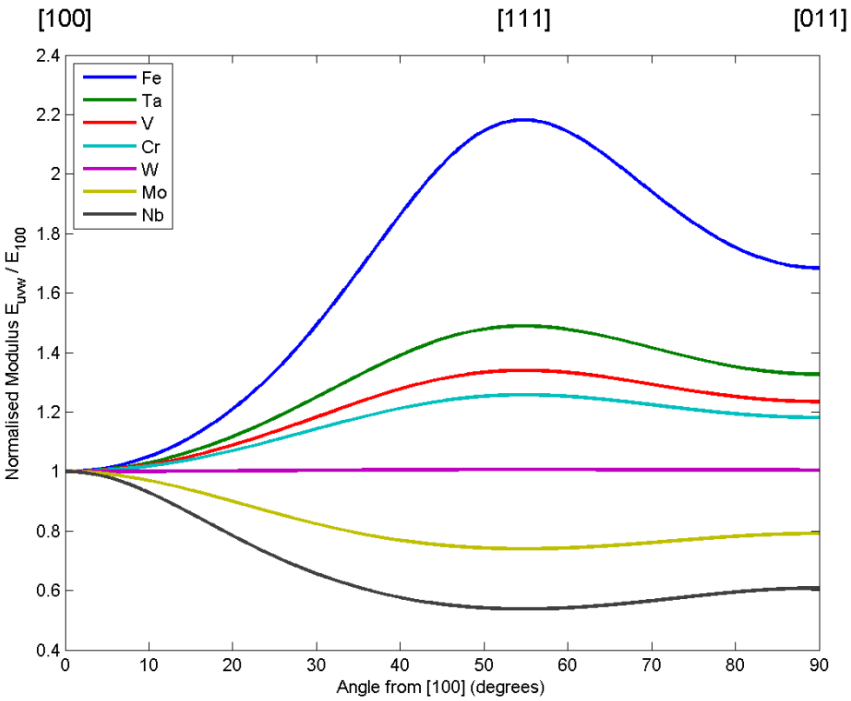


Figure 5-2: Normalised Young's modulus as a function of the angle from [100] towards [011] (in the $01\bar{1}$ surface) for several bcc metals (redrawn from [75]).

An alternative method of showing the anisotropy of elastic moduli is by the use of representation surfaces [115], in which the height of the surface at any point is equal to the magnitude of the particular elastic property (e.g. the Young's modulus or shear modulus), in that direction. Surfaces are shown in Figure 5-3 and Figure 5-4 for the Young's modulus and shear modulus of iron at 300 $K$, using elastic constants measured by Adams et al. [117] (see section 5.1.2.4). Young's modulus for iron is at its maximum along the <111> body diagonals and minimum along the <001> cube axes, where shear modulus is largest. Table 5-1 shows values of Young's modulus and shear modulus for iron at 300 $K$ calculated using these same constants, along the three major crystallographic directions.

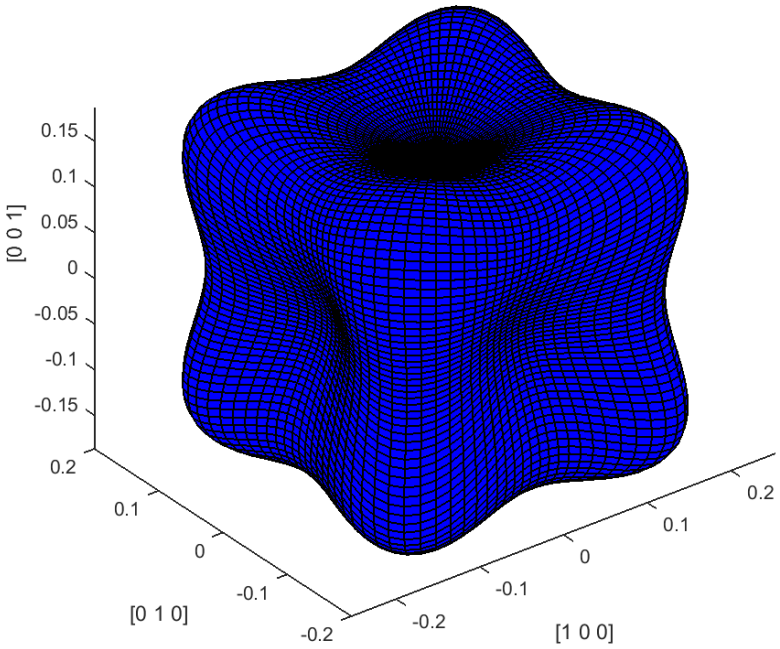


Figure 5-3: Representation surface for the Young's modulus of iron at 300 $K$, using constants measured by Adams et al. [117]. The length of the vector defining the surface in any direction is equal to $E$ in that direction (in units of $10^{12} N/m^2$).

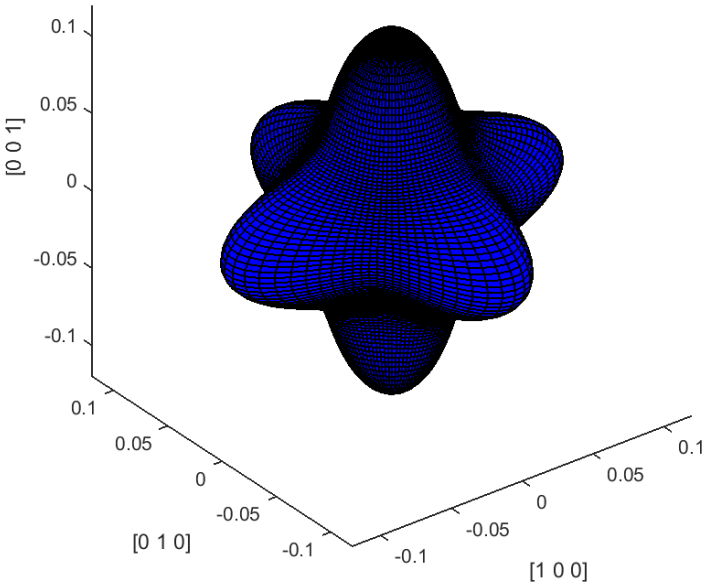


Figure 5-4: Representation surface for the shear modulus of iron at 300 $K$, using constants measured by Adams et al. [117]. The length of the vector defining the surface in any direction is equal to $G$ in that direction (in units of $10^{12} N/m^2$).

| | [100] | [110] | [111] |
|---|---|---|---|
| Young's modulus (GPa) | 132 | 219 | 282 |
| Shear modulus (GPa) | 116 | 68 | 59 |

Table 5-1: Young's modulus and shear modulus along the three major crystallographic directions in iron at 300 $K$, using equations (5-17) and (5-18), and constants from Adams et al. [117].

### 5.1.2 Measuring Elastic Constants

Methods for determining the elastic properties of materials are usually divided into two groups: static and dynamic. In this section, these will both be reviewed, and their relative advantages and disadvantages discussed.

#### *5.1.2.1 Static Methods*

Static methods involve subjecting test pieces to various types of loading (e.g. tension, compression, torsion or flexure [4]), and measuring the resultant strain (making sure the compliance of the loading system has been taken into account). Elastic moduli relating to the stress and strain can then be determined, including the Young's modulus, shear modulus, and Poisson's ratio. Often, the linear elastic portion of a test that has been continued to

higher loads to measure the plastic properties of a member can be used to measure the elastic moduli.

In order to ensure the reliability of static tests, extensive calibrations must be carried out, e.g. of the load cell to measure the force, and strain gauges or extensometers to measure the displacement. Various standards have been developed (listed in [4]) in order to ensure that quantities measured in different laboratories can be fairly compared. Constants measured using static techniques are typically accurate to $\pm 5\ \%$ [4].

#### *5.1.2.2 Dynamic Methods*

Dynamic methods involve either measuring the time taken for an ultrasonic pulse to pass through a material, or measuring the resonant frequencies of a test piece when subjected to vibration, both of which can be linked back to the fundamental elastic constants of the material, and its density.

The ultrasonic pulse method makes use of the fact that the speed of sound, $v$, in a material is dependent on its Young's modulus and density, $\rho$, via $E = \rho v^2$. The sound speed can be determined by measuring the time taken for a pulse to travel a certain fixed distance. Different types of sound wave (e.g. longitudinal, shear) can be used to determine different elastic constants. Constants can be measured using this method to within $\pm 0.1\ \%$ of the mean value [4].

The more widely used dynamic method is to induce vibration in a specimen, either mechanically by striking it with a steel ball attached to a rod, or by a sonic pulse. In the first case, either a contact sensor or microphone is placed near the bar to measure the resultant

vibration, with the fundamental frequency and the sample dimensions and mass used to determine the Young's modulus or shear modulus, depending on the excited mode. In the case of the sonic pulse, a bar is suspended by two wires, with an exciting transducer attached to one and a detecting transducer attached to the other. By varying the frequency of the input, the resonant frequency can be found by an enhancement of the detected signal (with the wire positions moved up and down the bar to identify the nodes and antinodes). Constants can be measured to within $\pm\ 0.1\ \%$ using this method [4].

#### *5.1.2.3 Differences between Static and Dynamic Methods*

The elastic moduli measured by static and dynamic methods have small fundamental differences due to the contrasting nature of the two types of test. In static tests, the stresses applied are slowly varying (i.e. quasistatic), such that there is plenty of time for heat to be transferred between the test specimen and its surroundings. These tests therefore take place under constant temperatures, i.e. they are *isothermal*. In dynamic tests on the other hand, the timescales involved are insufficient for heat transfer to take place, making such tests *adiabatic*. However, the difference between isothermal and adiabatic Young's modulus for iron at room temperature is $\sim 0.25\ \%$, which is less than the experimental uncertainty for most dynamic methods [118]. The isothermal and adiabatic shear moduli are always equal.

Static methods were the first to be developed historically, and are relatively simple to perform and analyse. However, they have generally been superseded by dynamic methods [12], which are held to be about 5 times more accurate for determining elastic constants [4]. The major disadvantage of static testing is that the accuracy with which stress and strain can be measured is limited. This can be particularly problematic with extremely stiff materials in which the displacement might not be great enough for the strain gauge to accurately

measure the strain [75]. Furthermore, the stresses used in static methods are relatively large compared with dynamic methods, meaning that a small amount of plasticity is likely to occur, limiting the accuracy of the determined elastic properties. In a round robin test, the standard deviation in measurements of the Young's modulus of an austenitic steel was 6 % using static methods and 0.5 % using dynamic methods [118].

Dynamic methods have the advantage that the test pieces can be much smaller (down to sub-mm-size [119]), and as the stresses involved are well below the elastic limit, a single sample can be reused multiple times to measure elastic moduli for a range of different conditions, e.g. temperatures or pressures. However, such methods are more complicated to perform and analyse.

A major drawback of both methods is that in order to measure the anisotropy of elastic moduli, single crystals of various orientations must be produced.

#### *5.1.2.4 Previous measurements of single crystal elastic constants for iron*

Being of fundamental importance as the basis of many practical materials, the elastic constants of iron have been studied extensively, using a variety of techniques. Several of these are collated in Table 5-2, with all the constants being obtained at room temperature and pressure. The constants in bold (either compliance or stiffness) are those quoted in the reference, with the others obtained using equation (5-15). Most of the literature makes use of dynamic methods, however one study listed in Table 5-2 uses static testing.

| Year | Author | $C_{11}$ | $C_{12}$ | $C_{44}$ | $S_{11}$ | $S_{12}$ | $S_{44}$ |
|---|---|---|---|---|---|---|---|
| 1931 | Goens and Schmid [120] | 236.88 | 140.63 | 116.01 | **7.57** | **-2.82** | **8.62** |
| 1946 | Hearmon [121]* | 228.09 | 133.48 | 110.86 | **7.72** | **-2.85** | **9.02** |
| 1961 | Rayne and Chandrasekhar [122] | **233.10** | **135.44** | **117.83** | 7.49 | -2.75 | 8.49 |
| 1965 | Lord and Beshers [123] | **228** | **132** | **116.5** | 7.62 | -2.79 | 8.58 |
| 1966 | Rotter and Smith [124] | **231.4** | **134.6** | **116.4** | 7.55 | -2.78 | 8.59 |
| 1968 | Leese and Lord [125] | **226** | **140** | **116** | 8.41 | -3.22 | 8.62 |
| 1972 | Dever [126] | **232.2** | **135.6** | **117.0** | 7.56 | -2.79 | 8.55 |
| 2006 | Adams et al. [117] | **230** | **134** | **116** | 7.59 | -2.79 | 8.63 |

Table 5-2: Experimentally obtained single crystal stiffness constants (GPa) and compliance constants ($TPa^{-1}$) for iron, using a range of different methods (* = Static measurement).

## 5.2 Method

### 5.2.1 Beam Design

In order to be able to determine the fully anisotropic elastic constants, the design of the beam for this experiment had to be such that both bending and torsion modes could be tested. To this end, an L-shaped beam was designed, with an isosceles right-angled triangle cross section, and having two shorter inside edges and two longer outside edges (see Figure 5-5). The sides of the beam were perpendicular to the sample surface for the inside edges, and at 45° to the sample surface for the outside edges, such that the two sides met directly below the inside edges. Such a design was necessary as attempting to adapt a 'conventional' equilateral triangle cross-sectioned micro-cantilever into an L-shape would have run into problems in the corner at the join between the two arms.

For the remainder of this chapter, the arm of the beam attached to the bulk material will be referred to as the 'encastre' arm, whilst the other arm shall be referred to as the 'free' arm.

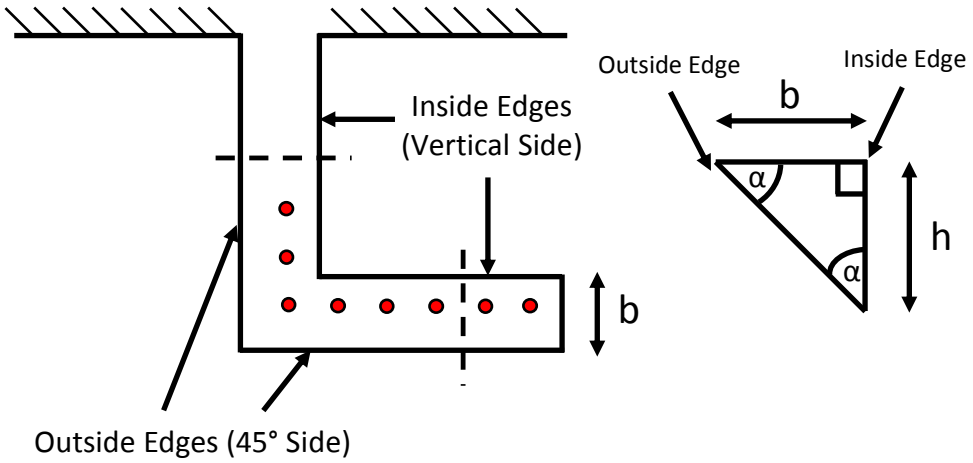


Figure 5-5: Schematic of the L-shaped cantilever design shown from overhead (left) and cross-sectionally at the position of the dotted lines (right). Red circles represent typical points at which the beam was indented. Outside edge = 30 µm, inside edge = 25 µm, $\alpha = 45°$, $b = h = 5\ \mu m$.

The size of the beam was picked as a compromise between several factors. As shown by Armstrong [75], beams with aspect ratios (the ratio of indented length to width) greater than 6 are reasonably approximated using the equations of simple beam theory, due to the effect of flexure at the non-encastre 'fixed' end being diminished as compared with lower aspect ratio beams. However, such beams take longer to manufacture in the FIB, and due to them being more compliant, can present challenges during indentation. Specifically, they are more likely to be damaged during scanning, and the target contact stiffness during the surface finding routine must be set lower, significantly closer to the noise floor, occasionally resulting in false surface detection. Furthermore, stiffer beams are more likely to show the indentation mark caused by the tip penetrating into the beam surface, improving the accuracy of the post-test analysis, as the loading positions can be more accurately determined. As a compromise between all of these factors, outside edge and inside edge lengths of 30 µm and 25 µm were chosen, respectively, with a beam width and thickness of 5 µm (see Figure 5-5).

### 5.2.2 Sample Preparation and EBSD

As a simple model system, pure iron supplied by EFDA was used, with a mean grain size of 183 µm (see section 6.2.1 for further details). A ~0.5 mm thick disc was cut from a rod ~10 mm in diameter, ground using SiC papers to a 4000 grit finish, and polished using colloidal silica. It was then mounted with silver dag on a JEOL stub for further experimentation.

Any crystal orientation could be used to probe the bending and torsion responses of the L-shaped beam, however for analytical ease, orientations with well characterised elastic properties were chosen. Initially, grains with surface normal directions of <1 0 0> and <1 1 0> were picked, allowing the bending and torsion response in both the <1 0 0> and <1 1 0> directions to be tested. Low resolution EBSD (step size = 25 µm) was used to create a coarse IPF map of the sample, from which candidate grains could be identified using the OIM software package. Regions centred on these grains were subsequently rescanned with greater care at a higher resolution (step size = 5 µm). Grains were picked which ideally were of a sufficient size for multiple beams to milled within.

Care was taken to precisely align the L-shape arms with the desired crystal orientations. Using the EBSD scan of the target grain, features (e.g. grain boundary segments) were identified which approximately aligned with the desired direction (e.g. [1 0 0]). Using these as a reference, several lines were FIB milled in a fan shape at a range of angles, parallel to the feature and at various angles away from it (see Figure 7-5). This fan shape was then re-scanned with EBSD, and the line closest to the desired direction was identified (using OIM) and used as a datum for all future milling in the grain. Figure 5-6 shows an IPF map of L-shaped cantilevers in two grains, with their arms aligned along major crystallographic directions.

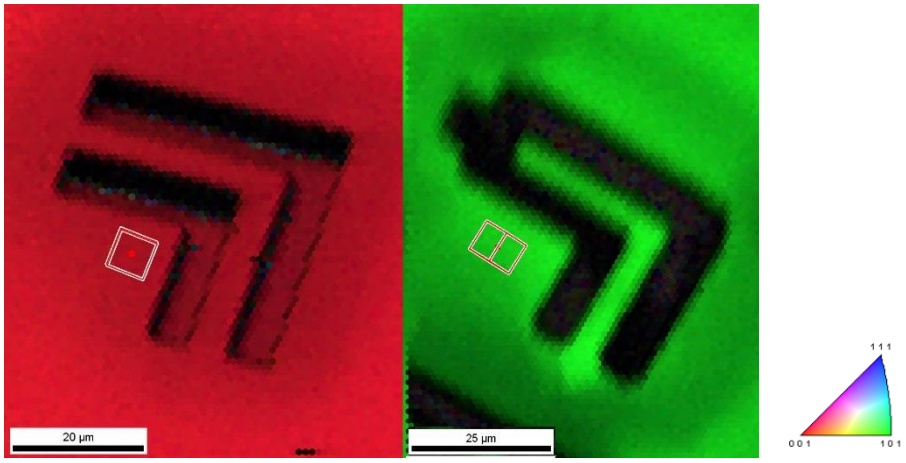


Figure 5-6: IPF maps (with image quality overlaid in greyscale) of L-shaped cantilevers milled in a [1 0 0] normal direction grain (left, trenches only) and a [1 1 0] normal direction grain. Unit cubes are shown to indicate crystal orientation.

### 5.2.3 Manufacture of L-shaped cantilevers

Manufacture of L-shaped cantilevers was conducted using either the FEI FIB 200 or the Zeiss Auriga, with an accelerating voltage of 30 $keV$. The process for manufacturing the L-shaped beams in the FIB was similar to that of regular triangular cross-section beams (see section 2.2.2), but with several additions. Firstly, a trench was milled leaving a rough 'plan view' outline of the beam, at a beam current of ~3000 – 5000 pA (see Figure 5-7 (a)). Although the required depth and width of the trench for an L-shaped beam is less than that of a typical 'straight' cantilever, due to the desired displacement being only within the elastic regime, a relatively deep trench was advantageous due to a smaller amount of re-deposition occurring during milling.

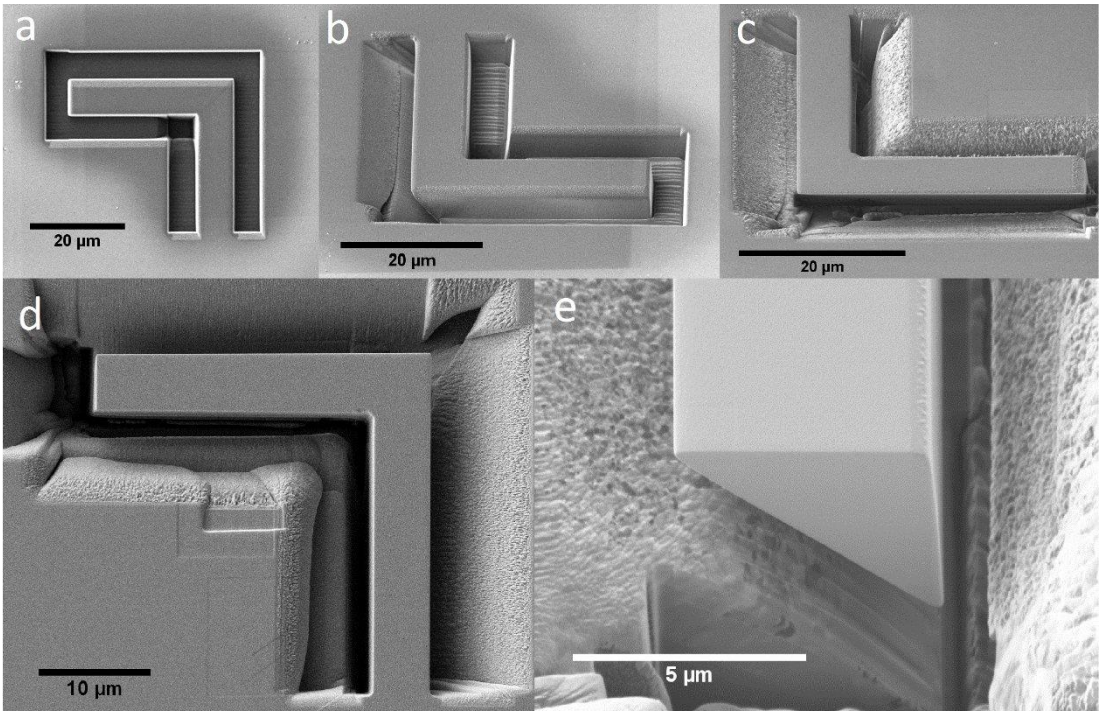


Figure 5-7: SEM images showing steps taken during L-shaped beam manufacture in the FIB. a) Initial trench milled at 3000 – 5000 pA; b) 'encastre' arm undercut at 3000 pA (45° tilt); c) 'free' arm undercut at 3000 pA and inside edges cleaned at 300 – 1000 pA (45° tilt); d) Outside edges and end cleaned at 300 – 1000 pA; e) Final beam, end view (30° tilt);

In the second step, the sample was tilted by 45° about the long axis of the 'encastre' arm, and undercut using a beam current of ~3000 pA (see Figure 5-7 (b)). The sample was then rotated by 90° about the sample surface normal, and the 'free' arm was similarly undercut (see Figure 5-7 (c)). The target width of both arms during these steps was ~50 % larger than the final width, so that these coarse steps could be performed at relatively high beam currents, without the beam tails and/or beam drift destroying the desired final cantilever shape, thus allowing for the final cleaning to be performed at lower currents.

Following this, the sample was returned to 0° tilt, and the inside edges were re-milled at ~1000 pA, ensuring that the beam was separated from the bottom of the trench by removing any material re-deposited on the underside during undercutting. This resulted in the beam being attached only at the fixed end shown at the top of the diagram in Figure 5-5. Particular care needed to be taken when performing any milling on the inside edge, as any small

mistakes could drastically alter the beam's mechanical performance, rendering it useless for accurate elasticity testing (and therefore wasting significant FIB time).

For the final step, each of the 4 edges were progressively milled down with smaller and smaller beam currents (down to ~300 pA), until the final beam dimensions were achieved (see Figure 5-7 (d) and (e)). Such cycling was necessary, as due to the increased number of milling angles compared to 'straight' cantilevers, there was a greater tendency for re-deposited material to build up on the underside.

### 5.2.4 Dimension Measuring in the SEM

After milling in the FIB, the L-shaped beams were measured in order to precisely record their dimensions. It was important to be as accurate as possible, as according to simple beam theory approximations, compliance is proportional to the cube of beam thickness (see equation (5-19)), meaning that any small errors can cause large differences in the analysis.

L-shaped beams were measured in the SEM to avoid causing excess ion implantation and damage associated with FIB imaging. Two different approaches were taken and compared to extract the dimensions. The first such method utilised the standard measuring approach used in micro-cantilever studies (see section 2.2.2), of tilting the sample to 30°, measuring the projected distance at this angle, and using basic trigonometry to calculate the beam thickness.

The second method was developed by Hardie [101], having recognised that commonly held assumptions of the first method (e.g. that the sample is parallel to the microscope stage) can lead to errors, particularly when measuring at significant tilt angles. To mitigate this, a stereo

imaging method can be used, in which images are recorded at two different tilt angles, and the relative difference between them is used to determine the beam dimensions. As this method is valid even in the case that the sample isn't flat with the stage set to 0°, it is less prone to error (as shown in [101]).

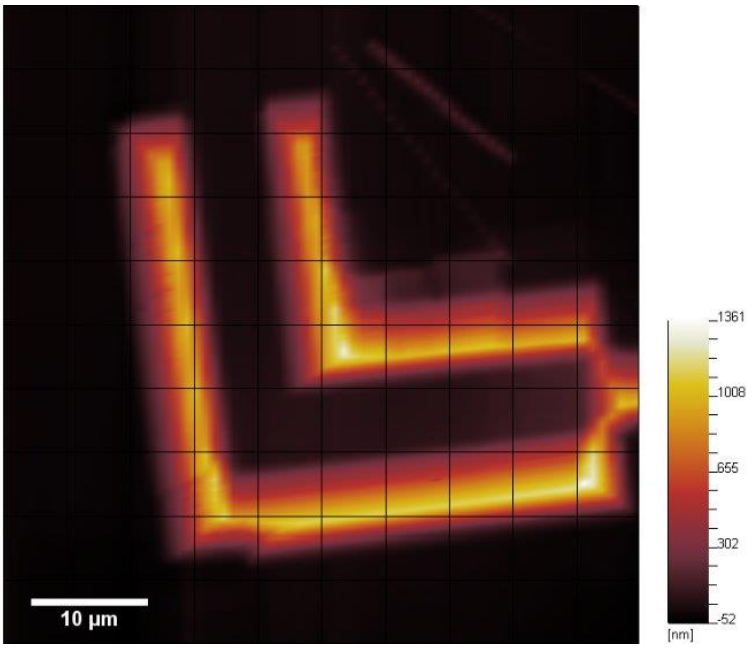


Figure 5-8: (Contact mode) AFM-like scan of an L-shaped cantilever, undertaken with using the nanoindenter.

### 5.2.5 Deflection in the Nanoindenter

The L-shaped beams were tested with the Nano XP, using the low load DCM mode, with the sample mounted on the "Nano Vision" stage. Prior to loading, the stage was scanned in a box pattern beneath the indenter tip, with a constant (low) load of 4 µN applied, allowing an (contact mode) AFM-like image of the sample surface to be generated. Although typically in micro-cantilever testing, a scan of the entire beam can be accomplished relatively easily, this proved problematic with the L-shaped beams. Whilst relatively low resolution scans could be performed without issue (see Figure 5-8), when more detailed scans were attempted (in order to more accurately place the indenter on the beam), the indenter often destroyed the beam being scanned (see Figure 5-9). To circumvent this, smaller areas were scanned instead

of the whole beam, with guide lines FIB-milled across the beam used to determine the exact indentation position (see Figure 5-10).

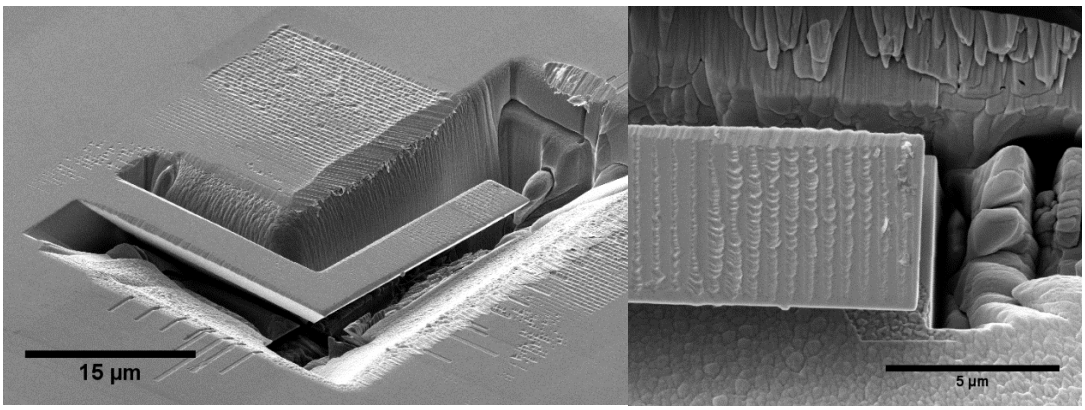


Figure 5-9: SEM images of L-shaped cantilever, damaged during AFM-like scan.

The indenter was placed roughly vertically over the centroid of the right angled triangle cross section (i.e. one third in from the inside edge), so that loading didn't cause any undesired torsion of arm being indented. In practise it was difficult to accurately position the indenter with respect to the beam width, however using finite element (FE) modelling (see section 5.3.2), the loading position on the beam can be fully accounted for. The indents were placed roughly as shown in Figure 5-5, with a separation of ~3 – 7 µm, and the order of loading starting from the furthest point away from the fixed end, moving progressively towards it. A standard MTS indenting procedure was used, in which the loading rate was set at 10 nm/s, and the unloading rate was approximately half of this. Each beam was loaded such that at each loading point only the elastic regime was tested. This was achieved by taking multiple indents at each point, of increasing depth, until a sufficiently large elastic regime had been probed, from which a linear fit could be made for further analysis. The maximum displacement set with the indenter software was gradually lowered as the indent position moved closer towards the fixed end, such that the maximum load was kept roughly constant for all positions.

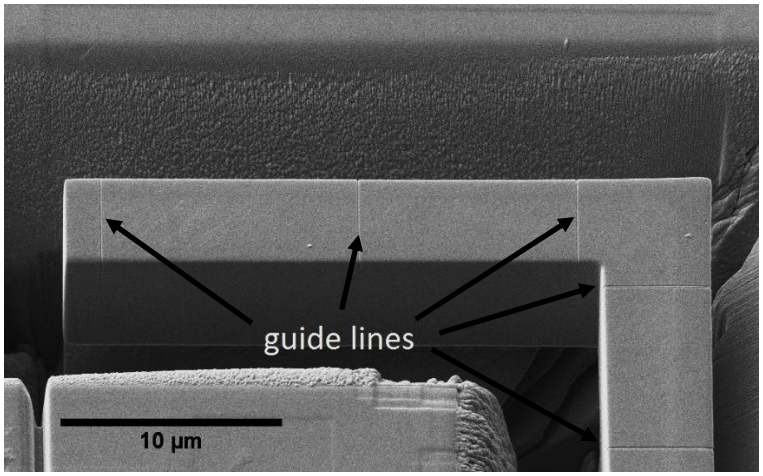


Figure 5-10: SEM image showing guide lines milled across beam, to aid the positioning of the indenter tip.

## 5.3 Results

The load-displacement response for different loading positions of an L-shaped cantilever in which both arms are aligned along <100> directions is shown in Figure 5-11. The numbers indicating the loading position of the particular test correspond to the labels seen in Figure 5-12. At loading positions 1 to 4 (along the 'free' arm), the total displacement of the beam comprises a bending response, in both arms, and a torsional response, in the 'encastre' arm. At loading positions 5 to 7 (along the 'encastre' arm), only bending takes place. As the indenter moves from the free end of the beam (curve 1) towards the fixed end (closest point - curve 7), the stiffness systematically increases.

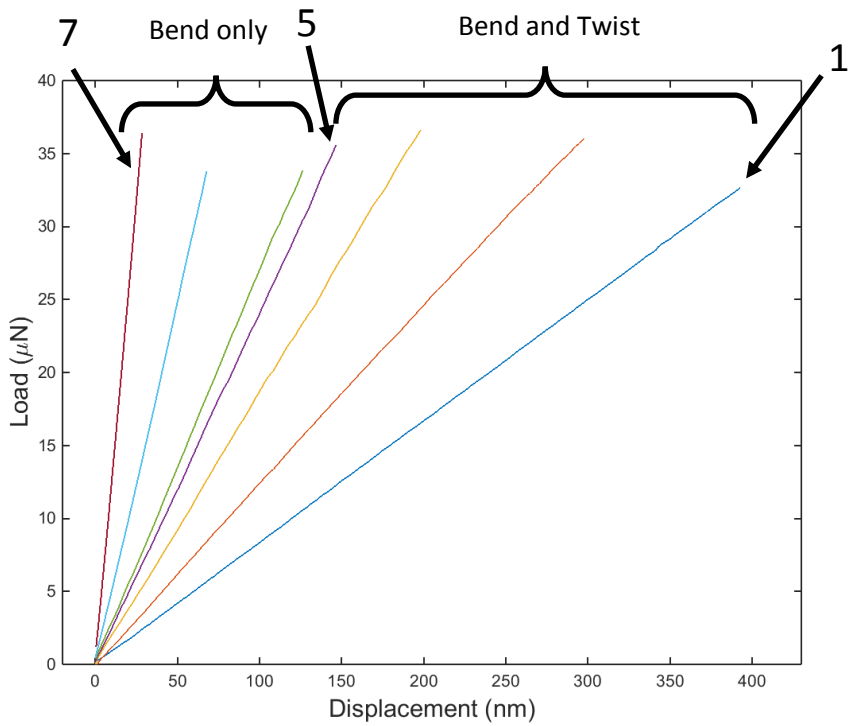


Figure 5-11: Load-Displacement curves generated by deflecting an L-shaped cantilever with both arms aligned along <100> directions (loading portion shown only).

In order for the analysis of the load displacement data to accurately generate elastic constants, an exact knowledge of the placement of the indenter on the beam is required. However, due to the bluntness of the Berkovich tip used to scan and indent the beam, the low loads typically applied often resulted in only very slight indent impressions, often on the threshold of detectability in the SEM. Where it was not possible to accurately determine the loading position using the SEM, the recorded position of the indenter head from the nanoindenter test file in combination with the AFM scan data was used. However, as the scan data only roughly defines the beam edges (see Figure 5-8), this method was prone to greater uncertainty than direct observation.

For one test, marks of unknown origin (dissimilar to indent impressions) were left on the beam by the indenter tip, allowing the indent positions to be accurately established in that case (Figure 5-12).

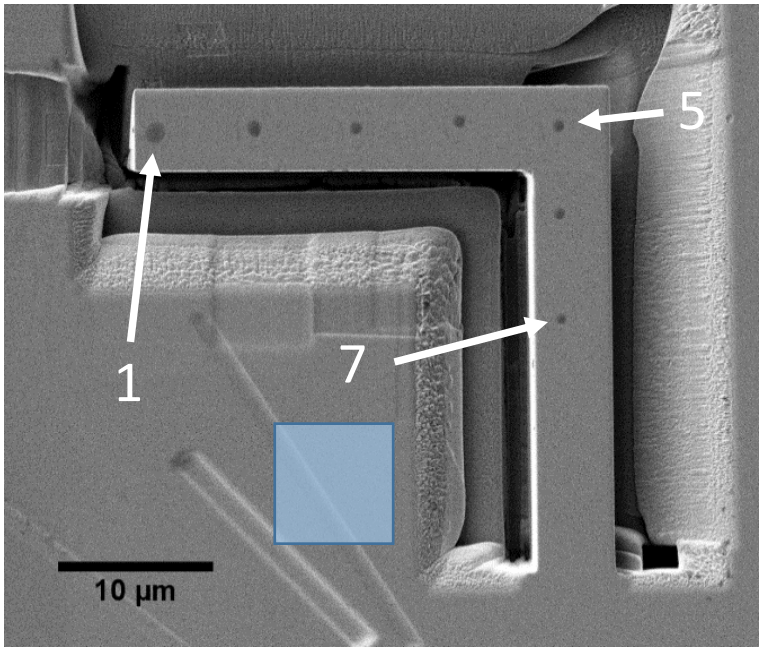


Figure 5-12: Post-test SEM image of an L-shaped cantilever. The nanoindenter tip has unexpectedly left marks where it has contacted the beam surface (unlike indent impressions). A unit cube is overlaid to indicate the approximate orientation.

### 5.3.1 Simple Beam Theory

The results of the experiment were first analysed using the equations of simple beam theory. Although this assumes a long and slender beam, which is completely rigid at the point of attachment to the bulk, and with an elastically isotropic material, it is useful as a method to make preliminary observations on the general trends of beam compliance vs loading position. The compliance, $S$, of a triangular cross section beam is given by:

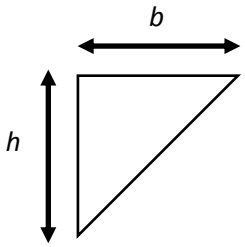


$$S = \frac{\delta_{bend}}{P} = \frac{L^3}{3EI_x} \tag{5-19}$$

$$I_x = \frac{bh^3}{36} \tag{5-20}$$

where $\delta_{bend}$ is the displacement at the loading position which causes bending in the beam, $P$ is the applied load, $L$ is the distance from the fixed end to the loading position, $E$ is Young's modulus, $I_x$ is the second moment of area with respect to the beam width direction, $b$ is the

beam width and $h$ is the beam thickness. For a beam undergoing pure torsion, the angle of twist, $\phi$, is given by:

$$\phi = \frac{TL}{GI_p} \tag{5-21}$$

$$I_p = \frac{b^3h + bh^3}{36} \tag{5-22}$$

where $T$ is the applied torque, $L$ is the beam length, $G$ is the shear modulus and $I_p$ is the polar second moment of area. Considering a torsion on the 'encastre' arm of the L-shaped cantilever caused by displacing the beam at a point on the 'free' arm, the torque is given by:

$$T = PL_2 \tag{5-23}$$

where $P$ is the applied load and $L_2$ is the distance from the loading point to the centroid position of the 'encastre' arm. Using small angle approximation, the angle of twist of the 'encastre' arm is:

$$\phi = \frac{\delta_{twist}}{L_2} \tag{5-24}$$

Substituting equations (5-23) and (5-24) into (5-21), gives:

$$\frac{\delta_{twist}}{P} = \frac{36L_1L_2^2}{G(b^3h + bh^3)} \tag{5-25}$$

where $L_1$ ($L$ from equation (5-21)) is the length from the fixed end to the centroid position of the 'free' arm. The total displacement of the L-shaped beam when indented along the

'free' arm, comprising of the bending response in both arms and the torsion response of the 'encastre' arm is given by:

$$\delta = \delta_{bend1} + \delta_{bend2} + \delta_{twist1} \tag{5-26}$$

with the subscript '1' denoting a displacement due to the 'encastre' arm and '2' denoting a displacement due to the 'free' arm. Therefore, using equations (5-19) and (5-25), the total compliance of the beam is given by:

$$S = \frac{\delta}{P} = \frac{12L_1^3}{E_1 b_1 h_1^3} + \frac{12L_2^3}{E_2 b_2 h_2^3} + \frac{36L_1 L_2^2}{G_1(b_1^3 h_1 + b_1 h_1^3)} \tag{5-27}$$

This shows that the response of the beam is highly sensitive to the loading position and beam thickness (and slightly less sensitive to the beam width), indicating the care that must be taken when measuring these parameters.

When indenting along the 'encastre' arm, with $L_2 = 0$, the final two terms disappear, giving an equation in which $E_1$ is the only unknown. Therefore plotting the beam compliance against $L_1$ and fitting a cubic function allows $E_1$ to be determined, via:

$$S = AL_1^3 \tag{5-28}$$

$$A = \frac{12}{E_1 b_1 h_1^3} \tag{5-29}$$

The predicted response when indenting along the 'free' arm is less simple, with $E_2$ and $G_1$ both being unknown. The beam compliance was calculated for each test from the load

displacement curves by fitting a linear function to both the loading and unloading portions of the curves. Figure 5-13 shows the compliance vs distance response for an L-shaped cantilever with both arms orientated along <100> directions (i.e. $E_1 = E_2$), when indenting along the 'free' arm, whilst Figure 5-14 shows the same relationship for indenting along the 'encastre' arm.

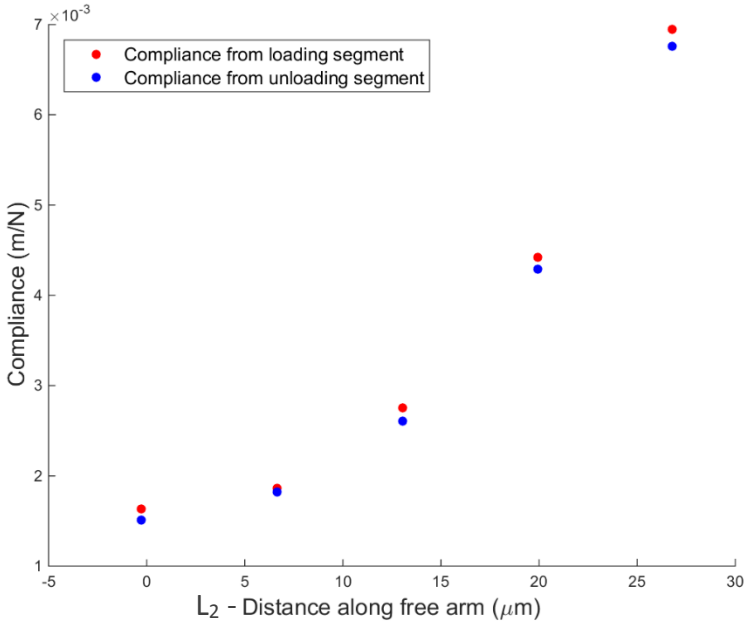


Figure 5-13: Compliance of L-shaped cantilever orientated with both arms along <100> directions, when indented along the 'free' arm, as a function of distance from the centroid position of the 'encastre' arm.

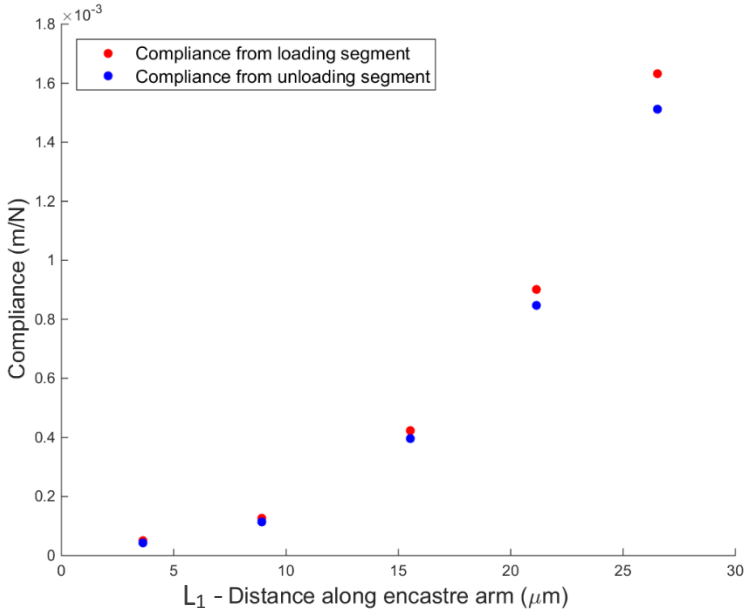


Figure 5-14: Compliance of L-shaped cantilever orientated with both arms along <100> directions, when indented along the 'encastre' arm, as a function of distance from fixed end.

Table 5-3 shows the Young's moduli of three L-shaped cantilevers in the direction of the 'encastre' arm, calculated by fitting a cubic function to the compliance vs distance data. Comparing these to literature values shows that simple beam theory analysis severely underestimates Young's modulus, with calculated values being approximately 60 – 70 % of the real values. However, this analysis does at least correctly show that the modulus along <110> is higher than along <100>, and the ratios of these values is approximately correct. The main reason for the low values of the Young's moduli is that the assumptions of simple beam theory are not met in this experiment, with the top surface of the beam being free to flex at the fixed end, causing extra compliance. Armstrong determined that this effect would be minimised in cantilevers with aspect ratios greater than 6 [63], however for all such loading positions in this analysis the aspect ratio is smaller than this. Although terms can be added to equation (5-19) in attempts to take into account the extra deflection, the complexity of the L-shaped cantilevers is such that this approach is unlikely to be accurate. This necessitates the use of Finite Element modelling to analyse the data in this chapter.

| Orientation | Modulus (loading) | Modulus (unloading) | Literature values |
|---|---|---|---|
| [100] | 79 | 87 | 132 |
| [100] | 93 | 100 | 132 |
| [110] | 178 | 213 | 219 |
| [110] | 147 | 164 | 219 |

Table 5-3: Young's modulus (GPa) along the 'encastre' arm of L-shaped cantilevers, calculated using loading and unloading compliances and simple beam theory equations, compared with literature values taken from Adams [117].

### 5.3.2 Finite Element Modelling

In order to determine the elastic constants from the load-displacement data, it was necessary to construct a Finite Element (FE) model, and subject it to loading similar to that seen experimentally. An anisotropic elastic model was used, with any plasticity taking place experimentally not factored into the analysis. As the single crystal elastic constants (and crystal orientation measured by EBSD) are input parameters for the FE analysis, it was necessary to establish the correct values from the data by varying them within the model until a suitably close match between simulated beam stiffness and experimental beam stiffness was found. All simulations in this thesis were conducted using the commercial FE code ABAQUS [127].

Although FE analysis is significantly more complex than using simple beam theory, it is able to more accurately match experiment, as the inbuilt assumptions of simple beam theory mean that stiffness is systematically underestimated in micro-cantilever studies [63]. Specifically, the requirement of the cantilever to be fully 'encastre' at the point of attachment to the bulk material is not met in reality, as the top surface of the beam at the fixed end is unconstrained, and can flex during bending. This has previously been taken account of by modifying the equations of simple beam theory [63], however FE models are able to fully capture such activity by simply applying the necessary boundary conditions and displacing

the beam. FE models can also fully take into account elastic anisotropy, unlike simple beam theory.

In order to conduct an FE analysis, first a representative geometry of the beam must be defined (including a suitably sized volume of the attached bulk material, or 'base'), for which material and section properties and crystal orientation are supplied. A mesh is then generated for the material volume consisting of an array of nodes, and elements to which these belong (see Figure 5-15). Boundary conditions are then applied, namely fixing the 'outer surfaces' of the base (to which the bulk material is attached) to be stationary, and displacing a node (see section 5.3.2.4) on the beam's surface downwards by a set amount at the load position, over a defined time step.

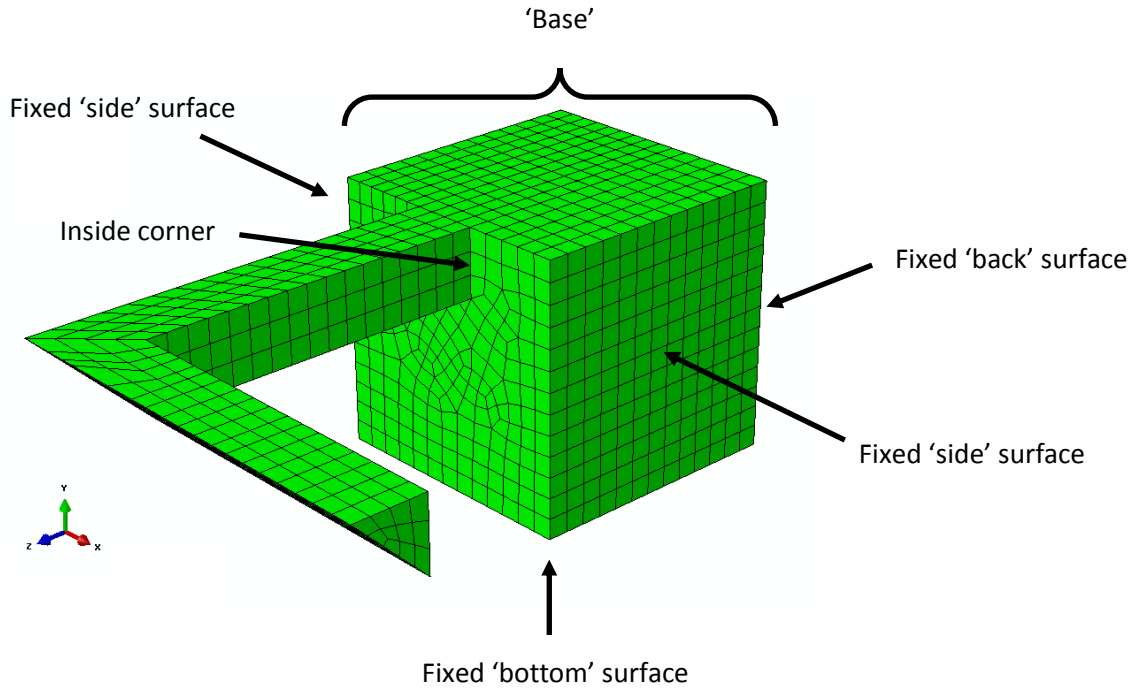


Figure 5-15: FE model of an L-shaped cantilever, including some 'base' material. The top side of the base, and the side attached to the cantilever, are free to move, whereas the other four sides are prevented from moving or rotating.

Before the model could be relied upon to realistically simulate experimental conditions, it was necessary to optimise it such that accurate results could be obtained without using up

too many computation resources. Such steps form a convergence study and will be described in detail below.

ABAQUS allows any system of units to be used, providing consistency is kept. In this case, all lengths (e.g. beam dimensions, displacement) are given in µm, whilst load is in N.

#### *5.3.2.1 Base*

As mentioned above, due to the flexure of the bulk material at the 'fixed' end of the beam, some volume of this material must be included in the analysis. In addition, the most highly stressed sections of the beam are at the fixed end, and such stresses significantly influence the surrounding base material. The base region was taken to be a cube with side length varied between 5 µm (the cantilever width) and 30 µm (the length of both arms).

For all the tests looked at in this convergence study (excepting those in section 5.3.2.4), a node on the top surface of the beam near the free end (see Figure 5-19, top) was displaced vertically downwards by a fixed amount (typically 1 µm), and the resultant reaction force at the node was calculated during the simulation. From this, the stiffness of the beam could be determined. All analyses were run in parallel on 8 cores of an Intel Core i7-3930K processor.

Figure 5-16 shows the effect on the simulated stiffness of varying the base size (whilst keeping mesh density constant), going from no base (i.e. fully encastred simple beam theory), to a large base with a side length of 30 µm. Shown on the right axis is the CPU time required to run the analysis for each test. The result converges at base side lengths of 15 – 20 µm, whilst the CPU time increases dramatically for 25 µm and 30 µm. As a compromise, a base

side length of 20 µm was chosen for the model. The difference between the stiffness for this base size and that of the 30 µm one is less than 0.5%.

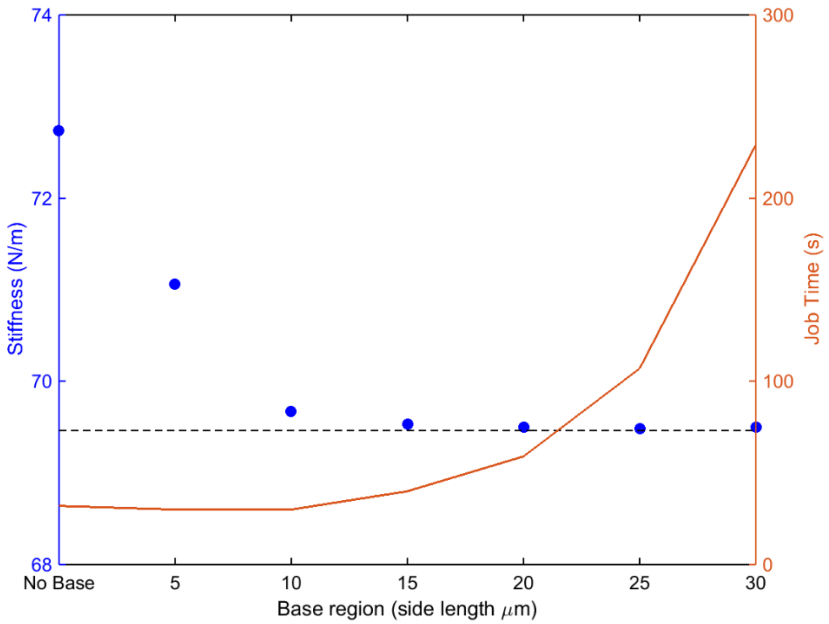


Figure 5-16: Simulated stiffness (left axis) as a function of base size, and the effect on job time (right axis), with a constant mesh density. The dotted line shows the stiffness at which convergence is reached.

#### *5.3.2.2 Mesh*

In FE analyses, it is always necessary to conduct a mesh convergence study to ensure that the most accurate answer can be obtained. Computational cost, in addition to disk space and memory requirement for such problems is roughly proportional to the square of the number of degrees of freedom for each node, which is 3 in this case [128]. Therefore, doubling the number of elements in a model causes computational cost to increase by a factor of $(2^3)^2 = 64$. This means that any increase in mesh density past the point at which the results are converged is a significant waste of CPU time.

Many different types of element are available in ABAQUS, however the ones of most relevance for this simulation are the continuum hexahedra (brick) and tetrahedra elements. These are available as either linear (first order) elements, with a node at each corner, or

quadratic (second order) elements, with additional mid-side nodes. The hexahedra elements are available with either full integration or reduced integration, whereas the tetrahedra elements are only available with full integration. The order refers to how quantities are interpolated to give values between nodes. Fully integrated linear elements are unsuitable for bending problems, as their edges are unable to curve, resulting in a non-physical increase in stiffness known as *shear locking* [128]. Linear reduced-integration elements are also unsuitable, due to the phenomenon of *hourglassing* [128], in which the stress components at the (single) integration point are zero, causing the elements to become unable to resist bending. Quadratic reduced integration elements can also exhibit hourglassing, however the modes are unable to propagate through the mesh. Figure 5-17 shows a mesh convergence test using quadratic hexahedra elements. Convergence is seen at just above 15000 elements, with very little difference in stiffness compared to the model with ~22500 elements. Similarly, Figure 5-18 shows a convergence test using quadratic tetrahedra elements, which converges at a similar CPU time (tetrahedral elements are more compact, hence the greater number). These results were produced by setting an average mesh density uniformly for the whole model. However, by setting the mesh density to be coarser at areas of low stress gradient (e.g. the base far away from beam), and finer where stress gradients are higher (e.g. the inside edge where the beam joins the base), accurate results can be obtained at a fraction of the computational cost of the uniformly fine meshed models. Mesh densities can be further refined around highly stressed regions by judiciously partitioning the beam into smaller regions (which are used to guide the meshing algorithms). An example of such a test is shown by the hollow circle in Figure 5-18, with the job time for this test given by the red cross.

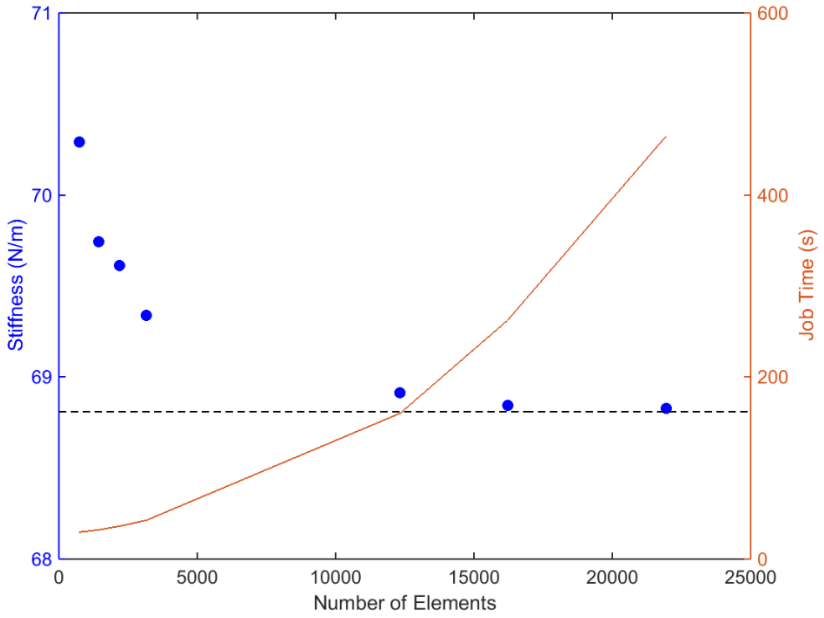


Figure 5-17: Convergence of simulated stiffness (left axis) with number of quadratic hexahedra elements, and the effect on job time (right axis).

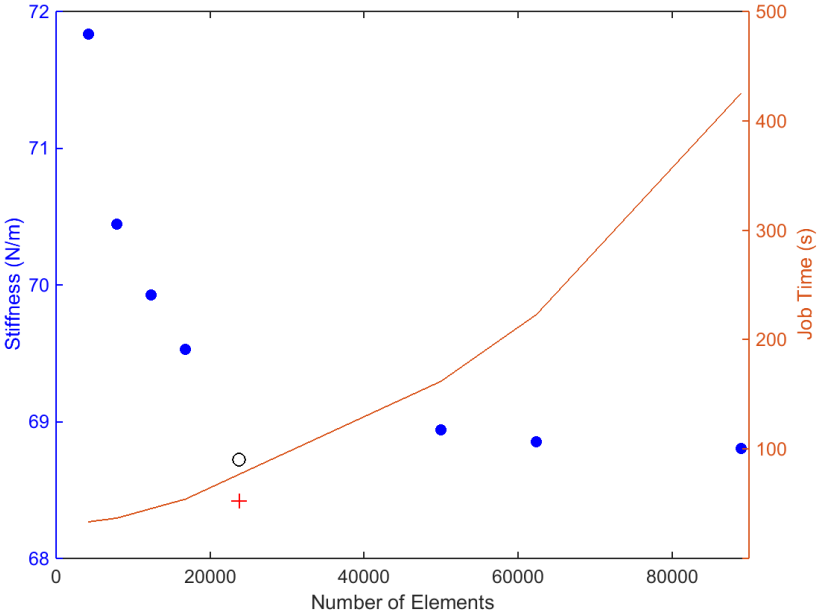


Figure 5-18: Convergence of simulated stiffness (left axis) with number of quadratic tetrahedral elements, and the effect on job time (right axis). The hollow circle shows the simulated stiffness of a model using a relatively coarse base, locally refined around the highly stressed region (the red cross gives the job time).

In order to locate the most highly stressed regions, where mesh refinement is most necessary, a simple model can be run, and the resultant Von Mises stresses plotted using the inbuilt ABAQUS visualisation module. This is demonstrated in Figure 5-19, showing the area

of maximum stress in both types of test to be on the underside of the beam at the 'fixed' end.

Both types of quadratic element (with reduced integration) perform well for this application, as shown in Figure 5-17 and Figure 5-18. However, due to the relatively complex geometry of the L-shaped beam, hexahedral elements can easily become distorted, leading to analysis errors, whereas tetrahedral elements are easily able to represent the beam shape. Therefore, quadratic tetrahedral elements (C3D10) were chosen for this model.

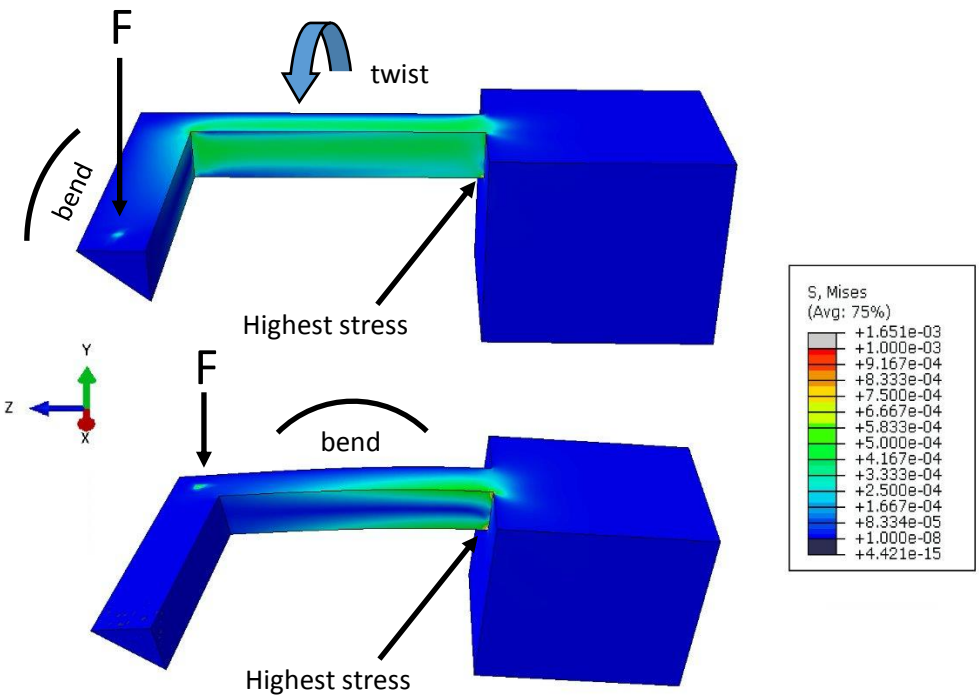


Figure 5-19: Von Mises stress of an FE model of an L-shaped cantilever (in $N/\mu m^2$), tested in 'torsion mode' (top) and 'bending mode' (bottom). The highest stress in both cases is found where the inside and outside edges meet at the fixed end of the beam. Labels indicate which arms are undergoing bending or torsion in each case.

#### *5.3.2.3 Sharp vs rounded joins*

In a simplified model geometry such as that seen in Figure 5-15, all the edges are straight, and the joins between the sides of the 'encastre' arm and the base are modelled as sharp corners. This leads to a 'stress singularity' [128], which can have an effect on the simulated

beam stiffness. Actual FIB-milled beams will have small fillets at such joins, which can be included in the ABAQUS model.

Figure 5-20 shows the effect on the simulated beam stiffness of adding a fillet to the inside corner join between the beam and the base (the line labelled 'Inside corner' in Figure 5-15), with fillet radii of 0.2 µm, 0.5 µm and 1 µm (the three red points). Stiffnesses from the mesh refinement test of Figure 5-18 are also shown for comparison. A fillet is only added at one location for simplicity and demonstration purposes, however in reality all of the edges and joins will exhibit some degree of smoothness. The effect of the fillet is to increase the stiffness of the beam, with the greatest increase seen for the larger fillet size ($r = 1\ \mu m$). This is due to the increased amount of material able to resist bending. Although this effect is significant, the addition of a fillet greatly complicates meshing the model. Furthermore it is very difficult using SEM images to accurately gauge the size and shape of fillets in real beams. However, a radius of 1 µm is likely an overestimate of the actual case and this causes only a 2.4 % increase in stiffness. At a more reasonable estimate of 200 nm, the effect is smaller still at 0.3 %. For these reasons, fillets will not be included further in the model, although the effect on stiffness is a factor for consideration when comparing simulations to experimental data.

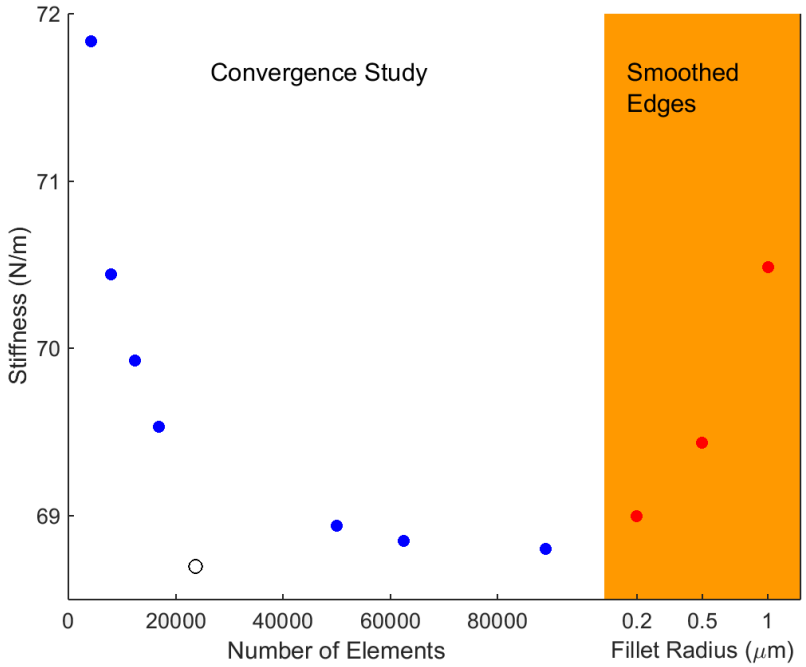


Figure 5-20: The effect on simulated stiffness (N/m) of adding a fillet to the inside corner join (see Figure 5-15), with a radius of 0.2 µm, 0.5 µm and 1 µm (red points). Points from the convergence study in Figure 5-18 are shown for comparison.

#### *5.3.2.4 Loading*

There are several ways in which the beam can be displaced in ABAQUS, most of which are not relevant for the current application (e.g. applying a pressure or moment). The simplest method is to displace one of the mesh nodes on the top surface of the beam by a specified amount, at a point corresponding to where the indenter contacts the beam experimentally (this method has been used in all previous tests discussed in this section). The load can also be applied by displacing a line of nodes across the surface of the beam. Alternatively, an indenter tip geometry can be meshed and positioned at the beam's surface, then some displacement can be applied to it, bringing the two surfaces into contact, and more accurately replicating the experiment.

The method of displacing a line of nodes on the beam's surface was previously used in FE analysis by Hardie [101]. However, when a line of nodes at the same length along the 'free'

arm as the loading point shown in the top of Figure 5-19 was displaced, the simulated beam stiffness was ~10% higher compared to loading a single node, a significant increase. This is due to the beam stiffness changing substantially when indenting at different points across the beam width (see next section). For this reason, this method of applying load to the beam was not used in any further simulations (such a technique may be more suited to conventional 'straight' cantilevers).

In order to model an indenter tip, a simple hemisphere was used. Although this shape is different to the Berkovich shape, perfectly sharp indenter tips are unsuitable for contact problems in FE analyses, as they cause severe stress gradients and can lead to unphysical results. Furthermore, real indenter tips are not perfectly sharp, and have a specified radius of curvature when purchased (typically 100 – 200 nm). The indenter tip used in this experiment was sufficiently old and well used that it would have been ground down to a greater radius of curvature than this.

The tip was modelled as a rigid body, represented using a two dimensional surface composed of quadrilateral and triangular rigid elements (R3D4 and R3D3). Such a method is used as diamond is much stiffer than iron, and therefore not expected to undergo significant elastic deformation. Furthermore, using a rigid body (as opposed to an elastically deformable one) greatly decreases the computational cost, as its movement can be completely described by the motion of one 'reference' node. Radii of curvature of the rigid hemisphere were given as $r = 2$ µm , $r = 1.5$ µm, and $r = 1$ µm, so that the general trends could be revealed. The analysis aborted due to errors when trying to apply a displacement of 1 µm using a hemispheres with a radius of curvature smaller than $r = 1$ µm.

To improve the accuracy of the FE analysis, the mesh density was increased on the beam surface at the point at which the indenter tip makes contact with the surface.

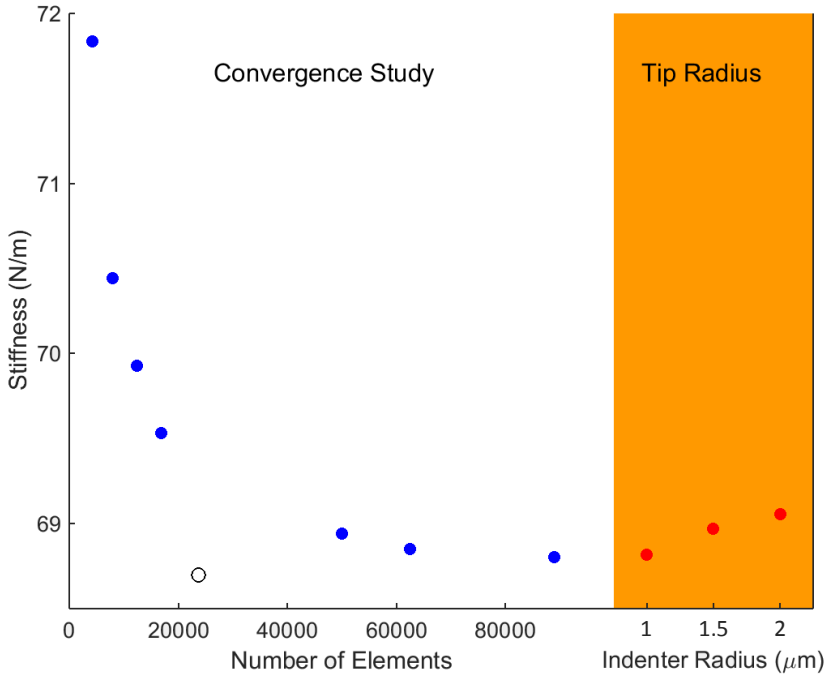


Figure 5-21: The effect on simulated stiffness (left axis) of using an indenter to displace the beam in FE analysis (red points). The radii of curvature are 1 µm, 1.5 µm (#10), and 2 µm (#11). Points from the convergence study in Figure 5-18 are shown for comparison.

Figure 5-21 shows a comparison of the stiffnesses from previous nodally loaded tests (shown in Figure 5-18), with those obtained using a meshed indenter geometry. The stiffness is seen to increase compared to a nodal test with a similar beam mesh (hollow circle) with the difference being largest for the biggest indenter radius (2 µm), at 0.5%. However, the CPU time required to perform the analysis increased significantly when using a meshed indenter, at ~250 – 300 seconds, compared to ~60 seconds for a nodal test. As this increase in complexity doesn't significantly affect the simulation results, but adds considerably to the computational cost, a meshed indenter wasn't used in further simulations.

#### 5.3.2.5 Sensitivity study

In order to ascertain the extent to which the model dimensions and loading points affect the simulation result, several of these parameters were varied and the resultant changes in simulated beam stiffness determined. This also gives insight into how the accuracy of various experimental measurements affects the results. Firstly, the effect of varying the loading position was investigated, both in the direction along the two arms of the L-shaped cantilever (Figure 5-22, left), and laterally across the width of both arms (Figure 5-22, right).

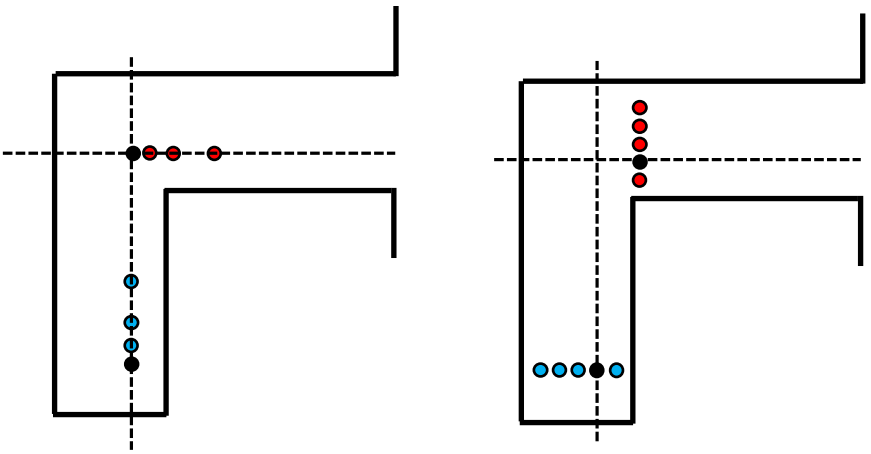

Figure 5-22: Schematic diagram showing the relative positions of loading positions varied along the lengths of the two arms (left), and over their widths (right) (not to scale). The dotted lines indicate the position of the centroids of each arm, and the solid black points show the reference 'zero' shift positions.

Figure 5-23 shows the percentage difference in stiffness caused by shifting the loading position along the beam arms at the locations shown in the left of Figure 5-22. In both cases, the stiffness increases as the loading position is moved closer to the built-in end, as expected. Changes in position on the encastre arm cause a greater percentage difference in stiffness compared to changes in position by the same amount on the free arm. This can be explained with reference to equation (5-27), in which the compliance of the beam is proportional to the square of the distance from the centroid position of the encastre arm to the loading point on the free arm, and the cube of the distance from the built in end to the distance along the encastre arm. Therefore changes in loading position along the encastre arm are expected to lead to greater changes in stiffness than changes in loading position along the free arm.

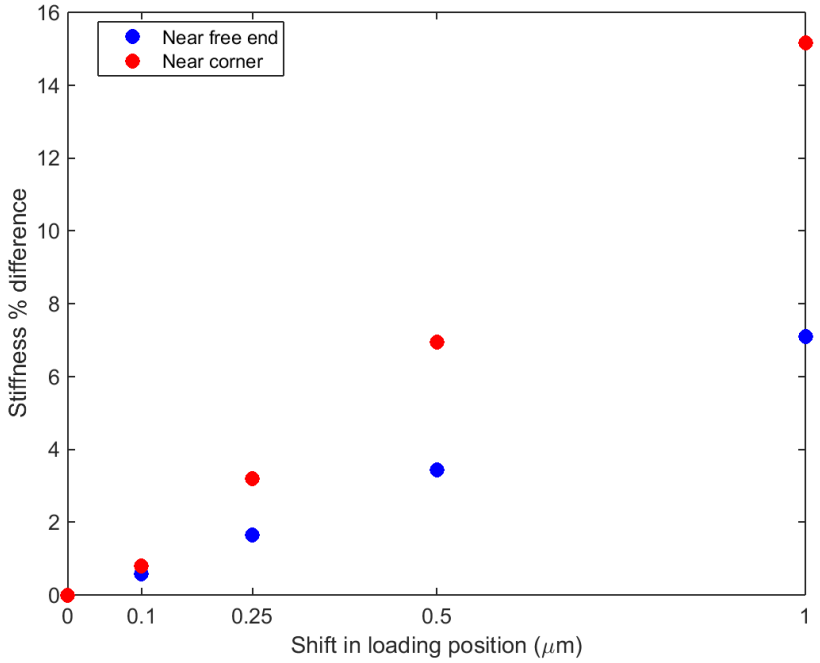


Figure 5-23: Percentage difference in stiffness caused by shifting the loading position along the free arm (blue) and along the encastre arm (red), at the positions described by Figure 5-22 (left).

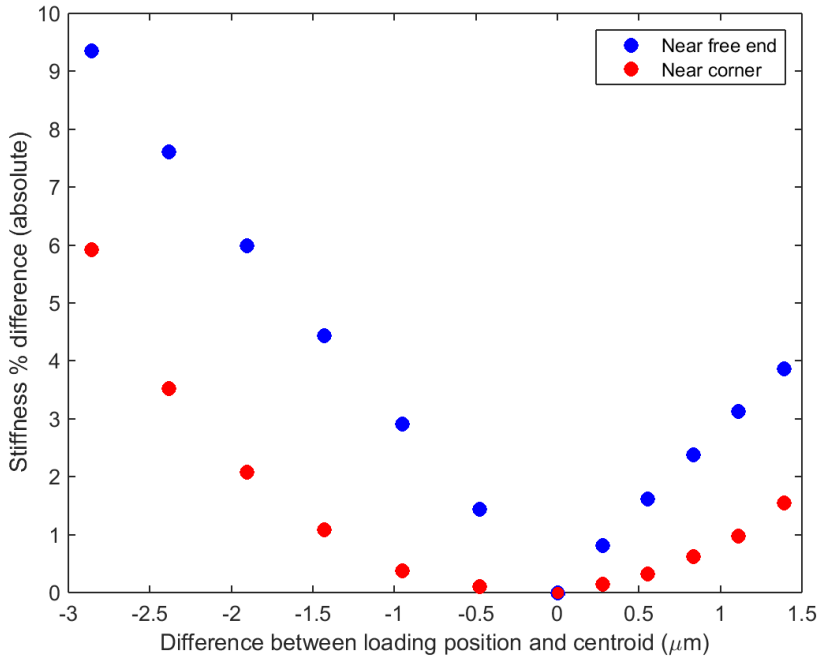


Figure 5-24: The absolute percentage difference in simulated stiffness caused by shifting the loading position across the width of the free arm (blue) and the encastre arm (red), at the locations described by Figure 5-22 (right). Positions are measured with respect to the centroid position in both arms.

Figure 5-24 shows the absolute percentage difference in stiffness caused by shifting the loading position across the width of both arms at the locations shown in the right of Figure

5-22. In this case, the simulated stiffness is more sensitive to changes in position over the width of the free arm as compared to changes over the width of the encastre arm. Small lateral changes in the loading position on the encastre arm do not significantly affect the results.

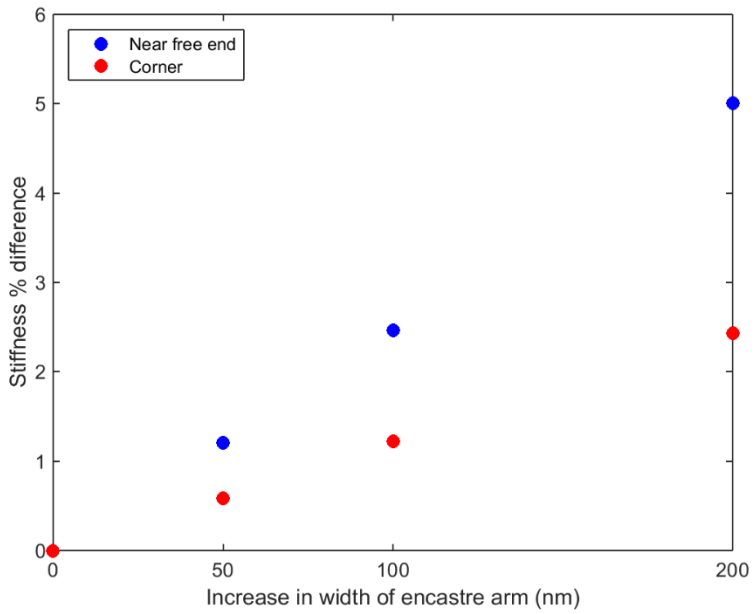


Figure 5-25: Percentage difference in stiffness caused by increasing the width of the encastre arm, when indenting near the free end (blue) and near the corner (red) of the beam (initial width = 5 µm).

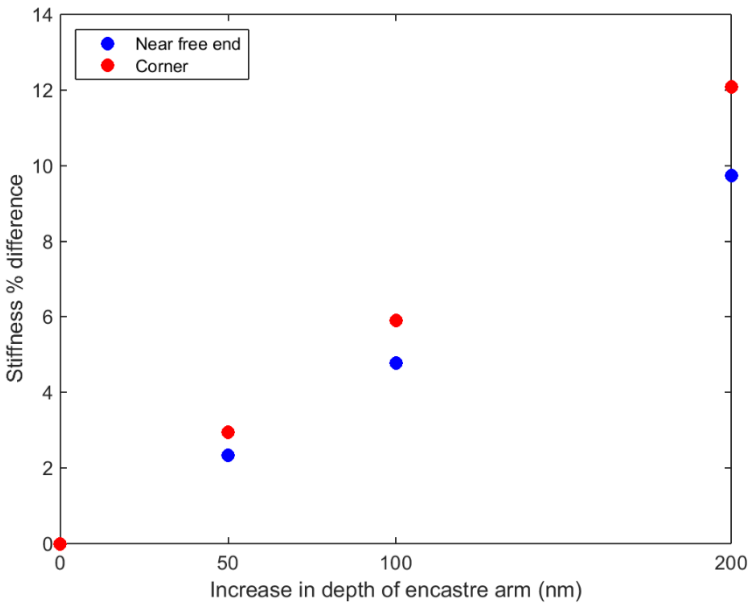


Figure 5-26: Percentage difference in stiffness caused by increasing the depth of the encastre arm, when indenting near the free end (blue) and near the corner (red) of the beam (initial depth = 5 µm).

Figure 5-25 and Figure 5-26 show the effect on simulated stiffness of changing the width and depth of the encastre arm, respectively. The resultant stiffness is moderately sensitive to changes in width, with the effect being greater when indenting near the free end (with a 200 nm increase causing a ~5 % stiffness increase) than at the corner of the beam (with the same increase in width causing a ~2.5 % stiffness increase). However, the sensitivity of the simulated stiffness to changes in depth is much larger, with a 200 nm increase in depth causing a ~10 % increase in stiffness. This is reflected by equation (5-27), in which the inverse cube of the encastre depth appears in both the first bending component and torsional component, whereas the inverse cube of encastre width appears only in the torsional component. Changes in the width and depth of the free arm were found to have a negligible influence on the resultant stiffness when the beam was loaded near the free end.

This study indicates that the simulation results are most sensitive to the measurement of the depth of the encastre arm, with relatively small differences in depth causing large differences in stiffness. Therefore great care should be made when measuring this parameter experimentally, as the error in measurement for this is likely to be the most important limiting factor for the overall accuracy of the analysis.

The extent to which an accurate knowledge of the loading positions on the beam affects the beam stiffness depends on the part of the beam being indented. On the encastre arm, small shifts up and down the length of the beam cause large differences in stiffness (Figure 5-23), whereas movements across the width of the beam affect the result relatively little (Figure 5-24). On the free arm, whilst shifts in loading position along the length of the arm still have a relatively large impact on the beam stiffness, movements across the width also have a large

impact, meaning that the lateral position of the loading position must be known relatively well.

The combined uncertainty in measured stiffness can be estimated with reference to equation (5-27), and by considering each individual measurement error and summing them in quadrature. Using this method results in an overall error of 7% being determined. However, due to the coupling of elastic constants in equations (5-17) and (5-18), in addition to a lack of clarity in how errors are propagated through the minimisation routine described in section 5.3.3, it is difficult to establish a minimum combined uncertainty of the determined elastic constants using the L-shaped microcantilever method.

#### *5.3.2.6 Matlab control*

To simplify the process of running ABAQUS simulations, and to more easily visualise the results, ABAQUS was called from MATLAB, using scripts developed by Ben Britton and Christopher Hardie. Following the procedure described in [101], an input file was generated within ABAQUS/CAE for each mesh tested, which was then copied into a folder from which it was called from MATLAB. Unique meshes were generated for each beam based upon the measured dimensions. For each test, displacements at prescribed locations were inputted as boundary conditions, and the resultant reaction force at the displaced node was given by the simulation.

### 5.3.3 Minimisation Routine

As there are three independent elastic constants to find in the analysis, coupled with many loading positions on both arms of the L-shaped beams, it would be extremely computationally intensive to fit the simulation to the experimental data by modelling over

the entire 4-dimensional parameter space. Therefore some degree of simplification must be employed to go about finding the global minimum. This section describes the process of arriving at such a minimisation routine.

Before conducting the analysis using real data, simulated data was used to test the validity of the process. The simulated dataset was generated using the constants determined by Adams et al. [117] at room temperature (see section 5.1.2.4), with 15 loading positions across both arms (see Figure 5-27), using the optimised FE model described in the previous section. For each test, a single loading point was nodally displaced by 1 µm, and the reaction force determined. Two different beam orientations were chosen, with the representative unit cubes shown in Figure 5-27. The complete set of simulated data using the target elastic constants were then considered to be the 'measured' stiffnesses. Guesses were then made at the elastic constants and further simulations conducted to generate 'calculated' stiffnesses. The differences between the 'measured' stiffnesses and the 'calculated' ones were minimised step by step, by adjusting the guesses made for the elastic constants.

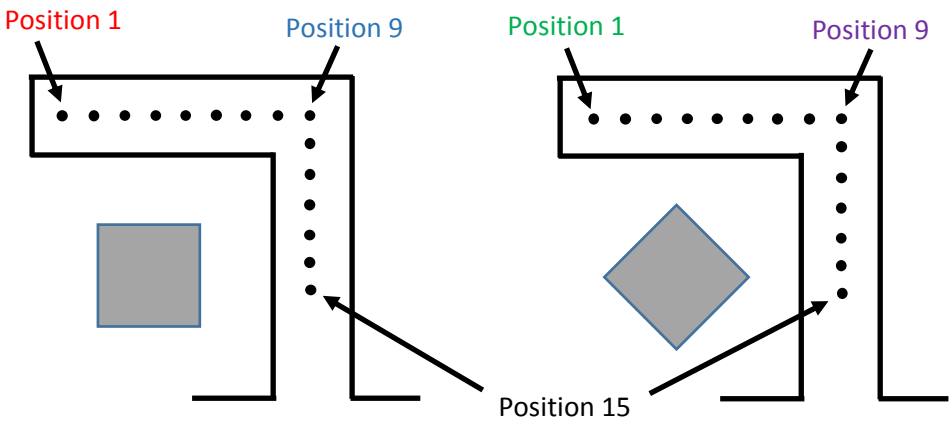


Figure 5-27: Schematic diagram showing the loading positions on two differently orientated L-shaped beams used to generate a simulated dataset. Unit cubes indicate the orientation of the two beams.

The ‘measured’ stiffness data as a function of loading position is shown in Figure 5-28 for loading positions 1 to 9. To arrive at these values by systematically varying the elastic constants, a procedure was used whereby in each step one of the compliance constants ($S_{ij}$) was varied whilst the other two were held constant. For each set of $S_{ij}$ values, the stiffness at a particular loading point (see below) was taken from the FE simulation, and the percentage difference between this and the ‘measured’ stiffness of the simulated dataset at the same loading point was calculated (see Figure 5-29, Figure 5-30 and Figure 5-31). The value of $S_{ij}$ for which the percentage difference was minimised was then passed to the next step. After three such steps (corresponding to the three independent compliance components), the entire process was repeated with as many loops as were required for the constants to converge to a solution. With each repeat of these loops the range and step size over which the compliance constants were varied was systematically reduced.

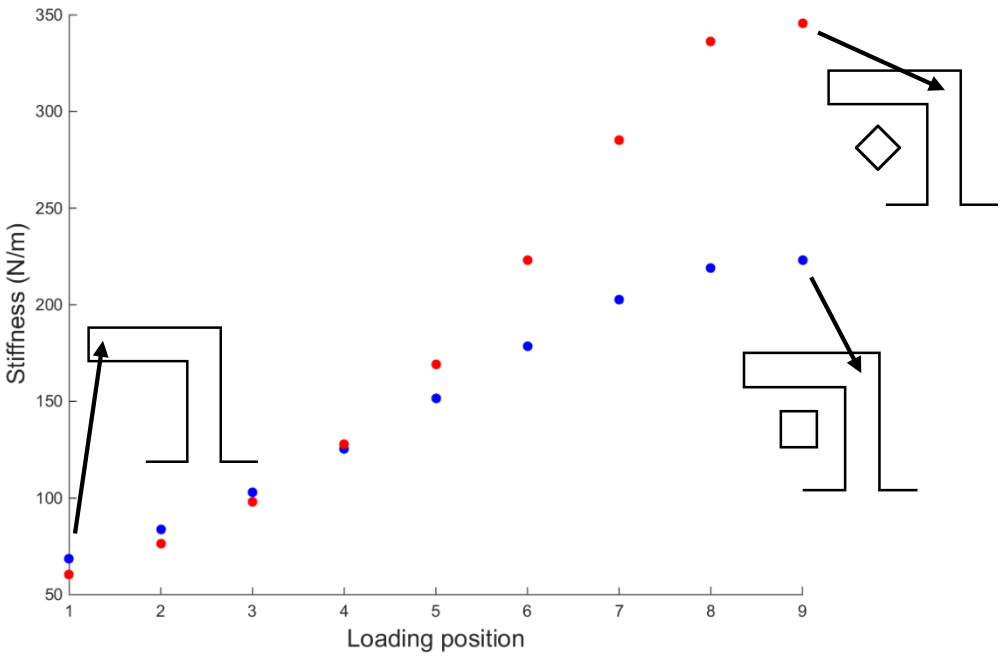


Figure 5-28: Simulated stiffness data from FE models of two differently orientated L-shaped cantilevers using elastic constants from [117], loaded at positions shown in Figure 5-27. In both beams the normal direction is <100>, with arms along <100> directions for the blue points, and <110> directions for the red points.

To minimise the amount of computation required, each step used only one beam orientation and loading position. The loading cases chosen were where the stiffness was most sensitive to changes in the elastic constant being varied. Although these loading positions could be guessed by considering equations (5-17), (5-18) and (5-27), a test run was undertaken in which for positions 1 and 9 on both beams (see Figure 5-27), each $S_{ij}$ was varied in turn whilst the other two constants were set to their literature values. Figure 5-29, Figure 5-30, and Figure 5-31 show the results of these tests, with the colour of the curves indicating the loading position and beam orientation corresponding to the coloured labels in Figure 5-27. For $S_{11}$, Figure 5-29 shows that the beam stiffness is highly responsive to changes in the constant at all positions tested, with the corner position (#9) on the <100> aligned beam showing the biggest change. Conversely, the beam stiffnesses on the <100> beam are very insensitive to changes in $S_{12}$ (Figure 5-30), but very sensitive at the corner position on the <110> beam. Finally, Figure 5-31 shows that the beam stiffness when loading at position 1 on the <100> beam is most sensitive to changes in $S_{44}$.

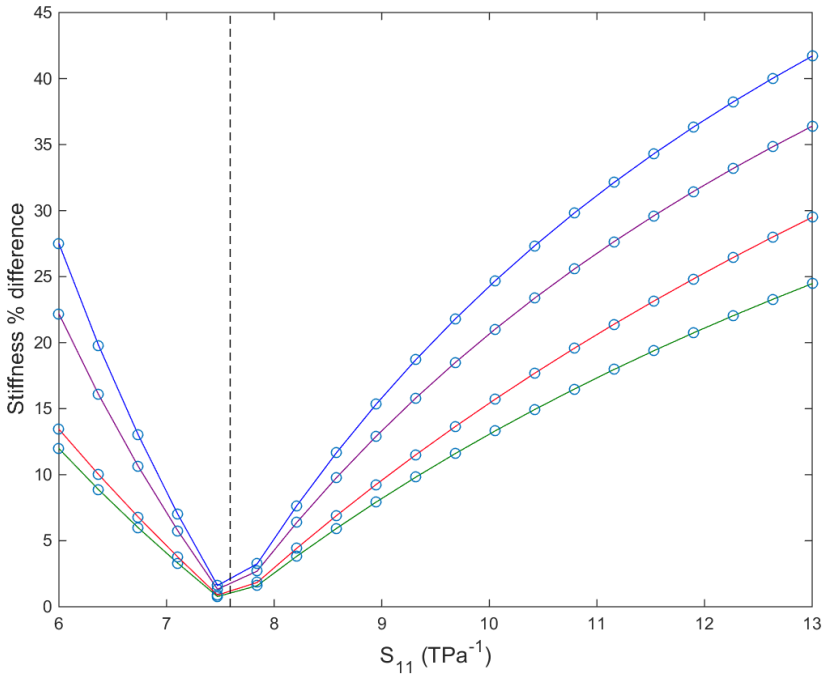


Figure 5-29: Percentage difference between simulated stiffnesses calculated with a range of $S_{11}$ values, and simulated stiffnesses using the literature $S_{11}$ value ($S_{11} = 7.59\ TPa^{-1}$, dotted line), at the four positions with coloured labels in Figure 5-27. $S_{12} = -2.79\ TPa^{-1}$ and $S_{44} = 8.63\ TPa^{-1}$ for all tests.

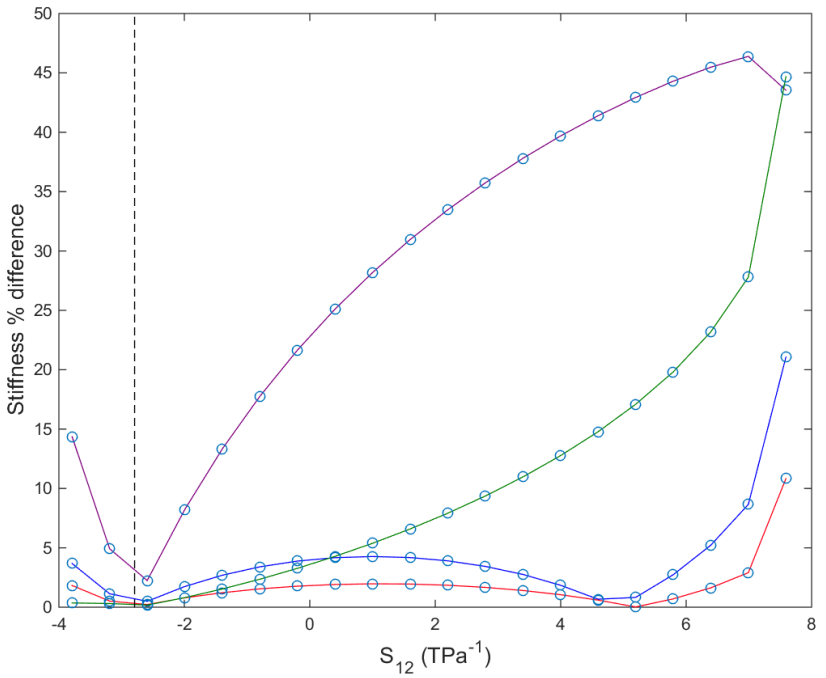


Figure 5-30: Percentage difference between simulated stiffnesses calculated with a range of $S_{12}$ values, and simulated stiffnesses using the literature $S_{12}$ value ($S_{12} = -2.79\ TPa^{-1}$, dotted line), at the four positions with coloured labels in Figure 5-27. $S_{11} = 7.59\ TPa^{-1}$ and $S_{44} = 8.63\ TPa^{-1}$ for all tests.

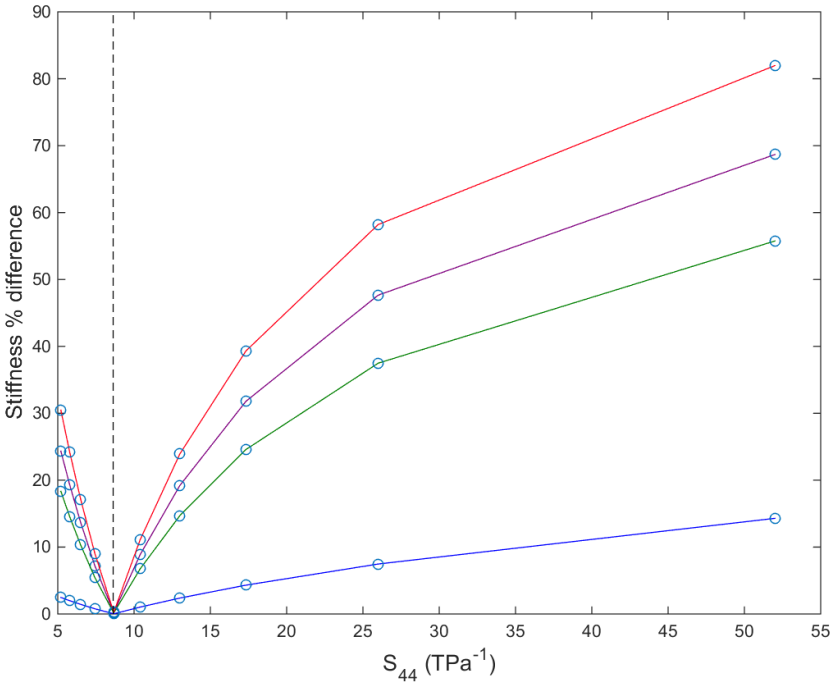


Figure 5-31: Percentage difference between simulated stiffnesses calculated with a range of $S_{44}$ values, and simulated stiffnesses using the literature $S_{44}$ value ($S_{44} = 8.63\,TPa^{-1}$, dotted line), at the four positions with coloured labels in Figure 5-27. $S_{11} = 7.59\,TPa^{-1}$ and $S_{12} = -2.79\ TPa^{-1}$ for all tests.

Having evaluated the stiffness vs loading position sensitivities for each of the constants, a minimisation route with the following steps was arrived at:

1. Loading at position 9, <100> orientated beam: vary $S_{11}$, keep $S_{12}$ and $S_{44}$ constant
    - minimum stiffness difference establishes new $S_{11}$ value
2. Loading at position 1, <100> orientated beam: vary $S_{44}$, keep $S_{11}$ and $S_{12}$ constant
    - minimum stiffness difference establishes new $S_{44}$ value
3. Loading at position 9, <110> orientated beam: vary $S_{12}$, keep $S_{11}$ and $S_{44}$ constant
    - minimum stiffness difference establishes new $S_{12}$ value

As an initial starting point, assuming the constants for iron to be completely unknown, isotropic assumptions were employed, with a Poisson's ratio of 0.3 and a range in Young's modulus of 50 – 500 GPa used as inputs (based on extreme values for metals). The $S_{ij}$ values were then calculated using the following isotropic equations:

$$S_{11} = \frac{1}{E} \tag{5-30}$$

$$S_{12} = -\frac{\nu}{E} \tag{5-31}$$

$$S_{44} = \frac{1}{G} \tag{5-32}$$

Where $G$ is given by:

$$G = \frac{E}{2(1+\nu)} \tag{5-33}$$

After one 'loop' in which these isotropic limits were used as initial values, in following steps the $S_{ij}$ values were varied around their previously located minimum, with the other $S_{ij}$ values held constant. In each subsequent loop a narrower range of values was used until the percentage difference between the simulated and 'guessed' datasets was sufficiently small. For the analysis using real experimental data (see next section), the constants were considered to have converged when the average difference between the values from one loop to the next was 1 % or less. Each step used 10 different $S_{ij}$ values with which to simulate the experiment. A flow chart showing the steps involved in the minimisation routine is shown in Figure 5-32.

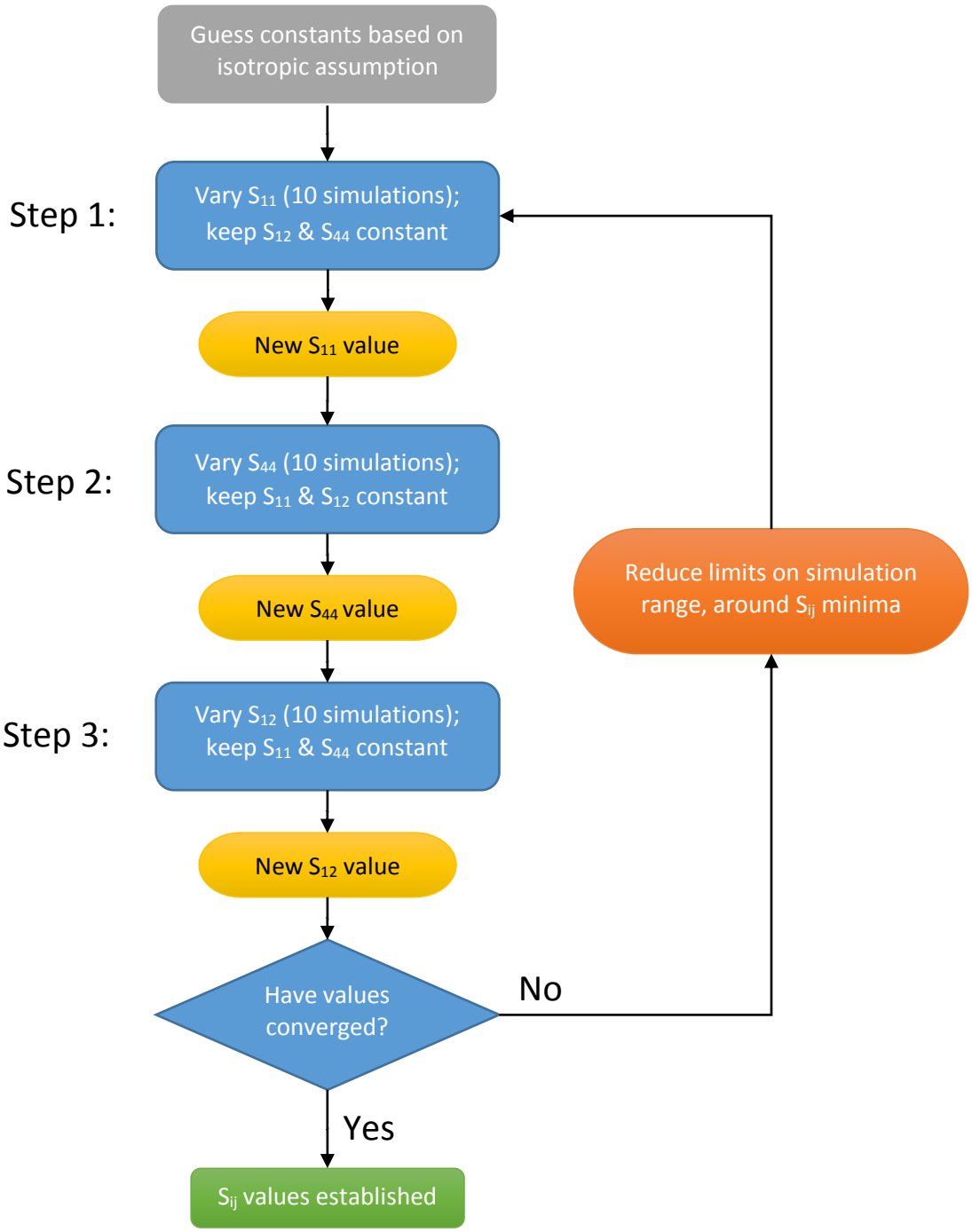


Figure 5-32: Flow chart showing the steps involved in the minimisation routine.

Figure 5-33, Figure 5-34, and Figure 5-35 show the percentage differences between the beam stiffnesses produced using FE models with literature $S_{ij}$ values (i.e. 'measured' stiffnesses), and those produced with varied $S_{ij}$ values (i.e. 'calculated' stiffnesses), for the locations and constants as described in the three steps above. It can be seen that the procedure used

successfully converges on all three constants after a small number of loops. This demonstrates the validity of using this method to extract all three elastic constants from stiffness data produced in L-shaped cantilever tests. In Figure 5-36, the minimised values of the constants after each step are normalised with respect to their literature values, showing the degree of convergence after 5 loops. After 5 loops, the percentage difference between the minimised values and the literature values are 0.18 %, 0.14 %, and 0.03 %, for $S_{11}$, $S_{12}$, and $S_{44}$, respectively.

For 5 loops through these steps each with 10 simulations, the total computational time was 212 minutes. If instead all three independent elastic constants were varied for each of the three loading cases then the computational time required would be a factor of 100 longer. The physically argued minimisation routine adopted thus has a very substantial efficiency gain.

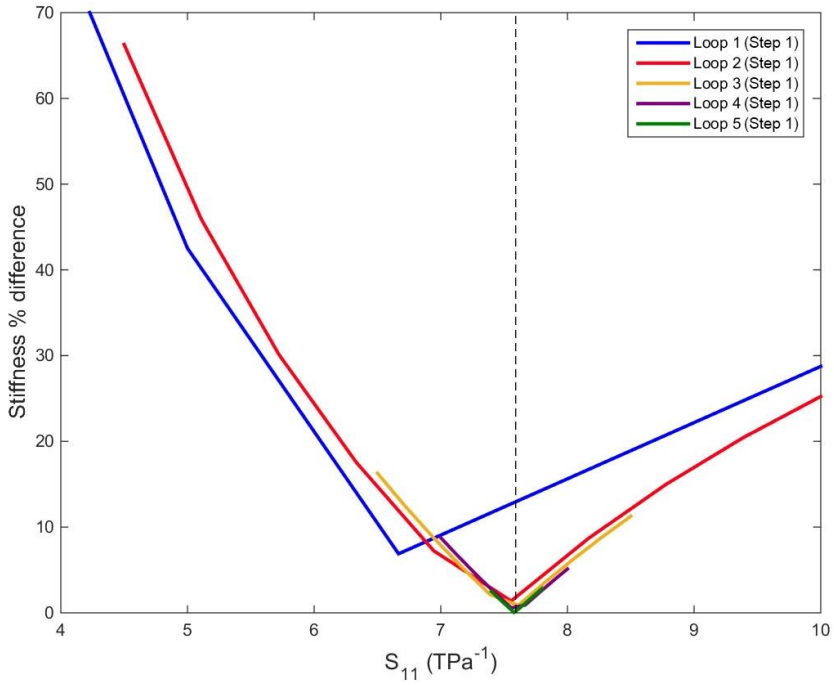


Figure 5-33: Percentage difference between the simulated beam stiffness at position 9, <100> orientated beam, using literature values of $S_{ij}$ values (dotted line) and the beam stiffnesses at the same location from the minimisation routine. Different colours show the different loops as the $S_{11}$ value converges (the total range of Loop 1 has been truncated to aid viewing).

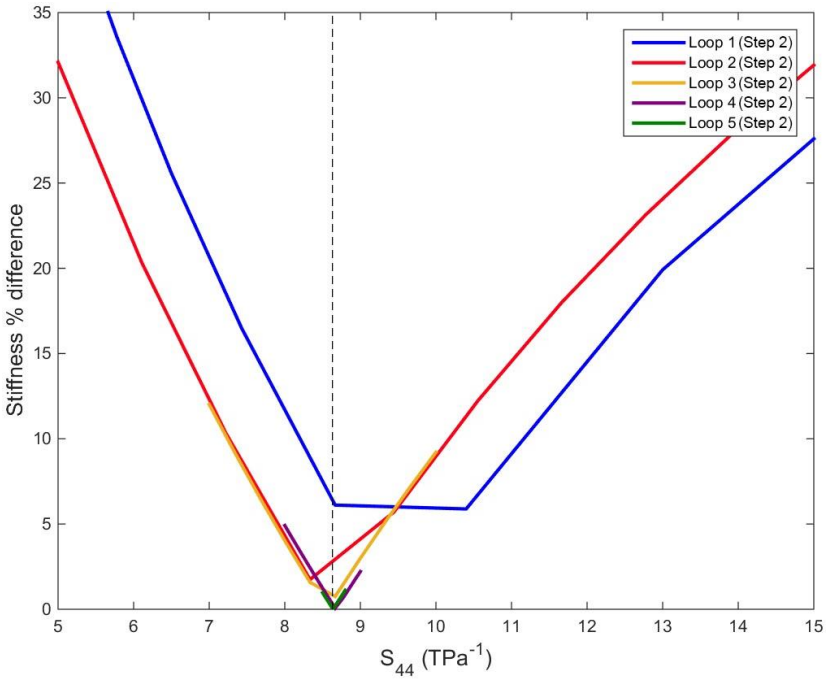


Figure 5-34: Percentage difference between the simulated beam stiffness at position 1, <100> orientated beam, using literature values of $S_{ij}$ values (dotted line) and the beam stiffnesses at the same location from the minimisation routine. Different colours show the different loops as the $S_{44}$ value converges (the total range of Loop 1 has been truncated to aid viewing).

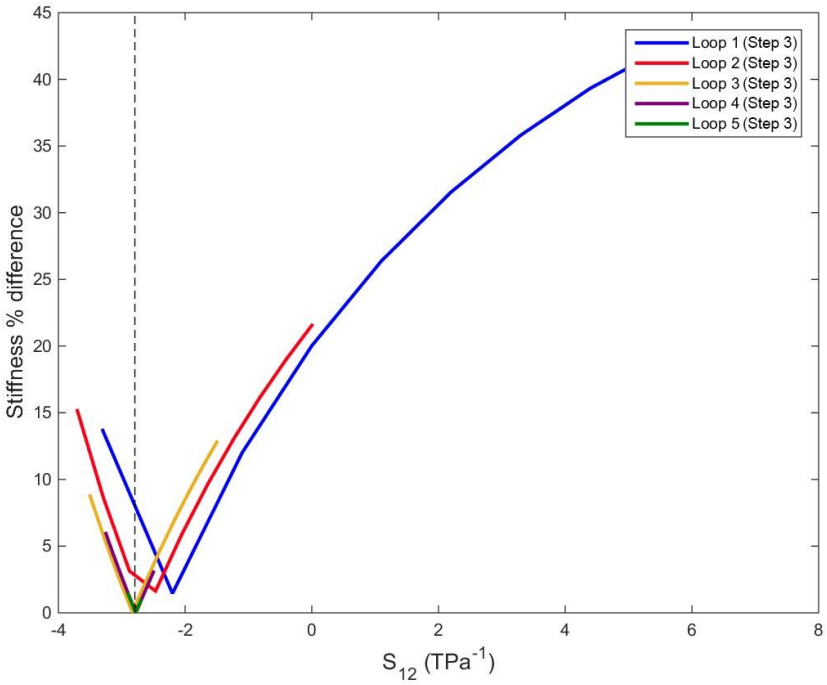


Figure 5-35: Percentage difference between the simulated beam stiffness at position 9, <110> orientated beam, (dotted line) using literature values of $S_{ij}$ values and the beam stiffnesses at the same location from the minimisation routine. Different colours show the different loops as the $S_{12}$ value converges.

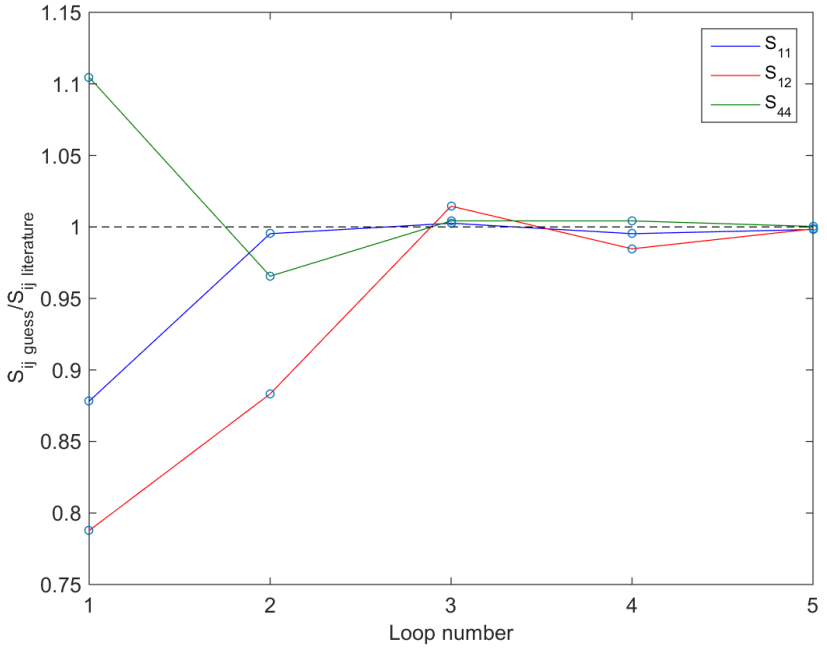


Figure 5-36: Minimised elastic constants normalised to their literature values, against the number of loops in the minimisation routine.

### 5.3.4 Analysis

There were five experimental datasets from different L-shaped cantilevers from which to extract the single crystal elastic constants. Of these, one was discarded due to a poor knowledge of the loading points, and another beam was in an orientation different to those considered thus far. Therefore, reliable datasets existed for one <100> aligned beam, and two <110> aligned beams. This allowed two minimisation routines to be undertaken, with steps 1 and 2 using the <100> beam, and step 3 using one <110> beam in one of the runs, and the other <110> beam in the other run. For each loading position required in the analysis steps, there were typically two to four repeat indentations, from which an average experimental stiffness could be calculated for comparison with the simulations.

Figure 5-37, Figure 5-38 and Figure 5-39 show the percentage differences between the experimental stiffnesses of the various beams at the relevant loading points, and the simulated stiffnesses generated with the FE model, during the second minimisation routine. In Figure 5-37 and Figure 5-39, each subsequent loop sees the stiffness difference decreasing towards converged values of $S_{11}$ and $S_{12}$. In Figure 5-38, the initial trough in the stiffness difference seen after 1 loop for $S_{44}$ shifts markedly for the subsequent loops. Although the initial trough is close to the literature value of $S_{44}$, this is likely to be coincidental, as the beam response when indenting near the free end of a <100> orientated beam has a large dependence on $S_{11}$, which is not at its literature value at this stage of the minimisation routine.

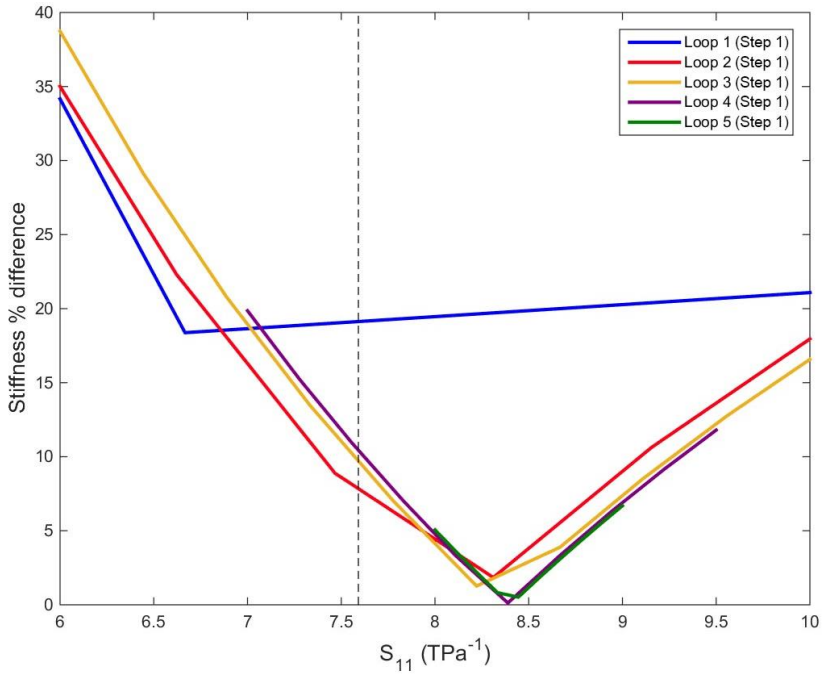


Figure 5-37: Percentage difference between the experimental stiffness of a <100> aligned L-shaped cantilever when indented near the corner, and the simulated stiffnesses using an FE model of the same beam indented at the same place, varying $S_{11}$ over 5 loops. The dotted line shows the literature value of $S_{11}$.

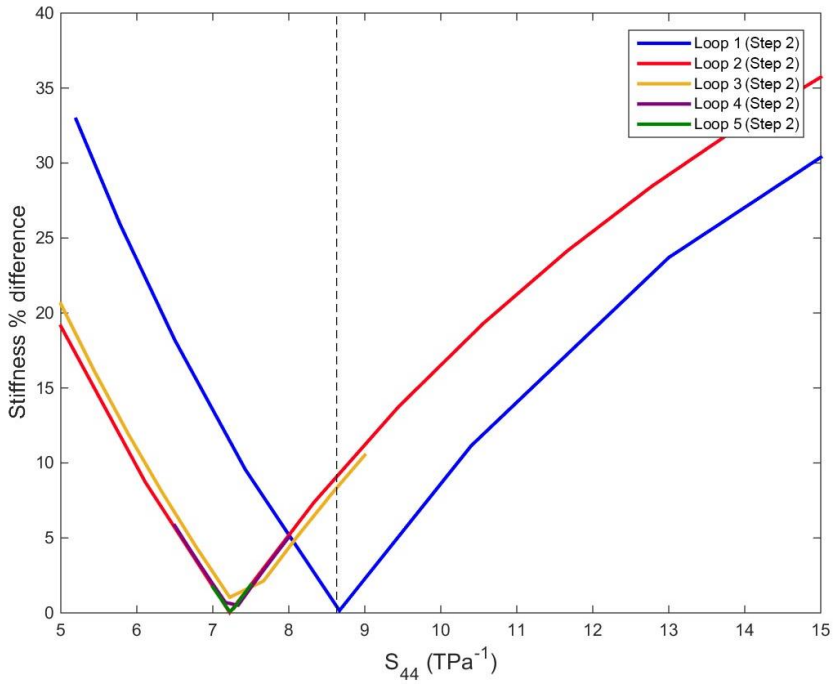


Figure 5-38: Percentage difference between the experimental stiffness of a <110> aligned L-shaped cantilever when indented near the free end, and the simulated stiffnesses using an FE model of the same beam indented at the same place, varying $S_{44}$ over 5 loops. The dotted line shows the literature value of $S_{44}$.

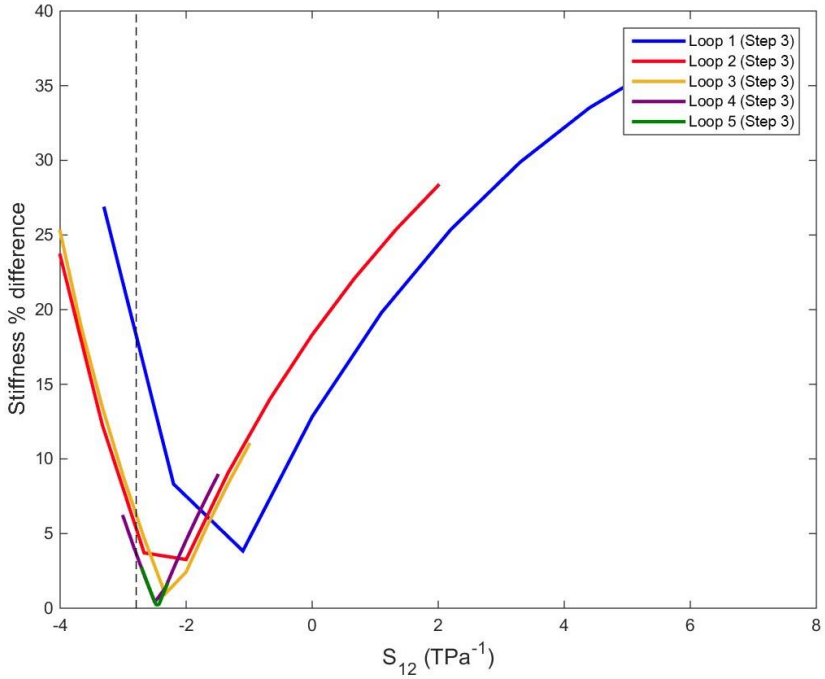


Figure 5-39: Percentage difference between the experimental stiffness of a <100> orientated L-shaped cantilever when indented near the corner, and the simulated stiffnesses using an FE model of the same beam indented at the same place, varying $S_{12}$ over 5 loops. The dotted line shows the literature value of $S_{12}$.

Table 5-4 shows the converged values of the compliance constants from the two minimisation routines after 5 loops in each, compared with literature values. All of the converged values closely approximate the literature values, with the exception of the $S_{12}$ value found during the first minimisation run, which is 1/3 the literature value. As the same experimental stiffnesses and loading points were used to minimise the $S_{11}$ and $S_{44}$ values in both minimisation runs, the values arrived at are similar. One drawback of this routine is that if the value arrived at for $S_{11}$ is too high from the simple bend test in step 1, then the value of $S_{44}$ is likely to always be made too low, as the loading position near the free end in step 2 depends on both $S_{11}$ and $S_{44}$. This is true for the values obtained in both runs, with $S_{11}$ overestimated and $S_{44}$ underestimated. The change in experimental dataset used during step 3 in the second minimisation routine results in a significant change in the value being minimised during that step, $S_{12}$.

| | $S_{11}$ | $S_{12}$ | $S_{44}$ |
|---|---|---|---|
| Adams et al.[117] | 7.60 | -2.79 | 8.63 |
| 1st Minimisation Run | 8.16 | -0.98 | 7.33 |
| 2nd Minimisation Run | 8.44 | -2.48 | 7.22 |

Table 5-4: Values of the compliance constants (in units of $TPa^{-1}$), arrived at after running through the minimisation routine described in section 5.3.3, with typical literature values for comparison.

In order to better understand how the converged compliance constants are related to mechanical behaviour, the Young's modulus and shear modulus were calculated using equations (5-17) and (5-18), for the same orientation range used in Figure 5-2. Figure 5-40 shows that the constants extracted from both runs give the correct trend of Young's modulus as a function of orientation. The first run gives the largest errors, with the Young's modulus in the [111] direction being 21% smaller than typical literature values. Table 5-5 shows the percentage differences between values calculated in this chapter and literature values. The second run matches typical literature values much more closely, with a maximum percentage difference of 10.1% for $E_{100}$. Figure 5-41 shows that both runs produce shear modulus quantities similar to those from literature, with similar percentage differences across all orientations.

| | $E_{100}$ | $E_{110}$ | $E_{111}$ | $G_{100}$ | $G_{110}$ | $G_{111}$ |
|---|---|---|---|---|---|---|
| 1st Run | 6.9% | 15.9% | 21.4% | 5.8% | 7.9% | 8.2% |
| 2nd Run | 10.1% | 4.8% | 0.7% | 2.2% | 6.7% | 8.1% |

Table 5-5: Percentage difference between Young's moduli and shear moduli calculated using converged constants and those from [117].

As a check that the constants arrived at using just two loading positions on the <100> aligned beam correctly reflected the mechanical behaviour at the other loading positions, simulations were run using these constants at all loading positions on the beam. Figure 5-42 shows that the difference between simulation and experiment is small across all the loading positions for this beam, validating the choice of loading positions as described in section 5.3.3.

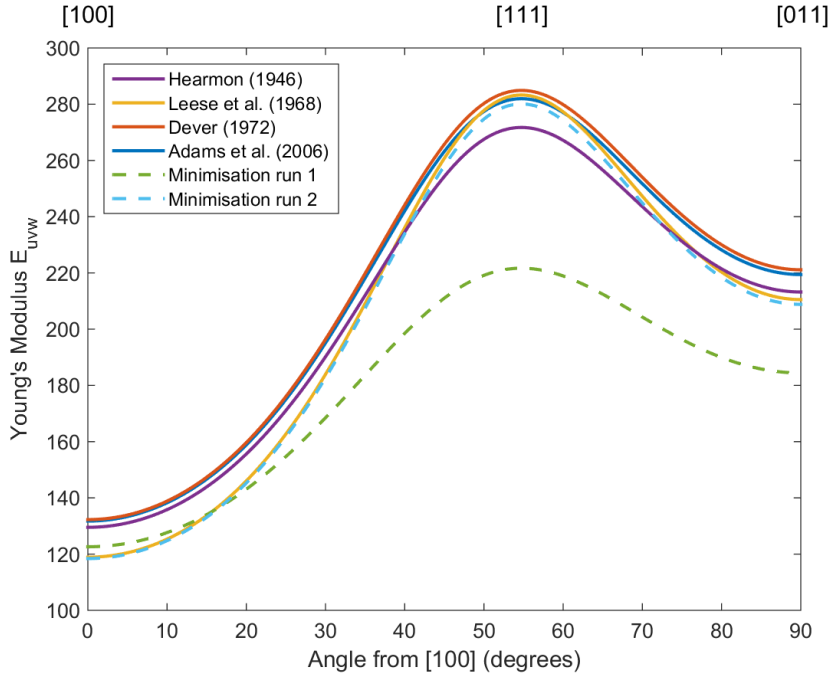


Figure 5-40: Young's modulus as a function of the angle from [100] towards [011] (in the $01\bar{1}$ surface) calculated from both the converged values of the compliance constants from the minimisation routine, and literature values for comparison.

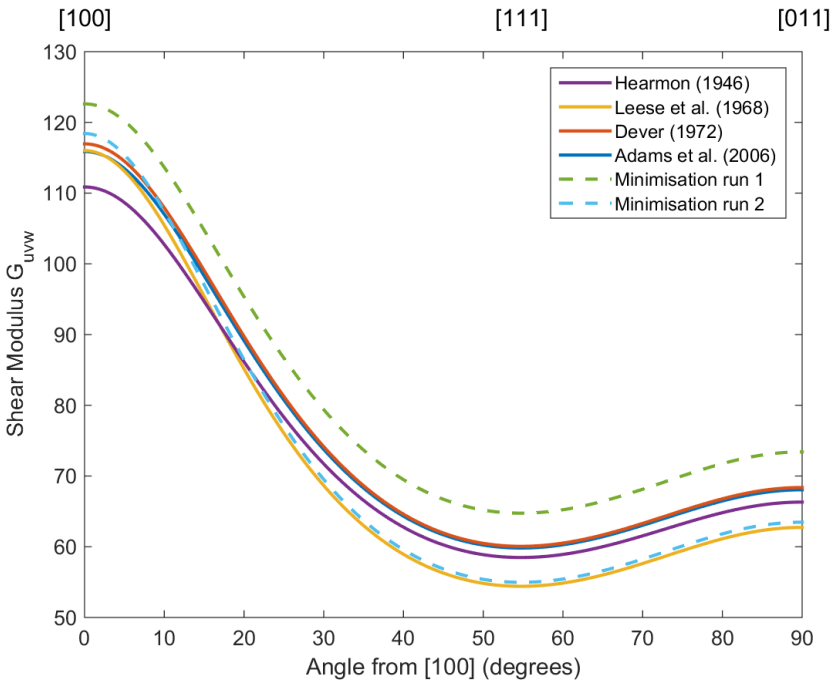


Figure 5-41: Shear modulus as a function of the angle from [100] towards [011] (in the ($01\bar{1}$ surface)) calculated from both the converged values of the compliance constants from the minimisation routine, and literature values for comparison.

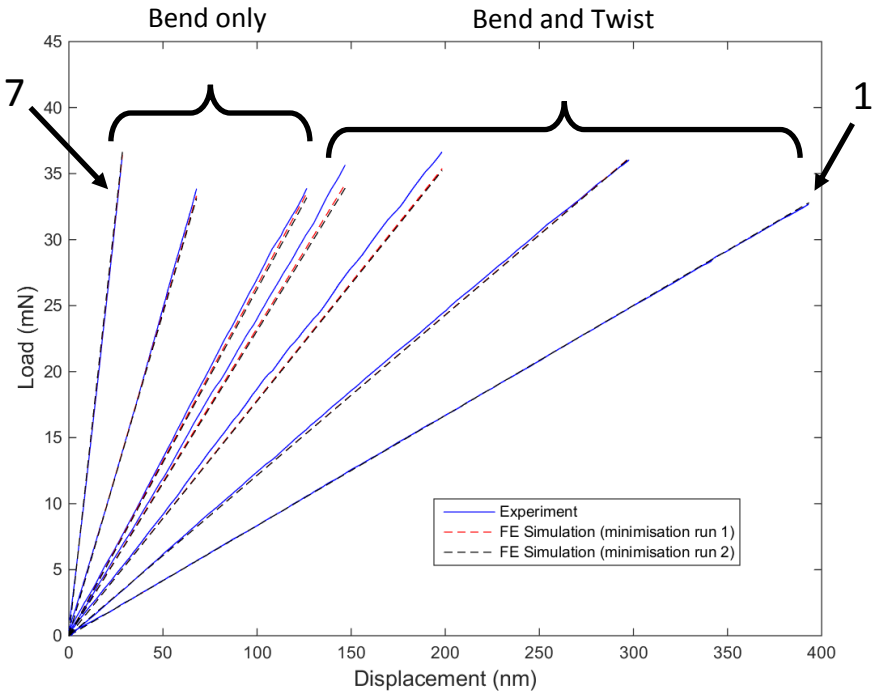


Figure 5-42: Experimental load-displacement curves from a <100> aligned beam (see Figure 5-11), compared with FE load-displacement curves generated using constants determined from a minimisation routine.

## 5.4 Conclusion

This chapter has established the validity of using novel FIB-milled L-shaped cantilevers to extract single crystal elastic constants. The trends in Young's modulus and shear modulus as a function of orientation were correctly reproduced, and in addition the absolute values for the second minimisation run were close to typical literature values (see Table 5-5).

A minimisation routine has also been successfully developed in which the problem of searching for a global minimum in a 4-dimensional parameter space has been achieved with a low computational cost.

The approach outlined in this chapter also has numerous drawbacks. The amount of time required to machine the beams, at approximately 12 hours, is significantly greater than for conventional equilateral triangle cross sectioned cantilevers, at ~3 hours for a 30 µm long,

5 µm wide beam. In addition, there is significant risk that the cantilevers once made can be subsequently destroyed whilst undergoing AFM-like scanning in the nanoindenter.

As with all such micromechanical work, the limiting factors in the accuracy of the analysis are likely to be the errors in measurement of the depth and width of the beams tested. Further work should be concerned with reducing measurement errors to a minimum, particularly of the encastre arm depth.

As the amount of experimental data that can be used in the minimisation routine is limited due to the time that the simulations take to run, it would be advantageous for future studies to concentrate on loading the beam at fewer locations, but increasing the accuracy with which the indent positions are known, for example by using a slightly sharper indenter tip, or displacing the beam further to create a deeper indent impression. Alternatively, to make better use of all the data collected in this experiment, and reduce the overall error, the minimisation routine could be adapted to incorporate some of the loading positions not considered already, with positions nearest to the most sensitive positions for each constant given higher weightings in the analysis.

Also, as only one beam with arms in the <100> direction was used in the final analysis, further beams in this orientation should be milled and tested, in order that the average error associated with the analysis can be better known. Having better verified the suitability of using L-shaped cantilevers to extract single crystal elastic constants, further tests on materials with unknown constants could be performed, in addition to tests involving a range of different temperatures in a high temperature nanoindenter. This test could also yield important mechanical information for materials only available in polycrystalline form.

# 6 Investigating the role of grain boundaries in ion-irradiated materials using nanoindentation

## 6.1 Introduction

Although many previous micro-mechanical investigations have employed the use of single crystals, or test pieces milled within single grains away from grain boundaries (see chapters 5 and 7), real engineering materials are typically polycrystalline in nature, and thus the interplay between dislocations and grain boundaries must be considered for a proper understanding of the bulk mechanical response.

Irradiation is known to have severe effects on the microstructure of materials, including the production of defects [129], radiation induced segregation [130], transmutation [2], swelling [131], cavity formation [132], hardening and embrittlement [133]. How such changes affect the interaction between dislocations and grain boundaries is of key importance for understanding how candidate materials will function under real world reactor conditions.

Grain boundaries properties have previously been studied using FIB-machined micro-cantilevers [66,71] (see section 2.2.2.3) and pillars [134--137], however it is time consuming to use this method to study a wide range of boundary types. In this chapter, 'straight' nanoindentation is used to probe mechanical properties near to and far away from grain boundaries, in both unirradiated and ion-irradiated materials, in order to gain an understanding of the role of grain boundaries during the deformation of materials in fusion reactors.

### 6.1.1 Hall-Petch Relation

In polycrystals, grain boundaries act as strengthening agents, inhibiting plastic flow by blocking dislocation motion. Dislocations pile-up at grain boundaries and their back stresses counteract the externally applied stress, with plastic deformation only able to continue once a high enough stress is reached such that slip can transfer into neighbouring grains. In smaller grains, the maximum number of dislocations in a pile-up (and therefore maximum stress) is reduced compared to that in bigger grains, meaning that the applied stress required to transmit slip across grain boundaries is greater [138]. Such behaviour is captured by the classic Hall-Petch relationship [139,140], which relates the increase in yield stress ($\sigma_{ys}$) with decreasing grain size ($D$) as:

$$\sigma_{ys} = \sigma_0 + k_y D^{-\frac{1}{2}} \tag{6-1}$$

where $\sigma_0$ represents the stress required to cause deformation within a grain, and $k_y$ indicates the strengthening contribution of the grain boundaries. This relationship has recently been called into question by Dunstan and Bushby who have found that much of the experimental size effect data is consistent with a $D^{-1}$ term [141].

The Hall-Petch effect has been found to break down at values of $D$ < 100 nm. At such grain sizes, the stress required to operate dislocation sources is greater than for other deformation mechanisms, e.g., grain boundary migration, dislocation generation in the boundaries and grain boundary sliding [138] (although this may be due to grain boundaries being 'cleaner' in fine grained material, with segregants spread over a much larger grain boundary area).

$\sigma_0$ and $k_y$ are material dependent parameters, but are also influenced by specific experimental and material factors [142], e.g. surface finish, thermomechanical history, texture, and deformation technique etc. Due to large variations in these factors with different studies, it is difficult to compare $\sigma_0$ and $k_y$ across different materials.

Although the Hall-Petch relationship successfully describes the response of materials on the macro-scale, it relates only to the average strength of grain boundaries [143]. This is problematic at small scales, where individual boundaries can provide greatly varying resistances to slip propagation. At such scales, it would be useful to be able to provide a measure of the specific resistance to slip transfer of different boundary types or misorientations.

### 6.1.2 Theory of Slip Transfer at Grain Boundaries

The barrier to plastic flow caused by grain boundaries can be overcome by dislocations transferring into neighbouring grains. This can occur in three ways [144]:

1) Direct transmission of dislocations from one grain into another,
2) Indirect transmission of slip, caused by local pile-up stresses activating sources on the other side of the boundary, or
3) Grain boundary dislocations can be punched out into the neighbouring grain.

The first case is relatively rare, as only certain grain boundary geometries can accommodate such dislocation motion. A very simple example is that in which the two slip planes intersect along a line in the boundary plane and the two Burgers vectors are identical (and along that

intersection line) (Figure 6-1). Ingoing screw dislocations can then simply cross slip across the boundary. In this case, dislocations will pile-up due to the difficulty of cross slip.

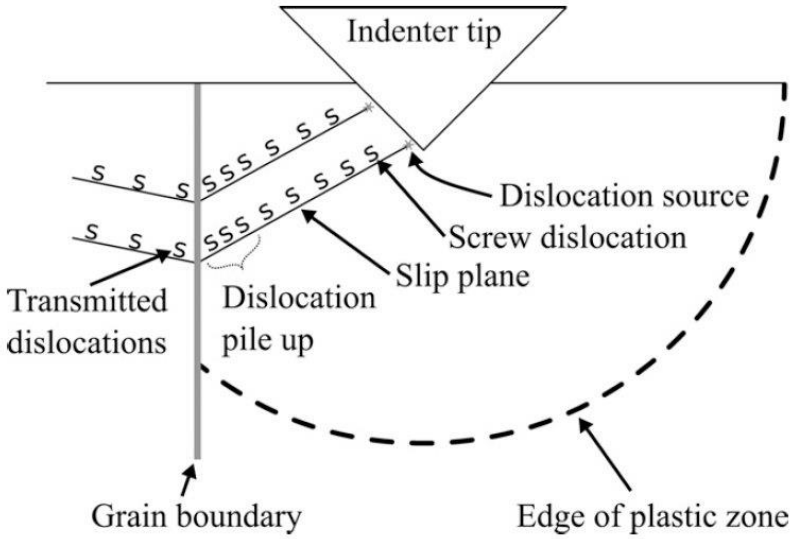


Figure 6-1: Schematic diagram showing the direct transmission of dislocations across a grain boundary, during nanoindentation (from [145]).

More generally, direct transmission can occur if the ingoing and outgoing slip planes intersect along a line in the boundary plane, but with different Burgers vectors. Such transmission is accompanied by the formation of a residual dislocation on the grain boundary, due to the requirement for the overall Burgers vector to be conserved. The form of the dislocation reaction is:

$$b_1 \rightarrow b_2 + b_{GB} \tag{6-2}$$

where $b_1$ is the Burgers vector of the incoming dislocation, $b_2$ is the Burgers vector of the outgoing dislocation, and $b_{GB}$ is the Burgers vector of the residual dislocation which remains in the boundary. If deformation continues at such a boundary, eventually multiple residual dislocations will build up and form a barrier to subsequent slip transmission (depending on whether the residual dislocations are glissile in the grain boundary plane, allowing such local

stress concentrations in the boundary to be relaxed via processes such as glide and climb [144]).

In the case of indirect slip transfer, the geometrical conditions for dislocations to directly move across the grain boundary are not met (or multiple residual dislocations have caused a barrier, as above). Instead, for slip transfer to occur, the local stresses from the pile-up at the grain boundary must be great enough that dislocation sources in the adjoining grain can be activated on new slip systems.

Lee et al. [146] have proposed three factors for determining the outgoing slip system in the case of indirect transmission of slip across boundaries:

1) The geometrical condition: the angle between the lines of intersection of the incoming and outgoing slip planes on the boundary should be minimised.
2) The resolved shear stress condition: the outgoing slip plane is determined by the plane experiencing the maximum resolved shear stress.
3) The residual grain boundary dislocation condition: the Burgers vector of the residual dislocation should be minimised.

Experimental and theoretical studies have supported these criteria [147--149].

### 6.1.3 Experimental Evidence of Slip Transfer

Slip transfer across grain boundaries has been previously studied using techniques such as etch pitting [150], slip line analysis [151,152], TEM [148,153--155], and AFM [156].

However, the work of most relevance to this chapter is that using nanoindentation near grain boundaries. This has been conducted in iron [142,143,145], a variety of iron-silicon alloys (ranging from 2.2 to 14 wt% Si) [154,157--160], interstitial-free steel [142,145,161], martensitic steel [155], molybdenum [160,162], niobium [163], $Ni_3Al$ [156], copper [142,145,164], zinc [97,142,145], and magnesium [97].

In several of these studies [142,143,145,157,159,160,163,164], the slip transfer phenomenon is observed as a displacement burst during the indentation at near constant load, consistent with the movement of a large number of dislocations. Such behaviour is similar to the initial pop-in(s) seen at low (< ~100 nm) displacements, associated with the transition from elastic to elasto-plastic loading (see section 2.1.2). However, so called "grain boundary pop-ins" can happen at loads significantly greater than initial pop-in loads, and with much larger displacement bursts [145].

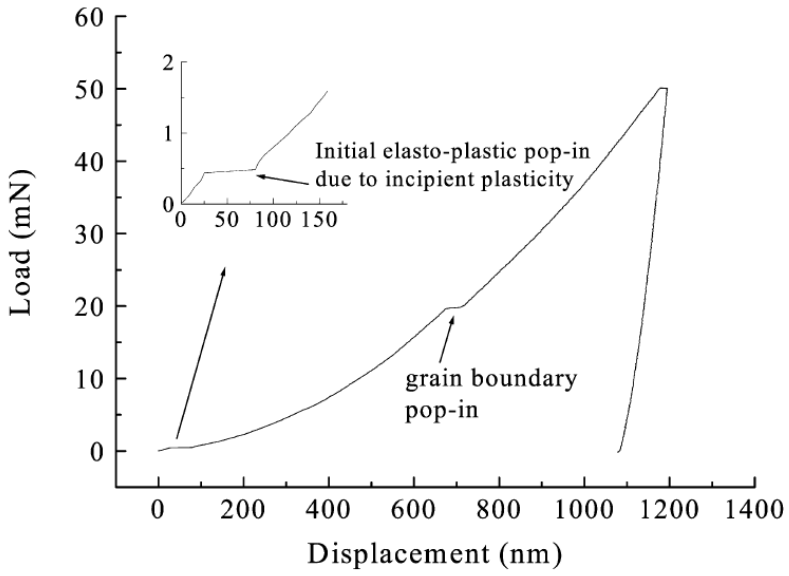


Figure 6-2: Load-displacement curve taken from an indent near a grain boundary in niobium. Both initial and grain boundary pop-ins are seen (from [163]).

Wang and Ngan observed grain boundary pop-ins when indenting near grain boundaries in polycrystalline niobium [163] (see Figure 6-2). They found that the critical pop-in load was dependent on the distance between the grain boundary and the indent, $d$, and that for any particular boundary, the ratio of the plastic zone size at the point of pop-in, $c$ (dependent on load, see equation (6-4)), to $d$ was roughly constant, but could vary between different boundaries.

Wang and Ngan also studied the relationship between grain boundary misorientation and slip transfer, finding that a greater misalignment between the most favourable slip systems on either side of a boundary resulted in a lower probability of observing a grain boundary pop-in. They rationalised misorientation using a factor $m'$ (previously defined by Wo and Ngan [156]), in which $m' = 1$ indicates perfect alignment, and $m' = 0$ complete misalignment:

$$m' = \cos(\alpha)\cos(\beta) \tag{6-3}$$

where $\alpha$ is the angle between slip plane normals of the best aligned slip planes, and $\beta$ is the angle between the closest slip directions on these planes (Figure 6-3). In Wang and Ngan's study, grain boundary pop-ins were only seen for $m' > 0.9$, i.e. those cases in which slip systems on either side of the boundary were well aligned.

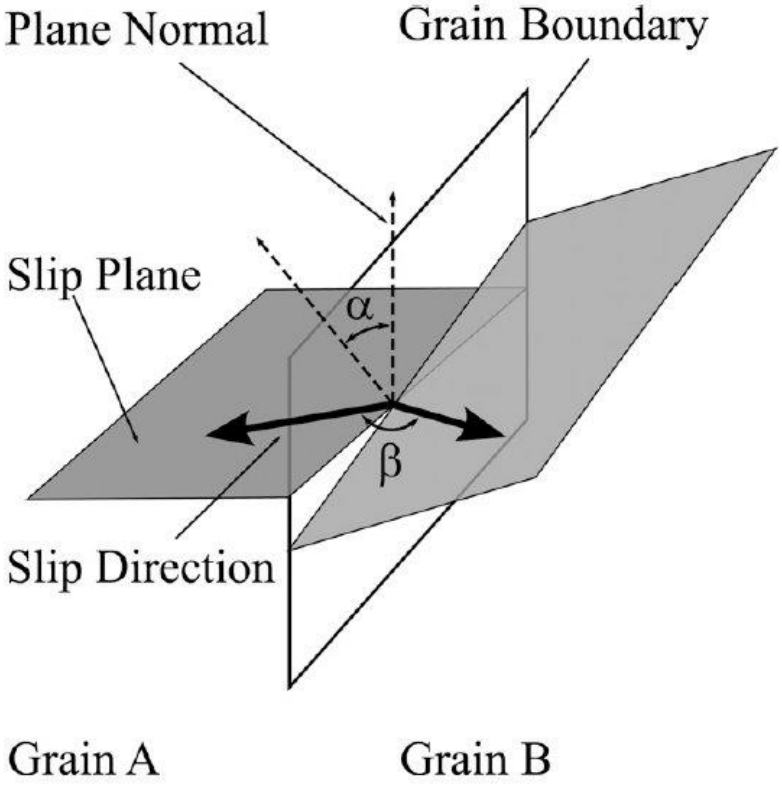


Figure 6-3: Schematic diagram showing the key parameters involved in the calculation of the misorientation factor, $m'$ (from [145]).

Randman found a grain boundary pop-in-misorientation relationship in commercially pure iron, observing that there was an inverse relationship between $m'$ and the critical stress intensity factor ($K_c$, see section 6.3.3.4) for the pop-in [143,145].

Britton indented near grain boundaries in two alloys of iron containing differing amounts of carbon: the commercially pure iron used by Randman (0.0119 wt% C) and interstitial free steel (0.0021 wt% C) [142,145]. The presence of grain boundary pop-ins was found to sensitively depend on the carbon content, being observed frequently in the commercially pure iron but not in the interstitial free steel. This was explained in terms of the carbon segregating to grain boundary dislocations and pinning them, in the form of classic 'Cottrell Atmospheres' [165], whereby a critical stress concentration needed to be reached for the dislocations to become unpinned, causing the observed pop-in. In the interstitial free steel,

grain boundary pop-ins were suppressed due to the lack of carbon pinning and thus easily activated dislocation sources.

Britton also indented near grain boundaries in materials of other crystal systems, namely copper (fcc) and zinc (hcp). No grain boundary pop-ins were observed in copper, however an influence of the boundary on the plastic zone of the indenter was inferred by a loading regime with a markedly different dependence of displacement on load. Wo and Ngan similarly didn't detect any grain boundary pop-ins in $Ni_3Al$, although SEM images depicted different slip trace and material pile-up regimes at the boundaries, which was linked with the same misorientation factor $m'$ noted above [156].

Fcc materials such as copper and $Ni_3Al$ are in general known to have lower Hall-Petch slopes ($k_y$) than bcc materials [163], therefore lower resistance to slip transfer at the boundaries is expected, resulting in the lack of grain boundary pop-ins observed.

### 6.1.4 Plastic Zone Size

For this chapter, it is useful to have an idea of the spatial extent of the plastic deformation emanating from the indenter tip (i.e. the plastic zone size), in order to study how it is related to factors such as hardening at grain boundaries and slip transfer.

Johnson's cavity model [22,166], originally developed for large indents [167], assumes that the plastic zone surrounding the indenter has a spherical stress distribution, which depends only on the geometry of the indenter, and the yield stress of the material. According to Kramer [168], this results in a plastic zone radius, $c$, under an applied load $P$, given by:

$$c = \sqrt{\frac{3P}{2\pi\sigma_{ys}}} \tag{6-4}$$

Several methods have been employed to measure the extent of the plastic zone, including etch pit analysis [33], AFM [97,142,168,169], high-resolution EBSD [30,97,142,143], and TEM [33,34,101,167].

Kramer used AFM to measure the extent of the plastic zone in various materials, finding that experimental data could be accurately fitted to equation (6-4), except in two cases where the indentation size effect dominated [168]. Chiu and Ngan also found that equation (6-4) was valid as a predictor of plastic zone size when using TEM to observe deformation under indents in $Ni_3Al$ [167].

In Chapter 4, plastic zone sizes of indents within grains of <100>, <110>, and <111> normal directions were measured using HR-EBSD and AFM. Although they were found to vary significantly with crystal orientation, values measured using HR-EBSD roughly agreed with those predicted by Johnson's cavity model.

Hardie used cross-sectional TEM to measure the size and distribution of plastic deformation beneath indents produced using a variety of different indenter geometries, in both unirradiated and ion-irradiated Fe-12% Cr, at depths ranging from 50 nm to 250 nm [170]. As in other TEM-based studies [34,167], he observed a heterogeneous network of dislocations, forming separate lobes due to the particular slip systems activated, rather than the spherical distribution of plastic strain given by Johnson's model. The ~500 nm thick ion-irradiated layer acted to suppress the extent of the plastic zone, with the effect being more pronounced at low indenter depths than at large depths, by which stage dislocations had penetrated into

the unirradiated substrate layer. Numerically, in the unirradiated sample, the plastic zone depth to indenter depth ratio varied from ~9 for low depths, to ~6 at higher depths, compared to ~8 at low depths and ~5.5 at higher depths for the ion-irradiated sample. This compares to previous estimates ranging from 4 to 10 for indentation experiments [101,171]. Using Johnson's formula, the plastic zone size is expected to be smaller in the case of irradiated materials, due to the increase in yield strength.

Randman used HR-EBSD line scans to measure the pile-up surrounding indents in iron, as a function of distance from both the face and apex [143]. Fitting data from indents of different sizes to equation (6-4) (using $c = c_{apex}$), he determined a value of $\sigma_{ys}$ which was in rough agreement with hardness values measured (via the Tabor relation (equation (2-1)). Substituting $\sigma_{ys}$ into equation (6-4) using $c = c_{apex}$, he determined a "shape correction factor" for Berkovich tips as follows:

$$c_{face} = A * \sqrt{\frac{3P}{2\pi\sigma_{ys}}} \tag{6-5}$$

where $A = 0.70$. However, using AFM, Britton found a shape correction factor of $A = 1.07 \pm 0.23$ in iron, and $A = 0.887 \pm 0.104$ in copper [142].

EBSD has also been conducted by Zaafarani et al. [30,31,172], using FIB sectioning to measure sub-surface lattice rotations. A disadvantage of this method is that some of the plastic strain may relax upon sectioning, in addition to FIB damage limiting the EBSD resolution.

A key drawback of Johnson's model is that it assumes a constant flow stress throughout indentation, which is inconsistent with the observed indentation size effect (see section 2.1.3).

It would be advantageous to be able to perform similar HR-EBSD and AFM measurements as were conducted in Chapter 4, of indents made in this chapter. However, it would be time consuming and unfeasible to measure every indent in such a manner, and therefore the simplification employed by equation (6-4) is useful. Furthermore, it should be possible to determine the broad differences in plastic zone size between unirradiated and ion-irradiated samples using such a model.

## 6.2 Method

### 6.2.1 Material and Sample Preparation

Arrays of indents were made in close proximity to grain boundaries, in both unirradiated and ion-irradiated Fe and Fe-C samples, supplied by EFDA. Compositions of these materials are shown in Table 6-1, in addition to comparisons with the materials used previously by Randman and Britton.

The processing route of the EFDA materials involved induction melting in a Hydrogen and Argon atmosphere, to remove impurities, followed by hot forming by forging ingots with a mechanical hammer at 1000 °C, further cold forming, and then annealing at 700 °C in an Argon atmosphere. Full details of this procedure can be found in [173].

| Alloy | C wt ppm | S wt ppm | O wt ppm | N wt ppm | P wt ppm | Cr wt ppm | Mean Grain Size (µm) |
|---|---|---|---|---|---|---|---|
| EFDA Fe | 3 / 4 | 2 / 2 | 5 / 4 | 2 / 1 | < 5 | < 2 | 183 |
| EFDA Fe-C | 50 / 48 | 2 / 2 | 3 / 2 | 1 / 1 | < 5 | < 2 | 265 |
| MCO Fe | 119 | < 1 | ? | ? | < 40 | < 100 | 50 |
| IF Steel | 21 | 100 | ? | 24 | 80 | ? | 10-30 |

Table 6-1: Chemical analysis of the EFDA alloys (after hot forming in blue, as-delivered in black) [173], commercially pure iron (from Metal Crystals and Oxides Ltd) [142,143], and 'Interstitial Free Steel' [142].

Materials from this process were cut into discs ~10 mm in diameter and ~0.5 mm thick. The samples were ground using SiC papers to a 4000 grit finish, and subsequently polished using colloidal silica. For further investigation in the nanoindenter, samples were mounted on JEOL stubs using silver dag.

The ion-irradiated Fe and Fe-C samples were implanted with Fe ions at the Ion Beam Centre in Rossendorf by Christopher Hardie [101]. Multiple ion charges (1+ to 3+), energies

(0.5 - 9 MeV) and beam currents were used, in an attempt to create as flat a damage profile as possible (Figure 6-4). These implantations with different conditions were performed sequentially, resulting in a sample containing layers of material with different irradiation histories, resulting in a potentially complex microstructure. However, as the plastic zone emanating from the indenter tip samples a volume much larger than that in its immediate vicinity (see section 6.1.4), minor local variations were felt to be of secondary importance. As shown below, the maximum depth of the flat-profiled damaged layer is ~2 µm (with the ion damage rapidly tailing off to zero at ~2.4 µm), with an average damage of 1.7 dpa, and many small dislocation loops expected within the layer.

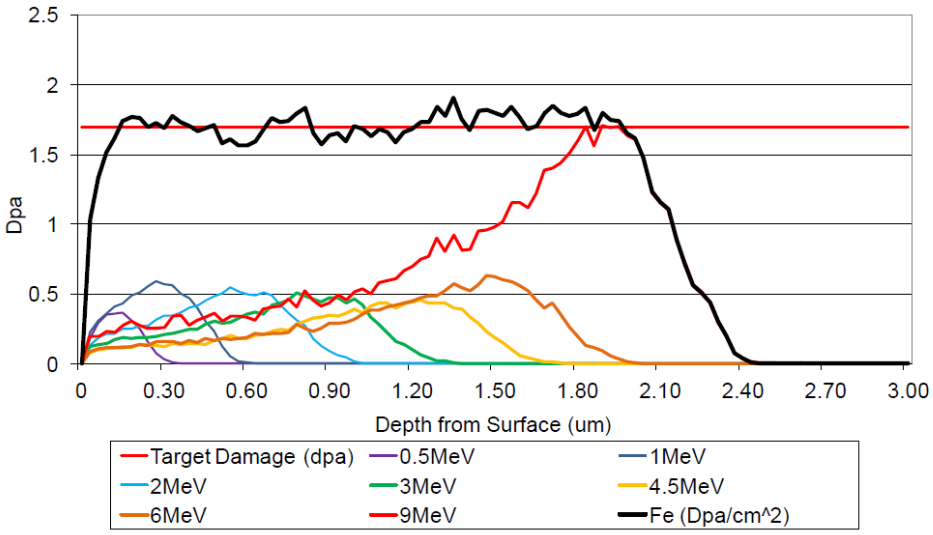


Figure 6-4: Predicted damage (in dpa) of the ion-irradiation conducted on EFDA material in Rossendorf (calculated using SRIM) (from [101]).

### 6.2.2 Preliminary Testing

Indents near grain boundaries were initially made in the Fe sample, however no grain boundary pop-ins were seen. With reference to the conclusions made by Britton with regard to carbon content [142], this is unsurprising, as this sample contains less carbon (4 wt ppm) than the interstitial free steel (21 wt ppm, see Table 6-1), in which grain boundary pop-ins

were also not apparent. Furthermore, there are no other obvious impurities present in the EFDA Fe which might pin dislocations at or near grain boundaries. This necessitated a move to the Fe-C sample, which has a carbon content (48 wt ppm) between that of the IF Steel and the commercially pure Fe (119 wt ppm), and might therefore be expected to exhibit grain boundary pop-in at grain boundaries. Such a material is also of more practical relevance, since most industrial ferritic steels contain a significant amount of carbon.

### 6.2.3 Grain Boundary Indentation in Fe-C

To test a wide range of indent to grain boundary distances, it is desirable to make a large number of indents per boundary. However, there is an upper limit to this number, as indents must be placed such that the plastic zone of one indent does not overlap with the plastic zone of a subsequent indent, impacting on its mechanical behaviour. As a compromise between these factors, a maximum indentation depth of 1.5 μm, and a separation between indent centres of 20 μm was chosen.

All indents were performed on the Nano XP, with a target indentation strain rate during loading of 0.05/s, a hold period of 10s at the maximum load, an unload to 10 % load at 4 mN/s, a hold period for 60 s to measure thermal drift, and a final unload at 4 mN/s.

In order to keep testing between different grain boundaries as consistent as possible, boundaries were chosen which, for a particular sample orientation, were parallel with the face of the Berkovich indenter. This ensured that the applied stress field impinging on a boundary was as similar as possible for each test, variations due to crystal orientation notwithstanding (see chapter 4). In practise, indents were deemed well aligned when the angle between the boundary and the indenter face were $\lesssim 20°$. For this reason, indents in

which the apex of the indent was closer to the boundary than the face of the indent were not considered, even if grain boundary pop-ins were seen during indentation.

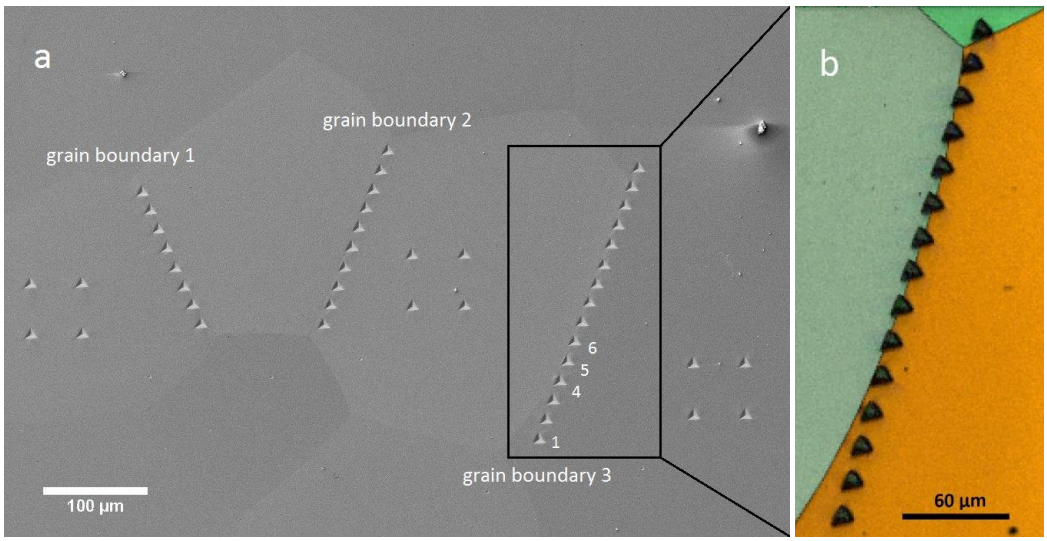


Figure 6-5: (a) SEM image showing three indent arrays adjacent to grain boundaries, and three 2-by-2 mid-grain indent arrays; (b) Surface normal direction IPF map (with image quality overlaid in greyscale) of grain boundary 3.


Figure 6-5 (a) shows an SEM image of an area in which several indent arrays have been made, both near grain boundaries (seen faintly by the change in image contrast from grain to grain), and mid-grain. For each grain boundary tested, the array is defined in the nanoindenter software by inputting the starting point, number of indents, spacing (as above), and choosing the angle in which the array is laid out in (picked such that a wide range of indent centre to grain boundary distances are achieved). For each grain boundary tested, mid-grain arrays (typically 2-by-2, see Figure 6-5 (a)) were made in the grains either side to the same depth, with 50 µm spacing in x and y between indents.

The grain orientations were not known prior to experimentation, but were probed afterwards using EBSD. An example IPF map is shown in Figure 6-5 (b), of the indent array denoted ‘grain boundary 3’ in Figure 6-5 (a).

The pile-up surrounding each indent was observed after indentation using the SEM. SEM micrographs were also used to measure the shortest distance from the centre of each indent to the grain boundary ($d$), in the event that the boundary was clearly observable. For some boundaries, it was necessary to use the FIB to apply a low milling current (e.g. 100 pA) for a short time to reveal the boundary's location more clearly, via the grain to grain variation in etching rate and the increased contrast when imaging with the $Ga^+$ beam.

## 6.3 Results

### 6.3.1 Grain Boundaries Tested

A summary of all nanoindentation undertaken near grain boundaries is shown in Table 6-2. Also shown is the number of indents in which the face of the indenter is closer to the boundary than the apex, and are therefore included in further analysis.

| | Tested boundaries | Total indents | Indents per boundary (average) | Total indents (face closest) | Indents per boundary (face closest) |
|---|---|---|---|---|---|
| Unirradiated Fe-C | 14 | 129 | 9.2 | 76 | 5.8 |
| Ion-Irradiated Fe-C | 18 | 175 | 9.7 | 132 | 7.3 |

Table 6-2: Summary of nanoindentation undertaken near grain boundaries.

Due to the limitations of the Nano XP system, it wasn't possible to accurately control the indent centre to grain boundary distance to better than ± 3 µm, although a rough range of distances could be achieved. Figure 6-6 and Figure 6-7 show histograms of the indent to boundary distances probed in the unirradiated and ion-irradiated Fe-C, respectively. The indent positioning relative to the boundaries was reasonably similar for the two cases.

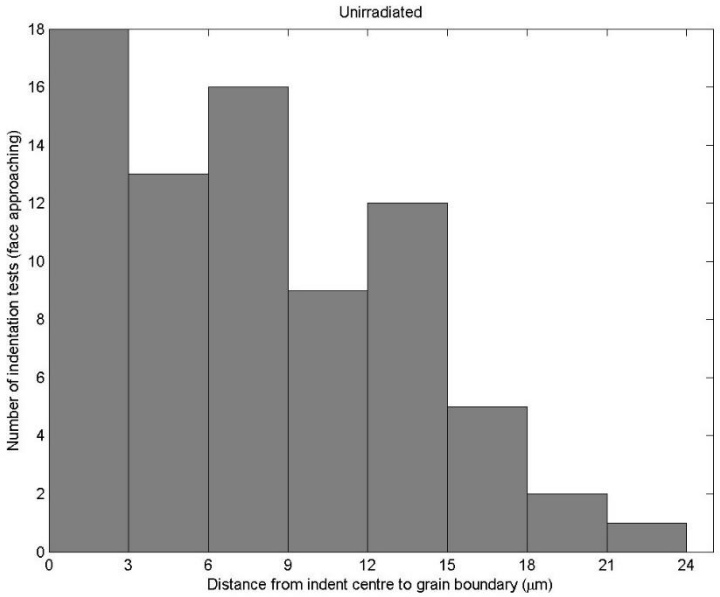


Figure 6-6: Histogram of probed indent centre to grain boundary distances in unirradiated Fe-C (indenter face closest to boundary).

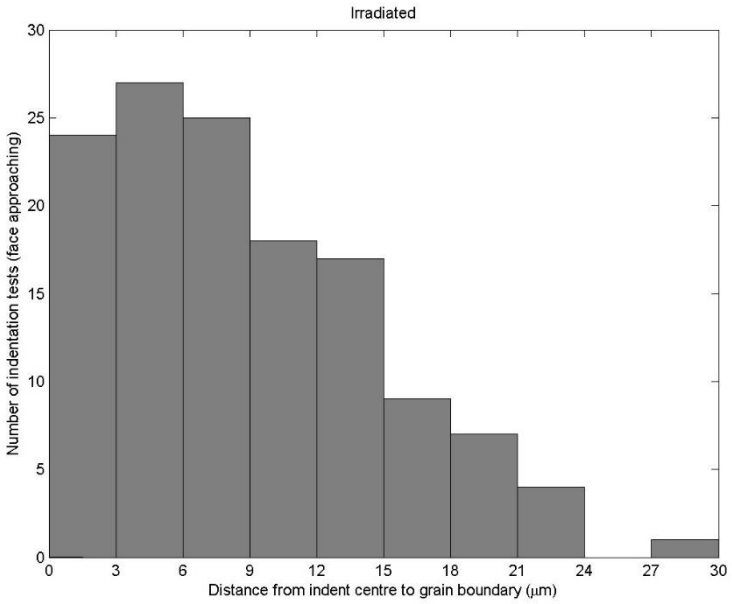


Figure 6-7: Histogram of probed indent centre to grain boundary distances in ion-irradiated Fe-C (indenter face closest to boundary).

Before discussing the evidence of slip transfer in both the unirradiated and ion-irradiated samples, some general comments concerning the differing response of the two materials will be made.

### 6.3.2 Differences in mechanical response between unirradiated and ion-irradiated samples

Figure 6-8 shows the nanoindentation load-displacement response of the unirradiated and ion-irradiated Fe-C samples, taken mid-grain. Each curve represents an average of the load-displacement behaviour from a single grain, with ~30 grains tested in each sample. The spread in the data for each sample is due to the effects of anisotropy on the mechanical response, due to the different orientations of the grains probed (see chapter 4).

The average maximum load reached is higher in the ion-irradiated sample (81.1 mN) than in the unirradiated sample (71.6 mN), demonstrating that some irradiation hardening has occurred. It can also be observed that the relative difference in applied load between the two samples is greater at shallow depths than at the full indent depth, e.g. the load at 500 nm depth during an average indent in the ion-irradiated material is 1.4 times the load reached in the unirradiated material, whereas the load at 1500 nm depth in the ion-irradiated material is 1.1 times that reached in the unirradiated material. The reason for this is that although the ion damage is relatively constant up to the full depth of the indent, the plastic zone emanating from the indenter tip samples a greater depth than this, as discussed previously (see section 6.1.4). Accordingly, the volume of material sampled in the ion-irradiated material includes an increasingly higher proportion of unirradiated substrate as the indenter penetrates deeper into surface.

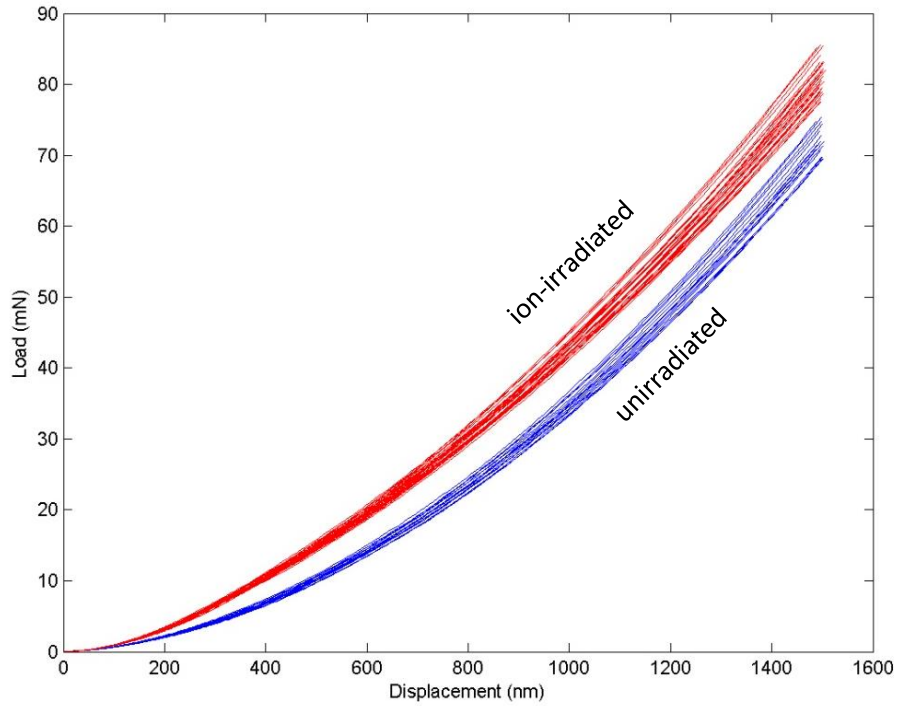


Figure 6-8: Load-displacement data (loading portion only) of indents in unirradiated Fe-C (blue) and ion-irradiated Fe-C (red), taken mid-grain.

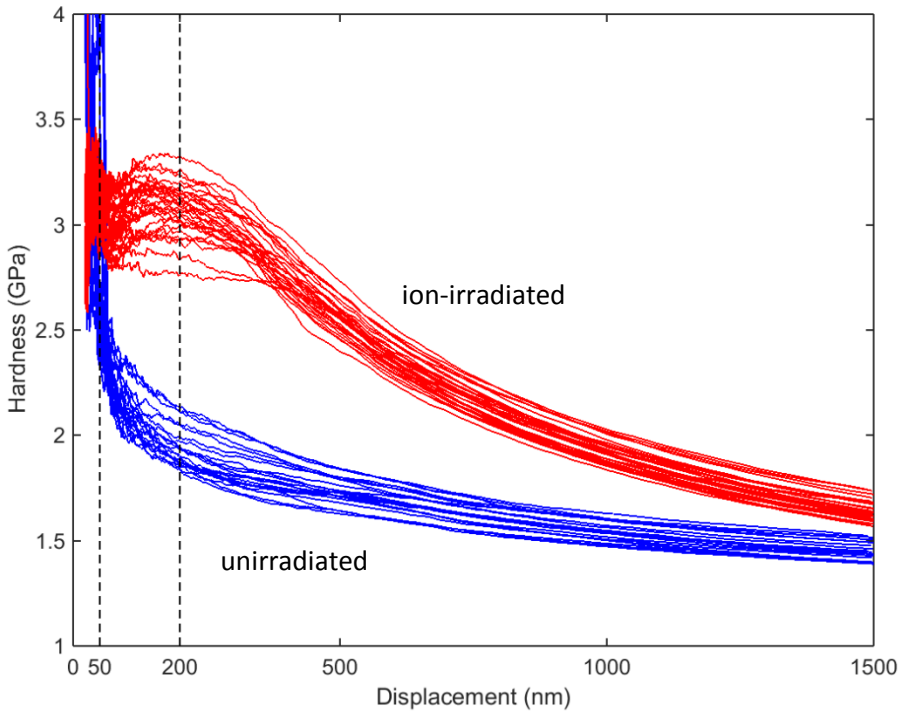


Figure 6-9: Hardness-displacement data of indents in unirradiated Fe-C (blue) and ion-irradiated Fe-C (red), taken mid-grain (dotted lines show range used for average CSM hardness values).

In addition to looking at the load-displacement curve, the CSM mode on the nanoindenter was used to give a measure of hardness as a function of depth (see section 3.1.2). Figure 6-9 shows that for the unirradiated material, following the early stage at very low displacements (< 30 nm), which has been cropped out due to large uncertainty in the data, a familiar indentation size effect is seen, with the hardness starting to plateau towards the full depth of the indent.

For the ion-irradiated material, after the initial low displacement region, the effect of the ion-implantation on the mechanical response of the material is evident, with hardness increased by roughly a factor of 1.5 compared to the unirradiated material over the first few hundred nanometres. The hardness doesn't increase with decreasing depths (< 200 nm) to the same degree as seen in the unirradiated material, due to the fact that the ion damage only reaches its peak from ~150 nm onwards (see Figure 6-4). After ~300 nm, there is a marked drop in hardness, showing both the increasing influence of the underlying unirradiated material, and the effect of the ISE. At the full depth of the indent, the hardness has started to plateau, approaching values seen at similar depths in the unirradiated material. The mechanical response at this depth is relatively unaffected by the implanted layer. At the lower displacement stage of the indentation (50 – 300 nm), scatter in the hardness values measured by CSM is greater in the ion-irradiated material compared to the unirradiated material, demonstrating the heterogeneous nature of the ion damage.

#### *6.3.2.1 Elastic-Plastic Transition*

Figure 6-10 shows the load-displacement data of representative indents made in the unirradiated Fe-C (blue) and ion-irradiated Fe-C (red) during the first 50 nm. In the unirradiated sample, purely elastic loading is seen for the first 18 nm, before a distinct pop-

in event associated with the sudden nucleation of dislocations is seen (see section 2.1.2). Conversely, the ion-irradiated sample shows a more consistent load-displacement response, with evidence of plasticity from the onset of loading. This is due to the ion-irradiated sample having a much greater density of dislocations present, therefore nucleation of new dislocations at some particular threshold is not needed to generate plastic flow.

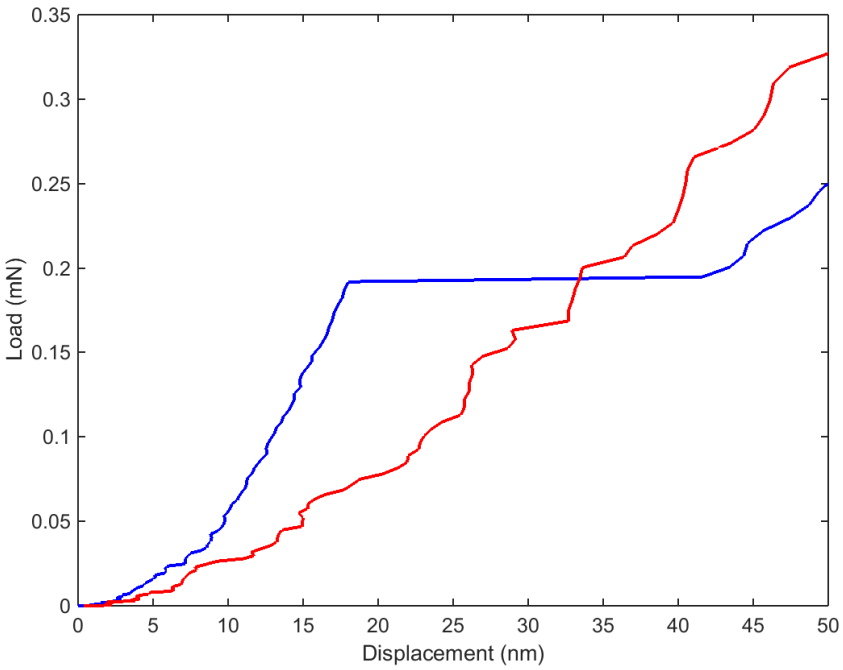


Figure 6-10: Initial load-displacement data of representative mid-grain indents from the unirradiated Fe-C (blue), and the ion-irradiated Fe-C (red). An elastic to elasto-plastic pop-in event is clearly seen in the unirradiated sample.

#### *6.3.2.2 Determination of Hardness*

For further analysis, it is useful to be able to extract single values of hardness from indents. Although hardness can be extracted from the maximum load reached during an indent, $P_{max}$ (see section 2.1.1.2), this doesn't take into account the depth dependent behaviour seen in Figure 6-9. Average CSM hardness values between depths of 50 nm and 200 nm were used, representing a compromise between the high scatter at low depths and sampling too much

of the unirradiated substrate at higher depths. This range was also used for average CSM hardness values by Hardie [101].

#### *6.3.2.3 Plastic Zone Size*

These average CSM hardness values can be substituted into Tabor's hardness relation (equation (2-1)), to give a rough estimate of yield strength. From this, the estimated plastic zone size according to equation (6-4) can be calculated, using values of load corresponding to the particular point of interest during the indent. At the full indent depth, the plastic zone is estimated to extend ~8.9 µm from the indenter apex in the unirradiated material, and ~6.6 µm in the ion-irradiated material. This suggests that at the indent spacing chosen (20 µm), the plastic zones of the indents do not overlap. Real measurements of the plastic zone size in Chapter 4 using the GND density distributions show that although there is good agreement with Johnson's cavity model when indenting in a grain with a <100> normal direction, for grains with <110> and <111> surface normals, the model overestimates the plastic zone size.

A rough measure of the plastic zone size can also be inferred with reference to Figure 6-9, by observing at what point the unirradiated substrate starts to influence the mechanical response in the ion-irradiated material. In the graph, the hardness starts to significantly drop at approximately 350 – 400 nm (equating to a plastic zone size 5 to 6 times the indenter depth), although it is hard to pinpoint the exact depth at which the role of the substrate starts to affect the results. This is due to the heterogeneous nature of the plastic zone, which depends on which particular slip systems are being activated, and therefore varies considerably according to crystallography. The depth of the ion damage will also vary

between grains [174], which due to the lack of crystallographic information in SRIM, is unaccounted for in Figure 6-4.

#### *6.3.2.4 SEM Images of Mid-grain Indents*

Figure 6-11 shows an SEM image of a typical indent in the unirradiated Fe-C sample (labelled '1' in Figure 6-5 (a)). Distinctive pile-up lobes are seen adjacent to the faces of the indent (particularly the left and right facing ones), extending to the edges of the image frame (c.f. section 4.3.2). By contrast, in Figure 6-12, showing two indents from the same grain in the ion-irradiated Fe-C sample, the pile-up is restricted to the immediate vicinity surrounding the indents. In Figure 6-12 (b), along part of the left-facing side of the indent, a high contrast ridge indicates that material is being pushed relatively high over a small region, as compared to the smoother gradients seen in Figure 6-11. Similar observations were made by Hardie found when comparing pile-up in unirradiated and ion-irradiated samples [101]. It should be noted that in both the unirradiated and ion-irradiated material, the exact shape and size of any pile-up features will be heavily influenced by crystallography (see chapter 4).

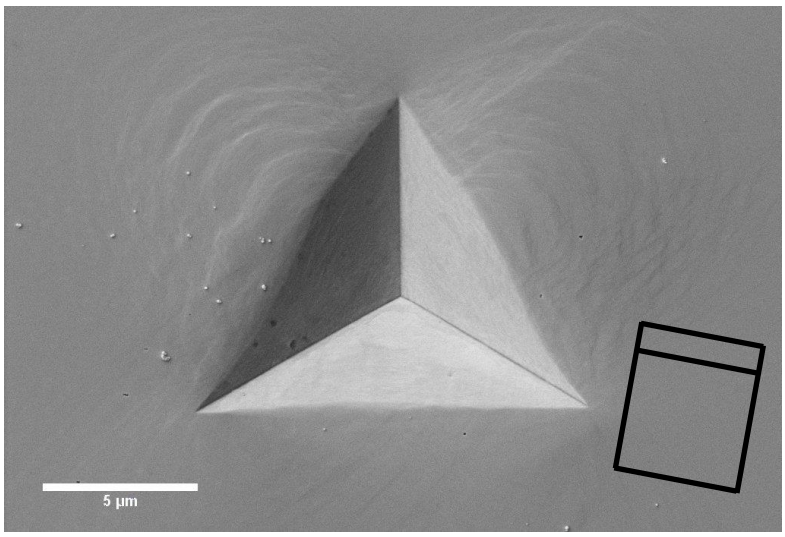


Figure 6-11: SEM Image of an indent in the unirradiated Fe-C sample (labelled '1' in Figure 6-5 (a), far from a grain boundary). The crystal orientation is shown by a wireframe overlay.

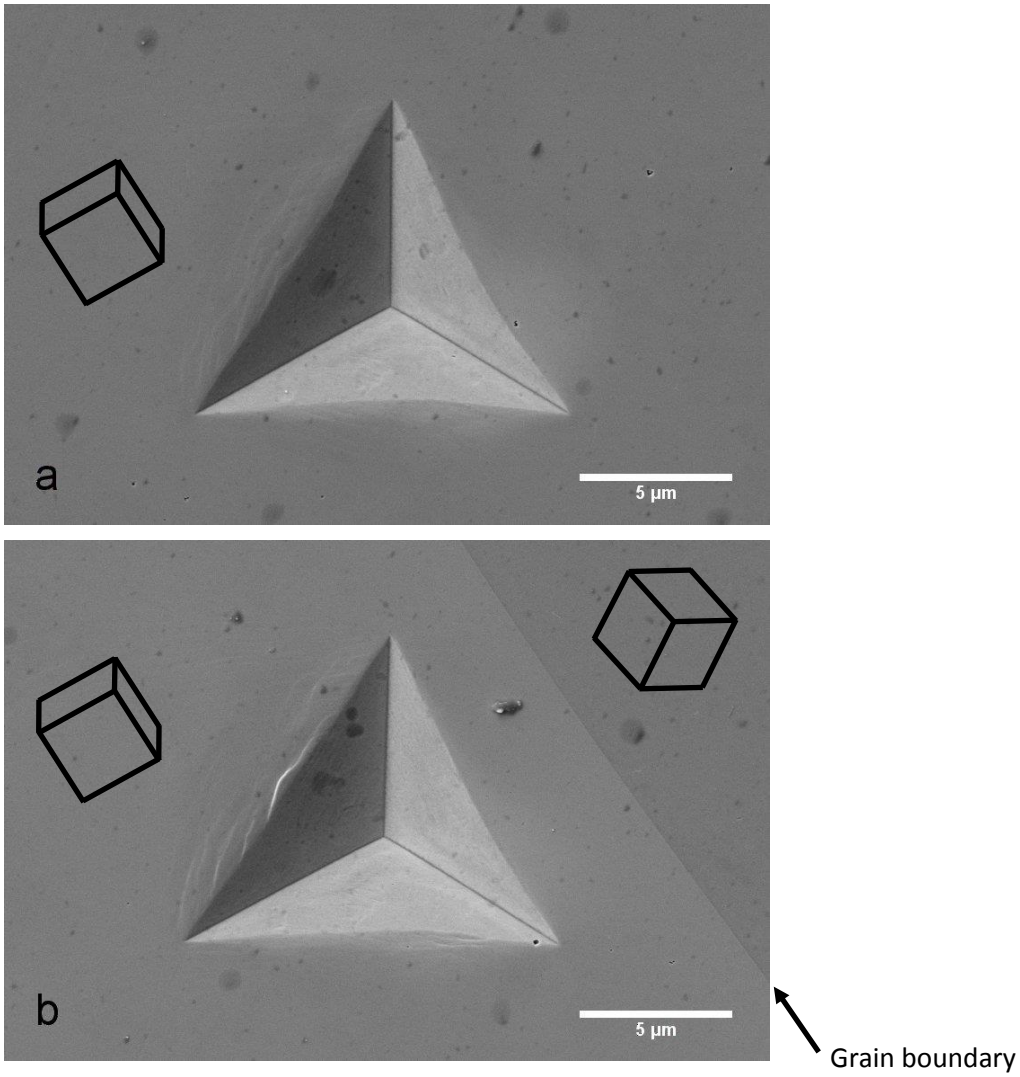


Figure 6-12: SEM images of two indents in the same grain of the ion-irradiated Fe-C sample, a) taken mid-grain, b) near a grain boundary, with wireframe overlays showing the crystal orientation.

### 6.3.3 Grain Boundary Behaviour

#### *6.3.3.1 Unirradiated Sample*

Figure 6-13 shows the load-displacement curves of two indents near the same grain boundary, in which grain boundary pop-ins are seen to occur. The hardness-displacement curves of the same indents are shown in Figure 6-14. Equivalent load-displacement curves showing grain boundary pop-ins in the higher carbon content MCO Fe (see Table 6-1) investigated by Randman [143] are shown in Figure 6-15.

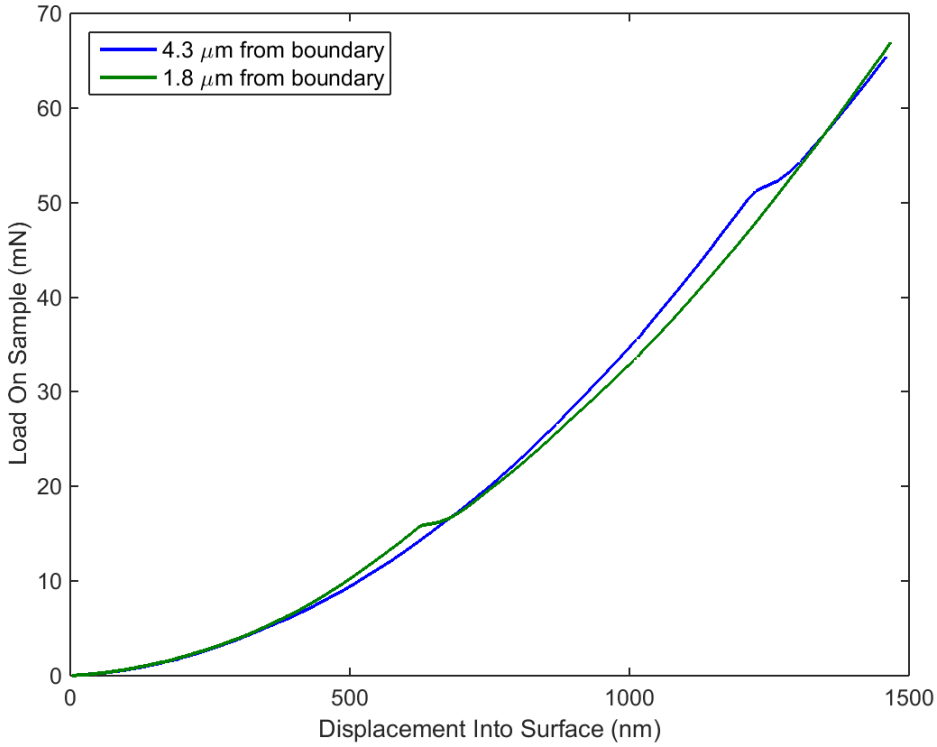


Figure 6-13: Load-displacement curves of indents near the same boundary in unirradiated Fe-C (loading portion only), in which pop-ins occur. The blue curve is 4.3 µm from the grain boundary; the green curve is 1.8 µm from the grain boundary.

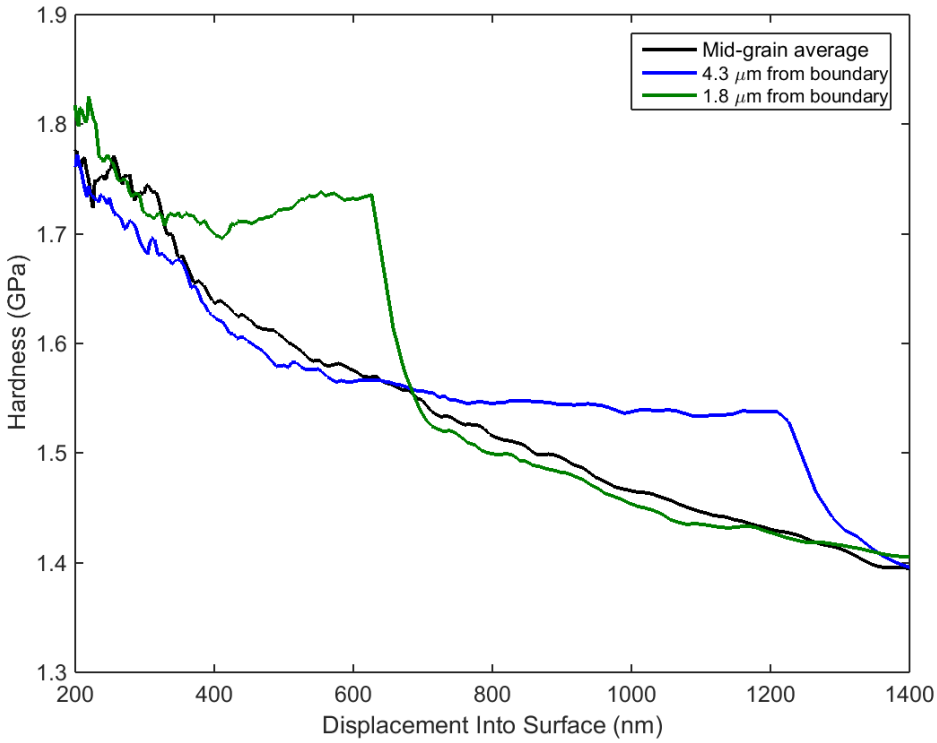


Figure 6-14: Hardness-displacement curves of the two indents shown in Figure 6-13, in addition to the mid-grain average.

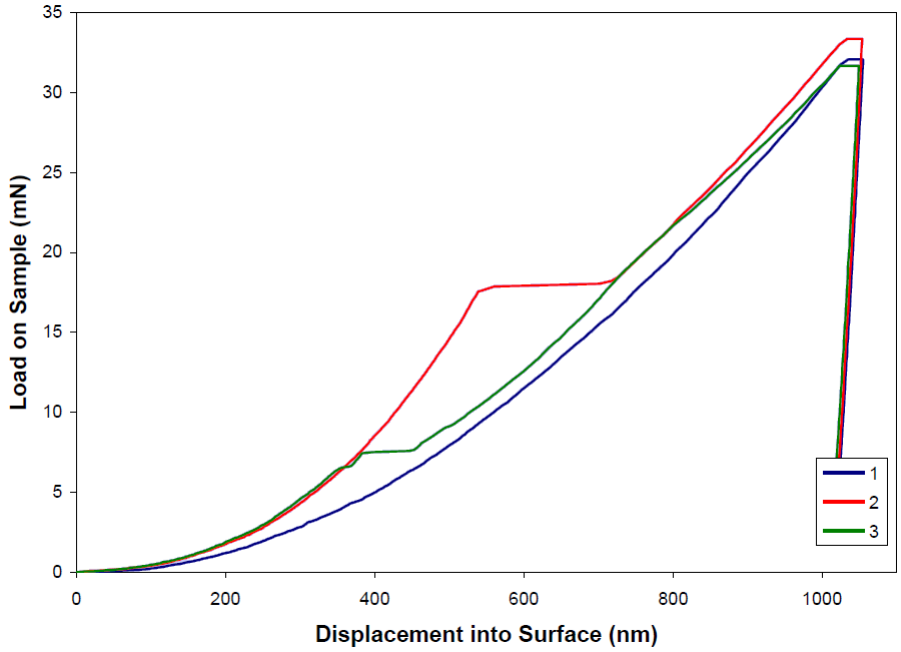


Figure 6-15: Load-displacement curves of indents in MCO Fe (119 C wt ppm), in which grain boundary pop-ins occur (from [143]). Indent 1 is 5.6 µm from the grain boundary, indent 2 is 4.4 µm from the grain boundary, and indent 3 is 2.0 µm from the grain boundary.

As described in section 6.1.3, the grain boundary pop-in is manifested as a sudden displacement burst in the material, whilst the load on the indenter tip is near constant. Before the moment of pop-in, the load-displacement curve steepens considerably, representing significant hardening until the barrier to slip is overcome (seen both in Figure 6-13 and Figure 6-15). This hardening (compared to the baseline mid-grain hardness) is also shown in the hardness-displacement graph (Figure 6-14), from ~800 – 1200 nm in the indent 4.3 µm from the boundary and ~350 – 600 nm in the indent 1.8 µm from the boundary.

As examining each load-displacement curve to look for evidence of pop-ins would be time consuming, a MATLAB code was written to automate the detection of pop-ins, and to record several key parameters for further analysis, such as pop-in load and displacement at its start, and the size of the displacement burst. The code examines the difference between successive displacement data points, and looks for larger than expected jumps. Each prospective pop-

in match must still be examined afterwards, as due to the small nature of pop-ins in the Fe-C material (meaning the code must be sensitive to these), false positives are sometimes found.

Of the 129 indents made near 14 grain boundaries in the unirradiated Fe-C, 24 grain boundary pop-ins were detected. The average displacement burst size was 33 nm (in Figure 6-13, the blue curve has a 30 nm displacement burst, and green curve has a 32 nm displacement burst). Although there is no mention of the average burst size in Randman's study, Figure 6-15 shows much larger pop-ins than in Figure 6-13, with indent 2 being approximately 180 nm, and indent 3 being approximately 70 nm. Assuming the two indents shown in Figure 6-15 are of a typical size for this material, it is likely that in Randman's study, the higher carbon content of the material enables dislocations to be pinned more readily at grain boundaries, as compared to the material in this study. A greater build up of stress is therefore possible, meaning that when the barrier to slip is overcome, the strain burst is greater.

For grain boundaries next to which pop-ins occur, the pop-in load is dependent on the distance between the grain boundary and the indent (as seen in other studies [143,159,163], see section 6.1.3). For example, the 'green' indent in Figure 6-13 is closer to the grain boundary than the 'blue' indent, and therefore pops-in at a lower load, and smaller indent size.

The size of the displacement burst was plotted against the indent centre to grain boundary distance in Figure 6-16. Although no clear trend is apparent, it is possible that this is due to the relatively low number of indents per boundary, whereas a study involving indents made at a greater range of distances away from a long grain boundary (e.g. in a bicrystal) might

provide better statistics for such a trend. It might be expected that indents made relatively closer to a grain boundary would exhibit smaller bursts, as the shorter distances involved would result in pile-ups containing fewer dislocations, and therefore fewer dislocations to burst into the next grain.

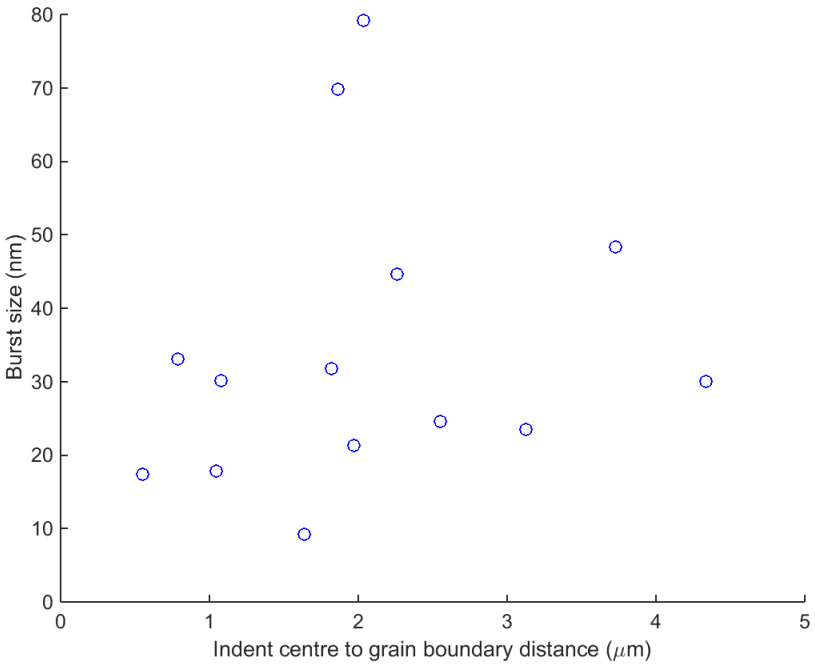


Figure 6-16: Displacement burst size (nm) as a function of indent centre to grain boundary distance (μm), for grain boundary pop-ins in unirradiated Fe-C.

#### 6.3.3.1.1 Linking load-displacement features to SEM Images

In Figure 6-17, on the left hand side, SEM images of 3 indents near the same grain boundary are shown (previously seen in Figure 6-5, labelled '4', '5', and '6'), with the distance $d$ getting progressively smaller in each case. On the right hand side, the load-displacement curves corresponding to these indents are shown, along with a load-displacement curve from the mid-grain (taken from an average of 4 indents). The corresponding hardness-displacement data is shown in Figure 6-18, in addition to that from an indent closer to the grain boundary, and average mid-grain hardness-displacement values.

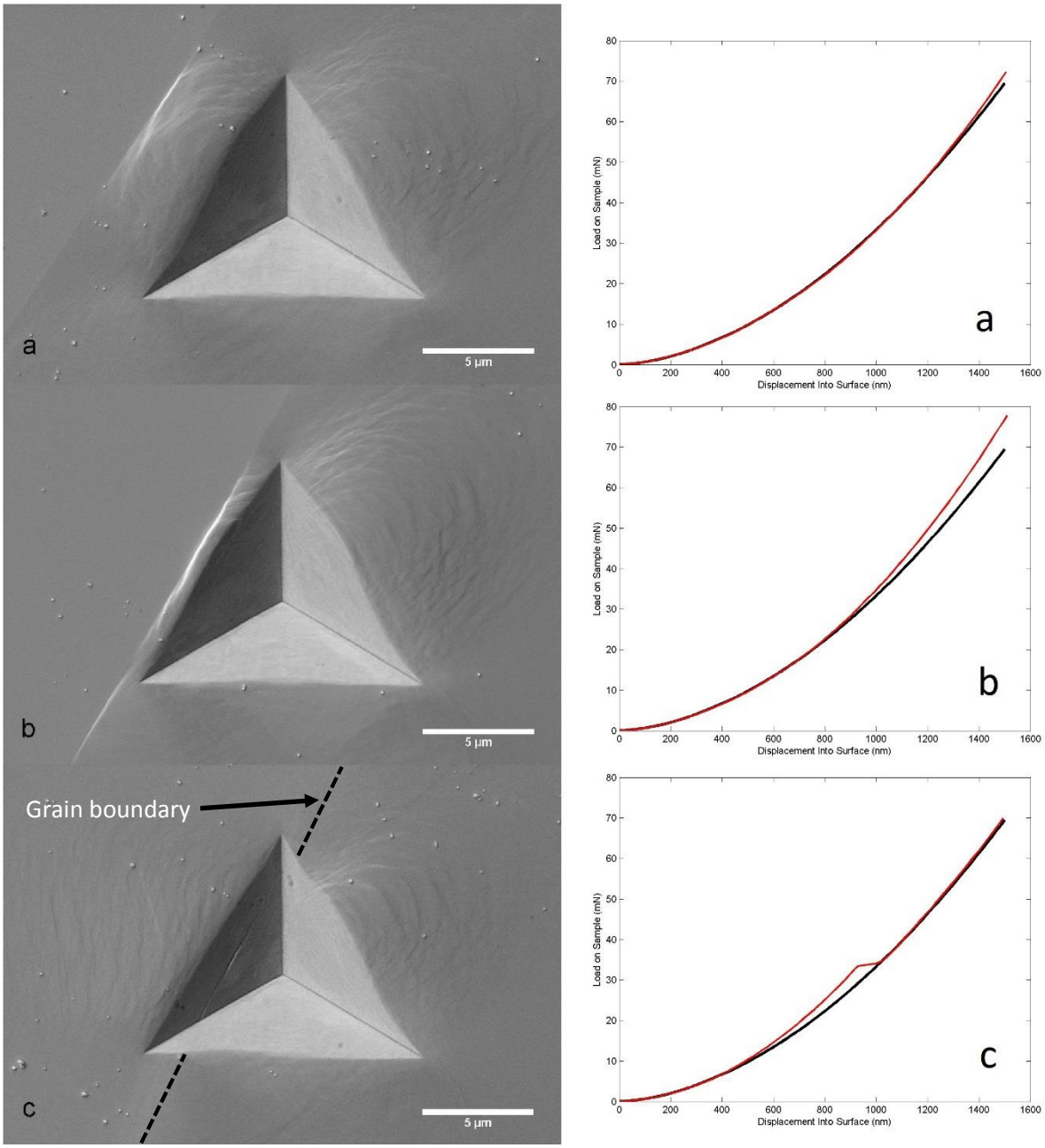


Figure 6-17: SEM images of three indents made in unirradiated Fe-C, (left), along with their corresponding load-displacement curves (right, in red). Indent a) is 7.5 µm from the grain boundary, indent b) is 4.4 µm from the grain boundary, and indent c) is 2.0 µm from the grain boundary. The average mid-grain response is shown in black.

In Figure 6-17 (a), with an indent in which $d = 7.5$ µm (no '4' in Figure 6-5), the pile-up lobe emanating from the left hand face of the indent can clearly be seen impinging on the grain boundary, indicated by a line of increased contrast. The effect of the barrier on the indentation response is relatively modest, as shown by the similarity of the load-

displacement curve to the average mid-grain curve, however at indenter depths > 1200 nm a small amount of hardening is present (see Figure 6-18, blue curve).

Figure 6-17 (b) shows an indent with $d = 4.4$ µm (no '5' in Figure 6-5), in which a greater amount of material is piled up against the grain boundary (demonstrated by the increased contrast). As in Figure 6-17 (a), the sample surface on the other side of the grain boundary appears flat and smooth in contrast to the notably rougher material which has been pushed up around the indent. The mechanical response is significantly affected by the barrier, with an increase in hardness of ~0.14 GPa at the full indent depth (see Figure 6-18, green curve).

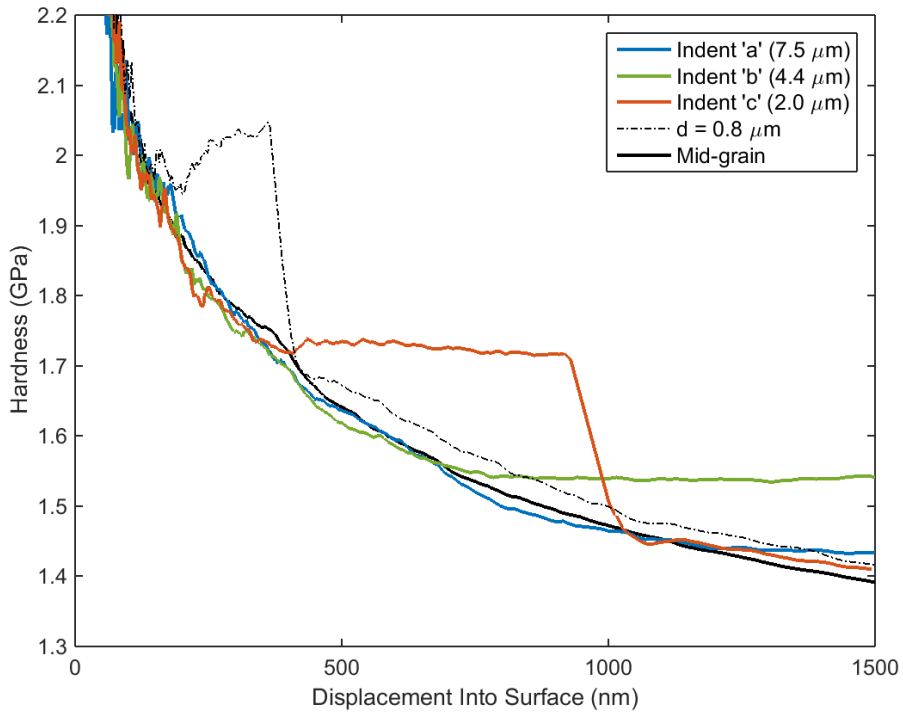


Figure 6-18: Hardness-displacement data corresponding to graphs marked 'a', 'b', and 'c' in Figure 6-17, with the indent centre to grain boundary distance shown in the legend. The dotted line shows the hardness response of an indent 0.8 µm from the grain boundary, whilst the black line shows average mid-grain values.

Finally, in Figure 6-17 (c), in which $d = 2.0$ µm (no '6' in Figure 6-5), the critical threshold to overcome the barrier has been reached at an indenter depth of ~900 nm, resulting in a burst of plasticity into the neighbouring grain. This is easily observed in the image by a series of

wavy lines extending out into the previously pristine surface. A significant amount of hardening is observed before the pop-in, rising to a maximum of ~0.21 GPa (see Figure 6-18, red curve). As in Figure 6-13 and Figure 6-15, the load-displacement data in Figure 6-17 (c) indicates that once the barrier to slip is overcome, there is no further hardening effect. In Figure 6-18, the dotted line shows the hardness-displacement curve of an indent even closer (0.8 µm) to the grain boundary, which pops-in at a shallower depth (~350 nm), and shows an even greater degree of hardening prior to the pop-in event, with a maximum increase of ~0.25 GPa. After the pop-in the hardness drops to values that are only slightly above that for the mid-grain indent.

#### *6.3.3.2 Ion-Irradiated Sample*

As compared to the unirradiated sample, clear evidence of grain boundary pop-in and sudden slip transfer across grain boundaries is much reduced in the ion-irradiated material. Using the automated code, in 175 indents made near 18 grain boundaries, only 11 grain boundary pop-ins were detected. The average burst size is also smaller, with a median value of 15 nm. This may be due to the added resistance provided by the ion damage in the grain into which there is slip transfer, causing smaller displacement bursts compared with the unirradiated sample.

The size of some the displacement bursts are such that they approach the limit of detectability via this method, being of a similar order to the average separation in displacement of data points. For example, Figure 6-19 shows an indent which has a barely perceptible kink just before 800 nm that has been detected by the MATLAB code. It is hard to ascertain from the load-displacement curve whether this is actually a pop-in like event or e.g. noise in the indenting system. However, Figure 6-20 shows that there is characteristic

hardening before this event. Due to the small nature of this displacement burst, it is possible than many similar events have been missed due to size.

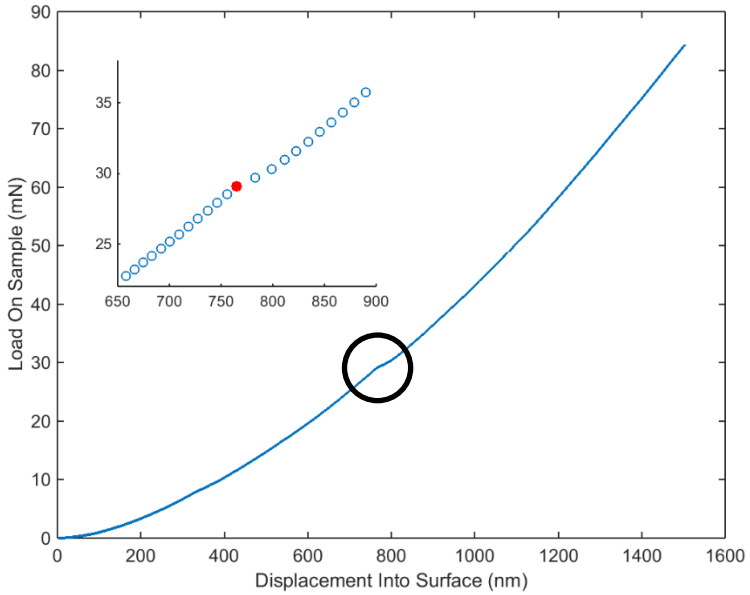


Figure 6-19: Load-displacement curve of an indent 2.9 µm from a grain boundary in ion-irradiated Fe-C, showing a small pop-in like kink just below 800 nm; Inset: Output from MATLAB code showing circled region with point of excursion highlighted in red.

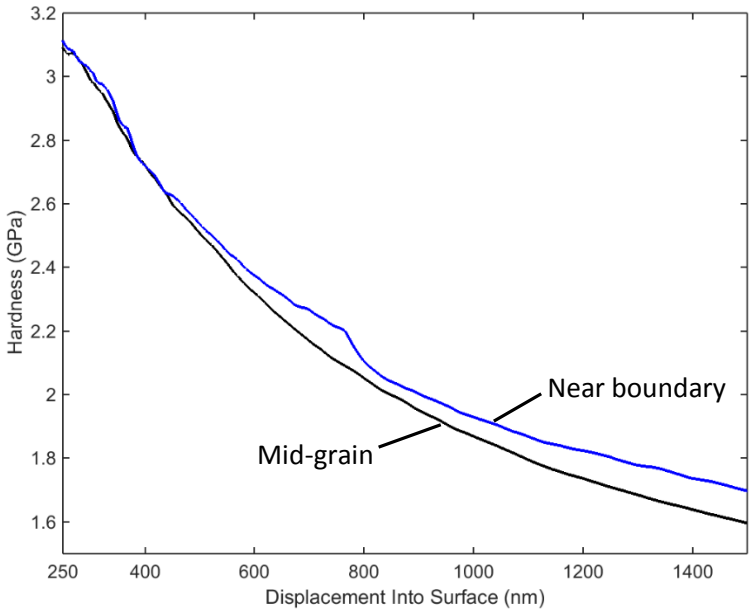


Figure 6-20: Hardness-displacement curve of the indent shown in Figure 6-19 (blue), with average mid-grain values in black.

Furthermore, in some cases, grain boundary pop-in-like behaviour is observed as less of a discrete event in which the indenter tip moves through the material unimpeded for some distance, but rather a gradual hardening and subsequent softening, or a subtle change of gradient in the load-displacement curve. Figure 6-21 shows the hardness-displacement data of 3 indents near the same boundary, along with average values taken mid-grain (black curve). Below 250 nm the hardness response is highly stochastic (potentially due to the nature of the ion damage at such depths) and therefore this region is omitted for the sake of clarity. In the first indent, 3.0 μm from the grain boundary (blue curve), the hardness response is similar to that of the mid-grain up until ~900 nm, from which point there is appreciable hardening. In the second indent, 1.7 μm from the boundary (green curve), hardening compared to the mid-grain response is seen from ~400 nm, peaking at ~750 nm, before gradually returning to mid-grain values by the full depth of the indent. Finally, in the third indent, 0.4 μm from the boundary (red curve), hardening relative to the mid-grain response is seen to peak at ~400 nm, before approaching mid-grain values at ~700 nm. This behaviour of rising and then falling hardness is similar to that seen in Figure 6-18, except that in the example of Figure 6-21, the amount of hardening is much lower, and the drop in hardness is less abrupt.

Such behaviour may indicate that, unlike in the unirradiated case, the grain boundary still provides some resistance to slip transfer, after the start of the reduction in hardness. Furthermore, after the dislocation barrier is overcome, resistance to dislocation motion is still likely to occur in the adjacent grain due to the ion damage present, resulting in the lack of a distinct displacement burst.

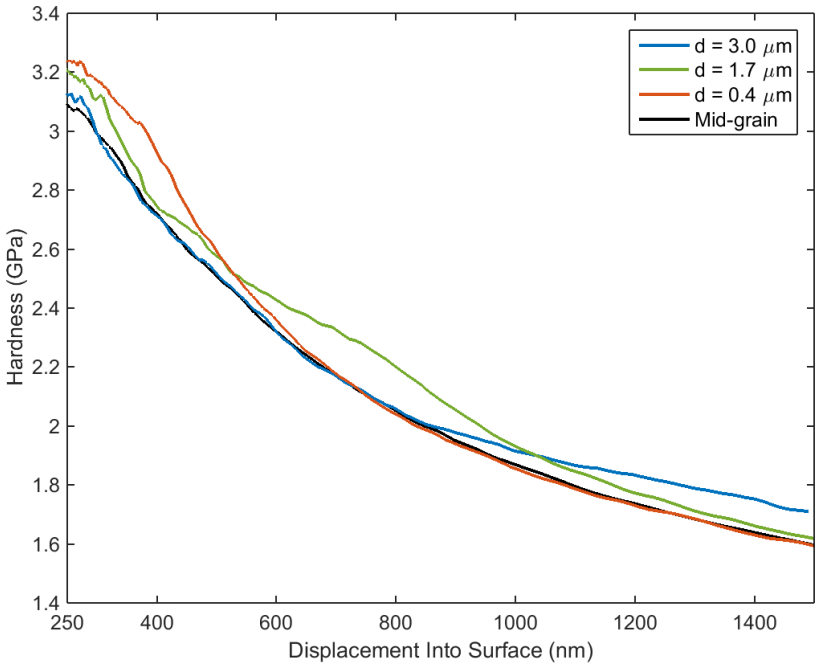


Figure 6-21: Hardness-displacement data of 3 indents near a grain boundary in ion-irradiated Fe-C, in addition to the average mid-grain values (black curve). The indent centre to grain boundary distances are shown in the legend.

An additional property of the irradiated material is that pop-in like behaviour is occasionally observed far away from grain boundaries, as seen in Figure 6-22, with $d = 17.5$ µm. According to equation (6-4), the size of the plastic zone at this point is roughly 3.4 µm, therefore the grain boundary cannot possibly influence the behaviour of the indent. It is possible that other features of the irradiated microstructure are also acting as barriers to dislocation motion, causing similar behaviour to that seen ordinarily near grain boundaries. It is also possible that this effect is caused by an unobserved subsurface grain boundary.

Such behaviour, in addition to the smaller average bursts, and the smoother transitions seen in Figure 6-21, make it much more difficult in the irradiated results to say with any degree of confidence if a particular indent is showing evidence of slip transfer, or stress build up due to a non-grain boundary feature of the microstructure.

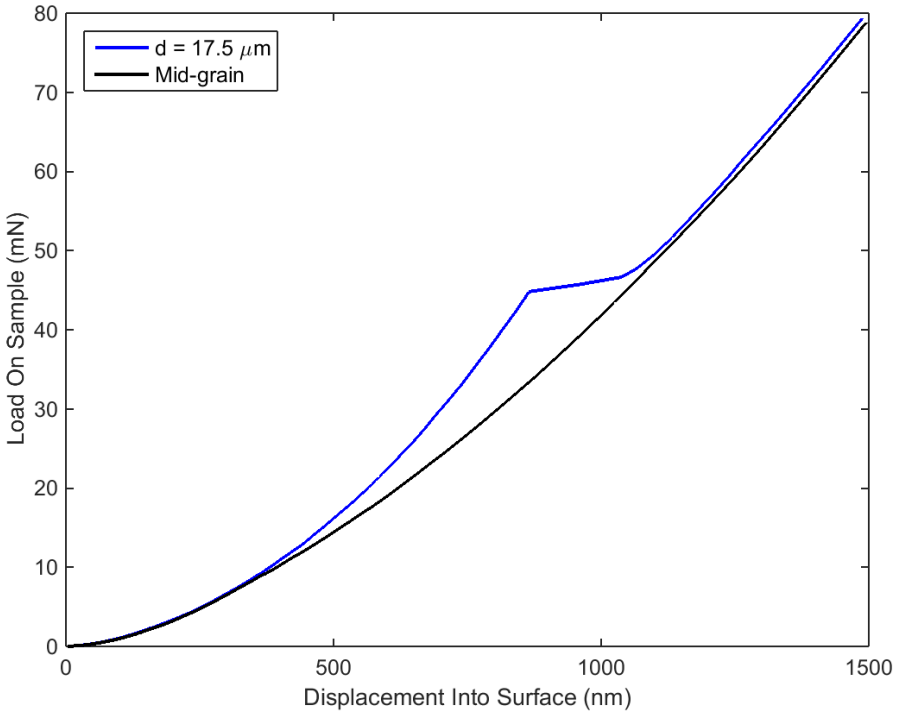


Figure 6-22: Load-displacement curve of an indent 17.5 µm from a grain boundary in ion-irradiated Fe-C (indent 1), along with an average mid-grain curve (indent 2).

#### *6.3.3.3 Hardness vs distance*

In order to better compare the hardness versus depth profiles observed in the unirradiated and ion-irradiated samples (for example the behaviour seen in Figure 6-21), CSM hardness values evaluated at selected depths can be plotted on the same graph as a function of grain boundary distance. Any depths over the range of the indent can be chosen for this, in the following examples depths are picked which best show the trends of hardness versus grain boundary distance, and highlight the comparisons between unirradiated and ion-irradiated samples most clearly.

Figure 6-23 shows such a plot of indents made at various distances from a selected grain boundary (the same set of results as observed in Figure 6-17 and Figure 6-18) in unirradiated Fe-C. Far away from the boundary (e.g. the points at ~15 µm and ~22 µm), the boundary has no effect on the mechanical response, and the difference in hardness at different depths is

caused purely by the indentation size effect. Nearer to the grain boundary, hardening is seen at increasingly smaller depths, e.g. at ~7.5 µm from the boundary hardening is first seen at 1400 nm indent depth, whereas at 5 µm, hardening is first seen at 900 nm indent depth. In the two indents closest to the boundary, pop-ins occur, at ~900 nm deep for the indent 2 µm from the boundary (red line in Figure 6-18), and ~350 nm deep for the indent at 0.8 µm (dotted line in Figure 6-18). At depths after the pop-in occurs, i.e. 1400 nm for the indent at 2 µm, and 460 nm for the indent at 0.8 µm, hardnesses return to values close to those seen at similar depths in indents far from the boundary (slightly higher for the closest indent). The plot also shows the greater increase in hardness as indents are made closer to the boundary (as seen in Figure 6-18).

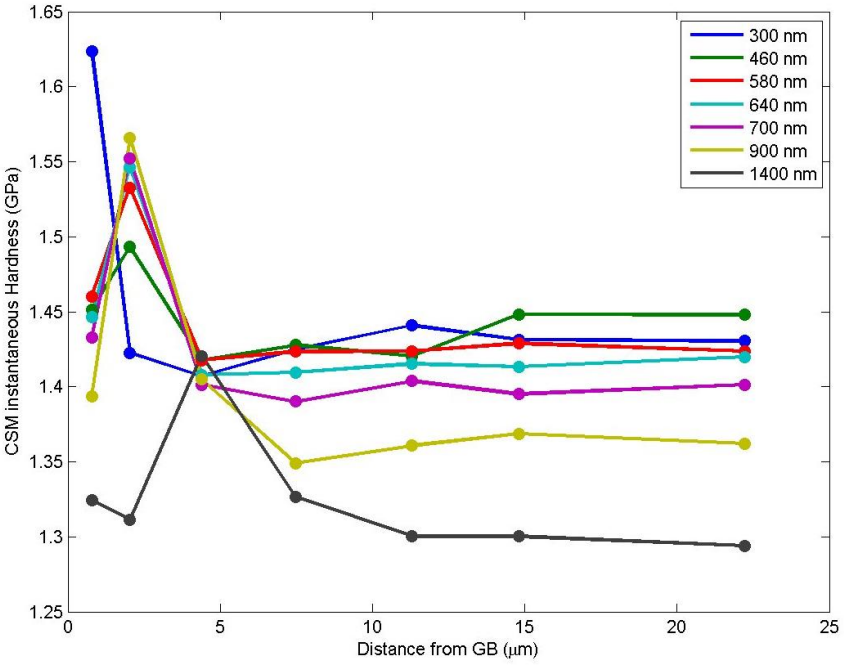


Figure 6-23: CSM Hardness evaluated at different indenter depths (key: top right) of indents made at various distances from the same grain boundary in unirradiated Fe-C (previously observed in Figure 6-17 and Figure 6-18).

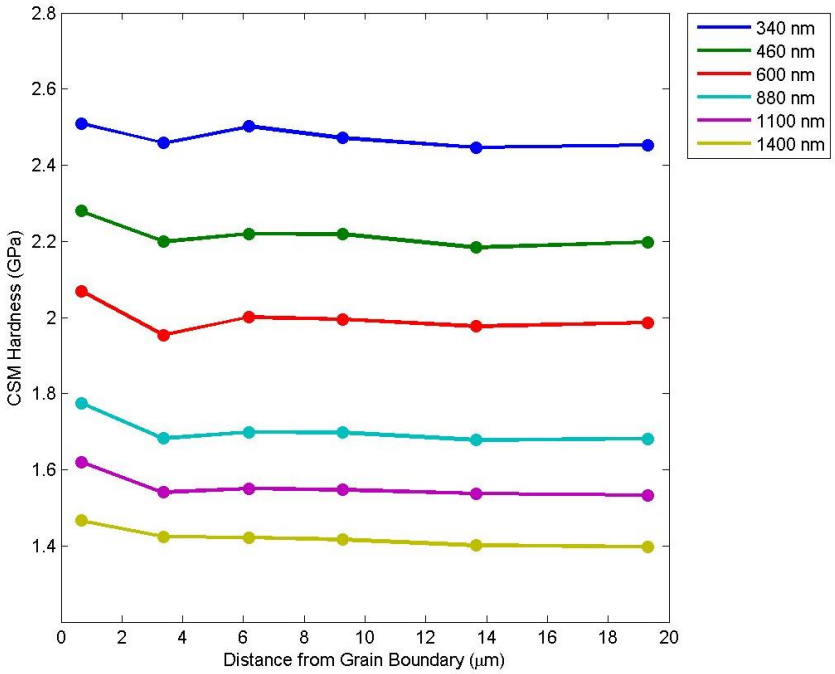


Figure 6-24: CSM Hardness evaluated at different indenter depths (see top right) of indents made at various distances from the same grain boundary in ion-irradiated Fe-C.

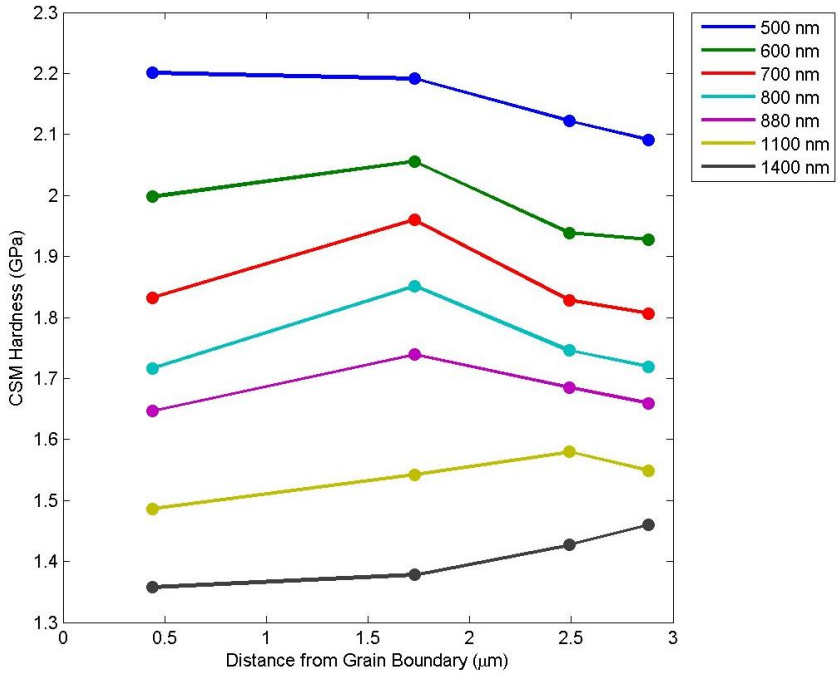


Figure 6-25: CSM Hardness evaluated at different indenter depths (see top right) of indents made at various distances from the same grain boundary in ion-irradiated Fe-C.

Figure 6-24 and Figure 6-25 show CSM hardness at various depths as a function of grain boundary distance for indents made near grain boundaries in ion-irradiated Fe-C. Due to the

ion-irradiation damage profile (see Figure 6-4), there is a much greater effect of indenter depth on hardness (see Figure 6-9, red curves), therefore the lines corresponding to different indenter depths are much more separated in hardness compared to those in Figure 6-23. The relative increase in hardness seen for indents near a grain boundary is much smaller compared to the unirradiated sample and also occurs closer to the boundary, with subtle changes in hardness seen in the two indents with d < 4 μm in Figure 6-24, and at similar grain boundary distances in Figure 6-25 (although the full trend with distance is not observed due to the limited range of distances probed). The reason for the grain boundary influence occurring over a smaller range could be due to the reduced size of the plastic zone surrounding the indenter (see section 6.3.2.3).

In Figure 6-24, the indent closest to the grain boundary is seen to experience increasing hardening compared to the other indents, with the peak increase occurring at an indenter depth of ~600 nm, and reducing at depths greater than this (suggesting that there may have been a relaxing of stress by slip transferring into the next grain).

Similarly in Figure 6-25 (showing results previously seen in Figure 6-21), there is a peak in hardness seen at increasingly shallower indenter depths as the indenter to grain boundary distance is reduced.

It is apparent from Figure 6-24 and Figure 6-25 that much of the effect of the grain boundary on the mechanical data is suppressed due to ion damage compared to the unirradiated sample. To investigate hardness versus distance trends in this sample more thoroughly, it would be desirable to make indents within a narrower range of $d$, closer to the boundary (due to the reduced plastic zone size). Such an experiment might be easier to perform by ion-

irradiating a bicrystal, and making a large number of indents in the proximity of the grain boundary, improving the statistics of any trends found.

#### 6.3.3.4 Stress Intensity Factor

It is useful to be able to provide a measure of an individual grain boundary's ability to resist slip transfer, in order that this can be compared between different boundary types and sample conditions (e.g. unirradiated vs ion-irradiation). As noted in section 6.1.3, the ratio $c/d$ (associated with grain boundary pop-ins) has previously been found to remain roughly constant for individual boundaries, but can vary between boundaries [163]. As the ability for a grain boundary to resist slip transfer should be independent of the distance at which a particular indent is made, it is sensible that the ratio $c/d$ should be included in such a measure.

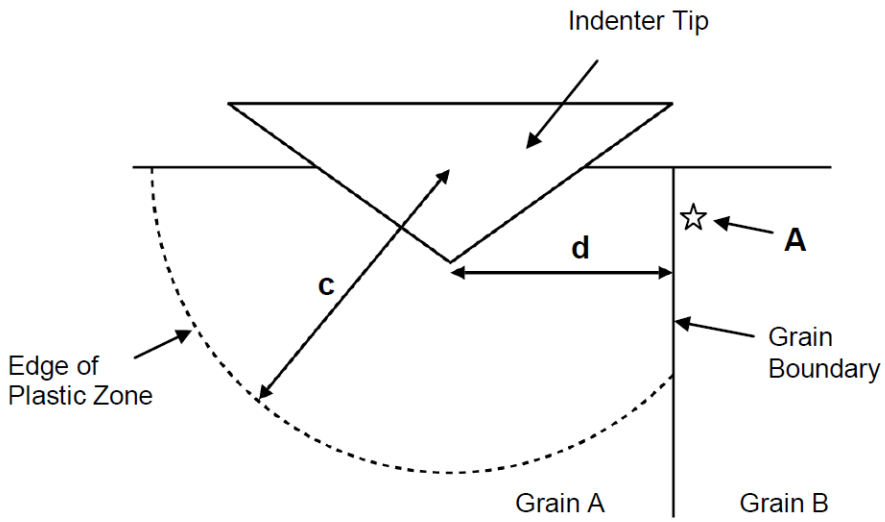


Figure 6-26: Schematic diagram showing the plastic zone of an indent impinging on a grain boundary, with a dislocation source **A** in the neighbouring grain (from [143]).

Wang and Ngan [163] and Randman [143,145] previously used Johnson's cavity model (see section 6.1.4) to estimate the critical stress intensity factor ($K_c$) for the emission of dislocations from a source in a neighbouring grain to the one being indented (see Figure

6-26). According to the model, the elastic stresses outside the plastic zone of the indenter are given by:

$$\sigma_r = -\frac{2\sigma_{ys}}{3}\left(\frac{c}{r}\right)^3, \qquad \sigma_\theta = \frac{\sigma_{ys}}{3}\left(\frac{c}{r}\right)^3, \tag{6-6}$$

$$\tau = \frac{\sigma_\theta - \sigma_r}{2} = \frac{\sigma_{ys}}{2}\left(\frac{c}{r}\right)^3$$

where $\sigma_r$ and $\sigma_\theta$ are the radial and hoop stresses, respectively, $r$ is the distance from the indent centre, and $\tau$ is the maximum shear stress. Adapting this to a situation in which the elastic zone impinges on a grain boundary, by setting $r = d$, gives a maximum shear stress at the boundary of:

$$\tau \approx \frac{\sigma_{ys}}{2}\left(\frac{c}{d}\right)^3 \tag{6-7}$$

If $r_0$ is the distance between the grain boundary and the source **A** in the next grain (see Figure 6-26), then the critical stress intensity factor, $K_c$, for dislocation emission is given by:

$$K_c = \tau\sqrt{r_0} \tag{6-8}$$

Combining equations (6-7) and (6-8), gives:

$$K_c \approx \frac{\sigma_{ys}\sqrt{r_0}}{2}\left(\frac{c}{d}\right)^3 \tag{6-9}$$

Both Wang and Ngan, and Randman give an approximation of $r_0 = 0.1$ μm, by considering the density of dislocation sources (equivalent to a dislocation density of $10^{14}$ $\mathrm{m}^{-2}$). It is expected that ion-irradiating the material will introduce many additional dislocation sources, however the exact number of these is difficult to determine. The yield stress value in

equation (6-9) can be determined from CSM hardness values using Tabor's relation (as mentioned in section 6.3.2.3). Given that $r_0$ is not known with any degree of accuracy for either the unirradiated or ion-irradiated material (and furthermore it will vary along the boundary), in addition to the invalid assumption in Johnson's cavity model of a completely isotropic material [143], the calculated value of $K_c$ will be useful only as an approximation, rather than an absolute value. Another error is introduced by using hardness values evaluated between 50nm and 250nm, at which depths the indentation size effect still influences the results. However, as these are systematic errors in the analysis, it should still be possible to observe a general trend of how this parameter varies with various factors, e.g. grain boundary misorientation.

Figure 6-27 shows $K_c$ for indents causing grain boundary pop-ins in both the unirradiated and ion-irradiated samples (solid circles, blue and red respectively), along with maximum values of $K_c$ for indents in which pop-ins were not seen (open circles). Grain boundaries in the ion-irradiated Fe-C appear to offer decreased resistance to slip transfer as compared to those in the unirradiated Fe-C. According to equation (6-9), $K_c$ is at first glance proportional to $\sigma_{ys}$, which is expected to increase due to irradiation, however $c \propto 1/\sqrt{\sigma_{ys}}$ via equation (6-4), which inserted into equation (6-9) gives $K_c \propto 1/\sqrt{\sigma_{ys}}$. Furthermore, $r_0$ is expected to decrease with irradiation, as the density of sources increases, therefore values of $K_c$ for indents in the ion-irradiated sample in Figure 6-27 are likely to be overestimated.

In the irradiated case, many indents without pop-ins have values of $K_c$ greater than in indents with pop-ins, and also at values which would be expected to cause slip transfer in the unirradiated material. It is possible that in some cases this is due to the effect of the

irradiation making the detection of slip transfer difficult through an obvious pop-in (see section 6.3.3.2).

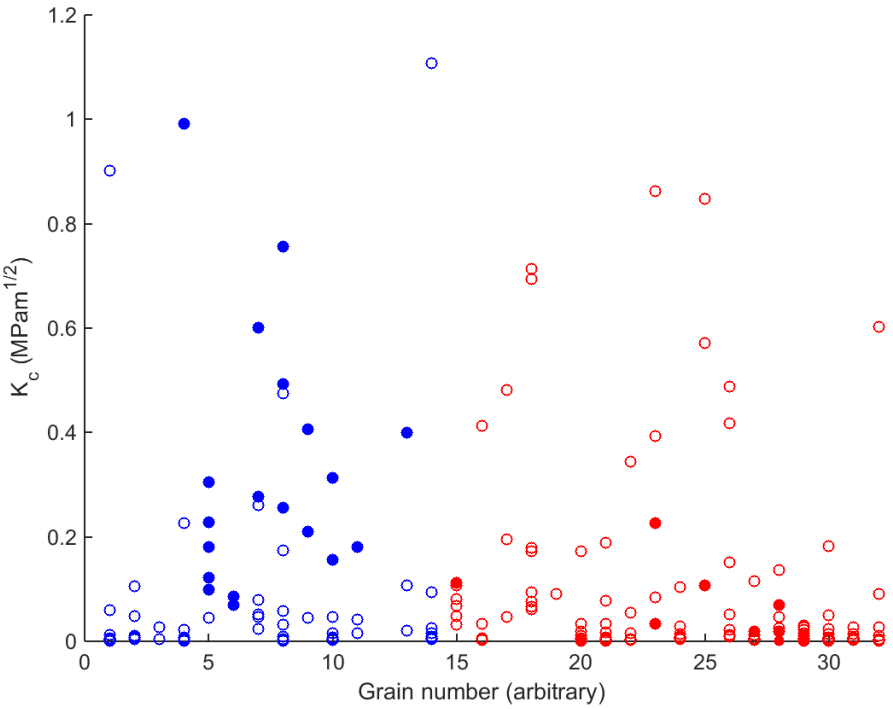


Figure 6-27: $K_c$ calculated for indents in the unirradiated Fe-C (blue) and ion-irradiated Fe-C (red). Solid circles denote indents with pop-in, whereas open circles denote indents without pop-in.

To study the relationship between $K_c$ and the type of grain boundary, a parameter which measures the important aspects of grain boundary geometry must be used. One of the simplest is the disorientation angle (previously used by Randman [143]), which measures the minimum angle through which one grain must be rotated in order to be in crystallographic alignment with its neighbouring grain. This can be simply calculated from measurements of orientation obtained by EBSD on each side of the grain boundary being considered.

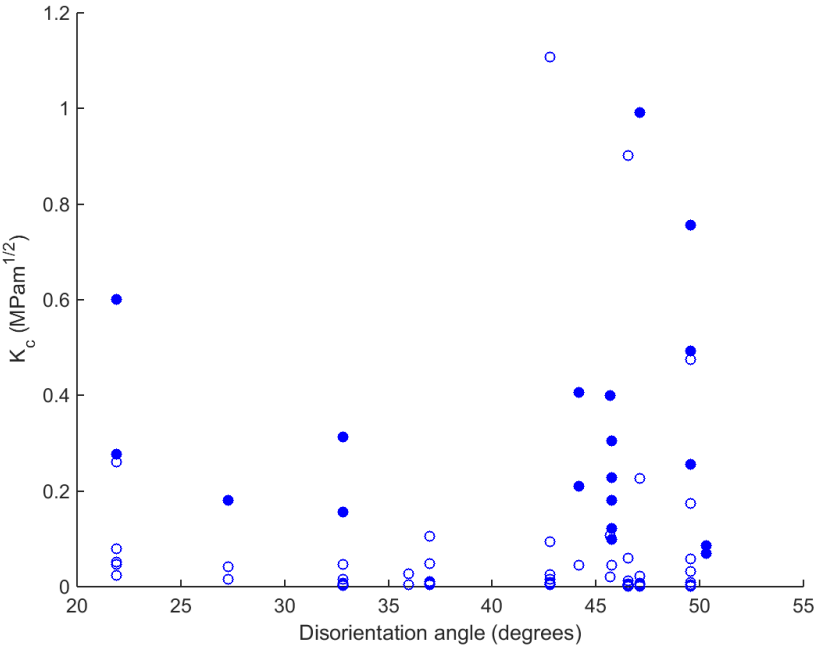


Figure 6-28: $K_c$ vs disorientation angle for unirradiated Fe-C (solid circles are indents with pop-in, open circles without pop-in).

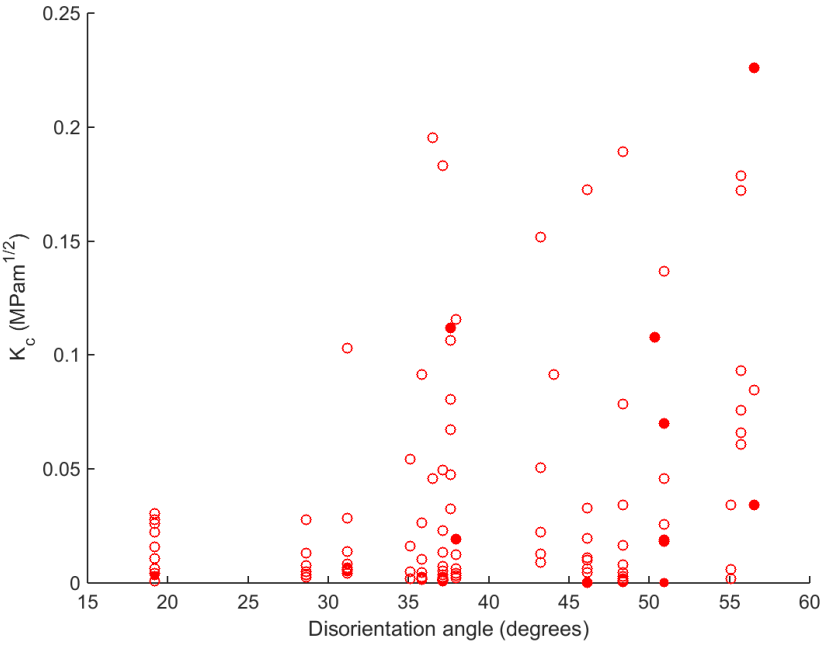


Figure 6-29: $K_c$ vs disorientation angle for ion-irradiated Fe-C (solid circles are indents with pop-in, open circles without pop-in).

Figure 6-28 and Figure 6-29 show $K_c$ for indents with and without pop-in, against disorientation angle for the unirradiated and ion-irradiated samples, respectively. A weak trend of increasing $K_c$ with increasing disorientation angle is seen in both cases. In Figure

6-29, several indents without pop-ins had $K_c$ values greater than $0.25\ \mathrm{MPam}^{1/2}$, however the range in $K_c$ plotted has been restricted in order to better see the trend for the indents with pop-ins.

Although disorientation angle is beneficial as an easily determinable measure of relative grain alignment, it fails to take into account the relevant slip systems being used on each side of the grain boundary. This limits its usefulness, as it is possible that neighbouring grains might have a large disorientation angle, whilst having well aligned slip systems. A better measure is $m$', previously mentioned in section 6.1.3 (see equation (6-3)). For a particular boundary, this parameter was calculated for all pairs of slip directions and slip planes on either side of the boundary, with the maximum value being used. As the material system being investigated is bcc, slip is assumed to be taking place on {110} or {112} planes, in the <111> direction. Figure 6-30 and Figure 6-31 show $K_c$ plotted against $m$' for the unirradiated and ion-irradiated samples, respectively. As the number of available slip systems in bcc iron is relatively large, all values of $m$' are found to be close to 1. Ignoring cases without pop-in, for both figures there is a general trend of decreasing $K_c$ with increasing $m$', although this happens within a broad range of values as opposed to a straightforward linear relationship.

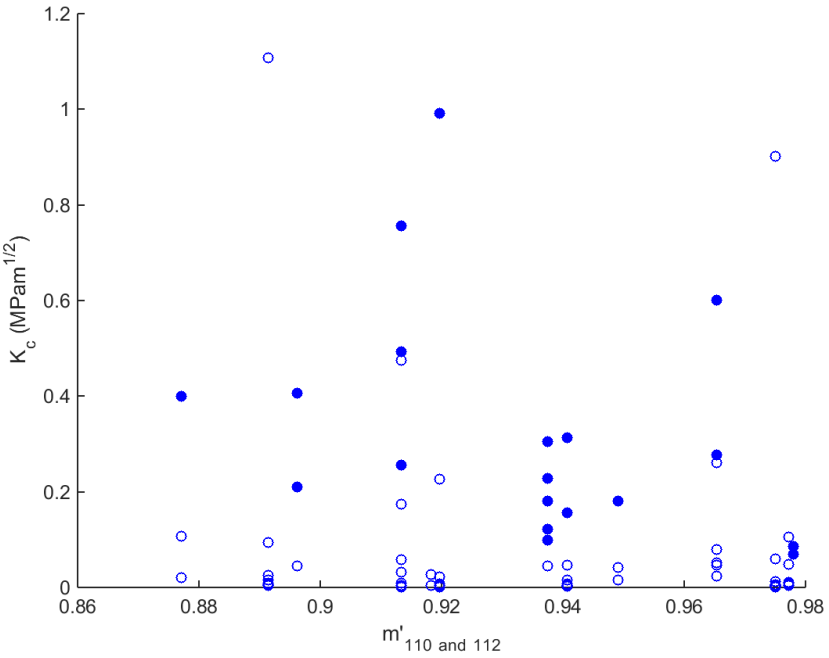


Figure 6-30: $K_c$ vs $m'$ for unirradiated Fe-C (with slip on {110} and {112} planes, in the <111> direction).

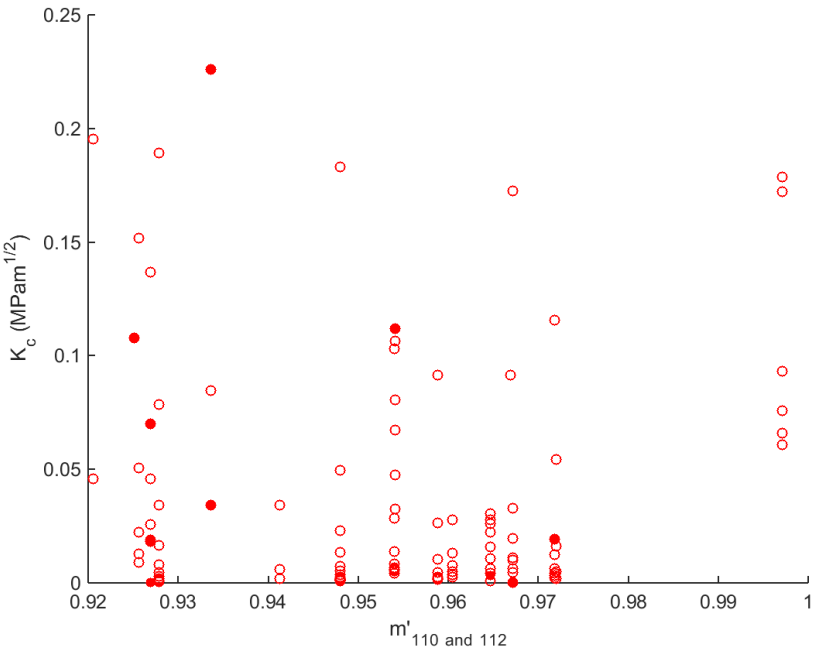


Figure 6-31: $K_c$ vs $m'$ for ion-irradiated Fe-C (with slip on {110} and {112} planes, in the <111> direction).

## 6.4 Conclusion

In this chapter, nanoindentation has been conducted near grain boundaries in unirradiated and ion-irradiated Fe-C, in order to study the influence of grain boundaries on mechanical properties in irradiated materials. As in other studies on polycrystalline materials [142,143,145,163], pop-in events were observed when indenting sufficiently closely to grain boundaries, at loads significantly greater than those seen at the elastic-plastic transition (see section 2.1.2). Such pop-ins were detected using an automated MATLAB code, and associated with characteristic hardening prior to the event. This hardening was linked to the proximity of the indent to the grain boundary, with a greater amount seen during indents closer to the boundary.

In the ion-irradiated material, fewer pop-in events were detected, with 8 % of indents with the indenter face closest to the boundary showing pop-in behaviour, as opposed to 32 % in the unirradiated material. The median displacement burst size was also smaller, at 15 nm in the ion-irradiated case compared to 30 nm in the unirradiated case. The irradiation resulted in behaviour near some boundaries whereby slip transfer was inferred via a change in hardening with depth (Figure 6-21), without a distinct dislocation burst being observed.

This difference in behaviour between the unirradiated and ion-irradiated samples was further inspected by plotting the CSM hardness at various indenter depths against the indent centre to grain boundary distance. In the unirradiated case, the influence of the grain boundary on the hardness was clearly observed, with sharp peaks in hardness seen at decreasing depths with decreasing grain boundary distances (Figure 6-23). In contrast, subtler changes in hardness were observed in the ion-irradiated sample, and also at closer proximity to the grain boundaries (Figure 6-24 and Figure 6-25). Due to the smaller plastic

zone emanating from the indenter tip in the irradiated material, predicted by equation (6-4), it would be desirable to make indents at a closer range of indent centre-grain boundary distances to better examine slip transfer in such materials. Furthermore, in order to better understand the interaction between an indenter's plastic zone and grain boundaries in the ion-irradiated material, it would be advantageous to directly measure the plastic zone size around the indents, using HR-EBSD and AFM, as in Chapter 4.

As a measure of the resistance of grain boundaries to slip transfer, the critical stress intensity factor for each boundary, $K_c$, was estimated in both samples. A comparison of the values calculated in each case (Figure 6-27) shows that grain boundaries appear to be less resistant to slip transfer in irradiated samples. Furthermore, some indents in the irradiated sample for which pop-ins are not seen have greater values of $K_c$ than those for which pop-ins do occur, suggesting that slip transfer may have happened but without an obvious pop-in event.

$K_c$ was found to be roughly proportional to the disorientation angle between grains and inversely proportional to $m$' for both samples, but with very weak trends seen for both. A limitation of using $m$' is that only the best aligned slip systems are used, whereas in reality multiple slip systems may contribute to the slip transfer phenomenon. It may be that using an average $m$' of some of the most likely slip systems, with suitable weightings attached, might provide a better relationship than the ones seen in Figure 6-30 and Figure 6-31.

A possible reason for the decreased resistance of grain boundaries in ion-irradiated materials is that the increased dislocation source density means that the average distance between the grain boundary and a source in the adjacent grain is likely to be lower. In addition to this, when a source in the adjacent grain operates, the presence of many small dislocation loops

means that newly generated dislocations are unable to move through the crystal unimpeded. This could lead to the smaller observed burst sizes, and also the behaviour seen in Figure 6-21, as the stress built up at the grain boundary cannot be relieved immediately.

Studies of FIB-machined specimens made at grain boundaries, in combination with post-testTEM and modelling, have the potential to provide more detailed information concerning the exact nature of the deformation occurring [70]. However, nanoindentation studies such as the one in this chapter can provide complementary information, and have the advantage that results can be obtained much more rapidly, allowing a greater number of boundaries to be tested. Future work on materials of greater direct relevance to nuclear applications (e.g. RAFM steels, tungsten) could help elucidate the role that grain boundaries play in these materials under real world reactor conditions.

# 7 Investigating the Size and Orientation Dependence of Micro-Cantilevers

## 7.1 Introduction

In recent years, the use of micromechanical testing to study ion-irradiated specimens has grown substantially [35,60,77]. For informing materials usage in future nuclear contexts, such tests have a great advantage over macro-scale tests of neutron irradiated specimens, due to their low cost, speed, and lack of radiological hazard. However, as described in chapter 2, the nature of plastic behaviour in such specimens is fundamentally different from macro-scale tests, due to the effect of the small probe size on dislocation activity. To be able to extract meaningful mechanical properties data from such small scale tests, it is important that the relationship between specimen size and plastic behaviour is understood.

In combination with EBSD, micromechanical testing also allows mechanical properties in particular orientations to be studied, for example elastic modulus (chapter 5) and critical resolved shear stress [39]. As micromechanical tests on ion-irradiated specimens can take place within single grains of large grained material (e.g. tungsten), such anisotropic effects can play an important role in the results obtained. Furthermore, investigating particular slip systems with small scale tests can play an important role in determining their contribution to the overall bulk properties of materials [72].

In this chapter tests on different cantilever sizes and orientations will be used to investigate these effects. As with chapters 4 – 6, iron will be used due to its importance as the basis of radiation resistant steels of relevance to future nuclear fusion reactors.

## 7.2 Method

Micro-cantilevers were milled in two different crystal orientations, such that a different number of slip systems could be activated in each case. One orientation was set up so that many slip systems would be operative, whereas the other was set up so that dislocation activity would take place on only one or two slip systems (see below). For the 'multiple slip' orientation, the chosen orientation (Figure 7-1) was with the beam aligned to a <100> direction, with the surface normal direction also <100>. In this configuration, 8 of the possible 12 <111> $\{1\bar{1}0\}$ slip systems are active, with each one having a Schmid factor of 0.41 (whilst the Schmid factor on the other 4 slip systems is 0).

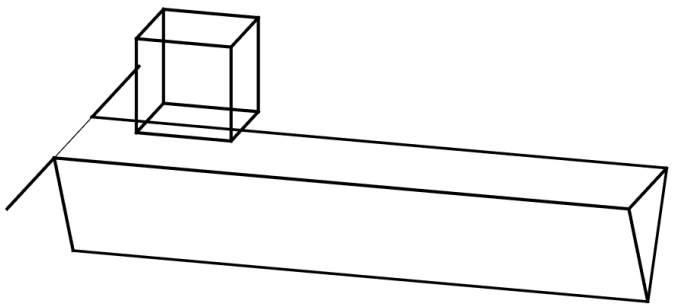

Figure 7-1: Schematic diagram of a micro-cantilever with a unit cube indicating the desired orientation (<100> normal direction, beam along <100> direction).

The 'single slip' orientation was chosen such that the most active slip system in the beam was in a plane strain state, i.e. with plasticity confined to the plane of bending, shown by the dotted line in Figure 7-2 (top). Furthermore, this slip system was set up to have a Schmid factor of 0.5, i.e. with the $(1\bar{1}0)$ slip plane normal and the $[111]$ slip direction both at 45° to the beam axis and in the plane of bending (Figure 7-2). This orientation gives a surface normal direction of $[89\,\bar{9}\,40]$, i.e. close to $[201]$. The plane strain configuration was partially motivated by a planned experiment in which foils were to be extracted from the beam along this plane after testing, and further investigated in the TEM. However, this orientation also

allows for the possibility of comparisons to be made with 2D modelling which is conducted with plane strain assumptions.

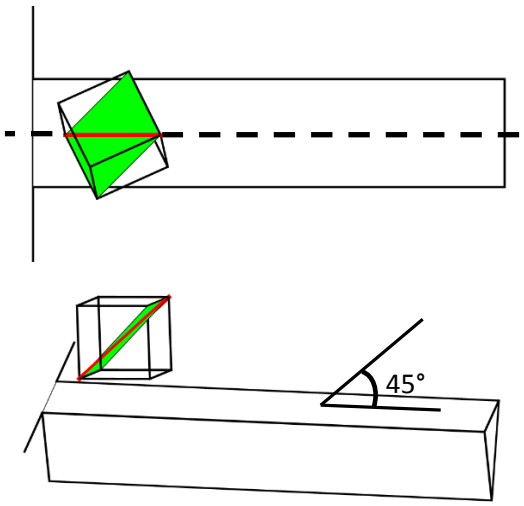


Figure 7-2: Schematic diagram of a micro-cantilever from above (top) and the side (bottom), with unit cubes indicating the desired slip plane and slip direction for the 'single slip' orientation.

Despite this desired 'single slip' state, due to many slip systems being available in bcc, another slip system with a Schmid factor of 0.47 is also present with this setup (Figure 7-3). However, Table 7-1 shows that other slip systems are less well aligned, therefore there is a significant difference between the number of slip systems available in the 'multiple slip' and 'single slip' orientations.

| Slip direction | $[111]$ | | | $[11\bar{1}]$ | | | $[\bar{1}11]$ | | | $[1\bar{1}1]$ | | |
|---|---|---|---|---|---|---|---|---|---|---|---|---|
| Slip plane | $(10\bar{1})$ | $(1\bar{1}0)$ | $(01\bar{1})$ | $(1\bar{1}0)$ | $(011)$ | $(101)$ | $(101)$ | $(110)$ | $(01\bar{1})$ | $(110)$ | $(011)$ | $(10\bar{1})$ |
| Schmid factor | 0.18 | 0.29 | **0.47** | 0.25 | **0.50** | 0.25 | 0.12 | 0.32 | 0.20 | 0.22 | 0.17 | 0.05 |

Table 7-1: Schmid factors and corresponding slip directions and slip planes for the orientation shown in Figure 7-2.

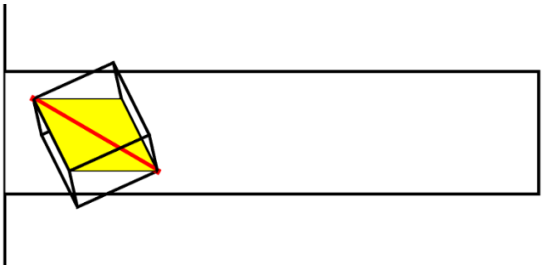

Figure 7-3: Schematic diagram of a micro-cantilever in the same orientation as shown in Figure 7-2, showing a slip system with a Schmid factor of 0.47.

Micro-cantilevers were milled within single grains of an iron polycrystal, thus enabling pseudo-single crystal experiments to be performed (see chapter 5). The material used, supplied by EFDA, has high purity as previously described in section 6.2.1 (see Table 6-1, 1st row). A ~1 mm thick semicircular slice was ground using SiC papers to 4000 grit, polished to a 20 nm colloidal silica finish, and then mounted on a stub with silver dag.

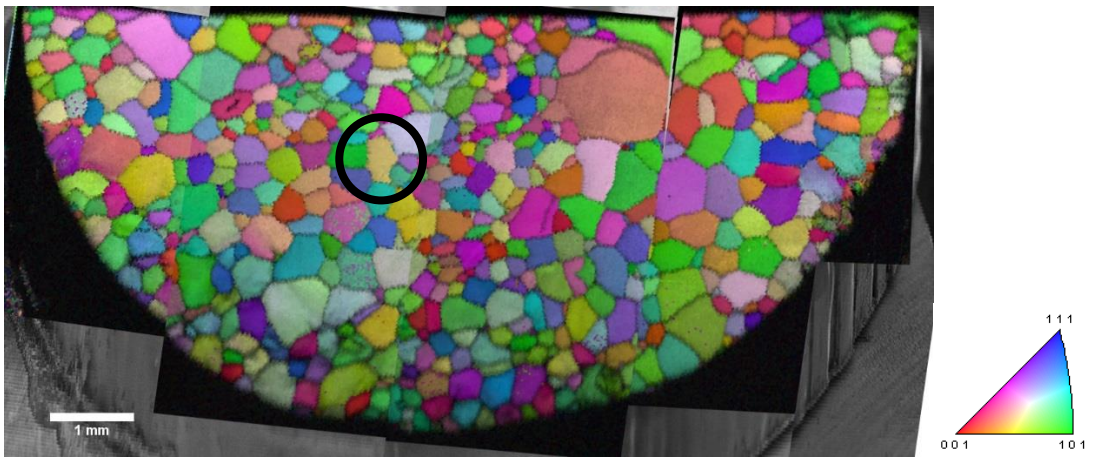


Figure 7-4: Normal direction IPF map (image quality overlaid in grayscale) stitched together from five low resolution EBSD scans. The circled grain is close to the desired orientation show in Figure 7-2 and Figure 7-3 (see Figure 7-5).

Low resolution EBSD scans (step size = 25 µm) were made of the sample surface, and then stitched together in order to locate grains with the orientations described above (Figure 7-4). With the grain selected (Figure 7-5, left), a procedure previously described in section 5.2.2 was used, whereby a series of lines were milled in a fan shape with the FIB, and then re-scanned with EBSD. This is shown in Figure 7-5 (right), with the line closest to the desired

beam direction (i.e. most aligned with the <111> body diagonal shown in Figure 7-2 in the case of the 'single slip' orientation) used as a datum for subsequent milling.

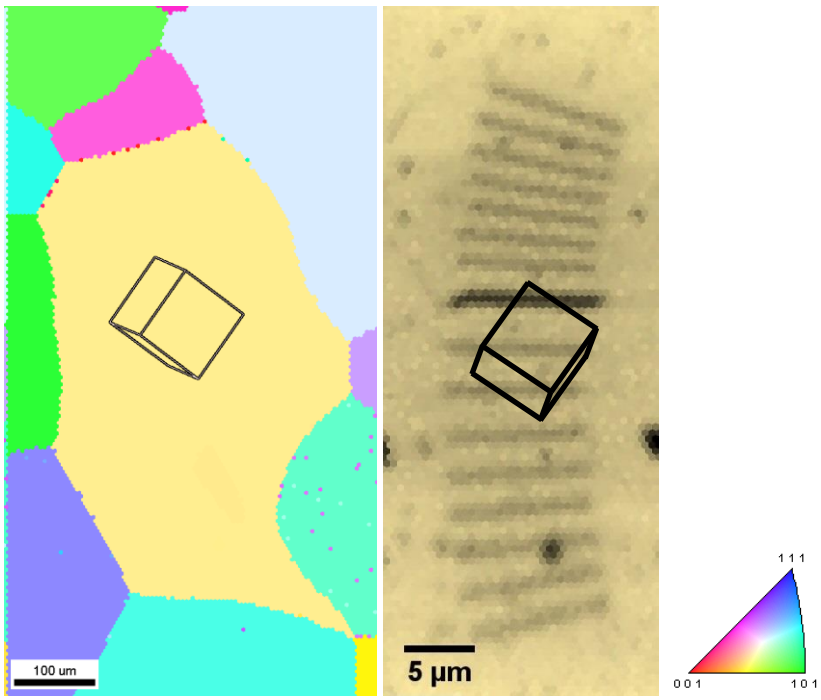


Figure 7-5: Normal direction IPF map of the grain circled in Figure 7-4 (left), and of FIB milled lines within this grain to aid with beam alignment (with image quality in grayscale, right).

Equilateral triangle cross section micro-cantilevers were milled in one grain close to the 'multiple slip' orientation, and one grain close to the 'single slip' orientation. The normal direction of the 'multiple slip' grain chosen was $[0.040\ 0.068\ 0.997]$, 4.5° from the desired orientation, whereas the normal direction of the 'single slip' grain was $[-0.339\ 0.081\ 0.937]$, 4.3° from the desired orientation. In the 'single slip' grain, to study the effect of size on plastic properties, three different beam sizes were used, with widths of 1 µm, 3 µm, and 5 µm, having lengths of 6 µm, 18 µm, and 30 µm respectively to maintain a similar aspect ratio. In the 'multiple slip' grain, only one beam size was used, with 5 µm width and 30 µm length.

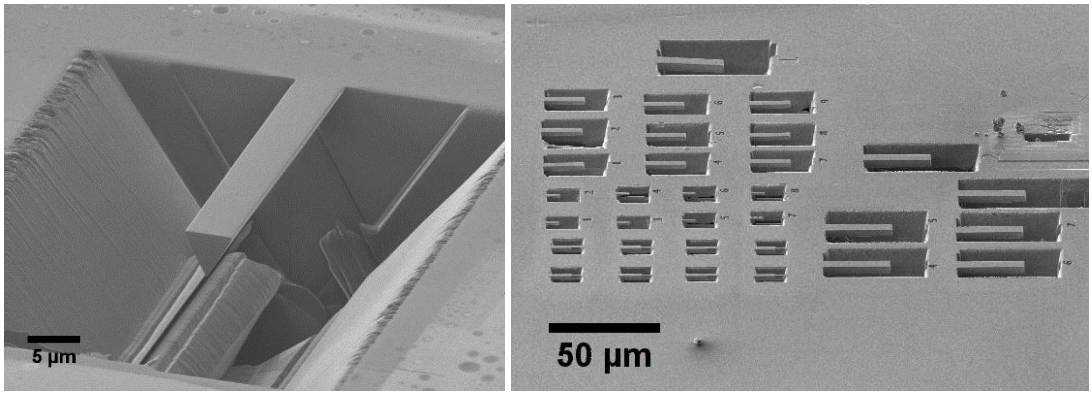


Figure 7-6: SEM image of a finished 30 µm by 5 µm micro-cantilever (left); SEM image of an array of differently sized micro-cantilevers within a single grain (right).

The standard fabrication method for micro-cantilevers was used, as described in section 2.2.2. Additionally, for the 1 µm wide beams, the method described in section 3.1.3 of milling lines at a set distance away from the fixed end so as to avoid having to directly scan the beams was used. An example of a finished beam, and an array of differently sized beams is shown in Figure 7-6. After milling a sample beam in each grain, a fine EBSD scan (step size = 1 µm) of the beam was performed to check that the orientation of the beam was correct (see Figure 7-7). If necessary, the angle of further beams in the grain was adjusted such that the desired orientations were obtained. After milling, the dimensions of each beam were measured in the SEM, before testing was conducted in the nanoindenter.

Micro-cantilevers were deflected in the G200, at 3 µm from their free ends for the 30 µm long beams, and at an identical aspect ratio for the other beam sizes. A constant displacement rate of 10 nm/s was used for loading. After testing, the beams were inspected in the SEM, in order to locate indent impressions on the surface, and to look for signs of slip traces and evidence of plasticity.

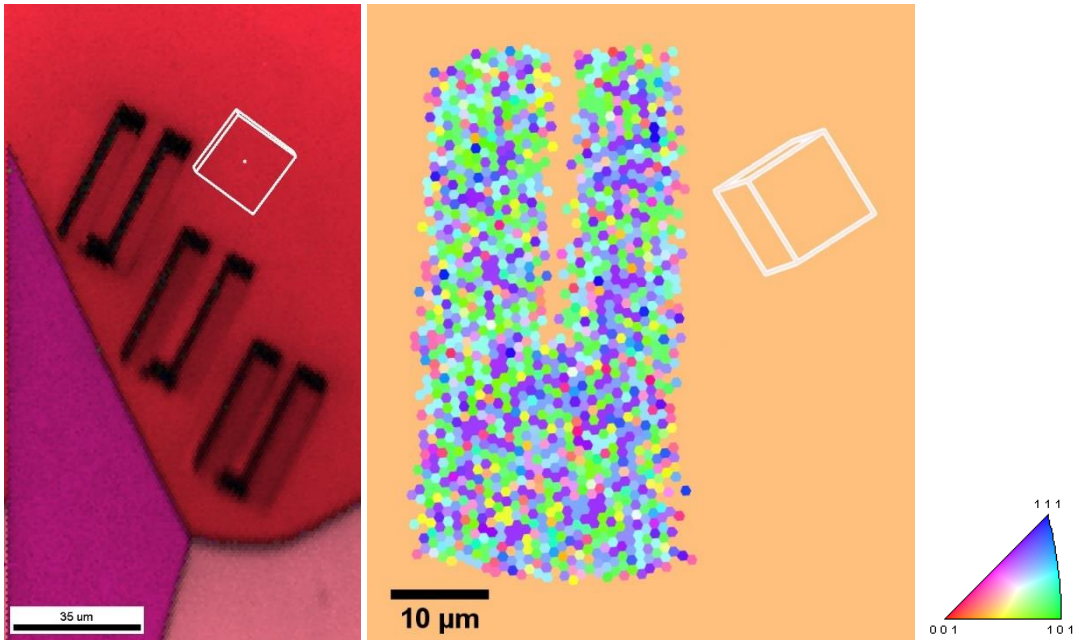


Figure 7-7: Normal direction IPF maps of cantilevers milled in the 'multiple slip' orientation (with image quality in grayscale, left), and the 'single slip' orientation (right), both with unit cube overlays.

## 7.3 Micro-Cantilever Size Effects

Figure 7-8 shows load-displacement curves for the three micro-cantilever sizes in the 'single slip' orientation. The behaviour in the plastic part of the curves is characteristically jerky, with load drops appearing frequently. There is also a large degree of scatter in the plastic response during loading, with some cantilevers showing a slight hardening, whilst others reach a load plateau or soften slightly.

In order to be able to make useful comparisons between the different beams sizes, load and displacement were converted into maximum stress and maximum strain, using simple beam theory. The location of these maxima in micro-cantilevers is the point at which the bottom apex meets the built-in end.

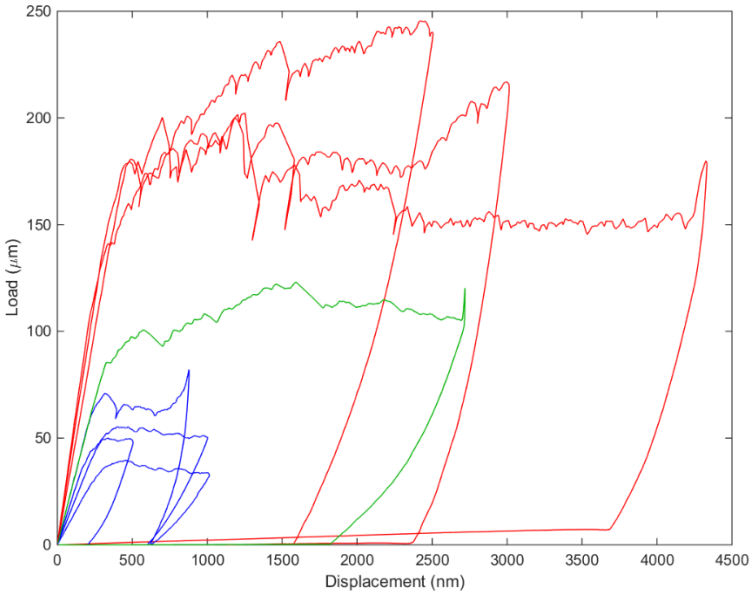


Figure 7-8: Load-displacement curves of micro-cantilevers in the 'single slip' orientation, with widths of 5 µm (red), 3 µm (green), and 1 µm (blue).

In simple beam theory, the flexure formula gives the stress ($\sigma$) in a beam due to the application of a bending moment ($M$) as:

$$\sigma = -\frac{My}{I} \tag{7-1}$$

where $y$ is the distance from the neutral axis in the plane of bending, and $I$ is the second moment of area, previously defined in equation (5-20). For an equilateral triangle cross section cantilever, the neutral axis is 2/3$^{rds}$ of the height of the beam ($h$) from the bottom apex, therefore the maximum stress occurs at $y = \frac{2}{3}h$, giving:

$$\sigma_{max} = \frac{2Mh}{3I} \tag{7-2}$$

With a bending moment generated by an applied load $P$ at a distance $L$ from the fixed end, substituting $M = PL$ and $I$ from equation (5-20) gives:

$$\sigma_{max} = \frac{24PL}{wh^2} \tag{7-3}$$

where $w$ is the beam width. The maximum strain can be obtained by substituting equations (7-3) and (5-19) into Hooke's law (equation (5-1)), giving:

$$\varepsilon_{max} = \frac{2h\delta}{L^2} \tag{7-4}$$

where $\delta$ is the displacement at the loading position which causes bending in the beam. Using these equations, and measurements of the beam dimensions in the SEM, Figure 7-9 shows the maximum stress-maximum strain curves of the 'single slip' data shown in Figure 7-8. The size effect is readily apparent, with the flow stress increasing from ~1 GPa to ~3-4 GPa when the beam width is decreased from 5 µm to 1 µm. The sudden increases in load seen near the end of loading for several beams is caused by the indenter tip touching the side of the trench, or the beam hitting the bottom of the trench, at which point the beam is unloaded.

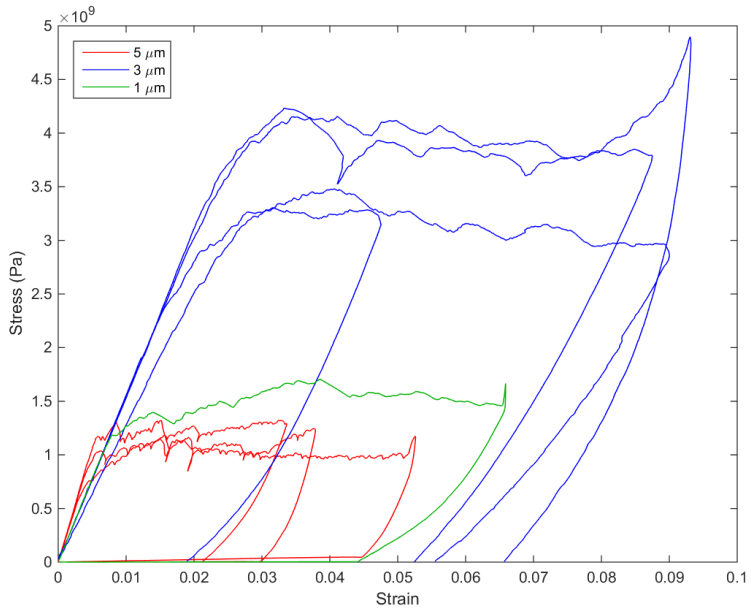


Figure 7-9: Maximum stress-maximum strain curves of micro-cantilevers in the 'single slip' orientation, with widths of 5 µm (red), 3 µm (green), and 1 µm (blue).

To further investigate the form of the relationship between flow stress and beam size, values of stress were extracted at several different strains, and different fits applied to them. Figure 7-10 shows the flow stress evaluated at 3 % strain, as a function of beam width. In keeping with previous small scale mechanics studies (e.g. micro-pillar testing [47]) in which log-log plots are commonly used, one way to rationalise the relationship between flow stress and specimen size is by using a power law of the form:

$$\sigma = Aw^n \tag{7-5}$$

where $A$ and $n$ are fitting parameters. For the data in Figure 7-10, $A$ was found through fitting to be $3.62$ whilst $n$ was equal to $-0.75$. In contrast, for the data shown in Figure 7-11, with flow stresses evaluated at 1.5 % strain, values of $A = 2.26$ and $n = -0.43$ were found. However, although widely used in the field of micromechanics, equation (7-5) implies that the flow stress of large scale tests should tend to zero. As this is clearly unphysical, an alternative approach can be used in which a constant term is included, such that flow stress as a function of beam width is given by:

$$\sigma = Aw^n + \sigma_0 \tag{7-6}$$

where $\sigma_0$ is the additional fitting parameter, corresponding to the bulk yield strength. Previously both experimental and theoretical studies have found that an exponent of *n = -1* fits data to this expression well [37,72,74,175,176]. Such an exponent has been physically justified in terms of back stresses from soft pile-ups at the neutral axis acting on dislocation sources [37,176], and the limited number of sources in sufficiently small specimens [37,176], in addition to the space available for dislocation source operation [74,175]. Following from

these studies, and to simplify the fitting of the data in this experiment, $n$ in equation (7-6) was forced to be equal to $-1$. Fitting parameters of $A = 3.20$ and $\sigma_0 = 0.45\ GPa$ were found for strains of 3 %, and $A = 1.42$ and $\sigma_0 = 0.86\ GPa$ were found for strains of 1.5 %. Figure 7-10 and Figure 7-11 show lines of fit using these parameters.

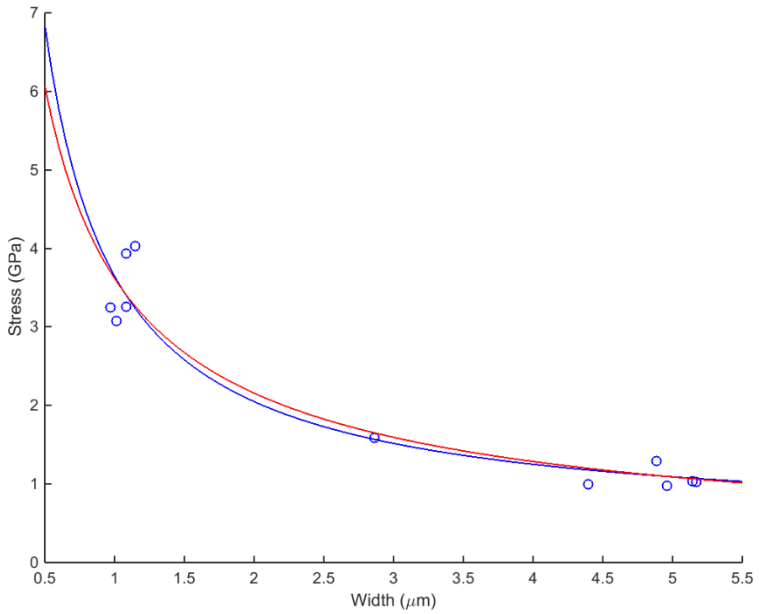


Figure 7-10: Flow stress at 3 % strain (GPa) as a function of beam width (µm) for beams in the 'single slip' orientation, fitted to a simple power law, $\sigma = Aw^n$ (red), and a constant plus one over fit, $\sigma = Aw^{-1} + \sigma_0$ (blue).

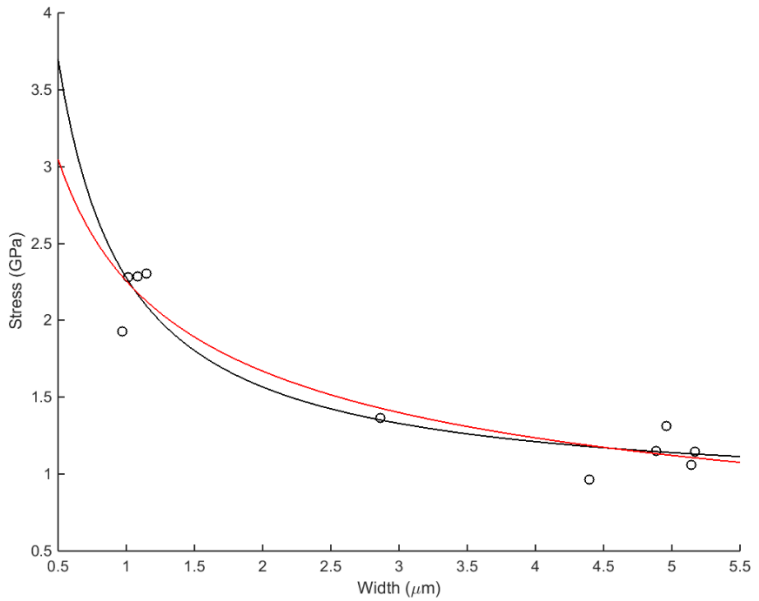


Figure 7-11: Flow stress at 1.5 % strain (GPa) as a function of beam width (µm) for beams in the 'single slip' orientation, fitted to a simple power law, $\sigma = Aw^n$ (red), and a constant plus one over fit, $\sigma = Aw^{-1} + \sigma_0$ (black).

Given that $\sigma_0$ represents the bulk strength, it should be expected to remain constant between the fits at both strains, whereas the above numbers appear to indicate the $\sigma_0$ roughly halves when going from 1.5 % strain to 3 % strain. However, given that the data points cover a relatively small range of beam widths there is a large degree of uncertainty in the fitting procedure. The 95 % confidence interval of the fitted bulk strength is $-0.07 < \sigma_0 < 0.97$ at 3 % strain and $0.62 < \sigma_0 < 1.01$ at 1.5 % strain. Clearly the lower limit at 3 % strain is unphysical, however the large degree of overlap between the two ranges indicates that there is consistency between both fits. Conversely, the 95 % confidence intervals for the other fitting parameter, which relates to the degree of the size effect, are $2.41 < \mathrm{A} < 3.98$ at 3 % strain and $1.07 < \mathrm{A} < 1.77$ at 1.5 % strain, showing the clear dependence of this parameter on the level of strain. To visual this, Figure 7-12 shows the 1.5 % and 3 % strain data points, with lines of fit for each using both the upper and lower confidence bounds. By inspection, the 1.5 % lines of fit (red) appear to have reached a constant stress at the maximum beam width, whereas the 3 % lines of fit (blue) still have a slightly negative gradient at this point. In order to obtain a more precise value for $\sigma_0$ a data point from a larger width beam (e.g. 10 μm) would be required.

An explanation for the strain dependence of $A$ is that a higher maximum strain implies a larger strain gradient, and a greater number of dislocations piled up at the neutral axis. This means that there is a bigger back stress acting to resist the operation of dislocation sources, leading to a stronger size effect than for beams at 1.5 % strain, where back stresses are smaller.

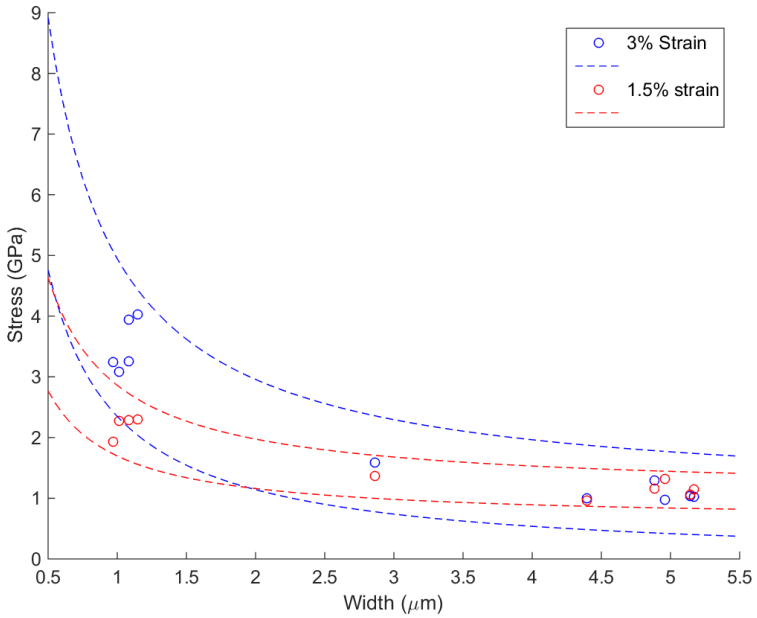


Figure 7-12: Flow stress at 1.5 % strain (red) and 3 % strain (blue) with the upper and lower 95 % confidence bounds used for the $\sigma = Aw^{-1} + \sigma_0$ fit (dotted lines).

## 7.4 Effect of Orientation on Micro-Cantilever Response

Figure 7-13 shows maximum stress-maximum strain curves for cantilevers in the 'multiple slip' orientation shown in Figure 7-7. The plastic flow is characteristically jerky, with many large strain bursts seen after the yield point. Compared to the beams seen in Figure 7-9, the unloading curves are straighter for the 'multiple slip' beams. The more curved unloading behaviour seen in Figure 7-9 is possibly due to some reversible plasticity taking place, due to back stresses from dislocations piled-up at the neutral axis, which relax upon unloading. With a greater number of active slip systems in the 'multiple slip' orientation, dislocation pile-ups at the neutral axis might be relatively weaker, leading to a lower stresses to relax upon unloading.

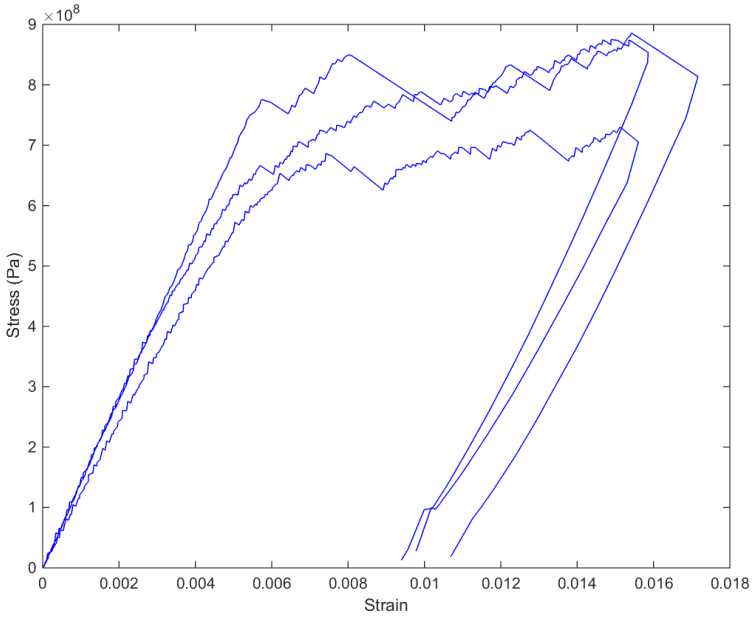


Figure 7-13: Maximum stress-maximum strain curves from micro-cantilevers in the 'multiple slip' orientation.

Figure 7-14 shows a comparison between the stress-strain behaviour of 5 µm wide beams in the 'multiple slip' orientation (blue) with those in the 'single slip' orientation (red). The experimental Young's modulus is calculated to be 133 GPa for the multiple slip beams, and 200 GPa for the single slip beams, compared to theoretical values of 132 GPa and 172 GPa, respectively. Although there are large errors associated with these values, the trend with respect to orientation is correct.

'Single slip' aligned beams are observed to reach yield and flow stresses a factor of ~ 1/3 higher than those in the 'multiple slip' beams, despite the fact that the Schmid factors of the best two aligned slip systems in the 'single slip' case are higher than those in 'multiple slip' case. However, as there is a higher number of active slip systems in the multiple slip case, this means that there is a greater availability of potential dislocation sources. Therefore, when the beam is loaded, there is a greater chance that dislocation sources requiring a lower stress to activate are present compared with the 'single slip' case, leading to a lower flow stress. In order to determine the exact nature of the deformation in both the 'single slip' and

'multiple slip' orientations, a greater range of testing conditions is required, including varying the dislocation source density in addition to the orientation, so that the competing effects of source density and slip system alignment could be determined.

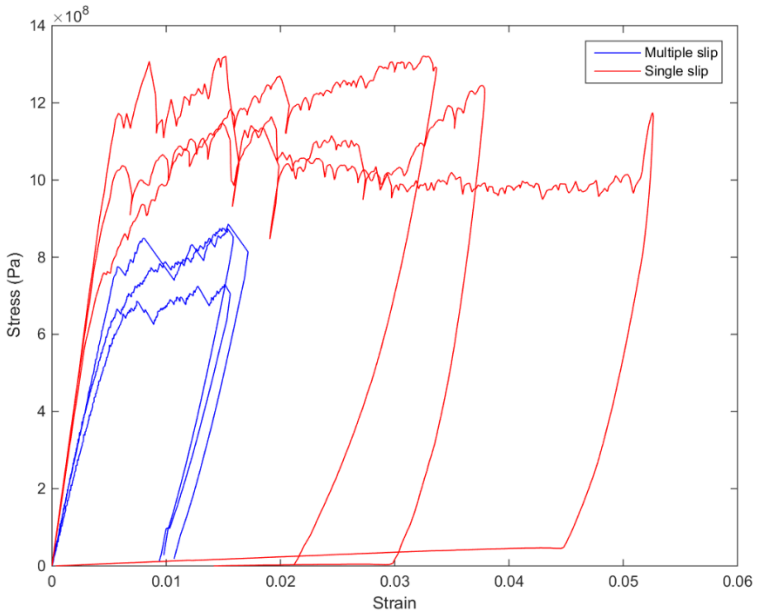


Figure 7-14: Maximum stress-maximum strain curves of micro-cantilevers in the 'multiple slip' orientation (blue) compared with micro-cantilevers in the 'single slip' orientation (red).

## 7.5 Conclusion

Micro-cantilevers in a range of orientations and sizes have been tested in order to investigate how these factors influence the mechanical response. The effect of size has been studied on beams in an orientation for which only a few slip systems are available. The flow stress increased substantially as the beam width decreases, in line with previous 'size effect' studies. In order to rationalise the relationship between flow stress and specimen size, two fits to the data were attempted. A power law of the form $\sigma = Aw^n$, which has been used extensively in previous studies was found to satisfactorily fit the experimental data, however the implication of a steadily decreasing flow stress with increasing specimen size was deemed unphysical. An alternative approach, with a constant term included and an exponent of *n = -1*

also fit the experimental data well, whilst being more realistic. Dunstan and Bushby [175] have argued that such an exponent is consistent with existing size effect data, and can be physically argued in terms of the space available for dislocation source operation.

The previous usage of power law fits in the micromechanics literature is a consequence of the use of log-log plots to which straight lines have been fitted. For example, Dou and Derby [47] have argued that all micro-pillar data can be fitted to a normalised power law with an exponent of $n = 0.66$. However, such plots have the potential to obscure underlying trends in the data. Furthermore, much of the size effect data has been collected on soft pure fcc metals, whereas bcc and hcp metals, with relatively larger $\sigma_0$ values, have been less studied.

The effect of orientation has also been studied, with beams of same size tested in a 'multiple slip' and 'single slip' configurations. The flow stress of the 'multiple slip' beams was approximately 2/3$^{rds}$ that of the 'single slip' beams, which was attributed to the greater availability of dislocation sources in the multiple slip beam. To give greater insight into this, it would be desirable to conduct a further study using a range of differently sized <100> aligned beams, to test the effect of specimen size on flow stress in this orientation.

To better understand the underlying mechanisms contributing towards the mechanical behaviour of micro-cantilevers, further work is needed to study the dislocation structures formed during testing, through ex-situ TEM [177] and HR-EBSD. By studying such processes, it should be possible to better understand the size dependent behaviour in such beams, and therefore to better know the conditions under which micro-cantilevers can be used as a proxy for large scale tests on fusion relevant materials.

# 8 Summary

In this thesis, small scale mechanical testing has been used to study a diverse range of materials problems. According to the particular application, either 'straight' nanoindentation or the testing of FIB-machined specimens in a nanoindenter have been used to extract mechanical results from micron-sized volumes of material. Both techniques have advantages and limitations, and a careful consideration of the desired information is necessary to guide the choice of which one to use.

In **Chapter 4**, the effect of crystal orientation on the indentation load-displacement, hardness and modulus of materials was tested. A clear relationship between hardness and orientation was established and plotted on an inverse pole figure, showing a 20 % increase in hardness for indents made in grains with a surface normal near the <111> or <110> direction, compared to the <100> surface normal. The elastic strain and lattice rotation fields surrounding selected indents in grains with these surface normals were examined using HR-EBSD, with strains and flow patterns showing highly orientation dependent behaviour. Lower bound solutions for GND density were calculated from the lattice rotations, showing variations in density closer to the indent in the <111> and <110> cases, compared to further field variations in the <100> case, potentially giving rise to the differences in hardness. No clear relationship between indentation modulus and orientation was observed, indicating the need for test specimens with a simpler stress state to extract meanful elastic properties.

Following on from this, a novel technique using an L-shaped micro-cantilever was developed, to extract the full set of cubic single crystal elastic constants from within a single grain of a polycrystal (**Chapter 5**). The L-shape design was able to do this by allowing the torsional response of the beam to be probed, making it possible to separate out the mechanical

response caused by constants which were previously coupled in simple bend tests. The beam was manufactured using the FIB, before being loaded at several points along both arms, within the elastic limit. For the analysis, the complexity of the elastic response necessitated the use of an FE model, which was thoroughly optimised to ensure its reliability. To circumvent the computational cost of independentally varying three constants over their entire parameter space, a minimisation routine was developed in which one constant was varied per step, for a beam orientation and loading position particularly sensitive to changes in that constant. The validity of this approach was established by applying it to simulated stiffness data generated using elastic constants from the literature. Two runs of the minimisation routine using different sets of real data yielded two sets of single crystal elastic constants. Values of shear modulus calculated using both sets of constants deviated from previous literature values by less than 10 %, whereas values of Young's modulus were a maximum of ~ 20 % out for the first run and ~ 10 % out for the second run. As a better understanding of the key experimental parameters for maximum accuracy in the analysis has now been established (i.e. measurement of the fixed arm depth and loading position), it is likely that further testing would be able to improve on these errors.

In **Chapter 6**, 'straight' nanoindentation was used to investigate the phenomenon of slip transfer at grain boundaries, with comparisons made between unirradiated and ion-irradiated materials. Grain boundary pop-in events were observed as evidence of slip transfer, and associated with the relaxation of pile-up stress due to the operation of a dislocation source in the grain adjacent to the one being indented. Such pop-in events were suppressed in the ion-irradiated sample, with fewer being observed, and the average size of the displacement burst smaller in those that were. The grain boundaries were shown to influence the hardness measured during indentation at a narrower range of indent to grain

boundary distances, and they had a weaker effect compared to boundaries in the unirradiated material (partially attributable to the smaller plastic zone size surrounding the indenter tip in the irradiated sample). The stress intensity factor for slip transfer was approximately calculated for both samples, with the lower values obtained in the irradiated sample indicating that grain boundaries offered less resistance to slip transfer than in the unirradiated sample. The stress intensity factor was found to be roughly proportional to the disorientation angle across the grain boundaries, and also showed a weak inverse trend with a factor taking into account the alignment of slip systems across the boundary, $m$'.

Finally, **Chapter 7** presented data obtained from differently aligned micro-cantilevers, with one set nominally orientated for 'single slip' and the other orientated for 'multiple slip'. For the 'single slip' set, three different beam sizes were tested to study the effect of specimen size on the measured mechanical properties. Flow stress for the different beam sizes was evaluated at 1 % and 3 % maximum strain, and the variation with beam width fitted to (i) a power law ($\sigma = Aw^n$), and (ii) an inverse function with a constant term ($\sigma = Aw^n + \sigma_0$). The data fit well to both expressions, however the latter function was more physically justifiable given a non-zero bulk strength. A lower flow stress was observed in the beams orientated for multiple slip as compared with the single slip orientation, despite the best aligned slip system in the single slip case having a higher Schmid factor than for the other orientation. This was explained in terms of the greater density of dislocation sources available in the multiple slip case, due to more slip systems being active, and therefore accomodating the plastic strain more easily.

These studies show the potential of small scale mechanical testing to investigate a range of different phenomena, using the simpler stress states but longer experiment times for FIB-

machined specimens, and the complicated stress states but better statistics and faster experiment times for ‘straight’ indentation. Due to the need to extract mechanical properties from thin damaged layers in order to better understand the properties of candidate materials for nuclear applications, both these techniques should be used, as they can provide complementary information to each other.

Further understanding of the size dependent plastic behaviour of micro-cantilevers is needed, including in ion-irradiated specimens, in order to be able to use such tests to extract real mechanical properties of fusion relevant materials.

# 9 References


[1] CCFE, *http://www.ccfe.ac.uk/images.aspx*, 2015.

[2] N. Baluc, Plasma Phys. Controlled Fusion **48**, B165 (2006).

[3] S. G. Roberts, *An ABC of Fusion Materials* [PowerPoint slides], Fusion Frontiers and Interfaces conference, York, May 2010.

[4] H. Czichos, T. Saito, and L. E. Smith, *Springer Handbook of Materials Measurement Methods* (Springer, 2006), p. 1208.

[5] J. B. Pethica, R. Hutchings, and W. C. Oliver, Philosophical Magazine A-Physics of Condensed Matter Structure Defects and Mechanical Properties **48**, 593 (1983).

[6] D. Tabor, Journal of the Institute of Metals **79**, 1 (1951).

[7] W. D. Nix and H. J. Gao, J. Mech. Phys. Solids **46**, 411 (1998).

[8] J. B. Pethica, R. Hutchings, and W. C. Oliver, Nuclear Instruments and Methods in Physics Research **209-210, Part 2**, 995 (1983).

[9] W. C. Oliver and G. M. Pharr, J. Mater. Res. **7**, 1564 (1992).

[10] M. F. Doerner and W. D. Nix, J. Mater. Res. **1** (1986).

[11] W. C. Oliver and G. M. Pharr, J. Mater. Res. **19**, 3 (2004).

[12] H. M. Ledbetter and R. P. Reed, J. Phys. Chem. Ref. Data **Vol. 2, No. 3**, 531 (1973).

[13] J. G. Swadener and G. M. Pharr, Philosophical Magazine A-Physics of Condensed Matter Structure Defects and Mechanical Properties **81**, 447 (2001).

[14] J. R. Greer, W. C. Oliver, and W. D. Nix, Acta Materialia **53**, 1821 (2005).

[15] O. Kraft and C. A. Volkert, Advanced Engineering Materials **3**, 99 (2001).

[16] P. Hosemann, C. Vieh, R. R. Greco, S. Kabra, J. A. Valdez, M. J. Cappiello, and S. A. Maloy, J. Nucl. Mater. **389**, 239 (2009).

[17] C. Heintze, C. Recknagel, F. Bergner, M. Hernandez-Mayoral, and A. Kolitsch, Nuclear Instruments & Methods in Physics Research Section B-Beam Interactions with Materials and Atoms **267**, 1505 (2009).

[18] C. Heintze, F. Bergner, and M. Hernandez-Mayoral, J. Nucl. Mater. **417**, 980 (2011).

[19] T. Miura, K. Fujii, K. Fukuya, and K. Takashima, J. Nucl. Mater. **417**, 984 (2011).

[20] T. L. Li, Y. F. Gao, H. Bei, and E. P. George, J. Mech. Phys. Solids **59**, 1147 (2011).

[21] L. Wang, H. Bei, T. L. Li, Y. F. Gao, E. P. George, and T. G. Nieh, Scr. Mater. **65**, 179 (2011).

[22] K. L. Johnson, *Contact Mechanics*, 2003), p. 452.

[23] Z. Wang, H. Bei, E. P. George, and G. M. Pharr, Scr. Mater. **65**, 469 (2011).

[24] S. Shim, H. Bei, M. K. Miller, G. M. Pharr, and E. P. George, Acta Materialia **57**, 503 (2009).

[25] K. W. McElhaney, J. J. Vlassak, and W. D. Nix, J. Mater. Res. **13**, 1300 (1998).

[26] E. Demir, D. Raabe, and F. Roters, Acta Materialia **58**, 1876 (2010).

[27] G. M. Pharr, E. G. Herbert, and Y. Gao, Annual Review of Materials Research, Vol 40 **40**, 271 (2010).

[28] H. Mughrabi, Materials Science and Engineering A-Structural Materials Properties Microstructure and Processing **387**, 209 (2004).

[29] J. J. Vlassak and W. D. Nix, J. Mech. Phys. Solids **42**, 1223 (1994).

[30] N. Zaafarani, D. Raabe, R. N. Singh, F. Roters, and S. Zaefferer, Acta Materialia **54**, 1863 (2006).

[31] N. Zaafarani, D. Raabe, F. Roters, and S. Zaefferer, Acta Materialia **56**, 31 (2008).

[32] T. B. Britton, H. Liang, F. P. E. Dunne, and A. J. Wilkinson, Proceedings of the Royal Society A-Mathematical Physical and Engineering Sciences **466**, 695 (2010).

[33] D. Kiener, K. Durst, M. Rester, and A. M. Minor, JOM **61**, 14 (2009).

[34] G. B. Viswanathan, E. Lee, D. M. Maher, S. Banerjee, and H. L. Fraser, Acta Materialia **53**, 5101 (2005).

[35] D. E. J. Armstrong, C. D. Hardie, J. S. K. L. Gibson, A. J. Bushby, P. D. Edmondson, and S. G. Roberts, J. Nucl. Mater. **462**, 374 (2015).

[36] M. D. Uchic, D. M. Dimiduk, J. N. Florando, and W. D. Nix, Science **305**, 986 (2004).

[37] C. Motz, T. Schoberl, and R. Pippan, Acta Materialia **53**, 4269 (2005).

[38] D. Kiener, C. Motz, T. Schoeberl, M. Jenko, and G. Dehm, Advanced Engineering Materials **8**, 1119 (2006).

[39] J. Gong and A. J. Wilkinson, Acta Materialia **57**, 5693 (2009).

[40] D. Kiener, W. Grosinger, G. Dehm, and R. Pippan, Acta Materialia **56**, 580 (2008).

[41] M. D. Uchic and D. A. Dimiduk, Materials Science and Engineering A-Structural Materials Properties Microstructure and Processing **400**, 268 (2005).

[42] M. D. Uchic, P. A. Shade, and D. M. Dimiduk, Annual Review of Materials Research **39**, 361 (2009).

[43] M. D. Uchic, P. A. Shade, and D. M. Dimiduk, JOM **61**, 36 (2009).

[44] O. Kraft, P. A. Gruber, R. Moenig, and D. Weygand, Annual Review of Materials Research, Vol 40 **40**, 293 (2010).

[45] J. R. Greer and J. T. M. De Hosson, Progress in Materials Science **56**, 654 (2011).

[46] J. R. Greer and W. D. Nix, Physical Review B **73**, 245410 (2006).

[47] R. Dou and B. Derby, Scr. Mater. **61**, 524 (2009).

[48] T. A. Parthasarathy, S. I. Rao, D. M. Dimiduk, M. D. Uchic, and D. R. Trinkle, Scr. Mater. **56**, 313 (2007).

[49] S. Brinckmann, J. Kim, and J. R. Greer, Phys. Rev. Lett. **100**, 155502 (2008).

[50] D. Kaufmann, R. Mönig, C. A. Volkert, and O. Kraft, Int. J. Plast. **27**, 470 (2011).

[51] J. R. Greer, C. R. Weinberger, and W. Cai, Materials Science and Engineering: A **493**, 21 (2008).

[52] A. S. Schneider, D. Kaufmann, B. G. Clark, C. P. Frick, P. A. Gruber, R. Moenig, O. Kraft, and E. Arzt, Phys. Rev. Lett. **103**, 105501 (2009).

[53] Q. Sun, Q. Guo, X. Yao, L. Xiao, J. R. Greer, and J. Sun, Scr. Mater. **65**, 473 (2011).

[54] S. Cheng, X. Wang, H. Choo, and P. K. Liaw, Appl. Phys. Lett. **91**, 201917 (2007).

[55] C. J. Lee, J. C. Huang, and T. G. Nieh, Appl. Phys. Lett. **91**, 161913 (2007).

[56] S. Korte and W. J. Clegg, Scr. Mater. **60**, 807 (2009).

[57] S. X. Song, Y. H. Lai, J. C. Huang, and T. G. Nieh, Appl. Phys. Lett. **94**, 061911 (2009).

[58] A. S. Schneider, B. G. Clark, C. P. Frick, P. A. Gruber, and E. Arzt, Materials Science and Engineering A-Structural Materials Properties Microstructure and Processing **508**, 241 (2009).

[59] D. Kiener, P. Hosemann, S. A. Maloy, and A. M. Minor, Nature Materials **10**, 608 (2011).

[60] E. M. Grieveson, D. E. J. Armstrong, S. Xu, and S. G. Roberts, J. Nucl. Mater. **430**, 119 (2012).

[61] H. Zhang, B. E. Schuster, Q. Wei, and K. T. Ramesh, Scr. Mater. **54**, 181 (2006).

[62] D. Kiener, C. Motz, and G. Dehm, J. Mater. Sci. **43**, 2503 (2008).

[63] D. E. J. Armstrong, A. J. Wilkinson, and S. G. Roberts, J. Mater. Res. **24**, 3268 (2009).

[64] Y. L. Chan, A. H. W. Ngan, and N. M. King, Journal of the Mechanical Behavior of Biomedical Materials **2**, 375 (2009).

[65] J. Gong and A. Wilkinson, Philosophical Magazine Letters **90**, 503 (2010).

[66] D. Di Maio and S. G. Roberts, J. Mater. Res. **20**, 299 (2005).

[67] D. E. J. Armstrong, M. E. Rogers, and S. G. Roberts, Scr. Mater. **61**, 741 (2009).

[68] D. Kiener, C. Motz, W. Grosinger, D. Weygand, and R. Pippan, Scr. Mater. **63**, 500 (2010).

[69] D. E. J. Armstrong, A. J. Wilkinson, and S. G. Roberts, Probing Mechanics at Nanoscale Dimensions **1185**, 7 (2009).

[70] H. Dugdale, D. E. J. Armstrong, E. Tarleton, S. G. Roberts, and S. Lozano-Perez, Acta Materialia **61**, 4707 (2013).

[71] D. E. J. Armstrong, A. J. Wilkinson, and S. G. Roberts, Philosophical Magazine Letters **91**, 394 (2011).

[72] J. Gong and A. J. Wilkinson, Philosophical Magazine **91**, 1137 (2011).

[73] W. L. Chan and M. W. Fu, Materials Science and Engineering A-Structural Materials Properties Microstructure and Processing **528**, 7674 (2011).

[74] C. Motz, D. Weygand, J. Senger, and P. Gumbsch, Acta Materialia **56**, 1942 (2008).

[75] D. E. J. Armstrong, *Measuring Elastic, Plastic and Fracture Properties using Micro-Cantilever Testing* (University of Oxford, 2009).

[76] A. R. Beaber, J. D. Nowak, O. Ugurlu, W. M. Mook, S. L. Girshick, R. Ballarini, and W. W. Gerberich, Philos. Mag. **91**, 1179 (2011).

[77] James Gibson and David Armstrong and,Steve Roberts, Phys. Scripta **2014**, 014056 (2014).

[78] D. Kiener, C. Motz, M. Rester, M. Jenko, and G. Dehm, Materials Science and Engineering A-Structural Materials Properties Microstructure and Processing **459**, 262 (2007).

[79] H. Bei, S. Shim, E. P. George, M. K. Miller, E. G. Herbert, and G. M. Pharr, Scr. Mater. **57**, 397 (2007).

[80] H. Bei, S. Shim, G. M. Pharr, and E. P. George, Acta Materialia **56**, 4762 (2008).

[81] J. Gong and A. J. Wilkinson, Acta Materialia **59**, 5970 (2011).

[82] Micro Materials, *http://www.micromaterials.co.uk/the-nano-test/nanotest-vantage/*, 2015.

[83] Hysitron, *http://www.hysitron.com/products/pi-series*, 2015.

[84] M. R. VanLandingham, Journal of Research of the National Institute of Standards and Technology **108**, 249 (2003).

[85] A. C. Fischer-Cripps and SpringerLink, *Nanoindentation* (Springer New York : Imprint: Springer, New York, NY, 2011), p. 282.

[86] X. Li and B. Bhushan, Mater Charact **48**, 11 (2002).

[87] D. Dingley, J. Microsc. -Oxf. **213**, 214 (2004).

[88] S. Kikuchi, Japanese Journal of Physics **5**, 83-86 (1928).

[89] B. L. Adams, Ultramicroscopy **67**, 11 (1997).

[90] J. A. Small and J. R. Michael, Journal of Microscopy-Oxford **201**, 59 (2001).

[91] A. J. Wilkinson, G. Meaden, and D. J. Dingley, Ultramicroscopy **106**, 307 (2006).

[92] A. J. Wilkinson, E. E. Clarke, T. B. Britton, P. Littlewood, and P. S. Karamched, J. Strain Anal. Eng. Des. **45**, 365 (2010).

[93] C. A. Volkert and A. M. Minor, MRS Bull **32**, 389 (2007).

[94] P. R. Munroe, Mater Charact **60**, 2 (2009).

[95] R. M. Langford and A. K. Petford-Long, Journal of Vacuum Science & Technology A-Vacuum Surfaces and Films **19**, 2186 (2001).

[96] D. Lloyd, Part II University of Oxford, 2011.

[97] E. Healy, Part II University of Oxford, 2013.

[98] A. J. Wilkinson and D. Randman, Philosophical Magazine **90**, 1159 (2010).

[99] A. J. Wilkinson and T. B. Britton, Materials Today **15**, 366 (2012).

[100] J. F. Nye, Acta Metallurgica **1**, 153 (1953).

[101] C. D. Hardie, DPhil University of Oxford, 2013.

[102] D. Rugg, M. Dixon, and F. P. E. Dunne, J. Strain Anal. Eng. Des. **42**, 269 (2007).

[103] M. Y. Lavrentiev, D. Nguyen-Manh, and S. L. Dudarev, Physical Review B **81**, 184202 (2010).

[104] M. Friak, M. Sob, and V. Vitek, Philosophical Magazine **83**, 3529 (2003).

[105] H. Zhang, B. Johansson, and L. Vitos, Physical Review B **79**, 224201 (2009).

[106] S. P. Fitzgerald and S. L. Dudarev, Proceedings of the Royal Society A-Mathematical Physical and Engineering Sciences **464**, 2549 (2008).

[107] S. L. Dudarev, R. Bullough, and P. M. Derlet, Phys. Rev. Lett. **100**, 135503 (2008).

[108] S. P. Fitzgerald, S. Aubry, S. L. Dudarev, and W. Cai, Modell Simul Mater Sci Eng **20**, 045022 (2012).

[109] S. P. Fitzgerald and Z. Yao, Philosophical Magazine Letters **89**, 581 (2009).

[110] S. Aubry, S. P. Fitzgerald, S. L. Dudarev, and W. Cai, Modell Simul Mater Sci Eng **19**, 065006 (2011).

[111] R. J. Talling, R. J. Dashwood, M. Jackson, S. Kurarnoto, and D. Dye, Scr. Mater. **59**, 669 (2008).

[112] J. M. Gere and B. J. Goodno, *Mechanics of materials* (Van Nostrand Reinhold Co., New York, 2012), p. 1098.

[113] J. F. Nye, *Physical properties of crystals, their representation by tensors and matrices* (Clarendon Press, Oxford, 1957), p. 322.

[114] G. E. Dieter, *Mechanical metallurgy* (McGraw-Hill, New York, 1961), p. 615.

[115] E. Schmid and W. Boas, *Plasticity of crystals with special reference to metals* (F.A. Hughes, London, 1950), p. 353.

[116] G. Simmons and H. Wang, *Single crystal elastic constants and calculated aggregate properties* (Southern Methodist University Press, Dallas, 1971), 34, p. 269.

[117] J. J. Adams, D. S. Agosta, R. G. Leisure, and H. Ledbetter, J. Appl. Phys. **100**, 113530 (2006).

[118] H. Ledbetter, Materials Science and Engineering A-Structural Materials Properties Microstructure and Processing **165**, L9 (1993).

[119] G. Li and J. R. Gladden, International Journal of Spectroscopy **2010** (2010).

[120] V. E. Goens and E. Schmid, Naturwiss. **19**, 520 (1931).

[121] R. F. S. Hearmon, Reviews of Modern Physics **18**, 409 (1946).

[122] J. A. Rayne and B. S. Chandrasekhar, Physical Review **122**, 1714 (1961).

[123] A. E. Lord and D. N. Beshers, J. Appl. Phys. **36**, 1620 (1965).

[124] C. A. Rotter and C. S. Smith, Journal of Physics and Chemistry of Solids **27**, 267 (1966).

[125] J. Leese and A. E. Lord, J. Appl. Phys. **39**, 3986 (1968).

[126] D. J. Dever, J. Appl. Phys. **43**, 3293 (1972).

[127] ABAQUS, Simulia Providence, RI: Dassault Systémes (2014).

[128] ABAQUS, Abaqus 6. 13 Getting Started with Abaqus: Interactive Edition (2014).

[129] M. T. Robinson, J. Nucl. Mater. **216**, 1 (1994).

[130] G. S. Was, J. P. Wharry, B. Frisbie, B. D. Wirth, D. Morgan, J. D. Tucker, and T. R. Allen, J. Nucl. Mater. **411**, 41 (2011).

[131] E. Wakai, N. Hashimoto, Y. Miwa, J. P. Robertson, R. L. Klueh, K. Shiba, and S. Jistukawa, J. Nucl. Mater. **283–287, Part 2**, 799 (2000).

[132] G. Ayrault, J. Nucl. Mater. **114**, 34 (1983).

[133] J. Henry, M. -. Mathon, and P. Jung, J. Nucl. Mater. **318**, 249 (2003).

[134] K. S. Ng and A. H. W. Ngan, Philosophical Magazine **89**, 3013 (2009).

[135] A. Kunz, S. Pathak, and J. R. Greer, Acta Materialia **59**, 4416 (2011).

[136] J. Y. Zhang, G. Liu, and J. Sun, Int. J. Plast. **50**, 1 (2013).

[137] P. J. Imrich, C. Kirchlechner, C. Motz, and G. Dehm, Acta Materialia **73**, 240 (2014).

[138] D. Hull and D. J. Bacon, *Introduction to Dislocations* (Butterworth-Heinemann, 2011).

[139] E. O. Hall, Proceedings of the Physical Society of London Section B **64**, 747 (1951).

[140] N. PETCH, Journal of the Iron and Steel Institute **174**, 25 (1953).

[141] D. J. Dunstan and A. J. Bushby, Int. J. Plast. **53**, 56 (2014).

[142] T. B. Britton, Part II University of Oxford, 2007.

[143] D. Randman, Part II University of Oxford, 2006.

[144] A. Sutton and R. Balluffi, *Interfaces in Crystalline Materials* (Oxford University Press, 1996).

[145] T. B. Britton, D. Randman, and A. J. Wilkinson, J. Mater. Res. **24**, 607 (2009).

[146] T. C. Lee, I. M. Robertson, and H. K. Birnbaum, Scripta Metallurgica **23**, 799 (1989).

[147] W. A. T. Clark, R. H. Wagoner, Z. Y. Shen, T. C. Lee, I. M. Robertson, and H. K. Birnbaum, Scripta Metallurgica Et Materialia **26**, 203 (1992).

[148] M. de Koning, R. J. Kurtz, V. V. Bulatov, C. H. Henager, R. G. Hoagland, W. Cai, and M. Nomura, J. Nucl. Mater. **323**, 281 (2003).

[149] N. Zhang and W. Tong, Int. J. Plast. **20**, 523 (2004).

[150] Brentnal.Wd and W. Rostoker, Acta Metallurgica **13**, 187 (1965).

[151] J. J. Hauser and B. Chalmers, Acta Metallurgica **9**, 802 (1961).

[152] P. J. Worthington and E. Smith, Acta Metallurgica **12**, 1277 (1964).

[153] Z. Shen, R. H. Wagoner, and W. A. T. Clark, Acta Metallurgica **36**, 3231 (1988).

[154] J. Gemperlova, A. Jacques, A. Gemperle, and N. Zarubova, Mater. Res. Soc. Proc. **652** (2001).

[155] T. Ohmura, A. M. Minor, E. A. Stach, and J. W. Morris, J. Mater. Res. **19**, 3626 (2004).

[156] P. C. Wo and A. H. W. Ngan, J. Mater. Res. **19**, 189 (2004).

[157] K. E. Aifantis, W. A. Soer, J. T. M. De Hosson, and J. R. Willis, Acta Materialia **54**, 5077 (2006).

[158] S. Pathak, J. Michler, K. Wasmer, and S. R. Kalidindi, J. Mater. Sci. **47**, 815 (2012).

[159] W. A. Soer and J. T. M. De Hosson, Mater Lett **59**, 3192 (2005).

[160] W. A. Soer, K. E. Aifantis, and J. T. M. De Hosson, Acta Materialia **53**, 4665 (2005).

[161] T. Ohmura, K. Tsuzaki, and F. X. Yin, Materials Transactions **46**, 2026 (2005).

[162] T. Eliash, M. Kazakevich, V. N. Semenov, and E. Rabkin, Acta Materialia **56**, 5640 (2008).

[163] M. G. Wang and A. H. W. Ngan, J. Mater. Res. **19**, 2478 (2004).

[164] Y. M. Soifer, A. Verdyan, M. Kazakevich, and E. Rabkin, Scr. Mater. **47**, 799 (2002).

[165] A. H. Cottrell and B. A. Bilby, Proceedings of the Physical Society of London Section a **62**, 49 (1949).

[166] K. JOHNSON, J. Mech. Phys. Solids **18**, 115 (1970).

[167] Y. L. Chiu and A. H. W. Ngan, Acta Materialia **50**, 2677 (2002).

[168] D. Kramer, H. Huang, M. Kriese, J. Robach, J. Nelson, A. Wright, D. Bahr, and W. W. Gerberich, Acta Materialia **47**, 333 (1999).

[169] D. E. Kramer, A. A. Volinsky, N. R. Moody, and W. W. Gerberich, J. Mater. Res. **16**, 3150 (2001).

[170] C. D. Hardie, S. G. Roberts, and A. J. Bushby, J. Nucl. Mater. **462**, 391 (2015).

[171] G. M. Pharr and W. C. Oliver, MRS Bull **17**, 28 (1992).

[172] E. Demir, D. Raabe, N. Zaafarani, and S. Zaefferer, Acta Materialia **57**, 559 (2009).

[173] J. Le Coze, *Procurement of Pure Fe Metal and Fe-based Alloys with Controlled Chemical Alloying Element Contents and Microstructure: Final Report On Model Alloy Preparation*, 2007).

[174] C. Erginsoy, A. Englert, and G. H. Vineyard, Physical Review A-General Physics **133**, A595 (1964).

[175] D. J. Dunstan and A. J. Bushby, Int. J. Plast. **40**, 152 (2013).

[176] E. Tarleton, D. S. Balint, J. Gong, and A. J. Wilkinson, Acta Materialia **88**, 271 (2015).

[177] R. Ding, J. Gong, A. J. Wilkinson, and I. P. Jones, Acta Materialia **76**, 127 (2014).